

**COMBINED EARTH-/STAR SENSOR
FOR
ATTITUDE AND ORBIT DETERMINATION
OF
GEOSTATIONARY SATELLITES**

Von der Fakultät Luft- und Raumfahrttechnik und Geodäsie
der Universität Stuttgart zur Erlangung der Würde eines
Doktor- Ingenieurs (Dr.-Ing.) genehmigte Abhandlung

vorgelegt von

Christopher T.F. Kühl

geboren in Mainz

Hauptberichter: Professor Klaus H. Well, Ph.D.

Erster Mitberichter: Professor Dr. techn. Klaus Janschek

Zweite Mitberichter: Hon.-Prof. Dr.-Ing. Eveline Gottzein

Tag der mündlichen Prüfung: 04. März 2005

Institut für Flugmechanik und Flugregelung
Universität Stuttgart
2005

„Nichts sieht hinterher so einfach aus, wie eine verwirklichte Idee.“

Wernher Freiherr von Braun (1912-1977)

Acknowledgement

At this point I want to thank all those, who made this thesis possible and helped in leading it to a successful end.

For guidance and control of this thesis, I want to thank my advisor Professor K. H. Well, Ph.D., director of the Institute for Flight Dynamics and Flight Control at the University of Stuttgart.

I am grateful to Professor K. Janschek for his advice and his contribution to this piece of work.

I want to express my gratitude to hon.-Professor Dr. E. Gottzein who initiated this research and laid the foundation to the results as they are presented and her continuous active support during this thesis.

There were many people involved in this project, all of which shall know that, even if they do not appear in this acknowledgement, their help was very much appreciated.

In particular I want to thank M. Melf and S. Manhart, *Astrium-Optical Instruments*, who provided me with the in-orbit results and helpful recommendations. In EADS-CRC, responsible for the image-processing algorithms, I want to thank Dr. H. Zinner and H. Diehl for their continuous support. Representing EADS Astrium GmbH, I want to thank Dr. W. Oesterlin and Dr. G. Lange whose personal and financial support was substantial for the successful introduction of the results to the space community.

The Daimler-Chrysler Fellowship Program provided me with valuable knowledge about social structures and first insights into company organizations.

Eumetsat very quickly and reliably provided me with data from the METEOSAT weather-satellite.

Finally I want to thank my parents; due to their support I was able to fully concentrate on my studies and successfully complete this thesis.

Kombinierter Erd-/ Stern-Sensor zur Lage- und Bahnbestimmung in geostationären Orbits

Thema der Arbeit ist ein Sensor zur autonomen Lage- und Bahnbestimmung von Satelliten, der auf der Active Pixel Technologie basiert. Der Einsatzbereich erstreckt sich hierbei von *niedrigen Orbits* (LEO), über *GEO Transfer-Orbits* (GTO) bis hin zu *geostationären Orbits* (GEO). Der Vorschlag zu diesem Ansatz ist in einem Patent der Daimler-Chrysler AG ([1]) niedergelegt. Das System charakterisiert sich durch zwei Beobachtungsrichtungen, deren Bilder über einen Strahlteiler auf einem Detektor kombiniert werden. Hierbei wird der Eingang zur Beobachtung der Erde durch einen Filter abgeschwächt, um ihre Helligkeit der der Sterne anzupassen. Durch die Kombination der Beobachtungsrichtungen führt man die Funktionalitäten eines Erd- und eines Stern-Sensors in einem einzigen Gerät zusammen. Diese Kombination ermöglicht sowohl die Bestimmung der inertialen Lage des Satelliten, als auch dessen Position relativ zur Erde.

Ziel der Doktorarbeit ist die Entwicklung und Bewertung der zur Lage-, Positions- und Bahnbestimmung benötigten Algorithmen, der Aufbau eines Prototyps und einer Testumgebung zur Verifikation der Funktionalität und der Leistungsgrenzen des Sensors. Die Bewertung der Anwendbarkeit der Algorithmen unter realen Bedingungen wurde für niedrige Orbits insbesondere durch die Auswertung eines Flugexperiments ermöglicht, bei dem ein Funktionsmuster des Sensors zur Rohdatengewinnung als Gastmission auf dem italienischen Technologiesatelliten MITA gestartet wurde. Für die Bewertung der Algorithmen unter den auf geostationären Orbit herrschenden Bedingungen wurden METEOSAT-Daten herangezogen. Die Ergebnisse dieser Experimente wurden durch weitere Laborexperimente und Messkampagnen gestützt.

Entsprechend ihres Inhaltes ist die Arbeit strukturiert: Besonderer Wert wurde hierbei auf die Bereiche Algorithmik, Simulation und Versuchsauswertung gelegt. Sie endet mit einer Zusammenfassung des Gesamtergebnisses und den im Laufe der Arbeit erkannten Besonderheiten des Systems.

Persönliche Leistungen dieser Arbeit betreffen

in den **bildverarbeitenden Algorithmen:**

- *Star-tracking* bei niedrigen Drehraten, welches ohne die Notwendigkeit einer Sternidentifikation Sterne nachverfolgen kann, und somit eine Drehratenbestimmung ermöglicht,
 - die Sternidentifikation bei großen Toleranzen in den Messungen,
 - die Implementierung von Lagebestimmungsalgorithmen unter Matlab,
 - die Untersuchung der Variabilität des Erdrandes,
-

- Genauigkeitsabschätzung der Algorithmen.

In den **Algorithmen zur Bestimmung von Position und Orbit**:

- die Beobachtbarkeitsanalyse für das vorgeschlagene System,
- die Entwicklung der Algorithmen zur Positionsbestimmung,
- die Entwicklung der Algorithmen zur Orbitbestimmung,
- Genauigkeitsabschätzung der Algorithmen.

Bezüglich der **Experimente und Testumgebung**:

- die Auswertung des Flugexperiments auf MITA,
- die Auswertung von METEOSAT Bilddaten,
- die Entwicklung einer Simulations- und Testumgebung unter Matlab,
- Aufbau, Durchführung und Auswertung von Laborexperimenten in Form eines *Optical Functional Testbed* (OFTB) mit Simulationsumgebung und Funktionsmuster,
- sowie Planung, Durchführung und Auswertung von Feldexperimenten zur Gewinnung von realen Bilddaten.

In Zusammenarbeit mit Astrium-*Optische Instrumente* und EADS-CRC wurden des Weiteren durchgeführt:

- die Simulation der *Point-Spread-Function* (PSF) bei nicht-verzeichnungsfreien Optiken,
- die Entwicklung von Algorithmen zur Sternmittelpunktbestimmung (*Centroiding*),
- *Star-tracking* bei hohen Drehgeschwindigkeiten,
- die Entwicklung von Algorithmen zur Erdrand- und Erdmittelpunktbestimmung,
- die Entwicklung einfacher Kalibriermethoden mit Hilfe von Sternmessungen,
- die Auswertung der Flugdaten.

Hierbei lieferte EADS-CRC insbesondere wesentliche Teile der Bildverarbeitungsalgorithmen.

Zusätzlich wurde das System im Rahmen einer Diplomarbeit (Behrenwaldt [2]) zu einem **Opto-Inertialen System** ausgebaut.

Im Rahmen dieser Arbeit wurden drei Veröffentlichungen ([3, 4, 5]) publiziert, sowie zwei Patente ([6, 7]) beim Deutschen Patentamt eingereicht.

Abstract

The subject of this work is a sensor for autonomous attitude and orbit determination of satellites, based on active pixel technology as it has been proposed in the patent on a „Combined Earth-/Star-Sensor System and Method for Determining the Orbit and Position of Spacecraft“ developed at Daimler-Chrysler ([1]). The sensor covers a wide range of applications, ranging from *Low Earth-Orbits* (LEO) over *GEO Transfer-Orbits* (GTO) to *Geostationary Earth-Orbits* (GEO). The system is characterized by two non-collinear lines-of-sight, which are combined by a beam splitter which as well provides attenuation of the Earth's magnitude. Hereby images of a Star-field, perpendicular to the Earth vector, and the Earth are projected on a single focal plane thereby merging the functionalities of a Star-sensor and an Earth-sensor in a single instrument. The use of such a sensor combination facilitates the determination of a satellite's attitude as well as its position relative to the Earth.

Goal of this work is the development and evaluation of the algorithms necessary for determination of attitude, position and orbit, the setup of a prototype and a laboratory test-environment for verification of the system's feasibility and performance. Particular support for the system's feasibility in LEO was given by a successful flight experiment of a functional model of the proposed sensor on the Italian technology-satellite MITA. The validation for GEO was performed using images provided by METEOSAT. The flight data is supplemented by field- and laboratory- experiments.

This work is divided into sections covering algorithms, simulations and experiments. It closes with the conclusions drawn, the lessons learned from the investigations and a summary of the results.

Personal contributions are the following:

In the **image-processing algorithms**:

- Star-tracking without need for Star-identification for low angular rates,
- Star-identification when dealing with high tolerances,
- Implementation of algorithms for attitude determination using Matlab,
- Investigations on the variability of Earth-horizon measurements,
- Estimation of the expected accuracy.

In the **algorithms on determination of position and orbit**:

- Observability analysis of the proposed system,
 - Development of algorithms for position determination,
-

- Development of algorithms for orbit determination,
- Estimation of the expected accuracy.

And in the **experimental validation**:

- Evaluation of the flight experiment on MITA
- Evaluation of METEOSAT images
- Development of a simulation and test environment using Matlab,
- Setup, execution and evaluation of laboratory experiments, including test environment and functional model in form of an *Optical Functional Testbed* (OFTB),
- Setup, execution and evaluation of field experiments.

Further topics were covered in cooperation with *Astrium-Optical Instruments* and EADS-CRC:

- Simulation of the *Point-Spread-Function* (PSF) for simple optics,
- Star-center determination (Centroiding),
- Star-tracking without need for Star-identification for high angular rates,
- Earth-horizon and Earth-center determination,
- Calibration of optics using Star-pattern images,
- Data acquisition in field experiments,
- Evaluation of flight data.

EADS-CRC in particular contributed essential parts to the image processing algorithms.

As part of a master thesis (Behrenwaldt [2]) the sensor was extended to an opto-inertial system.

In the process, three papers ([3, 4, 5]) were published and two patents ([6, 7]) were submitted for acceptance at the European Patent Office.

Contents

1	Introduction	1
1.1	Motivation	1
1.2	Status of Current Developments	4
1.2.1	Attitude and Orbit Determination	4
1.2.2	Star-sensors	5
1.2.3	Earth-sensors	7
1.2.4	Detectors	8
1.3	Goal of the Thesis	9
1.3.1	Attitude and Orbit Determination	9
1.3.2	Star-sensors	10
1.3.3	Earth-sensors	10
1.3.4	Detectors	10
1.4	Required Investigations	11
1.5	Organization of the Thesis	12
2	Preliminaries	17
2.1	Data-Processing in Star-sensors	17
2.2	Measurement Noise	18
2.3	Coordinate Systems	19
2.4	Attitude Determination	23
2.5	Position Determination	25
2.6	Orbit Determination	26

3	Image Processing Algorithms	27
3.1	Attitude Determination From Star-Measurements	28
3.1.1	Detection of Stars	29
3.1.2	Centroiding	31
3.1.3	Star-Identification	44
3.1.4	Attitude Determination	49
3.1.5	Star-Tracking	56
3.1.6	Initial estimate of the expected accuracy	64
3.2	Earth-Vector Determination	66
3.2.1	Earth-Horizon Detection	66
3.2.2	Earth-Center Determination	72
3.2.3	Initial estimate of the expected accuracy	79
4	Evaluation of the Image Processing Algorithms	81
4.1	Simulations on the Attitude Determination From Star-Measurements	81
4.1.1	Probability of success and computational burden	81
4.1.2	Expected Attitude Accuracy from Star-Observations	84
4.2	Simulations on the Earth Center Determination	86
5	Algorithms on Position and Orbit Determination	89
5.1	Position Determination Using the Combined Earth-/Star-Sensor	89
5.1.1	Deduction of an algorithm for position determination of a satellite	91
5.1.2	Initial estimate of the expected accuracy	92
5.2	Orbit Determination from Consecutive Position Measurements	97
5.2.1	Composition of a Kalman-Filter for Position and Orbit Determination	97
5.2.2	Observability of the proposed system	103
5.2.3	Initial estimate of the expected accuracy	107

6	Evaluation of the Algorithms on Determination of Position and Orbit	109
6.1	Simulations on the Position Determination Using the Combined Earth-/Star-Sensor	109
6.2	Simulations on Orbit Determination from Sequential Position Measurements	111
7	Experimental Validation of the Developed Algorithms	117
7.1	Experiments - Sources	117
7.1.1	MITA Satellite Experiments	117
7.1.2	Laboratory Experiments with a Complete Sensor Suite	121
7.1.3	Field Experiments	124
7.1.4	METEOSAT Data	125
7.2	Experiments - Results	126
7.2.1	Experiments on Star-Measurements	126
7.2.2	Experiments on Earth-Measurements	133
7.2.3	Experiments on the Position-Determination	140
7.3	Experiments - Conclusions	141
8	Operational Aspects	143
8.1	Acquisition	143
8.2	Critical Mission Phases	144
8.2.1	Mission Scenarios	148
8.2.2	Interpretation of the results	153
8.3	General Considerations	155
9	Lessons Learned and Conclusions Drawn	157
9.1	Lessons Learned	157
9.1.1	Lessons Learned From MITA	157
9.2	Recommendations	159
9.3	Conclusion	162

Bibliography	165
A Appendix	171
A.1 Algorithms	171
A.1.1 Star-Identification, Example	171
A.1.2 Extended Wahba Problem	177
A.1.3 Orbit Determination	179
A.2 Simulations	181
A.2.1 Simulation Environment	181
A.3 Experiments	184
A.3.1 Camera Parameters for cameras used in the experiments	184
A.3.2 Flight Experiment	185
A.4 Miscellaneous	190
A.4.1 Accuracy Requirements	190
A.4.2 Sources of Perturbations	191
A.4.3 Abbreviations & Nomenclature	192
A.5 Curriculum Vitae	196

List of Figures

1.1	Principle of Sextant-Sensor	2
1.2	Sensor-suite of a typical geostationary satellite	4
1.3	Star-tracker and LEO Earth-sensor	5
2.1	Explanation of the planes used in the definition of inertial coordinate-systems	19
2.2	Hill-System	20
2.3	LVLH-System	21
2.4	Body-fixed coordinate system as defined for MITA	22
2.5	Sensor coordinate-system as defined for MTS-AOMS on MITA	22
3.1	Flowchart Sextant-Sensor	27
3.2	Flowchart Star-Sensor	28
3.3	Specified Regions for Star-Detection	30
3.4	Point Spread Function as determined for a Star observed under various angles of incidence and different locations of the detector relative to the focal plane, grid size approx. $80 \times 80 \mu\text{m}^2$ (as reference: pixel size $7 \times 7 \mu\text{m}^2$, detector size approx. $7.2 \times 9 \text{mm}^2$).	33
3.5	Effect of photon-noise on centroiding accuracy in x - and y -direction of a Star being spread over approx. 3×5 pixels, as a function of the Star's visual magnitude.	35
3.6	Schematics of a „simple“ four-lenses consumer optics	36
3.7	Assumptions made for the varying sensitivity across a pixel (left) and photosensitive area of a pixel (right)	38
3.8	Errors made in x - and y -direction in the determination of Star-centroids, when using the „center-of-intensity“-approach for different locations of the detector relative to the focal plane (simulation results)	39

3.9	Nominal (dashed) vs. determined (solid) trajectory of Star-center in y -direction, showing a non-bijective behavior (simulation results)	40
3.10	Expected Errors in Centroiding when rotating the PSF of a Star being 8° off-axis with a detector $+0.1$ mm behind focal plane (simulation results, based on 15 steps per pixel)	41
3.11	Consequences drawn from the different accuracies in x - and y -direction. Centroids in area „1“ provide better accuracies in y -direction, centroids in area „2“ in x -direction.	42
3.12	Use of Centroiding Correction-Tables	43
3.13	Star-Identification Process	44
3.14	Use of <i>a priori</i> information on valid combinations of angles in the triangle composition	46
3.15	Consistency check by comparison of the sense of rotation of the triangle in sensor coordinates to the sense of rotation as given in the Star-catalog	47
3.16	Schematic of parallel use of LARM and the Star-identification process.	57
3.17	Schematics of LARM. The Star-tracking is performed using a reduced „Star-identification“ based on the Centroids of the previous image. In the image the matched Star-patterns are connected by solid lines, the unmatched Stars-patterns by dashed lines.	58
3.18	Schematics of HARM. The Star-tracking is based on two consecutive images, supplemented by the Star’s trace, as it is observed due to the satellite’s rotation during exposure.	59
3.19	Schematics of HARM search grids	63
3.20	Flowchart Earth-Sensor	66
3.21	Search Grid using a GEO-observation as example	67
3.22	Possible Observations of the Horizon as seen from LEO (approx. 300 km orbit height)	71
3.23	Visualization of the necessary transformations to enable circular fitting of measurements (exaggerated eccentricity)	72

3.24	Explanation of the different cost-functions used in the optimal fitting of circles and ellipses	74
3.25	Visualization of the systematic mis-estimation due to fitting a circle to an ellipse (exaggerated eccentricity)	76
3.26	Schematics of the elliptical perception of the Earth as seen under large viewing angles	77
3.27	Comparison of a circle and the simulated image of the horizon as seen from a LEO	78
3.28	Curvature of horizon as seen from LEO	79
4.1	Introduction of noise ($\Delta x, \Delta y$) to the nominal Star-position	82
4.2	Definition of the inter-Star-angle and its nominal accuracy	82
4.3	Probability of correct identification using 5 Stars for different sensor accuracies and different tolerances	83
4.4	Computation Time as a function of tolerance, normalized to 0'' tolerance; Example: 30'' results in a 3.7 times higher computation time necessary for identification .	84
4.5	Attitude Accuracy as a function of number of observed Stars determined for different noise-levels as parameter (10''-60'' in steps of 10''). The star denotes the mean of the accuracy, the dots the results for the different noise-levels. The deviation from the expected inverse square-root of the number of Stars is mainly due to the varying position of the Stars on the detector.	85
4.6	Visualization of optical pathlength when dealing with horizon measurements . . .	86
4.7	Intensity distribution normal to the horizon, analytical result using the preliminaries of an exponentially decreasing air-density and the optical pathlength as defined in fig. 4.6	87
5.1	Coordinate Systems and final formulation of Position Determination Point Solution	90
5.2	State Space Schematics of the Hill-System (defined by A and B) and the Corresponding Observation (defined by C and D)	104
6.1	Construction of the Star-sensor coordinate system for simulations	109

6.2	x -Position Accuracy of the satellite in the ECI reference system, for varying attitudes. The red-colored areas are areas of low accuracy, the blue areas those of high accuracy. e_x , e_y and e_z are the components of the Star-sensor's LOS-vector.	110
6.3	Comparison of error in the orbit radius determination with (green,solid) to without (red,dotted) distance information (GEO, orbit duration 86164sec)	113
6.4	Comparison of error in the orbit radius determination with (green,solid) to without (red,dotted) sensor outage (blue, step function, duration approx. 75 min) (GEO, orbit duration 86164sec)	114
6.5	Comparison of error in the orbit radius determination with (green,solid) to without (red,dotted) high precision orbit propagation, both with sensor outage (blue, step function, duration approx. 75 min) (GEO, orbit duration 86164sec)	115
7.1	Schematics of Italian micro-satellite MITA (<i>Minisatellite Italiano a Tecnologia Avanzata</i>) with Flight Experiment MTS-AOMS; Orbit: 450km, 87.3° (nearly Sun-synchronous [SSO])	118
7.2	Laboratory setup as assembled and used for functional tests	122
7.3	Graphical User Interface of Simulation-Software	123
7.4	Setup in the Bavarian Alps for verification of the Star-identification algorithm	124
7.5	Eumetsat's geostationary weather-satellite METEOSAT	126
7.6	Image obtained using the FillFactory IBIS1 APS-detector Camera	127
7.7	Image obtained using the laboratory setup. The circles denote the position of calibration-„Stars“ given by the OESS. The „Stars“ are seen directly the Earth through the partially transmissive mirror.	128
7.8	Image obtained during a field experiment, including identification of the Stars. The insert shows the location of the identified Stars within the „Big Dipper“	129
7.9	Shape of a Star observed 6.6° off of the LOS, image centered about the brightest pixel	130
7.10	Spin rate of Earth as determined by LARM during field experiment from consecutive images	131
7.11	Artificial 1° Star-smear by superposition of 46 consecutive images taken during field experiment	132

7.12	Image obtained using a 75 mm ground-based telescope, including identification of the Stars.	133
7.13	Comparison of various filters for Earth horizon detection	134
7.14	„Earth“-horizon and -center determination as tested in the laboratory	135
7.15	Image acquired by the METEOSAT-satellite with the result of the Earth-center determination as presented	136
7.16	x -Position of Earth center throughout a day’s cycle, circular fit (dotted) and adapted circular fit (solid)	137
7.17	Cloud coverage throughout the year	138
7.18	Orbit height as determined from MITA images (reference orbit height approx. 450km)	139
8.1	Centered vs. oblique view of Earth, Example: GEO	145
8.2	Image of Sun in unattenuated Star-FOV	145
8.3	Image of Sun at Rim of Earth-FOV	146
8.4	Image of Sunrise in Earth-FOV	147
8.5	Sensor Outages in GEO, centered Earth, Star-LOS in orbit plane	149
8.6	Sensor Outages in GEO, centered Earth, Star-LOS out of orbit plane	150
8.7	Sensor Outages in SSO, oblique Earth, Star-LOS in orbit plane	150
8.8	Sensor Outages in SSO, oblique Earth, Star-LOS out of orbit plane	151
8.9	Sensor Outages in GTO, oblique Earth, Star-LOS in orbit plane	152
8.10	Sensor Outages in GTO, oblique Earth, Star-LOS out of orbit plane	153
9.1	Freeing the center of the FOV for Star-observations	162
A.1	Image to be identified	172
A.2	Star-patterns contained in the Star-catalogue	172
A.3	Parameter Settings Concerning the Orbit Propagation	183
A.4	Parameter Settings Concerning the Simulation	183

A.5	Graphical User Interface, diagnostic mode	183
A.6	Measurement Principle of Angular Rate Sensor (DRS-MM1.0, Bosch)	189
A.7	Perturbations as a function of orbit radius (see [28])	191

List of Tables

1.1	APS specifics as compared to CCD technology	9
3.5	Assumptions made in photon-noise determination	35
3.6	Example for use of correction tables	43
3.9	Comparison of Attitude Determination Algorithms	55
5.1	Formulation of Kalman-Schmidt-filter	99
7.1	Technical Data of Flight-Experiment Platform	118
7.2	Technical Data of Active Pixel Sensor	120
7.3	Technical Data of the MTS-AOMS System	120
7.4	System Accuracies	142
8.1	Definition of sensor-states	144
9.1	Extensions to a „multi-mode sensor“by choice of (adaptive) filters	160
9.2	Expected System Accuracies	163
A.1	Unit vectors to the measurements [-]	173
A.2	Angles between measurements [°]	173
A.3	Unit vectors contained in the Star-catalogue [-]	174
A.4	Angles between Stars in catalogue - Part 1 [°]	174
A.5	Angles between Stars in catalogue - Part 2 [°]	174
A.6	Matching Angles	175
A.7	Matching Triangles	175

A.8 Matching Polygons	175
A.9 Technical Data IBIS1-APS-Detector (Flight-Experiment)	184
A.10 Technical Data IBIS4b-APS-Detector (Laboratory-Experiment, Field-Experiment)	184
A.11 Technical Data PCS-2112-LM-x-APS-Detector (Laboratory-Experiment, Field-Experiment)	184
A.12 Technical Data of Magnetic Field Sensor	186
A.13 Technical Data of Angular Rate Sensor	189
A.14 Accuracy Requirements (3σ) of Typical Missions	190

Chapter 1

Introduction

1.1 Motivation

The determination of the position of a satellite is one of the major tasks throughout the lifetime of satellite - and sometimes even longer than that. While nowadays the position of satellites is mostly determined based on observation by ground stations, there is a tendency towards autonomous attitude and orbit determination of satellites. The goal of this work is the investigation of a new system for on-board-autonomous attitude and orbit determination in orbits ranging from *Low Earth-Orbits* (LEO) over *GEO Transfer-Orbits* (GTO) to *Geostationary Earth-Orbits* (GEO), using a novel micro-technology sensor-assembly. The investigations include the assessment of available algorithms and hardware, the combination of these to form the desired sensor-suite, the development of the necessary algorithms to enable the desired functionality of a combined sensor for attitude and orbit determination as well as the experimental validation and characterization of the system.

The main drivers for autonomy are the need for mission critical timing of maneuvers and to cover unpredicted loss of communication. These needs primarily arise in Earth-orbits, yet they play an important role in the case of planetary exploration. In inter-planetary flight the additional limitations in tracking budgets and capabilities come into play. In the proposed fashion, the sensor can serve as primary system for attitude and orbit determination as well as a back-up system in the case of failure of primary systems, such as GPS/Star-sensor combinations. The advantage of a sensor working in the visible regime to GPS is the insusceptibility to microwave radiation, as e.g. present in satellites equipped with a *Synthetic Aperture Radar* (SAR) payload.

In particular, this research is based on the Ph.D.-thesis „Einsatz richtungsmessender Sensoren in der autonomen Bahnregelung geosynchroner Satelliten“ by Juckenhöfel ([8]), the evolving *Active Pixel Sensor* (APS) technology and a patent on a „Combined Earth-/Star-Sensor System and Method for Determining the Orbit and Position of Spacecraft“ developed at Daimler-Chrysler

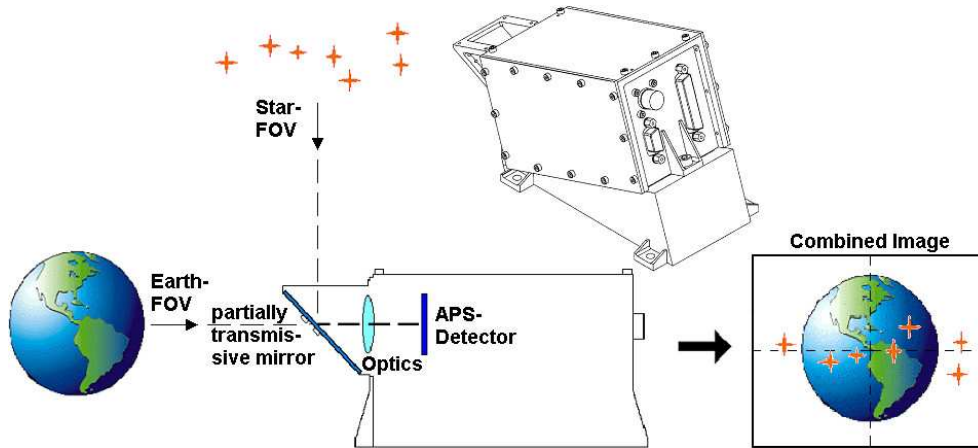


Figure 1.1: Principle of Sextant-Sensor

([1]). The algorithms developed in the frame of this thesis were evaluated and verified in specialized simulations and experiments accompanying their development. Experimental evaluation and validation is based on data provided by the *Micro-Tech.-Sensor for Attitude and Orbit Measurement Systems* (MTS-AOMS) flight-experiment on the *Minisatellite Italiano a Tecnologia Avanzata* (MITA) ([9]), laboratory experiments, including the setup of a functional breadboard, field experiments and METEOSAT images. In particular, the images obtained by the MTS-AOMS and METEOSAT were evaluated with regard to the Earth-horizon as perceived from *Low Earth Orbits* (LEO) and *Geostationary Earth Orbits* (GEO), respectively. The experiments in their union served as a system-level validation of feasibility and performance.

The sensor as it will be investigated is capable of observing two *Fields Of View* (FOV) for observation of the Earth and the Stars, respectively. The two FOVs are combined on the detector by means of a beamsplitter as can be seen in fig. 1.1. The reason for using one of the FOVs for Star-observations, the second for Earth-observation is derived from the necessity to determine the attitude as well as the position of the satellite relative to the Earth, while attenuating the Earth's brightness. The partially transmissive mirror reflects 91 % of the Star-light onto the detector, while transmitting only 9 % of the Earth's brightness. The Earth's intensity is furthermore reduced by a filter, on which the partially transmissive coating is applied. The system such reduces the intensity by a factor of 4000.

It will be shown that only these two measurements are sufficient for autonomous attitude and position determination of a satellite in the inertial reference system. The satellite's attitude matrix is determined using the feature of an *autonomous Star-tracker*. The attitude is in general described by a rotation matrix, also called the *Direction Cosine Matrix* (DCM). In brief, the DCM consists of three orthogonal vectors, which define a right-hand coordinate system. The orientation of this

coordinate system in the *Earth-Centered-Inertial* (ECI) reference-system is determined using the vector measurements to the observed and identified Stars, the unit vectors to which are known in the ECI reference-system. The position is then determined by using the Earth-image in order to find the Earth-vector in sensor coordinates and then transform it into the inertial system by using the attitude matrix gained from the Star-images. The coordinate systems are explained in greater detail in chpt. 2, the algorithms leading to knowledge of the satellite's attitude and position are discussed in chapters 3 and 5.

The detector itself operates in the *visible* (VIS) regime, thus providing an image as it would be observed by a regular camera. The reason for this is the possibility of working with low-cost and technically undemanding components. The reason for using APS technology is given in the low cross-talk between adjacent pixels, resulting in the possibility of observing very bright objects close to very dim ones. Another advantage over *Charge Coupled Device* (CCD)-technology lies in the possibility of selective readout of specified pixels, without changing their noise, as was the case in CCD-readouts. The idea of using a single basis for both FOVs, arises from the need to reduce misalignments due to thermal deformations. It additionally allows for reduction of the system's mass, power consumption, complexity and cost.

The effect of time-varying misalignments was investigated by Juckenhöfel ([8]) leading to the conclusion that, while it is in principle possible to determine a satellite's position with non-collocated sensors, it results in complex calibration procedures, which necessarily are time-varying and dependent on the satellite's attitude and position relative to Sun and Earth. Additionally vibrations of the satellite introduce a noise of higher frequency into the system. These problems are diminished by the proposed setup, which has been flown and validated during the MTS-AOMS experiment as part of ESA's *Technology Flight Opportunity* (TFO)-program. The mission was successfully completed after approx. 400 days, the effective experiment time was 229 days. The reason for the change from the proposed experiment duration of three years was completion of the primary mission. Nevertheless, to the author's knowledge, the experiment is so far the longest in-orbit test of *Micro-System-Technology* (MST) components.

The accuracy requirements taken for reference are based on typical requirements for satellites in geostationary (GEO), medium (MEO) and low (LEO) Earth orbit. They were chosen to be 0.1° in position and the equivalent of $1/10^{th}$ pixel in the Star-center determination, which resulted in an attitude accuracy of approximately 10 arcsec in pitch and yaw and 50 arcsec in roll.

Throughout this work, the algorithms presented have been optimized for use in Matlab. This is due to the presence of standard mathematical functions and visualization options inherent in Matlab. For this reason, the explanation of mathematical functions is limited to those not present in the software tool.

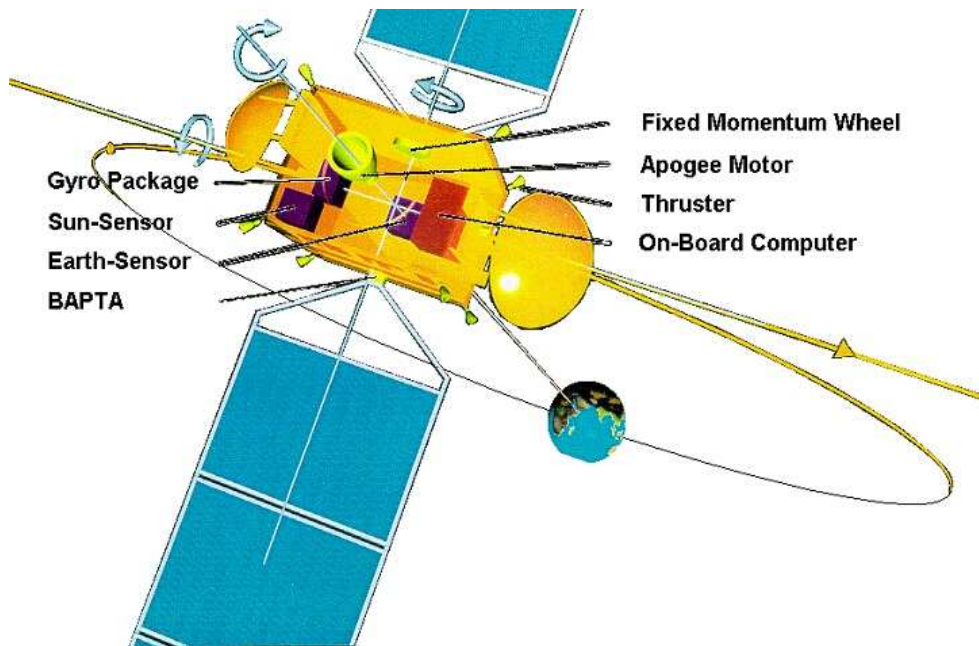


Figure 1.2: Sensor-suite of a typical geostationary satellite

1.2 Status of Current Developments

1.2.1 Attitude and Orbit Determination

To date, the **attitude determination** of GEO satellites is primarily based on a combination of Earth- and Sun-sensor measurements, requiring a sensor suite, which is distributed throughout the satellite (see fig. 1.2). In particular, the Sun-sensors usually consist of at least three individual sensors to guarantee a circumferential view. The problem associated with the attitude determination by use of a combination of Earth- and Sun-sensors is that the attitude can only be determined as long as the Earth and Sun are visible in the appropriate sensor. Thus, this combination is only applicable to detection of small deviations from a nominal Earth-orientation. Star-sensors overcome this drawback by their advantage of using Stars as references. In turn, in order to determine whether any axis is oriented towards the Earth, they need the information on the satellite's position. Examples for a Star-tracker and a LEO Earth-sensor are shown in fig. 1.3. The satellite's **position determination** usually is performed by ground stations via tracking. Several different tracking mechanisms are put to use, ranging from passive systems, which do not need any infrastructure on the satellite (e.g. Radar), over semi-passive/ semi-active measurements which need passive elements, such as retro-reflectors on the satellite (e.g. *Satellite-Laser-Ranging* (SLR)) to systems using active components on the satellite, using the downlink-delay for distance measurements. GPS-receivers for satellites are currently under development, forming a „semi-autonomous“ system, which is dependent upon



Figure 1.3: Star-tracker and LEO Earth-sensor

an existing infrastructure, i.e. GPS satellites, but otherwise provides the satellite's position without further need for ground stations ([10]). An approach similar to the one proposed, but used primarily to provide a three-axes Earth-reference in GEO was published by the EDO Corporation, Barnes Engineering Division („Three Axis Earth-/ Star-Sensor“, [11]). The Star-observation was restricted to Polaris and near-polar Stars, thus limiting the sensor to equatorial orbits. Another approach which was based on the sextant-principle was proposed with the *Space Sextant* by Magee ([12]) which was later-on refined by Mikelson ([13]). The system was characterized by a highly complex mechanical setup using two telescopes, which were designed to rotate relative to each other. In this fashion the angle between a Star or Star-pattern and the Earth- or Moon-limb was to be determined. The system was flown in 1983, yet, to the author's knowledge, results of this mission have not been published to date.

1.2.2 Star-sensors

Since the dawn of Star-trackers, the principle changed from single-Star sensors, like the *Polaris-sensor*, to *Star-pattern sensors*, which acquire multiple Star-images. In the beginning, these patterns were mostly predetermined prior to their mission. With the advance of computational power and detector technology, so-called *Star-trackers* or *autonomous Star-trackers* emerged, which were able to autonomously track and identify Stars supplied by a Star-catalogue. Following the Star-identification process, the determination of the satellite's, or to be precise: the sensor's, attitude can be determined using a multitude of algorithms (see e.g. [14]).

The following section will give a short overview on the current status and design of off-the-shelf

Star-sensors. It is to be seen in context with the high interrelation with the sensor as presented in this work.

While the APS-technology is under extensive investigation in current Star-sensor developments, commercially available Star-sensors up to date are based on CCD-technology. The main distinction can be made between Star-cameras, only supplying the Star-measurements, and *autonomous Star-sensors*, which, in addition to supplying the Star-measurements, detect false measurements and return the sensor's attitude. In this case, often *Star-tracking* is performed, where the Stars are not actually identified in each step, but only in the acquisition and later-on tracked in their movement across the detector. Jet Propulsion Laboratory (JPL) provides the following definition, with a slightly different nomenclature:

- *Star-camera* detects images of Stars,
- *Star-tracker* includes a camera plus hardware/software that puts out some intermediate level of information, such as a list of Star centroids in the spacecraft coordinate-system,
- *Stellar Compass* is a Star tracker plus software that can identify Stars and figure out the spacecraft attitude.

A wide range of definitions is being used, when it comes to the point where the attitude is provided by the sensor suite. Apart from *Stellar Compass*, nomenclatures like *Intelligent Star-tracker* and *Autonomous Star-tracker* are those most commonly used.

An intensive study on the design of hard- and software for Star-sensors is published by Schmidt, Jena-Optronik GmbH (DJO) ([15]). The particular sensor is the „Intelligent Modular Star and Target Tracker“, which has been developed in the frame of the ESA-project SETIS. Major limitations in the design of Star-sensors arise from the obtainable *Signal-to-Noise Ratio* (SNR). Due to the limits in the exposure time because of system specifications (e.g. data-rate, maximum angular rates), and the necessity to be able to observe a minimum number of Stars in the FOV at any given time, the desired SNR leads to requirements on the optical system, which can not always be fulfilled.

A comparison of „standard“ Star-sensors shows similar requirements on data-rate and number of observed Stars. The major difference is given by different FOVs, ranging approximately from $4^\circ \times 4^\circ$ to $20^\circ \times 20^\circ$. The mean is found to be approximately equal to an area of $135^\circ{}^2$, respectively a FOV with the angular dimensions of about $9.5^\circ \times 11^\circ$. The image is detected on a pixel grid with approx. $250 \cdot 10^3$ pixels², or 456×553 pixels², respectively. The detection limit is in the order of $7.2m_V$. A comparison of the Star-catalogues proves to be insignificant, since in many cases mission-specific catalogues are used. Comparing only those covering the com-

plete hemisphere, they contain approx. 5600 Stars, with the angular-separation-catalogue containing inter-Star-angles up to 0.5° . The mean number of tracked Stars amounts to be six, not counting the „Advanced Stellar Compass“ ([16]), which tracks all available Stars (mean 60) and thus would have presented an illegitimate increase on the average. Data-rate in most cases was between 1 Hz and 10 Hz , the achievable accuracy about the more accurate axes pitch and yaw is approximately one arcsecond ($1/3600^\circ$) at a maximal angular rate of about $0,1^\circ/\text{s}$.

In the comparison of Star-trackers, two parameters concerning accuracy are of major interest: the bias, and the *Noise Equivalent Angle* (NEA). The NEA is a statistical error in the attitude, arising from „true“ noise sources like the dark current noise, photon noise, discretization noise, noise introduced by the electronics and similars. They tend to affect the centroiding accuracy of the Stars, thus leading to an angular error in the attitude determination, which defines its name.

The definition of the bias is slightly more complicated, since it deviates from the common understanding, in comprising various sources of errors, which do not change or do not change significantly throughout the satellite's lifetime, but can not be or are not calibrated. This means that they include misalignments, but as well effects of the optics and deformations of the detector itself. In general, the bias can be reduced, through thorough investigation of the system, further calibration and changes in the hardware. No convention on the combination of these two error sources has been agreed upon, to date. Two major procedures are applied: one adding the bias and NEA geometrically, as with two independent noise sources, the other adding them linearly, since the bias can not be treated as a noise-process. These two procedures need to be discriminated, when comparing the overall accuracy of a Star-sensor system.

1.2.3 Earth-sensors

While the use of a detector in the visible regime is a common choice for Star-trackers, it is rather uncommon for Earth-sensors. Typical Earth-sensors nowadays are *infrared* (IR) Earth-sensors. This means they observe the Earth in the IR regime at around $1400 - 1600\text{ nm}$, which is the emission-band of CO_2 . Using only that specific region of the IR results in a more homogeneous intensity distribution, than using a larger fraction of the IR, which results in a rather inhomogenous appearance of the Earth (see [14]). The advantage of using the IR in general is its observability throughout all orbit phases. Using Earth-sensors which observes the Earth in the visible regime, commonly called *Albedo-sensors*, this is not necessarily given: In that case the Earth might not be visible when the satellite is in the eclipse. An IR-sensor will still receive a signal, since the Earth, even at night, is much warmer than the surrounding Universe and thus emits a detectable level of IR-radiation. Furthermore, in general the resultant *Signal-to-Noise* (S/N) level is higher than that

of Albedo-sensors ([14]). To the author's knowledge, no investigation on this topic, using modern CCD- or APS-detectors, resulted in commercial applications ([17, 18]). A rather uncommon, and to the author's knowledge never commercially available, realization was a three-axes Earth sensor in the *ultraviolet* (UV) regime („Apparatus for determining 3-axis spacecraft attitude“, [19, 20]). The idea of this sensor was to use UV-imaging of the ozone layer as observation. The Stars as well were observed in the UV and the image was mapped onto a single UV-detector. Using the information of the observed Stars, the sensor not only provided information on the Earth-vector, but on the attitude matrix as well. The problem with the UV-sensor was the system's complexity, which resulted from a large FOV, observed by a ball-lens, which in turn resulted in the need for field-flattening optics based on optical fibers.

1.2.4 Detectors

The main difference dealt with in the scope of this thesis is the difference between CCD and APS detectors.

The CCD and the APS are the two most commonly used sensor technologies to date. Both are composed of silicon using similar foundries. The different manufacturing processes, though, make them very different in capability and performance, ultimately providing them with different strengths and weaknesses. The main difference between CCD and APS imagers is that the charges generated in a CCD need to be transferred to a „centralized“ amplifier, while in an APS each pixel contains its own charge to voltage amplifier. This reduces the effective area available for detection of incident photons and results in a larger modulation of the sensitivity across the pixel, yet reduces the probability of failures of complete rows, as they may occur in CCDs.

The advantages of current CCD-technology, as it is for instance used in camcorders, lies in its heritage, a higher sensitivity and a high fillfactor, which allows for a more accurate determination of the observed Stars' visual magnitudes. Another advantage is the well known and well defined penetration depth of photons into the photosensitive material. In APS-technology, this depth is less well defined, leading to higher inaccuracies in the determination of the Stars' centers in case of higher angles of incidence.

The advantages of APS-technology are given by their high dynamic range, when for instance using a logarithmically scaled detector, the low cross-talk between adjacent pixels as well as the opportunity of directly addressing sub-arrays. They are tolerant to high illumination levels, allowing for direct Sun-observation without immediate destruction of the detector, as it is the case with standard CCDs. This allows for larger FOVs, which have a higher probability of Sun-incidence. Furthermore, they are inherently tolerant to radiation, thus making them the right choice for space-based

Table 1.1: APS specifics as compared to CCD technology

Advantages	Disadvantages
<ul style="list-style-type: none"> • high dynamics (with logarithmic detector) • low cross-talk • tolerant to high illumination levels • simplified electronic supply voltages • low power requirements • simplified read-out electronics • random access to pixel regions of interest 	<ul style="list-style-type: none"> • low fillfactor (α-silicon as solution) • higher noise (\approx factor of 20 in noise-electrons) \rightarrow lower signal-to-noise ratio • uncertainty in physical behavior concerning the penetration depth of photons • lower sensitivity

sensors. Additionally, the electrical setup is simplified by use of a common voltage in the read-out and processing electronics, whereas in the case of CCDs two or more supply-voltages are required. As a result, they are a cost-effective alternative in the design of medium-accuracy Star-trackers. A summary is given in table 1.1. For more in-depth information on the status and technology of CCD and APS detectors be referred to the numerous sources available on this topic, as e.g. [21].

1.3 Goal of the Thesis

1.3.1 Attitude and Orbit Determination

In the system under investigation, the **attitude determination** is performed using Star-images, thus eliminating the problem associated with the collinearity: when the Earth, the satellite and the Sun form a straight line, the satellite's attitude is unobservable with an Earth-/ Sun-sensor combination. Furthermore, the vector towards the Earth-center is determined, providing an alternative 2-axes attitude. In a further step the **position determination** is changed to be **on-board-autonomous**, alleviating the need for ground-based standard procedures, as surveillance and command of station-keeping maneuvers. This takes autonomy a step further than the development of GPS-receivers for satellites, which depend on an existing infrastructure, i.e. GPS satellites and the availability of their signals and information, and such form a „semi-autonomous“ system (see [10]).

1.3.2 Star-sensors

As the proposed system uses the functionality of a Star-sensor based on APS-technology, major parts of the thesis deal with the algorithms required in order to evaluate images obtained by the APS-detector. These algorithms in particular contain the detection, centroiding, tracking and identification of Stars and the subsequent attitude determination. In total, the system qualifies as an *Autonomous Star-tracker*. The developed algorithms will be evaluated and validated using data obtained by the MTS-AOMS, laboratory experiments and field experiments performed in the Bavarian Alps.

1.3.3 Earth-sensors

The determination of the Earth-center from Earth-images provides the system with the additional feature of an Earth-sensor. As the Earth is observed using the same detector as for the Star-images, the development of algorithms for evaluation of Earth-images in the visual regime is required. In particular, algorithms to determine the Earth-horizon and the Earth center are needed for all desired orbits. These orbits include LEO and GEO orbits, as used by MITA and METEOSAT, respectively. In total, the system qualifies as an *Albedo-sensor*. The developed algorithms will be evaluated and validated using data obtained by the MTS-AOMS, laboratory experiments and METEOSAT images.

1.3.4 Detectors

In contrast to the commercially available CCD-technology, the proposed sensor system is based on the arising APS-technology, which is under extensive investigation in current Star-sensor developments. The chosen APS-technology offers the advantages of selective readout of specific pixels and a high reduction in the cross-talk between adjacent pixels, offering the possibility of high repetition rates and of observing very bright objects, such as the Earth, close to very dim ones, such as Stars. The choice of the APS-technology requires specifically tailored algorithms concerning the centroiding, as they are not, in general, composed of point-symmetrical pixels.

1.4 Required Investigations

Resulting from the desire to develop a sensor capable of on-board autonomous attitude and orbit determination with the features as introduced above, the following list of topics to be covered and ultimately merged has been compiled:

Image Processing Algorithms

- Centroiding for sub-pixel accuracy in determination of Star-positions
- Star-Tracking for rate determination without need for gyros or information on the satellite's attitude
- Determination of Earth-horizon in the visible regime for Earth-reference
- Tracking of horizon to reduce computational load

Algorithms on Position and Orbit Determination

- Combination of Earth- and Star-information for attitude and orbit determination, resulting in inertial- and *Local Vertical, Local Horizontal* (LVLH)-attitude
- Simulation and Error Analysis of the combined system, including prediction of the achievable accuracy in attitude, rate and position

Experimental Validation

- Concept and setup of optical functional testbed (OFTB) for validation of core-algorithms and rapid-prototyping
- Preparation for sensor tests on the OFTB and in the Optical Test Facility, transfer of software to PC and simulator, resulting in a Breadboard of core-functions
- Evaluation of data gathered in MITA flight-experiment for determination of the system's capabilities and limitations
- Evaluation of experiments, leading to verification of core-functions and recommendations for necessary improvements
- Extension to optical-inertial-system for functional redundancy over short periods
- Definition and Preparation of future flight experiment, including recommendations gained from flight experiment on MITA

All of these tasks are successfully completed in this work.

1.5 Organization of the Thesis

This document is segmented in various sections in order to successively lead to a complete picture of the investigations carried out. In order to do so, the main body is divided into several parts, outlining the approach: In the first part the algorithms and computer simulations for image processing and position- as well as orbit-determination, which were used and developed to process the sensor data, are presented and discussed. They are followed by a chapter on the experimental validation of the sensor's functions and the stability of the data processing, which accompanied their development. It contains the description of the experimental setups realized and used throughout this thesis, including details on the MITA sensor, the laboratory installation set up at EADS Astrium GmbH, München, and the field experiments, followed by the discussion of the data and results obtained. The investigations end in a discussion on operational aspects, the lessons learned and conclude with the achievements of this work.

Chapter 2 precedes the main body with the principles of **data-processing in Star-sensors**, the modeling of **measurement noise**, as it is treated throughout this thesis, as well as the introduction of the **coordinate systems** used. It further explains the main preliminaries on **attitude determination**, **position determination** and concludes with an introduction to the **orbit determination** using position measurements.

Chapter 3 introduces on the **image processing algorithms**, which are divided in those related to the Star-observations (chpt. 3.1) and to the Earth-observation (chpt. 3.2).

The **attitude determination from Star-measurements** in chpt. 3.1 is based on various algorithms on processing Star-observations. This begins with the necessary detection and extraction of possible Stars from the image. In chpt. 3.1.1 an approach is presented, which is based on the knowledge of the Star-image's intensity distribution. Starting with a simple threshold, the extraction is further refined by approximate knowledge of the distinct intensity ratios of neighboring pixels in case of Star-presence. This detection step is followed by the centroiding process as discussed in detail in chpt. 3.1.2. Centroiding in this case denotes the determination of the Star-center to an accuracy below the pixel level by using *a priori* knowledge on the optical system. As will be shown in chpt. 3.1.2, there are several issues, when dealing with a large FOV in combination with simple, commercial optics, as chosen for the proposed system for reduction of system price and mass. The centroiding process is followed by the identification of the observed Stars, explained in chpt. 3.1.3. The algorithm developed in this framework is a first acquisition, polygon-matching approach, based on a catalog containing the angular separation between Stars as well as a standard Star-catalog for Stars in the visible regime (Hipparcos, [22]). The Star-identification is ensued by attitude determination, as it is described in chpt. 3.1.4. Attitude determination is based on the

known directions towards Stars in the ECI reference-system, which are mapped onto the directions as perceived by the sensor using the attitude matrix. Several algorithms for determination of the attitude matrix have been compared, out of which the *Singular Value Decomposition* (SVD) was chosen due to its reliability and speed when using Matlab. The attitude determination is followed by a chpt. 3.1.5 on Star-tracking. Star-tracking provides the means of determining the rotation of the satellite without need for Star-identification. This is of high value when initializing the sensor, as the Star-identification, with no prior information of the satellite's approximate attitude, might take too long for determination of the actual spin rate through differential images. The chapter on the Star-algorithms closes with a prediction of the obtainable attitude accuracy (chpt. 3.1.6).

The **Earth-center determination** is addressed in chpt. 3.2. The process, again, starts with a detection and extraction, this time of the Earth-horizon, as explained in chpt. 3.2.1. Again, a threshold is augmented with known local properties, which have to be fulfilled in order for a point to be accepted as a possible part of the horizon. Since local criteria turned out not to be sufficient to guarantee horizon points, additional global criteria were investigated. Once an adequate set of points is found, these points are passed to the determination of the Earth-center, as discussed in chpt. 3.2.2. It turned out that, again, it is beneficial to use *a priori* knowledge, this time about orientation and oblateness of the Earth in order to achieve higher accuracies. The chapter, as well, closes with a prediction of the obtainable accuracy for LEO and GEO (3.2.3).

Chapter 4 on the **evaluation of the image processing algorithms** is divided into the simulations necessary for verification of the algorithms concerning Stars (chpt. 4.1) and the Earth (chpt. 4.2).

The **simulations on the attitude determination from Star-measurements** are introduced in chpt. 4.1. The simulations carried out deal with the questions concerning reliability and computational burden in chpt 4.1.1 as well as the achievable accuracy in chpt. 4.1.2. The simulations are performed in a parameterized fashion, in order to take different levels of expected centroiding accuracy into account. The simulations confirmed the correct approach in the Star-identification algorithms, while additionally providing an estimate on the necessary computation time, which turned out to be approximately quadratically dependent on the tolerance specified for the Star-identification. The accuracy of the attitude determination proved to be approximately proportional to the inverse of the square-root of the number of measurements, as it is expected from statistical considerations.

The **simulation on the Earth-center determination** is explained in chpt. 4.2 and is kept rather short. An analytical approach on the intensity distribution of the atmosphere as seen from a satellite was derived, taking into account the *optical pathlength*, meaning the length an imagined ray of light stays within the atmosphere prior to reaching the spacecraft as well as an assumed exponential decay of the atmosphere's density. The overall exponential decay of the perceived horizon intensity

led to the idea of using a filter for detecting exponential slopes, rather than the transgression of a threshold.

Chapter 5 concentrates on the **algorithms on position and orbit determination**, which are divided in those used for the determination of the satellite's position (chpt. 5.1), which is independent of attitude dynamics and orbit of the satellite, and the orbit determination (chpt. 5.2), which requires knowledge of the orbit dynamics and allows for increase in the position accuracy.

The position-determination in chpt. 5.1 develops the mathematical formulation of the problem with the preliminary of a known Earth-vector and attitude matrix. It is shown that a direct procedure, using vector measurements only, results in a vector towards the satellite. This vector is given in the ECI reference-frame. The distance from the Earth center to the satellite is determined using the apparent Earth diameter. The algorithm itself has a straight-forward explanation: The satellite's position can be shown to be a transformation of the Earth-vector as observed by the sensor aboard the satellite into the ECI-reference system by use of the satellite's known inertial attitude (chpt. 5.1.1). This results in a closed form solution for the effects of errors in the Earth-vector and the attitude on the determination of the satellite's position: The total variance can be shown to be approximately the sum of the variances of the two functionalities (chpt. 5.1.2).

The orbit determination is addressed in the final chapter of the algorithms section, chpt. 5.2. In addition to the satellite's position, velocity information is included in the state, establishing the opportunity of increasing the position accuracy. Using the additional information furthermore allows for the determination of the orbit parameters and the LVLH reference-system as defined in chpt. 2. Two Kalman-filters are presented in chpt. 5.2.1. One of these uses the satellite position as observation, the other the vector towards the satellite. The latter relieves the system from using another measurement disturbed by noise: the apparent Earth-radius, which additionally might contain a bias due to cloud cover and the difficulty of determining the true horizon in the visible regime. Both algorithms are developed such that they allow for sensor failures. In chapter 5.2.2 the observability of the proposed system is proven in the *Hill*-reference system, since it allows for an easier representation. The prove has been carried out in the ECI-system as well, using Maple, confirming the results as obtained from the Hill-system. The definition of the coordinate systems used is given in chpt. 2.

Chapter 6 on the **evaluation of the algorithms on position and orbit determination** is divided into the simulations necessary for verification of the algorithms concerning the position (chpt. 6.1) and the orbit (chpt. 6.2).

The steps followed for a **simulation on the position determination** are described in chpt. 6.1. The results from this chapter are used to verify the results from chpt. 5.1, especially to show the

accuracy's dependency on the attitude and position of the satellite. This simulation is used for the *point solution* only, meaning that no filtering is applied at that level.

The **simulations on orbit determination from sequential position measurements** closes the simulation chapter. The simulations are used for tests on the so-called *dynamic solution*, which solves for the satellites state using filtering of the point solution. The accuracy of the propagation, in the Kalman-Filter as well as in the simulation, can be chosen arbitrarily, ranging from the use of Keplerian-motion only to a *High Precision Orbit Propagator* (HPOP) which takes into account a wide range of disturbances. The simulations showed that the Kalman-filter fulfills the purpose of increasing the position accuracy and determination of the satellite's orbit, even in the case of realistic sensor outages in the range of up to 90minutes.

Chapter 7 presents the **experimental validation** and starts with the introduction of the **experimental sources** in chpt. 7.1.

A wide range of experiments has been carried out, the sources employed being the MTS-AOMS on-board of the MITA satellite experiment as described in chpt. 7.1.1, the laboratory experiments as outlined in chpt. 7.1.2, the field experiments carried out as explained in chpt. 7.1.3 and the METEOSAT data specified in chpt. 7.1.4.

This is followed by the **experimental results** in chpt. 7.2. The chapter contains the experimental validation of the performance of the proposed system in terms of Star-measurements (chpt. 7.2.1), Earth-measurements (chpt. 7.2.2) and the combined position-determination (chpt. 7.2.3), which finally proves the algorithms consistency.

The chapter ends with the **experimental conclusions** in chpt. 7.3, where a comparison between the experimental results and the analytical predictions for the system's accuracy is performed.

Chapter 8 on the **operational aspects**, when dealing with a purely optical system for attitude and orbit determination, succeeds the experimental section and ends the body of this work.

The operational aspects include the **acquisition** (chpt. 8.1), **critical mission phases** (chpt. 8.2) and concludes with remarks on **general considerations** (chpt. 8.3) to be minded.

Chapter 9, containing the **lessons learned and conclusions**, finally closes this work.

The text is supplemented with an **Appendix** (chpt. A), containing further information on **algorithms, simulations** and **experiments** as well as the **nomenclature and abbreviations** used.

Chapter 2

Preliminaries

The principle task of the combined Earth-/Star-sensor is the determination of the satellite's attitude and position in the inertial coordinate system, where the position-vector is pointing from the center of the Earth to the satellite. The data obtained by the sensor itself is given in the body-fixed system of the satellite. The attitude then has to be represented in a notation which relates the orientation of the body-fixed to the inertial coordinate system. This can be done by either a rotation matrix or in quaternion notation. The angular relation between the two coordinate systems can be obtained from the Star-measurements. The position can then be determined using the Earth-vector, as obtained from the Earth-center determination, and rotating it into the inertial system by means of the previously obtained rotation matrix.

The length of the position vector can be determined by different methods. One of them is to use the apparent angular radius of the Earth for a calculation of the distance, the other the application of a filter to make use of the satellite's angular velocity about the Earth, which can be related to the orbit height. The same principle obviously holds for other central bodies than the Earth. This chapter will introduce the basic assumptions, coordinate systems, processes and equations used throughout the thesis.

2.1 Data-Processing in Star-sensors

The data-processing generally used in autonomous Star-sensors is divided in two principal sections: The image acquisition including low-level pre-processing and the digital processing of the data. The image acquisition includes the amplification of the signal, so-called *correlated double sampling* for reduction of noise, the *dark reference clamp* for elimination of the bias as well as the subsequent analog-to-digital conversion. The digital data is then processed in two further steps: the object-extraction and the object-identification. The object-extraction includes the identification of false signals caused by pixel defects and radiation (*Single Event Upsets (SEU)*). Pixel defects can

be treated in different ways: their individual values can for instance be substituted by their predecessor, successor, or their mean value. In case of a confirmed object-extraction, the object is passed to an algorithm determining the objects' center by means of centroiding. The result is a corrected position of the object's center in pixel-coordinates, thus including the x - and y -position. The x - and y - position is then translated into a unit-vector. In case of ideal optics, this step is a straightforward process. In real optics, often enough, the process is more involved, as optics-irregularities need to be included. These effects will be dealt with in detail in chpt. 3.1. The determination of the vectors towards the measurements is followed by a Star-identification. In an extended logic, objects which are not Stars can be excluded. In general, Star-sensors comprise different modes for different angular and data rates.

At start-up, when no *a priori* information is available, the Star-sensor has to perform a first acquisition, taking into account all Stars. Since the complete Star-catalogue has to be searched, this in general results in a computation time greater than the commonly required data rates of 1 Hz or 10 Hz. Once the acquisition was successful, the Star-sensor is switched to a *Tracking Mode*. In this mode the approximate attitude can be deduced from the previous measurements, resulting in a smaller catalogue, which needs to be searched for Stars. The expected attitude is calculated using the angular rate of the satellite, either through knowledge provided by rate-sensors, or by estimation from the attitude's time history. In the case of tracking, ideally, no identification needs to be performed, since the Stars' identification is known during the tracking process. New Stars, which enter the FOV are already known, due to the information in the catalogue. Exceptions occur in cases, when a Star is temporarily out of sight, either due to pixel defects, SEUs, or obstruction by other objects (commonly referred to as *extended objects*). In that case, they are excluded from the tracking list and sometimes re-tracked, once they reappear in the FOV.

2.2 Measurement Noise

As in most technical processes, the measurement noise can be divided in two components: physically and technologically based noise. Technologically based noise comprises those components, which can be reduced by a more advanced technology, such as better electronics. Physical limitations arise, when Stars are observed: since the measured quantity, i.e. the Star's photons, are quantized and limited in number, the noise level is dependent on the Star-intensity, obeying a Poisson-distribution. This leads to a standard deviation which is dependent on the intensity and the observation time. In particular σ relates to

$$\sigma_{\text{photon-count}} = \sqrt{I \cdot t} \quad (2.1)$$

with the intensity parameter I in [photons/second] and the camera's exposure time t in [seconds]. Note that the photon-noise is not Gaussian, not additive and not independent of the signal.

A combination of physically and technologically influenced noise is found in thermally induced noise, which in the case of typical APS-detectors doubles each 7°K . The centroiding noise, which ultimately defines the Star-center determination accuracy, in general is approximated by a Gaussian distribution (e.g. [23]), being proportional to the square-root of the observed Star's intensity. This dependency and the influence of the Star's position on the detector on its centroiding accuracy, which will be explained in greater detail in chpt. 3.1.2, leads to the idea of introducing different weights for different Stars in the attitude determination, as proposed in the Appendix A.1.2.

2.3 Coordinate Systems

The three basic coordinate systems needed in the scope of this thesis, are the aforementioned *inertial* and *body-fixed* coordinate system, plus an extra system: the *sensor system*. The systems are related by appropriate transformation matrices T_{yx} , which converts vectors from coordinate system x to system y . A strict distinction needs to be drawn between the *sensor system* and *detector coordinates*: While the sensor system defines a 3D coordinate system, the detector coordinates are the 2D coordinates of a point on the detector. Therefore e.g. a vector to a Star in the sensor system already includes effects of the optical system, while the Star's detector coordinates, if not further processed, are measurements with no information on the direction towards the Star.

The *inertial system* is based on the solar-system's ecliptic. In particular, the origin of the *Sun-*

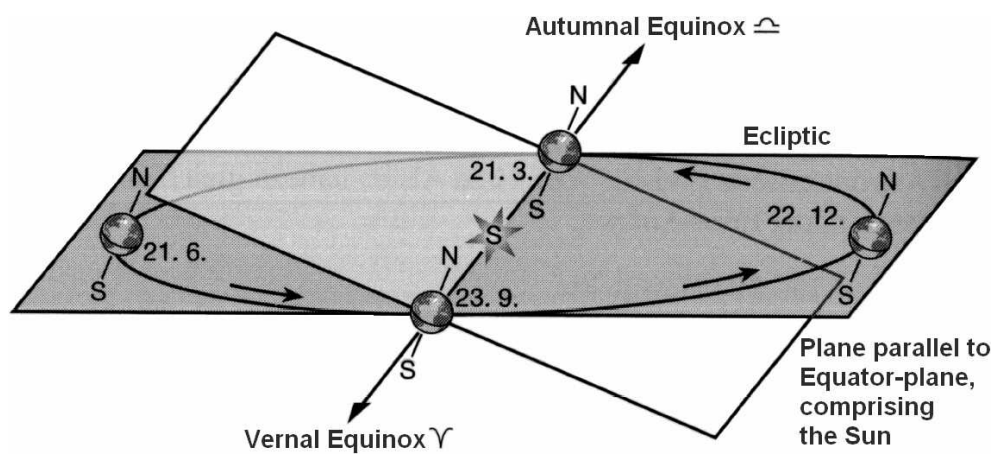


Figure 2.1: Explanation of the planes used in the definition of inertial coordinate-systems

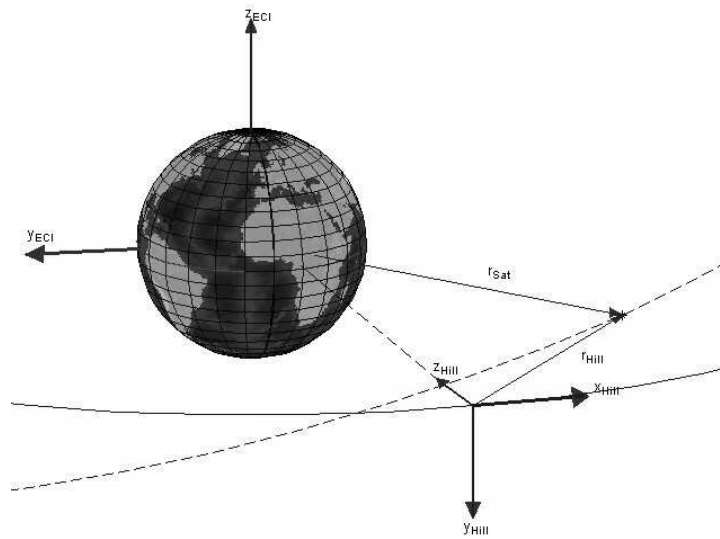


Figure 2.2: Hill-System

centered Inertial (SCI) reference system is in the center of the Sun and the orientation of the axes is defined by the vernal equinox as the x -axis and the normal to the ecliptic as the z -axis. The y -axis is chosen to result in an orthogonal, right-hand coordinate system. The vernal equinox is defined by the intersecting line of two planes: the Earth's orbit-plane and the Earth's equator-plane. At the time of autumn, when both planes comprise the Sun, the vector from the Sun towards the Earth coincides with the vector pointing towards the vector defining the vernal equinox. These dependencies can be seen in fig. 2.1. Due to the precession of the Earth's rotation axis, this results in a time-varying orientation of the inertial coordinate system, with a period of approximately 26000 years. Various coordinate systems can be defined along these axes, the two most important of which, for Earth-satellites, are the SCI and the *Earth-centered Inertial* (ECI)-system. As evident from the nomenclature, the coordinate system's origin is located in the center of the Sun and the Earth, respectively. In the following, any reference to an „inertial“ coordinate-system will refer to ECI unless otherwise specified. The difference in the origin of two reference systems ideally needs to be taken into account when using SCI-based Star catalogues, since it changes the apparent direction towards a Star. This effect, called *parallax*, is neglected in the following, since the resulting change in the apparent direction is below the detection limit, even when „close“ Stars are observed (e.g. *Proxima Centauri*: $\pm 0.765''$). This affects the equations in that no offset between the coordinate systems needs to be considered.

A coordinate system which is based on the knowledge of the satellite's nominal orbit is the *Hill* system (fig. 2.2). In the Hill-system the origin of the coordinate system is defined by a reference orbit. Therefore only deviations of the spacecraft's position relative to the reference are evaluated.

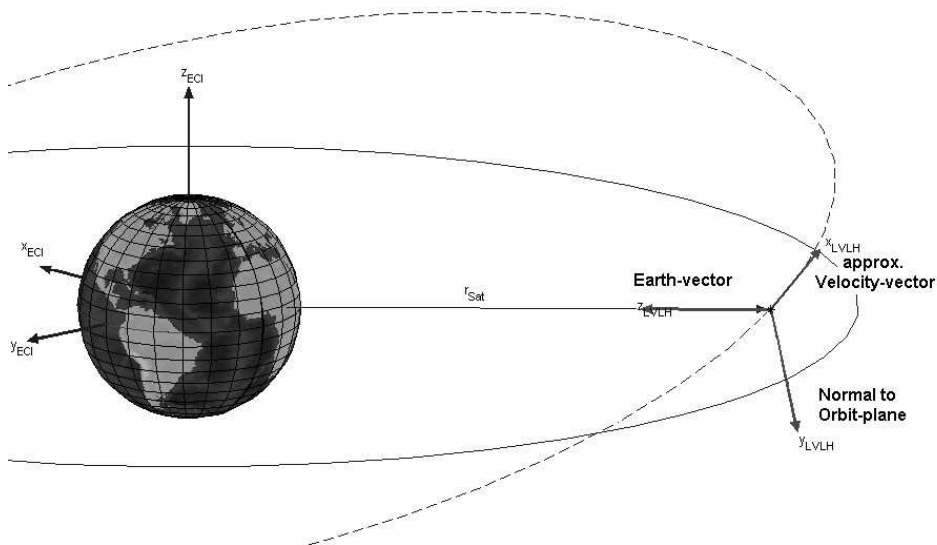


Figure 2.3: LVLH-System

This results in a simpler formulation of the system's transition matrix and immediate knowledge of errors in the satellite's position. The axes are chosen such that z_{Hill} is radial, y_{Hill} is perpendicular to the orbit plane and x_{Hill} completes the rectangular coordinate system.

While these coordinate systems are used to describe the satellite's position and attitude in space, the systems to follow are primarily used for the satellite's attitude. The LVLH is closely related to the Hill-system with the sole difference that the system's origin is identical to the satellite's *actual* position. The axes are again defined such that the z -axis always is oriented towards the center of the Earth, so parallel to the position-vector, the y -axis is perpendicular to the orbit plane and the x -axis completes the rectangular coordinate system. In circular orbits, the x -axis coincides with the velocity-vector. A schematic of this system can be seen in fig. 2.3. The advantage in using the LVLH as reference for the satellite's attitude is given by its orientation: in case of an Earth-pointing satellite, the nominal attitude needs to be aligned with the LVLH-system, leading to a time-invariant attitude.

The body-fixed coordinate system is less stringently defined. Depending on the type and orientation of the satellite, the system's orientation can be chosen freely, while in most cases it is either chosen to coincide with the principle axis, resulting in a diagonal inertia tensor, or to use a geometrical symmetry to simplify the integration of other systems, such as an additional sensor system. In the case of MITA, as seen in fig. 2.4, the coordinate system is aligned with the rectangular shape of the satellite structure. In this particular case, the y -axis coincides with the nominal flight-direction, the x -axis with the nominal Earth-direction.

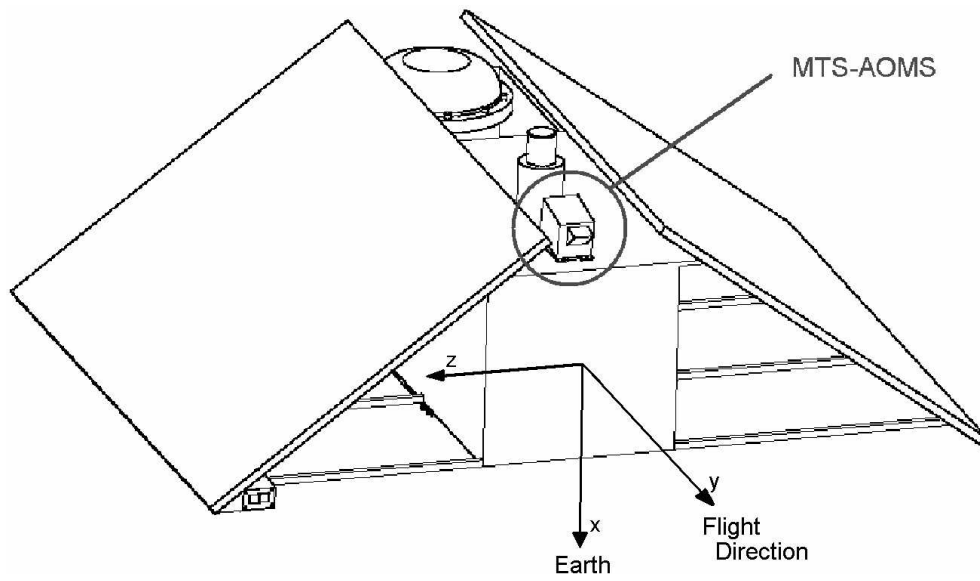


Figure 2.4: Body-fixed coordinate system as defined for MITA

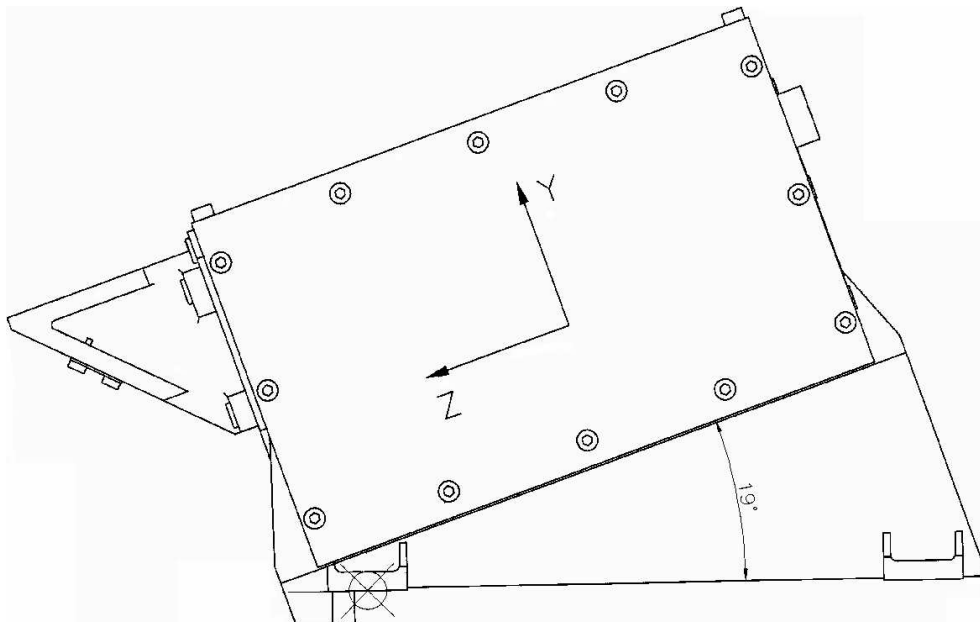


Figure 2.5: Sensor coordinate-system as defined for MTS-AOMS on MITA

In most cases, mission specific sensors will not be co-aligned with the body-fixed system, but rather have a coordinate system tailored to their specific needs. In the case for MTS-AOMS on MITA, as seen in fig. 2.5, the choice for an individual coordinate system arose from the necessity to observe the horizon, which in turn resulted in a tilted camera system. In the assembly as shown, the sensor's x -axis is co-aligned with the satellite's z -axis.

2.4 Attitude Determination

In order to determine the orientation of the satellite in the inertial reference system, attitude determination is vital. The basis for attitude determination by Star-sensors is the fact that the Star-catalogue, which is used to identify the observed Stars, as well contains the vectors towards those Stars in the inertial system. For high-accuracy attitude determination, the influence of the parallax needs to be taken into account, since it changes the apparent direction towards a Star. Since this effect is at most $\pm 0.765''$, and therefore below the accuracy expected for the system under investigation, it is neglected in the following. Another effect to be accounted for in high-accuracy attitude determination is the *aberration*. This effect changes the apparent observation-angle due to the spacecraft's velocity in combination with the finite speed of light. The change in the apparent angle towards the Star depends on the angle between the spacecraft's velocity vector and the vector towards the Star. It is greatest, if these two lines are perpendicular and then results in a mis-estimation of the attitude in the order of $30''$ for a geostationary orbit. Again, the effect is neglected in the following, as it can be easily be included in the on-board software in combination with the knowledge of the satellite's state-vector.

The Star-sensor determines the apparent Star-vectors in the sensor-system. These vectors are obtained using a so-called centroiding process, which identifies the position of the Star-center on the detector to better than one pixel. This step is followed by an expansion to a unit-vector, which needs to take into account the optics used, if no ideal optics can be assumed. The Stars now need to be identified by use of a Star-identification procedure. In general, these procedures use the angular distances between the observed Stars and compare them to a catalogue containing all possible distances. Since this solution is not necessarily unique, the angular distances and the appropriate Stars are combined to triangles and higher order polygons, thus leading to a Star-pattern recognition in order to increase the identification probability. The angular distances are the only absolute measurement to be gained from Star-observations. Therefore, even though there are variants of this procedure, most algorithms use this baseline.

Another measurement, which is fairly absolute, is a Star's brightness. This information, though,

is mostly used in the verification process only, since it is less accurate. Reasons for this are, for instance, the different spectral classes present in Stars, which result in different intensity levels detected by the sensor due to its wavelength dependent sensitivity and wavelength dependent absorption in the optics.

Having found a valid Star-identification, it is now possible to determine the attitude of the sensor by using the relation

$$\underline{b} = A \cdot \underline{r} \quad (2.2)$$

with \underline{b} as the vector to the Star as determined by the measurement, A as the (unknown) attitude matrix and \underline{r} as the reference vector to the Star, being represented in the inertial reference system. This system can be solved for A as soon as more than one observation is available.

This attitude matrix now contains the information on the orientation of the Star-sensor in the inertial reference-system. The components of A are necessarily redundant, since the orientation can be expressed in terms of the three *Euler* angles, namely yaw, pitch and roll.

$$A(\phi, \theta, \psi) = \begin{bmatrix} \cos(\psi) \cos(\phi) - \sin(\theta) \sin(\psi) \sin(\phi) & \cos(\psi) \sin(\phi) + \sin(\theta) \sin(\psi) \cos(\phi) & -\cos(\theta) \sin(\psi) \\ -\cos(\theta) \sin(\phi) & \cos(\theta) \cos(\phi) & \sin(\theta) \\ \sin(\psi) \cos(\phi) + \sin(\theta) \cos(\psi) \sin(\phi) & \sin(\psi) \sin(\phi) - \sin(\theta) \cos(\psi) \cos(\phi) & \cos(\theta) \cos(\psi) \end{bmatrix} \quad (2.3)$$

In this representation it is vital to note, that the order, in which the rotations ϕ , θ and ψ are performed is not arbitrary. For the equation as given above, the order is ϕ about the z -axis, then θ about the new x -axis and finally ψ about the latest y -axis.

An alternative expression is the quaternion, which consists of four components, which describe the axis of rotation and the rotation angle. This representation is only redundant due to the requirement of the axis of rotation being a unit vector.

$$A(q) = (q_4^2 - |\underline{q}|^2) \cdot I + 2 \cdot \underline{q} \underline{q}^T - 2q_4 \cdot [\underline{q} \times]. \quad (2.4)$$

In this notation $[\underline{q} \times]$ is equivalent to the widely used $\tilde{\underline{q}}$, defining

$$\underline{a} \times \underline{b} = [\underline{a} \times] \cdot \underline{b} = \tilde{\underline{a}} \cdot \underline{b}. \quad (2.5)$$

The advantage of the quaternion as opposed to the Euler angles is that it provides mathematical functions for successive rotations and requires no trigonometrical functions while still showing no singularities.

In the case of small angles, the relation between the quaternion and the Euler angles is fairly simple:

$$q = \frac{1}{2} \begin{bmatrix} \theta & \psi & \phi & 2 \end{bmatrix}^T. \quad (2.6)$$

Having determined the attitude of the sensor in the inertial system, it is now possible to determine the satellite's attitude using the known relation between the sensor and the body-fixed coordinate system.

2.5 Position Determination

The position of most satellites and probes is related to a target body, rather than the Sun. In the case focused on in the scope of this thesis, the target is the Earth, which here coincides with the central body, about which the satellite orbits. This will become of importance in the orbit determination. Since the position is needed relative to the Earth, the Earth-vector (in sensor coordinates) is a required measurement. The identification of the Earth in commonly used Earth-orbits, meaning orbits, which are not too far away from the Earth, is not a major difficulty. In this case the Earth can easily be distinguished from Stars and the Moon by its apparent angular radius. The determination of the Earth's center, however, represents a computationally and algorithmically difficult task. This mainly originates from the type of sensor being used, which observes the Earth in the VIS. The observation in VIS results in the unobservability of those parts of the Earth, which are not lit by the Sun, thus reducing the number of horizon points to be used for the determination of the Earth's center. This is in contrast to Stars, which are light sources by nature and do not cover a large number of pixels. That way, the center is determined rather by determination of the center of intensity, than by evaluating a horizon.

Once the center of the Earth is determined, the corresponding unit-vector is known in the body-fixed system as $\mathcal{L}_{\text{Earth, body-fixed}}$. To be of value for the determination of the position in the ECI-system, eq. (2.2) can be used by pre-multiplying the equation with the inverted attitude matrix determined in the attitude determination. The obtained vector then represents the vector from the satellite towards the Earth in inertial coordinates. In order to obtain the unit vector from the Earth towards the satellite it needs to be multiplied by -1 , resulting in

$$\mathcal{L}_{\text{Satellite, inertial}} = A^{-1} \cdot (-\mathcal{L}_{\text{Earth, body-fixed}}). \quad (2.7)$$

At this point, the distance from the Earth towards the satellite can be determined by using the apparent angular radius α_{Earth} of the Earth and its known radius R_{Earth} . Using basic trigonometry

results in

$$R_{\text{Satellite, inertial}} = R_{\text{Earth}} / \sin(\alpha_{\text{Earth}}).$$

Using the system as proposed, ideally no additional information on attitude or orbit dynamics are needed for determination of the satellite's position.

2.6 Orbit Determination

To gain further information on the satellite's state and to increase the position determination accuracy, it is desirable to include the known orbit dynamics in the position determination process. This is realized in a Kalman-filter, where the position is part of the state and the knowledge of the orbit dynamics is used in the propagation-step. The same is possible in order to increase the attitude determination accuracy, where it has been extensively studied (e.g. [24, 25, 26, 27]). The advantage in the case of position-filtering lies in the increase in the accuracy and furthermore in the increase in information: The filtering at the very least estimates the satellite's velocity. This information can be used to determine the satellite's orbit, which in turn allows for determination of the satellite's attitude in the LVLH reference frame (fig. 2.3).

The orbit dynamics used in this context are determined using a Runge-Kutta 4 integration algorithm to include the accelerations involved. Apart from the Earth's gravitation (g), „perturbations“ from Sun (a_{Sun}), Moon (a_{Moon}), airdrag (a_{airdrag}), solar pressure ($a_{\text{solar pressure}}$) and the inhomogeneity of the Earth's gravitational field (a_{inhomog}) were taken into account. Other perturbations were not taken into account, but can be added easily. For Earth-satellites in proximity to Earth, other perturbations are negligible, as apparent from fig. A.7 in the Appendix (taken from Montenbruck, [28]). In the transition matrix used for the Kalman-Filter the accelerations are linearized about the operating point, using only the gravitational accelerations. In this regard, the observation might exhibit special characteristics: if the observation is in form of a unit vector, with no distance information, the observation itself needs to be represented as a linearized sub-space of the state. In particular, the observation represents the normalized position, resulting in a non-linear observation. The resulting Kalman-filter, which is linearized in the process as well as in the observation, is denoted a Kalman-Schmidt-filter (see [29]).

Chapter 3

Image Processing Algorithms

The following chapter will present the set of image processing algorithms developed and selected for the evaluation of the data gathered by the Sextant-Sensor. These algorithms represent a major effort within the thesis.

As apparent from eq. (2.7), the necessary information for position determination is the knowledge of the satellite's attitude and the vector towards the Earth, as seen from the satellite. In the following, as illustrated in fig. 3.1, the documentation will start with the algorithms needed for the attitude determination from Star-measurements. This will be followed by the determination of the Earth-center using Earth-horizon measurements. The final step, which combines the information extracted from the images to obtain the position of the spacecraft, is explained in detail in chpt. 5.1.

Starting from the image acquisition, candidates for Stars need to be extracted from the acquired image. Before the actual direction towards the Stars in the sensor system can be determined, errors due to system-specific characteristics have to be corrected. The corrections include the effect of the optics used and detector design (chpt. 3.1.2). Following this step, the Stars need to be identified (chpt. 3.1.3). The final step is to determine the attitude of the sensor in the inertial space (chpt. 3.1.4).

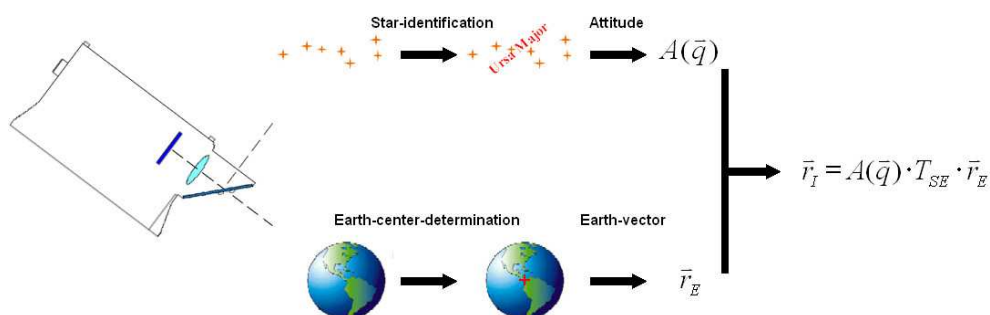


Figure 3.1: Flowchart Sextant-Sensor

The Earth-sensor, as explained previously, observes the Earth in VIS, resulting in a more complicated approach when dealing with the observations as compared to sensors using the IR image of the Earth. Following the acquisition, the Earth-horizon (chpt. 3.2.1) needs to be detected under a wide range of possible illumination conditions prior to the determination of the Earth-center (chpt. 3.2.2). After the horizon is found, the Earth-vector in the sensor system can be evaluated and passed to the subsequent data-processing. As the Earth-vector is a unit-vector defining the direction towards the Earth the additional information on the current orbit radius defines the position of the Earth in coordinates of the sensor system.

The combination of the attitude-matrix and the Earth-vector finally leads to the determination of the satellite's position. The distance from the center of the Earth to the satellite can be deduced from the apparent Earth-diameter, which is necessarily determined in the Earth-center algorithm. It might be of interest to note that to this point no information on the orbit or the satellite's dynamics is needed. The only system-specific parameter is the transformation matrix T_{SE} , which relates the attitude of the Earth-FOV to that of the Star-FOV (see fig. 3.1).

3.1 Attitude Determination From Star-Measurements

The following sections deal with the procedure followed to obtain a valid attitude information exclusively from the Star-image data.

The process from the Star-detection to the attitude output, as shown in fig. 3.2, will be discussed. Besides the final task of attitude determination, main emphasis will be put on the necessary precursors centroiding and Star-identification.

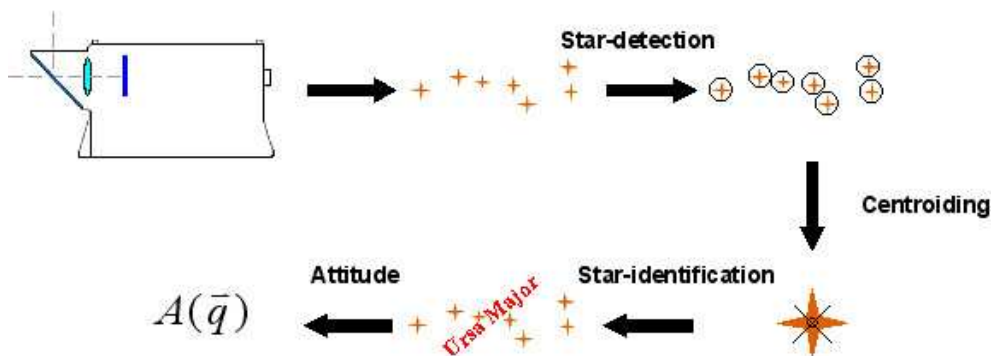


Figure 3.2: Flowchart Star-Sensor

3.1.1 Detection of Stars

The first step following the acquisition of a Star-image is the extraction of Stars from the image data. The challenge in this is to find a distinction between true Stars and events as *Single Event Upsets* (SEU), meaning spurious spikes, for instance due to proton impact on the detector as well as „extended objects“, such as other satellites, the Moon or even the Earth within the FOV. Other effects to be accounted for are given for instance by stray light, plumes and solar panels. In general, larger objects can easily be dismissed as not applicable. This is not always the case, though, resulting in the need to track Stars which were once acquired. A special case is the Rosetta mission, where the tail of a comet posed the problem of disturbing the Star-tracker due to reflection of sunlight on the tail's particles, which is erroneously detected as Stars ([30]).

In order to extract Stars from the image, a sequence of steps has to be applied, to provide a high probability that only true Stars are detected.

3.1.1.1 Algorithm for the Star-Detection Process

In the following a schematic step-by-step approach of the Star-detection process is presented. The constants given are those used in the detection of Stars on images obtained by the PixeLink-camera using the PCS-2112-LM-x-APS-detector. The details of this camera can be found in the Appendix A.3.1.

Step 1: **Threshold**

As a starting condition all pixels of the detector with their detector coordinates (x_i, y_i) exceeding a defined threshold are chosen as the center of a candidate region R_i . The size of each region is set to be $5 \text{ pixels} \times 5 \text{ pixels}$. The threshold is set to be approx. 6% of the full dynamic range of 65536 discretization steps given by the 16bit data-format.

$$\text{Signal}(x_i, y_i) > \text{Threshold} \quad | \quad \text{Threshold} = 4000$$

Step 2: **Requirements on the candidate region**

In order to assure that only Stars are extracted, the candidate region R_i needs to fulfill the following requirements:

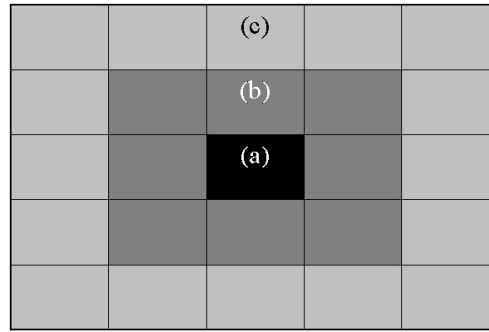


Figure 3.3: Specified Regions for Star-Detection

$$\begin{aligned}
 \max(R_i) &= \text{Signal}(x_i, y_i) \\
 \max(R_i) &> 1.6 \cdot \text{mean}(R_i) \\
 \max(R_i) &> 5 \cdot \text{mean}(Inner_i) \\
 \text{mean}(Inner_i) &> 1.15 \cdot \text{mean}(Outer_i)
 \end{aligned}$$

The $Inner_i$ and $Outer_i$ subsets of the region are defined as depicted in fig. 3.3, areas b) and c), respectively. Area a) is the center of the region, in the case as presented it consists of only one pixel.

This step eliminates false candidate regions and supplies those regions, where the highest illumination intensity is in the center. This is then used to determine the *center of illumination intensity*.

Step 3: Determination of the *center of illumination intensity*

For the determination of the center of illumination intensity ($[c_x, c_y]$) it is necessary to first determine the *noise floor*, which serves as an offset to the Star-signal. This is determined by calculating the mean of the pixels adjacent to the outer limits of the $Outer$ region. Then the center is determined by determination of the center of the pixel values corrected by the noise floor in the same manner as when determining the center of mass:

$$[c_x, c_y]^T = \frac{1}{\sum_i (\text{Signal}(x_i, y_i) - \text{NoiseFloor})} \sum_i ((\text{Signal}(x_i, y_i) - \text{NoiseFloor}) \cdot [x_i, y_i]^T).$$

If two Stars are within the selected region, and the first set of requirements is passed, the center will not be the center of either of the two Stars, but a combination of both. For this reason, the Star-catalogue contains a *proximity flag*, which marks Stars with a second Stars in their immediate proximity and is used to exclude this measurement from the attitude determination process.

This result is later-on refined in the Centroiding process.

A test of the proposed algorithm on a sequence of images showed that, while it sometimes lost Stars, it very scarcely chose false „Stars“. This behavior is preferable to the other possibility, which is detecting all Stars, but at the cost of introducing false measurements. The reason for that is that, as long as there are about 5 correctly recognized Stars, an identification reliability of about 98% is obtained, while incorrect Star recognition typically leads to a higher probability of a false identification.

3.1.2 Centroiding

Once a detection of Stars has been successful, the center of each Star has to be determined. A natural way to start the process is to determine the „center of illumination intensity“ by calculating an equivalent to the center of mass but using intensity levels as the „distributed mass“. This step leads to an accuracy which is influenced by two major sources of errors. For one point, we have several noise sources to deal with, ranging from those, which can be improved by design (e.g. quantization noise, dark current) to those, which can't (e.g. photon noise). Additionally we have to take into account the level of knowledge available on the camera system. In particular, this requires the calibration of the optical system. To further increase the accuracy, the actual intensity distribution of the Stars on the detector has to be taken into account. This *centroiding* process is strongly influenced by the choice of the optical system. In principle, the centroiding process has to determine the function, which relates the true vector to the observed Star to the position on the detector as determined using the „center of illumination intensity“. This knowledge can then be used to get the direction towards the Star from the measurements made. Due to the strong interrelationship between the optics, the detector and the centroiding process, the centroiding algorithms are specific to each choice of hardware components. Other effects, like thermal distortion, changes in the parallax and the aberration due to the finite velocity of light, are not considered in this work, since their influences are either too dependent on the system used or below the expected accuracy. The final result of this chapter is a correction table, which can be used to correct the measurements by making best use of the knowledge on the optical system.

3.1.2.1 Algorithm for the Centroiding Process

In the following a schematic step-by-step approach of the centroiding process is presented.

Step 1: **Determining the *Point Spread Function* (PSF)**

In order to precisely determine the position of a Star on the detector, it is vital to know the nominal shape of its image on the detector. Due to the optics used and its strong dependency on the position and orientation of the detector relative to the focal plane (fig. 3.6), this shape is not necessarily a point or, as often used, a Gaussian intensity distribution. Furthermore the image is dependent on the wavelengths λ present in the incident light. As the Star can be interpreted as a point source of light, its image on the detector is equivalent to the PSF of the optical system, which describes the intensities of the image at the detector coordinates (x, y) of a point-source as a function of its angles of incidence (α_x, α_y) relative to the detector axes.

$$\text{PSF}(x, y) = f(\text{Optics, Detector position, Detector orientation, } \lambda, \alpha_x, \alpha_y)$$

The PSF is a non-trivial function which has to be determined for the system used by analysis, calibration or a combination of both. Typical shapes of Stars as obtained from an optical system as the one used in the experiments which are to be presented can be seen in fig. 3.4.

Step 2: **Determination of the true Center of Illumination Intensity**

Using the knowledge on the PSF of the optics used, it is now possible to take further effects based on the detector into account. These in particular are the sensitivity of the pixel as a function of the position within a pixel (fig. 3.7, left), the shape of the photosensitive area of the individual pixels (fig. 3.7, right) and the sensitivity to different wavelengths. These properties are different for various types of detectors due to the manufacturing process and the optimization of the chip geometry.

Including these effects, it is now possible to determine the true center of illumination intensity for any Star under any angle of incidence. The resulting differences in the true Star-center to the center of intensity for a Star which is linearly moved across a pixel can be seen in figures 3.8, 3.9 and 3.10.

Again, this relation is a non-trivial function which has to be determined for the system used by analysis, calibration or a combination of both.

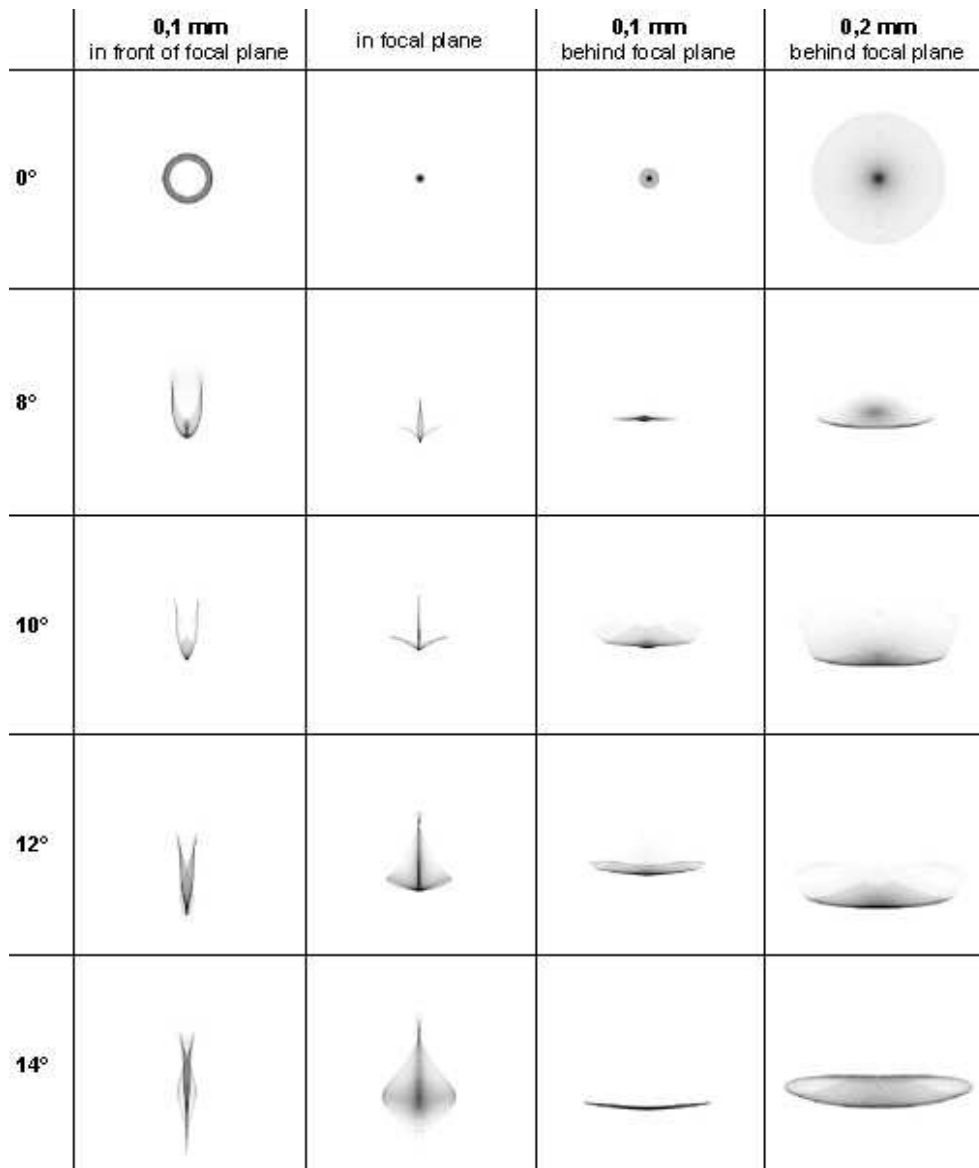


Figure 3.4: Point Spread Function as determined for a Star observed under various angles of incidence and different locations of the detector relative to the focal plane, grid size approx. $80 \times 80 \mu\text{m}^2$ (as reference: pixel size $7 \times 7 \mu\text{m}^2$, detector size approx. $7.2 \times 9 \text{mm}^2$).

Step 3: Building a Correction Table

Knowing the detector coordinates of the centers of illumination intensity as a function of the true Star-center, it is now possible to invert this knowledge and determine the position of the true Star-center by using the perceived center of illumination, as long as the relation is bijective. It is shown in fig. 3.9 that this is not always the case, yet this effect is excluded in the following process.

The correction table contains the true Star-position in detector coordinates as a function of the observed center of intensity in form of *optical coordinates* which can directly be transformed to α_x and α_y as introduced above and to unit vectors in sensor coordinates pointing towards the Star.

Since the relation is not necessarily described by a closed form solution, correction tables are used. As the function is shown to be comparatively smooth, a discretization to ten steps per pixel is chosen (see fig. 3.12.). The correction table itself is compiled for every 50th pixel.

Step 4: Correction of the Center of Intensity

Knowing the center of illumination intensity and the correction table, the true direction towards the Star is determined by using the table in the form presented in table 3.6 and the corresponding fig. 3.12. The corrected detector coordinates are then translated into a unit vector towards the Star in the sensor coordinate-system.

In the following, the process is explained in greater detail.

3.1.2.2 Additional information on the Centroiding Process

In the investigations on the centroiding process, a variety of effects has been addressed. The first effect to be introduced is the purely physical effect of photon-noise, as introduced in eq. (2.1). This photon-noise, in connection with a Star being spread over approx. 3×5 pixels with the assumption of an approximately Gaussian intensity distribution, leads to an inaccuracy of the Star-center determination as a function of the Star's visual magnitude, which is shown in fig. 3.5.

The characteristics of the sensor system and the additional assumptions on the optics needed for the simulations are given in table 3.5. The simulated system is based on the optics used in the laboratory- and field-experiments. All that is needed in order to determine the photon-noise, is the number of photons which are detected. These are dependent on the type of the Star under observation, its intensity and the optics used. The type of Star is of importance, as it defines the emitted spectrum. Since the detector is not homogeneously sensitive to radiation of all wavelengths, this information is of importance, as it influences the number of detected photons, and thus the

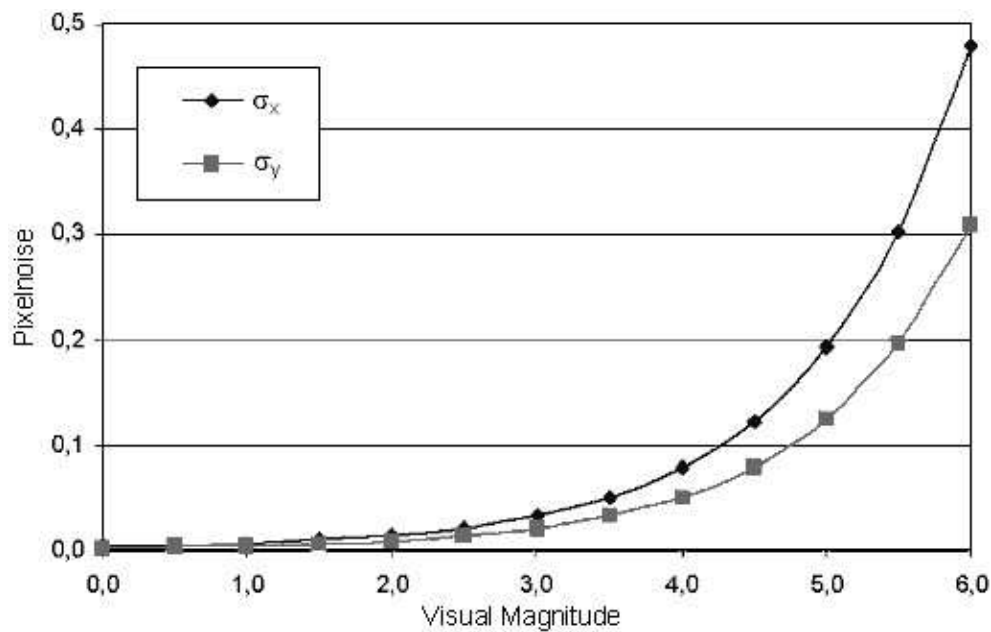


Figure 3.5: Effect of photon-noise on centroiding accuracy in x - and y -direction of a Star being spread over approx. 3×5 pixels, as a function of the Star's visual magnitude.

perceived intensity: even if the integrated intensity over all wavelengths is the same, two Stars can therefore be detected with different accuracies, depending on their emitted spectrum.

The reason for the different accuracies in x and y in fig. 3.5 result from the non-symmetrical image (smear) of the Star, which depends upon the optics and the location of the Star-image on the detector. It should be stressed that the noise levels shown are physical limits, which can only

Table 3.5: Assumptions made in photon-noise determination

Exposure Time:	1/10s
Aperture:	\emptyset 10mm \square 79mm ²
Bandwidth:	400nm (500nm .. 900nm)
Quantum Efficiency	50%
Fill-Factor	70%
Star-image size (smear)	$3 \times 5 = 15$ Pixel ²
Resulting Photon-Flux:	3×10^5 Photons (with observation of a Star of Visual Magnitude 0)

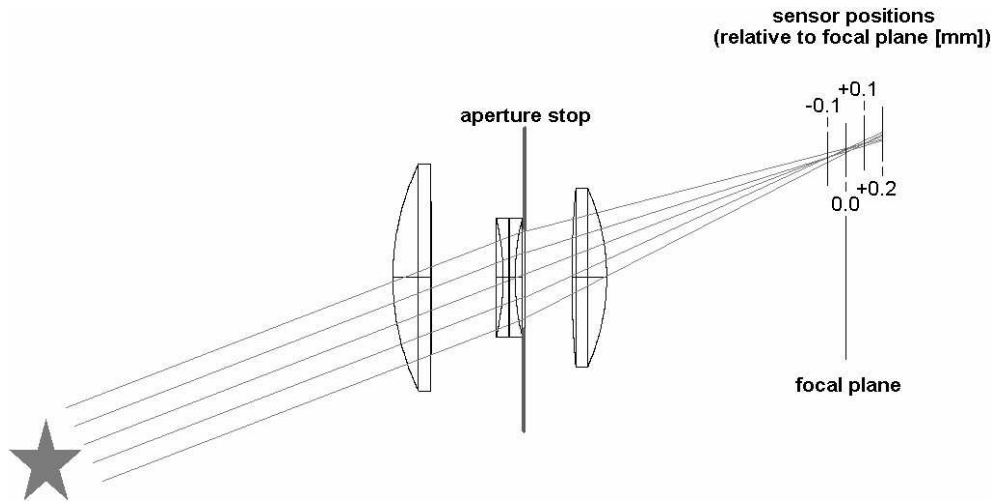


Figure 3.6: Schematics of a „simple“ four-lenses consumer optics

be improved by changing the system’s principal setup, like changing the aperture or the exposure time. They can not be improved by reducing the noise introduced by any component. The exposure time in general can be assumed to be fixed, as it is primarily defined by the system’s update rate (e.g. 1 Hz). Even if the exposure time could be changed, its usefulness is diminished as soon as the satellite possesses an angular rate. In this case, the Star-image would greatly be influenced by the satellite motion, thereby diminishing and at higher rates annihilating the effectiveness of the centroiding process. The only component, which could beneficially be changed would be the optical system, in particular its focus, thus reducing the Star-smear and increasing the intensity level. This, in turn, has a negative influence on the centroiding process: As a simple example, if we chose the Star to be focused onto a point with infinite intensity, the photon-noise would be negligible, the position of the Star, though would not be known any better than to the pixel level, since all that is known, is the pixel, which receives the energy.

This shows that, in order to be able to determine the center of a Star to sub-pixel level, it is necessary to have the image of the Star being spread over several pixels. This is achieved by deliberately defocusing the optical system. As was shown, there is a trade-off which has to be made when the image size is chosen, since the illumination level reduces with an increase in the number of illuminated pixels, which in turn increases the influence of other noise sources, such as the photon noise. A typical value is an image smear of approx. 3×3 pixels² to 5×5 pixels². In addition to have the Star spread out, in order to further increase accuracy, the shape of the Star-image needs to be known. Typically, Star-images as obtained when using high-quality optics are assumed to possess either a nearly constant or a Gaussian intensity-distribution, holding

$$Signal(x, y, c_x, c_y) = \frac{1}{2\pi\sigma^2} \cdot e^{-((x-c_x)^2+(y-c_y)^2)/(2\sigma^2)}, \quad (3.1)$$

with (x, y) being the point of interest, (c_x, c_y) being the actual Star-center and σ being the variance of the Gaussian PSF. A closer investigation of the system, though, showed that this assumption does not hold in the case of simple consumer optics with four lenses, as it has been used throughout these investigations (see fig. 3.6). The *Point Spread Functions* (PSF) of a Star as observed with such an optical system are shown in fig. 3.4. The PSF is unique for different optical setups, as it describes the physical, refractive behavior of the optics. It is thus determined using ray-tracing techniques for the optical system used.

This leads to the second effect, which influences the centroiding accuracy: the choice of the optical system. It becomes readily apparent that, using consumer optics as the one presented, even the assumption of a Gaussian intensity distribution only holds if the Star is observed in the direction of the line-of-sight. In the special case of the sensor proposed, this will nearly never be the case, since the Earth is observed at that place and thus will cover a non-negligible area in that region. Even if the Star is observed in the center of the FOV, it is still not necessarily shaped as expected: if the detector is shifted 0.1 mm in front of the focal plane, the Star is observed as a torus, rather than displaying a point or a Gaussian shaped intensity distribution.

The third effect is on the detector level, where two major detector properties need to be taken into account, when investigating the centroiding performance: as mentioned, the detector itself, especially today's APS-detectors, does not have a *fillfactor* of 100%, meaning that not all of the detector's area is photo-sensitive. Another property is the varying sensitivity across a pixel. Both properties are based on three physical features of the detector(see e.g. [31]):

- Diffusion of the generated electrons, in particular lateral diffusion. This is often referred to as diffusion length.
- Optical transmission of coatings and wiring layers (electronically conductive, optically transparent) on the surface of the substrate.
- Active and passive elements (e.g. A/D converters and transistors) which are included in the APS-design.

A further property influenced by the lateral diffusion is the cross-talk. If electrons are generated in one pixel, due to the concentration gradient generated in the photosensitive layer, some electrons traveling along the gradient reach the adjacent pixels. This effect is more eminent in CCDs than in APS-detectors, as the layer in CCDs is thicker, than in APS, thus allowing for a longer traveling time of the electrons prior to reaching the electrodes, and such resulting in a higher cross-talk. The advantage of a thicker layer is the higher sensitivity, which is an aforementioned advantage of the CCDs vs. APS-technology. As the cross-talk in APS-detectors is relatively low, it will be neglected in the following investigations.

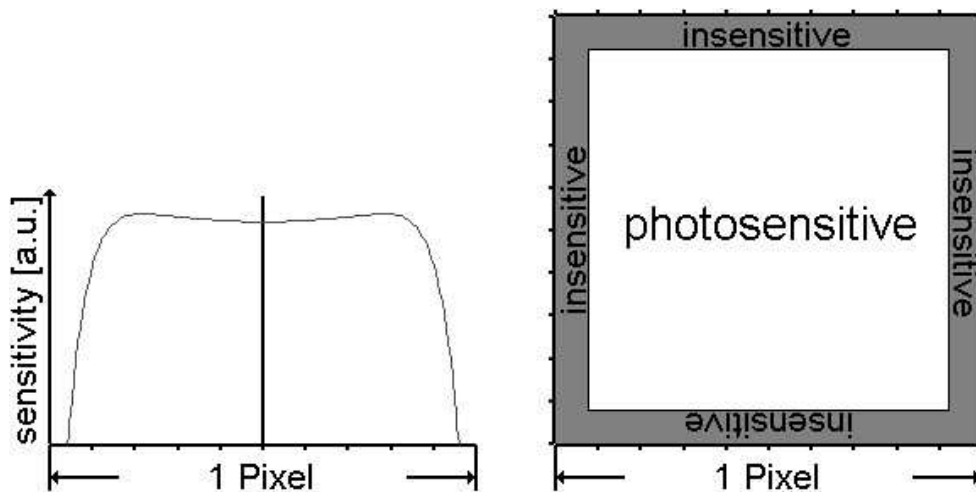


Figure 3.7: Assumptions made for the varying sensitivity across a pixel (left) and photosensitive area of a pixel (right)

In the investigations on the optical system, as far as necessary, the following assumptions have been made, based upon the chosen APS-detector and „typical“ sensitivity functions: the fillfactor is set to be 70%, leaving 30% of each pixel insensitive to incoming photons. In APS-detectors this is the area used for signal conditioning. The sensitivity within each pixel is assumed to be „hat“-shaped. Both assumptions are visualized in fig. 3.7

Taking these effects into account, the simulation of a Star moving linearly over the pixel grid results in a difference between the actual Star-center and the determination of the center of intensity by using the individual pixel values of the Star-image. This effect is shown in fig. 3.8. The simulated Star is 8° off-axis and moves linearly over one pixel with the motion being discretized to 14 steps in the images shown. In the picture series, two lines can be seen in each image. This can be explained, by again looking at the PSFs in fig. 3.4: since the Star-images are not point-symmetrical, they result in different achievable accuracies in the two axes.

Closer observation leads to the assumption that it might be beneficial to defocus the system such that the detector is located slightly behind the focal plane. This leads to shapes, where the center is more accurately determined along one of the two directions. Placing it further back is not a valid choice, since it would further reduce the intensity level of the individual pixels, such increasing the error due to photon noise. Placing the detector in front of the focal plane results in a high variation of the determined center, when a Star moves across the pixel possessing a non-photosensitive area, which makes a calculation of the „real“ center more susceptible to errors.

The most important property of the resulting curve, though, in order for it being used as a cali-

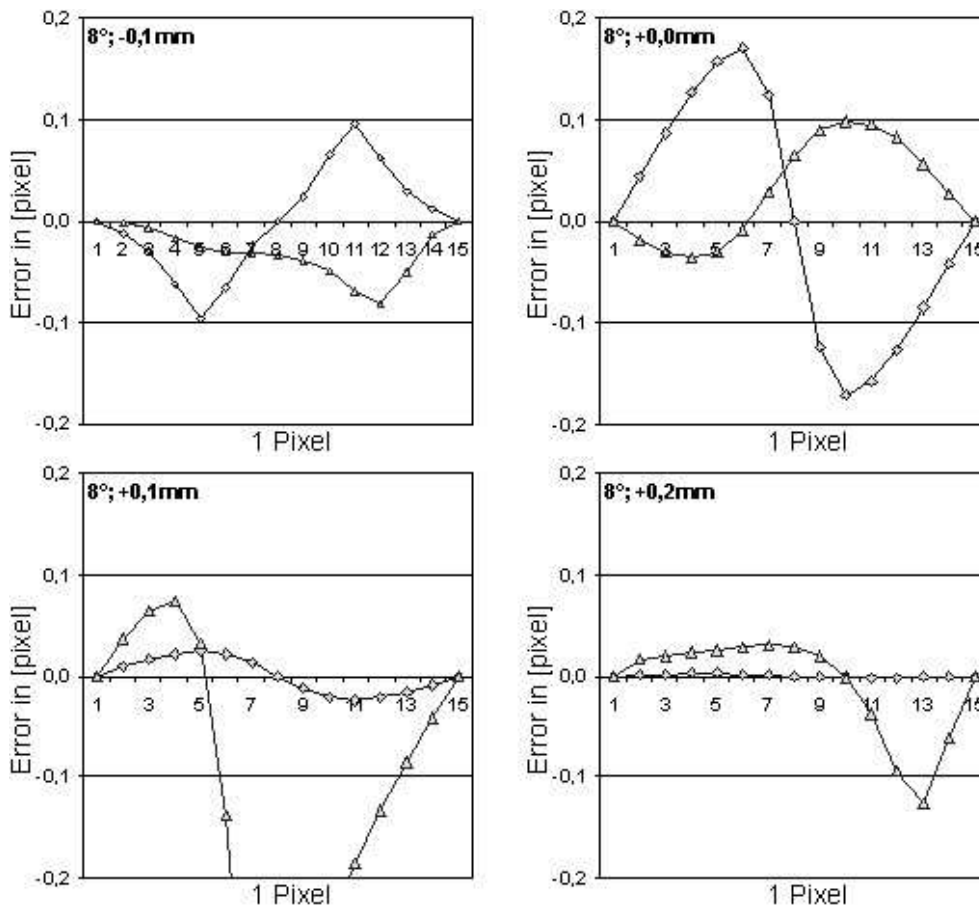


Figure 3.8: Errors made in x - and y -direction in the determination of Star-centroids, when using the „center-of-intensity“-approach for different locations of the detector relative to the focal plane (simulation results)

bration function, is the uniqueness of its inverse. This eliminates the possibility of centroiding the worse direction of the chosen Star-image, since, when looking at its trace, as plotted in fig. 3.9, it is obviously impossible to assign a single „true“ value to all measured locations, since some of them occur as often as three times throughout the course of the Star across one pixel. The reason for nevertheless choosing this seemingly unfavorable location will be explained in the next paragraph. Similar comparisons have been carried out for various observation angles, which supported these results.

Having decided upon moving the detector slightly behind the focal plane, the behavior of the centroids motion when rotating the Star-image with respect to the detector's grid have to be investigated. This occurs if the Star is not on one of the detector's axes, which are assumed to be centered and aligned with the grid's orientation. As already pointed out, due to their non-point-symmetrical features, the centers of the Star-image are different in their accuracy. This becomes readily apparent in fig. 3.10. It can be seen that, as the image rotates, the axes change their accuracies- until

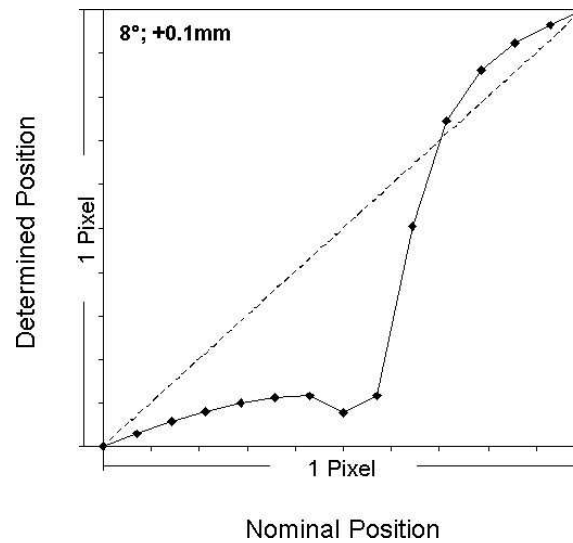


Figure 3.9: Nominal (dashed) vs. determined (solid) trajectory of Star-center in y-direction, showing a non-bijective behavior (simulation results)

finally, the previously worse axis becomes the better. As indicated, this results in regions of different choices for the chosen value. The regions can be seen in fig. 3.11, where it is schematically shown that the value chosen depends on the section, in which the Star is located. Namely, if the Star is within a section closer to the y-axis, the value, which is more precise, is the x -location of the Star, if the Star is in a section closer to the x -axis, consistently the y -location possesses a higher precision. It should be noted that it is in principle beneficial, to use measurements which are more accurate in one direction, than in the other, as long as the „better“ measurement is better than the equivalent measurement with a uniform accuracy. This is in contrast to current attitude determination algorithms which assume uniformly distributed accuracies in the centroids. Of course, this approach implies a certain requirement on the Star-distribution on the detector: In order to determine a valid and precise attitude, measurements from different regions of the detector need to be made, covering the regions for better determination of the x - and the y -value, respectively.

The use of the knowledge gained by this investigation results in the possibility to reach a higher precision in the centroiding process. This is achieved by using the known relation between the actual Star-center and the center of illumination. In a practical approach this relation can be obtained by analysis, as demonstrated above, by calibration or by a combination of these two methods. To include these corrections with sufficient accuracy and high efficiency, a discretization method was used. In a first step, the correction within a pixel is based on the first rounded decimal of the uncorrected pixel value. This results in correction tables as introduced in *Step 3* with 11×11 correction-values per pixel (10 + opposite edge). In a second step, the number of correction-tables is reduced to be available every i pixels. The corrections are assumed to be equal for all quad-

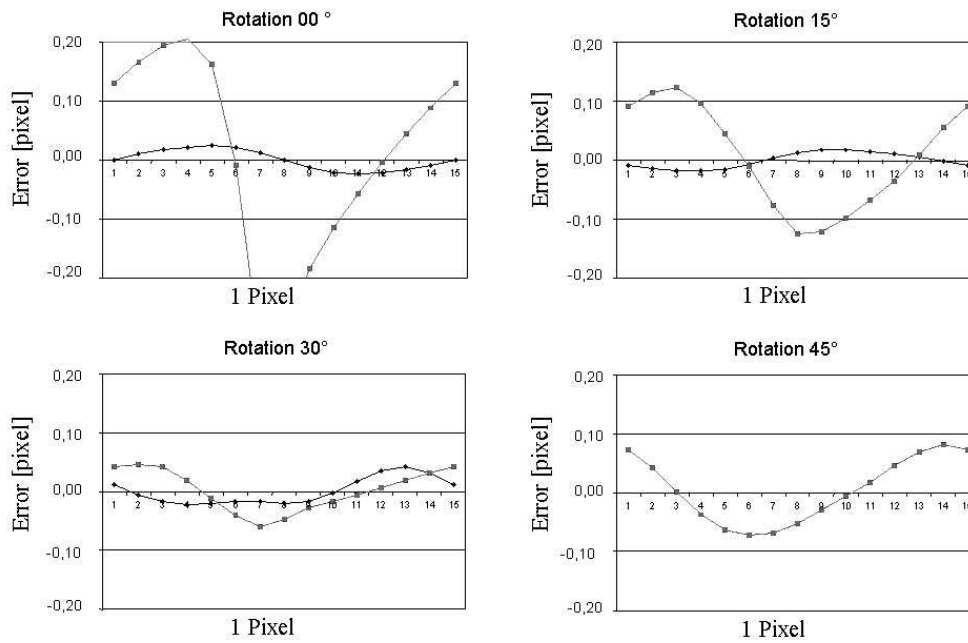


Figure 3.10: Expected Errors in Centroiding when rotating the PSF of a Star being 8° off-axis with a detector $+0.1$ mm behind focal plane (simulation results, based on 15 steps per pixel)

rants, so the tables are only given for one quadrant. Note that they are not assumed to be equal in each octant, since possible differences in the pixel's x - and y -dimensions need to be covered. The correction-values are then linearly interpolated within and between the correction-tables to be consistent with the observed pixel. Thus, instead of using the actual correction-values at the given points, it might be necessary to change the correction-values such that the error made during interpolation is minimized.

In particular, the correction-tables used are chosen by the integer value of the *optical coordinates* of the center pixel. In this nomenclature the *optical coordinates* denote the location of a Star on the detector relative to the optical center. The optical center, again, is given in integer values. This is permissible, since the shape of the PSF does not vary drastically, when moving the optical center by one pixel. Additionally, it is necessary for the correction to precisely know the Star's center within the pixel grid, since it takes into account the pixel's sensitivity function. Note that the PSF is not the apparent motion across the pixel, when the Star is being moved. The chosen correction-tables are used to interpolate the correction-value in x - and y -direction. The correction-values from the four correction-tables are chosen by the rounded first decimal. The corrected optical coordinates can now be used to determine the unit vector towards the Star in the sensor system

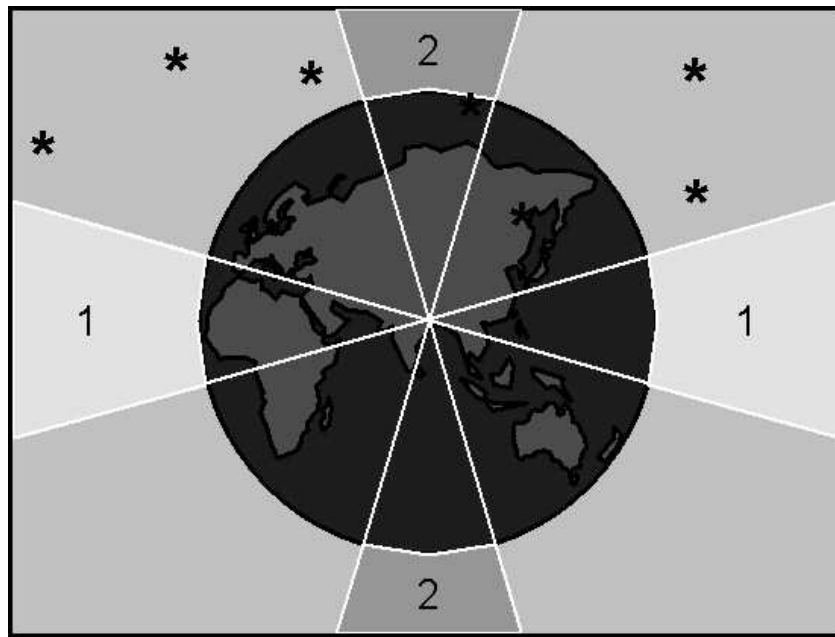


Figure 3.11: Consequences drawn from the different accuracies in x - and y -direction. Centroids in area „1“ provide better accuracies in y -direction, centroids in area „2“ in x -direction.

using the relation

$$\underline{b} = \frac{1}{\sqrt{x^2 + y^2 + f^2}} \begin{bmatrix} x \\ y \\ f \end{bmatrix}, \quad (3.2)$$

with x and y being the corrected optical coordinates of the Star and f being the focal length of the optical system. In reality, this formulation holds for ideal optics only and needs to be augmented by corrections for optical distortions, such as *barrel* or *pincushion distortion*. In order to use it directly, these effects need to be taken into account in the creation of the correction tables.

An example for this procedure is given in table 3.6.

The investigations showed that the lense system must satisfy a certain level of accuracy, since too inferior optics might lead to costly algorithms or even uncorrectable Star-images. Thus, in order to achieve accuracies of better than $1/10^{th}$ pixel, several conditions need to be met. Important factors are a large aperture for high illumination levels and a quality of the optical system which keeps the distortions of the PSF low enough for smooth calibration functions.

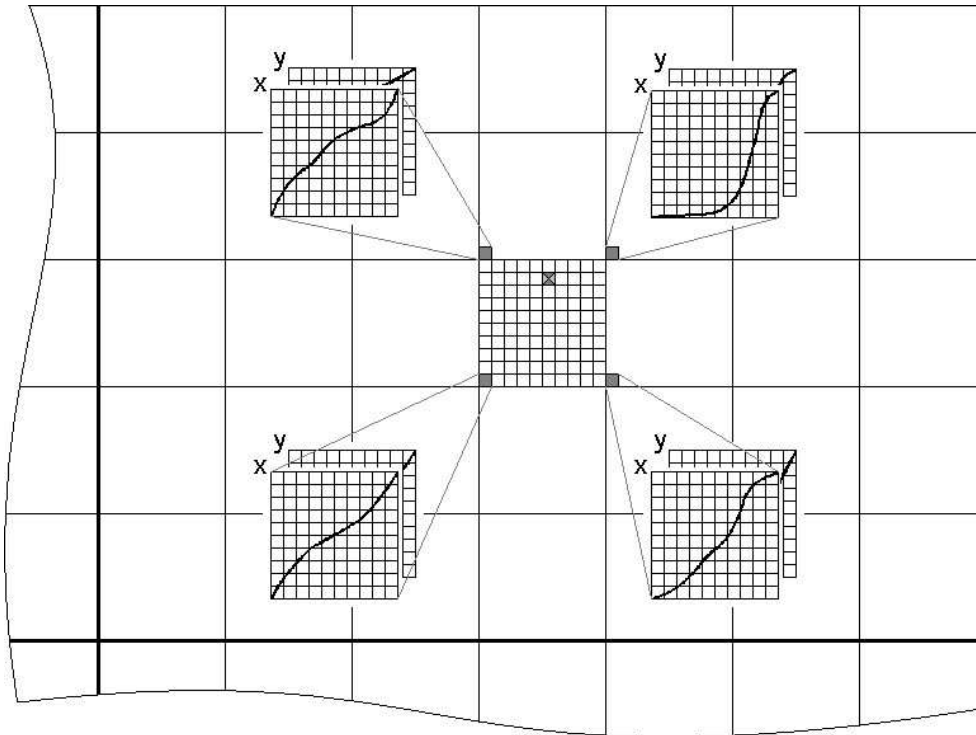


Figure 3.12: Use of Centroiding Correction-Tables

Table 3.6: Example for use of correction tables

Premises:	Correction-tables Star-center, uncorrected, <i>pixel coordinates</i> Optical Center:	each 50 pixels [1000.360; 712.740] [620; 512]
Applied to:	Star-center, uncorrected, <i>optical coordinates</i>	[380.360; 200.740]
Calculations:	Correction-tables used: Index to correction-value used: Linearly interpolated correction-values:	[350; 200] [350; 250] [400; 200] [400; 250] [4; 7] e.g. [0.051; -0,032]
Solution:	Star-center, corrected, <i>optical coordinates</i> :	[380.411; 200.708]

In total, the fundamental law is further sustained that a high quality measurement sets the basis for a high quality result, whereas the improvement of low quality measurements by means of algorithms is always limited. It was shown though, that in a wide range, the accuracy can be improved by using an advanced algorithm, as the one presented, to compensate the deficiencies of the sensor package.

3.1.3 Star-Identification

After successful Star-detection and centroiding, it is still necessary to identify the Stars observed. Star-identification links the vectors as determined in the Star-sensor reference system to the appropriate vectors in the inertial reference system in order to determine the satellite's attitude.

In the special case of the optics used, we have to overcome two challenges: one is the desired large FOV, in order to simultaneously observe Stars and the Earth. This, in principle, does not represent a difficulty in the algorithms, but increases the necessary computational power and memory size due to the necessarily larger Star-catalog, or, to be more precise, the larger angular-separation catalog. The second is not as easily overcome: the use of a simple consumer optics. This optics results in a higher inaccuracy in the determination of the Star-centroids and thus results in the need to have a higher tolerance with respect to false identifications.

The Star-identification algorithm developed in the frame of these studies has the advantage of a user defined output. This includes the opportunity of comparing all possible identifications to an identification history to improve the system's reliability. In contrast, typically used identification algorithms (e.g. [32]) only provide the most likely identification.

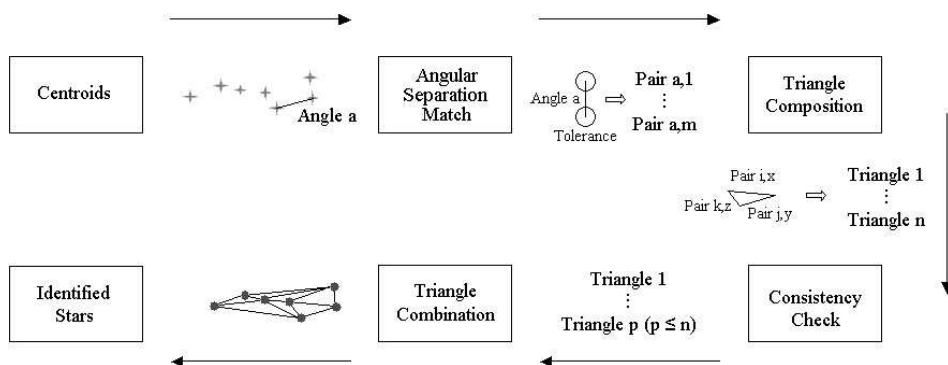


Figure 3.13: Star-Identification Process

The algorithm, which systematically solves a combinatorial optimization problem in minimizing the error made in the assignment of Stars and Star-patterns to the measurements, consists of various components which successively increase the unambiguosness of the identification. The steps can be seen in fig. 3.13.

3.1.3.1 Algorithm for the Star-Identification Process

In the following a schematic step-by-step approach of the Star-identification process is presented.

Step 1: Angular Separation Match

For all possible angles β_{ij} between the measurement vectors \underline{b}_i and \underline{b}_j pointing to possible Stars, which are determined by the centroiding process and the knowledge of the optical system, find the Star-pairs consisting of Stars s_p and s_q in a Star-catalog with a separation angle ρ_{pq} which matches the angle between measurements with tolerance ε . (See schematic in fig. 3.14.)

$$|\beta_{ij} - \rho_{pq}| < \varepsilon \quad |i \neq j$$

Due to inaccuracies in the Centroiding process this allocation does not necessarily result in a unique solution.

Step 2: Triangle Composition

Combine all allocated Star-pairs p_{ij} that share common Stars and measurements to Star-triangles t_{ijk}

$$\subset (p_{ij}, p_{jk}, p_{ki}) = t_{ijk} \quad |i \neq j \neq k$$

This step already eliminates most of the invalid allocations.

Step 3: Consistency Check

The *sense of rotation* $Sense_b$ of the triangle composed of the measurement vectors \underline{b}_i , \underline{b}_j and \underline{b}_k is compared to $Sense_r$ composed of the Stars with the vectors \underline{r}_p , \underline{r}_q and \underline{r}_r . For this procedure, the vectors towards the Stars and the measurement vectors are compared in the following fashion:

$$\begin{aligned} Sense_b &= (\underline{b}_j \times \underline{b}_i) \cdot \underline{b}_k \\ Sense_r &= (\underline{r}_j \times \underline{r}_i) \cdot \underline{r}_k \end{aligned}$$

The match is only valid, if both results have the same sign and, ideally, the same value. A visualization is given in fig. 3.15, which shows the senses of direction with the consistent triangle vs. a triangle composed with the use of a false Star, denoted 7'.

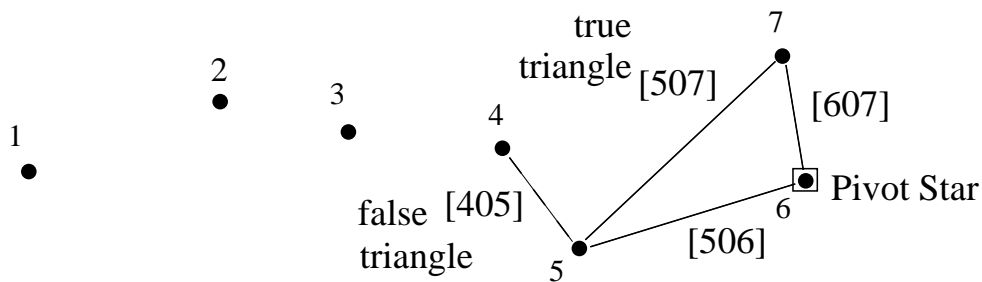


Figure 3.14: Use of *a priori* information on valid combinations of angles in the triangle composition

Step 4: Triangle Combination

The found triangles are combined along common sides to form polygons ($n_{[...]}$) in order to further increase the probability of a correct Star identification. Further triangles are added to the polygon in the same manner as often as possible, leading to polygons consisting of at most as many corners as the number of centroids in the given image. In addition to the increase in the identification probability, this step combines „connected“ individual identifications.

$$\begin{aligned} \subset (t_{ijk}, t_{hij}) &= n_{hijk} && | h \neq i \neq j \neq k \\ \subset (t_{ghi}, n_{hijk}) &= n_{ghijk} && | g \neq h \neq i \neq j \neq k \\ &\vdots && \end{aligned}$$

In the case of a unique solution this leads to a single polygon containing all found triangles. Even in less favorable cases this leads to a small number of possible solutions.

Step 5: Choice of the most likely solution

In the end a criterion is defined to choose the „most likely“ solution with the help of parameters which are determined throughout the identification process. A typical criterion is to choose the identification which identified the largest polygon with the least mean-square error in the separation angles as a secondary condition. Alternatively, a weighted least-square criterion, using for instance the size of the polygons, so the number of presumably identified Stars, as weight, can be defined.

The likelihood for a false identification is further reduced during the recurrent process by use of a time-history.

In the following, some of the individual steps are explained in greater detail. An example is given in the Appendix A.1.1.

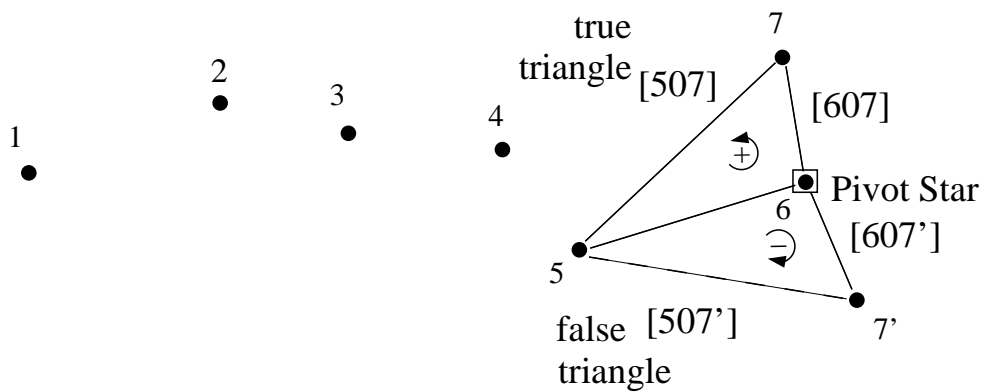


Figure 3.15: Consistency check by comparison of the sense of rotation of the triangle in sensor coordinates to the sense of rotation as given in the Star-catalog

3.1.3.2 Additional information on the Star-Identification Process

In *Step 2* matching Star-pairs are searched for in order to perform a **triangle composition**. In order to reduce the number of comparisons and thus reduce the number of false identifications, the Star-pairs found are stored in a way such that the information on the pattern of the measurements on the detector is preserved. This results in a selectivity to only built sensible triangles, in a sense that the angles taken into account truly compose a triangle. The use of this information can be seen in fig. 3.14. A true triangle therefore is only found, if the Star-pairs taken from the catalogue as well as the corresponding measurements compose „true“ triangles.

Step 4 is a **triangle combination** in which the triangles are searched for common Star-pairs. Again, the measurements and the candidate Stars are treated in their union to ensure that not only the common Stars connect two triangles, but that the triangle is consistent with the measurements as well. Obviously, it would be possible to combine all triangles with at least one common Star. It was assumed beneficial, though, to combine along common sides. This provides another information which is determined throughout this identification: the error being made in the identification process. For each found Star-pair which is assumed to correspond to a measured separation, the deviation between the two is saved along with the Star-data as an error signal. When the triangles are assembled, the squared errors of the individual sides are added up. Similarly, when combining triangles, the errors of each individual triangle are added up. In the case of a complete identification of all triangles involved in building the structure, every single side is used the same number of times and no connection between a triangle and the rest of the structure is based on a single point connection. This as well means that the number of combined triangles, which is being tracked throughout the process, is identical to the theoretical value expected for the number of triangles

which can be found using the given number of observations. This introduces an error, in the case that not all sub-triangles composing the structure are found, since in that case not all sides would be used the same number of times. Nevertheless, when comparing the same number of triangles with respect to their mean error, this value still is of relevance. In a second step, succeeding the identification process, the difference in the angular distances between all identified Stars is determined, which is a more adequate measure of the introduced error when comparing structures with a different number of triangles.

The reason for not necessarily taking the largest structure as a valid identification is the presence of false „Stars“ in the image. Since they can not be distinguished from „real“ Stars throughout the identification, the only way of sorting them out is by means of an „adequate logic“ in the identification process. In the end, the adequate logic is introduced by definition of a criterion to chose the „most likely“ solution with the help of parameters which can be determined throughout the identification. In the current version, it seems to be sufficient, to chose the identification which identified the most measurement-points with the least mean error per triangle. The tool is prepared, though, to chose any given ratio (e.g. „error“/„(number of triangles)““) or any user supplied rule. This is made possible by the option of receiving all sub-results along with the identification deemed the most likely, which is one of the most important features of the algorithm. It enables the identification of observed Stars even in the presence of high measurement errors. Even if the correct solution might not be the most likely, there is a very high possibility that it is included in the output. By use of a time history, for example, the correct identification can be extracted from the record. Following a successful identification, the identified Stars can be tracked to further check the consistence of consecutive identifications.

The opportunity of having all possible identifications at hand, was highly valuable for the evaluation of the data gathered by the flight experiment. The uncalibrated and uncorrected data as gathered using a COTS-optics needed the tolerance to be increased up to 240” before a valid identification was achieved.

The disadvantage so far is the use of Matlab, which requires high computational power. This can be reduced though, using appropriate search routines (e.g. [33],[34]). In order to decrease computation time, investigations have been carried out, taking into account the specific demands of a large FOV. This has been done, for instance, by reducing the Star-catalog’s size by taking into account the observation probability of Stars, homogenizing the Star-density or taking into account only those triangles with a certain distribution of Stars (e.g. [35, 36]). Since a detailed investigation of these algorithms and possibilities would represent an autonomous field of research, it has not been carried out in the frame of this thesis.

3.1.4 Attitude Determination

The final step required to obtain the attitude from the Star measurements is to relate the vectors to the identified Stars in the reference frame of the detector to the inertial reference frame.

Various algorithms can be used to determine in this way the attitude from the vector measurements obtained through the Star identification. While all of them perform a minimization, different approaches are possible. In principal these involve different choices of achieving a real and orthogonal attitude matrix representing a rotation while preserving lengths and angles. Furthermore, they can be divided in those which determine a rotation matrix and those which determine the corresponding quaternion in a direct fashion. Quaternions are an attitude representation in vector form, with only one redundant parameter. The vector contains the information on the rotation angle and the axis, about which the system needs to be rotated. It requires the constraint of unity length, but possesses no singularity. The quaternion in our case is composed as

$$q = \begin{bmatrix} \underline{q} \\ q_4 \end{bmatrix}, \text{ with } |q|^2 = 1. \quad (3.3)$$

\underline{q} is the axis of rotation, multiplied by the sine of the rotation angle, q_4 is the cosine of this angle. This definition is of importance, as there are two major conventions being used: one having the „angle“ as first entry, and the „rotation axis“ below, the other one as the one shown above.

The basic idea for all algorithms is the formulation of a cost-function in the so-called *Wahba*-problem, first mentioned in 1965 ([37, 38]):

$$L(A) \equiv \frac{1}{2} \cdot \sum_i a_i \cdot |\underline{b}_i - A \underline{r}_i|^2. \quad (3.4)$$

In this notation, a_i denotes the weight, given to the corresponding measurement \underline{b}_i which is related to the vector in the inertial reference system \underline{r}_i through the attitude matrix A . Obviously, as it is determined from observations, which are subject to noise, A itself possesses a covariance, an estimate of which is given in chpt. 3.1.6.

3.1.4.1 Algorithm for the Attitude-Determination Process

In the following a schematic step-by-step approach of the attitude-determination process is presented.

Step 1: Definition of the attitude-determination problem

The *Wahba*-problem can be solved by solving the *singular value decomposition* (SVD) of the following equation:

$$B = \sum_i a_i \underline{b}_i \underline{r}_i^T$$

in the form of

$$B = U \Sigma V^T$$

where U and V are orthogonal, the singular values in Σ are arranged as

$$\Sigma_{11} \geq \Sigma_{22} \geq \Sigma_{33} \geq 0.$$

Step 2: Determination of the optimal attitude matrix

After performing the SVD, the optimal attitude matrix is determined by

$$A_{opt} = U \text{diag}[1, 1, \det(U) \cdot \det(V)] V^T.$$

In the following, the origins of the attitude-determination algorithm is explained in greater detail.

3.1.4.2 Additional information on the Attitude-Determination Process

In the following, a few methods for attitude quaternion determination will be presented. The presentation will be followed by a section on the expected attitude determination accuracy. The discussion is based primarily on references [39] and [14].

The first method is the „straight forward“ solution, based on the pseudo-inverse of the system

$$\underline{b} = A \cdot \underline{r} \tag{2.2}$$

with \underline{b} as the measurement, A as the (unknown) transformation matrix and \underline{r} as the reference vector, which represents \underline{b} in the inertial reference system. Due to the interdependency of the components of A , the system can be solved as soon as more than one observation is available. Formally, the solution can be obtained as

$$A = \mathcal{B} R^T \cdot [R R^T]^{-1}. \tag{3.5}$$

with

$$\mathcal{B} = \left[\underline{b}_1, \dots, \underline{b}_i \right] \quad | \quad i > 2$$

as a matrix containing the measurements and

$$R = \left[\underline{r}_1, \dots, \underline{r}_i \right] \quad | \quad i > 2$$

as the matrix containing the corresponding reference vectors. The requirement of „ $i > 2$ “ contradicts the knowledge that the attitude can already be obtained with the use of two observations.

To satisfy this condition, in the case of two observations, a third, artificial, measurement as well as the corresponding reference, has to be generated, in order to be able to solve for A . This is done by providing the vector product of the two measurements as well as that of their reference vectors. The result is a linearly independent „pseudo-measurement“. Using this type of attitude determination, it is possible to introduce an alternative feasibility check in the Star-identification: instead of combining possible Star-pairs to triangles, the attitude corresponding to each Star-pair can be determined and used for choice of the most-likely identification by determining the most-likely attitude. In the case of two or three measurements, instead of building a pseudo-inverse, the regular inverse of a 3×3 matrix can be used. As is readily understood, in the form presented, no weighting of the individual measurements is performed.

The problem when determining A with a pseudo-inverse results from the way the system is solved: instead of solving for an optimal rotation matrix, an optimal solution in the least-squares sense is found. This in general results in a non-orthogonal matrix A , which has to be orthogonalized prior to being used for attitude information and quaternion determination, since in both cases a proper, real, orthogonal matrix is of uttermost importance. This is the reason, why solutions, not taking into account the constraint given by A 's nature will in most cases perform suboptimally, despite optimally solving for the transformation matrix from \underline{r} to \underline{b} . In order to orthogonalize the resulting matrix, the following algorithm is used ([38]):

$$A_{orthog} = A \cdot [A^T A]^{-\frac{1}{2}}. \quad (3.6)$$

A slightly different approach, already including the orthogonality constraint on A , is used in the *Singular Value Decomposition* (SVD) as introduced in chpt. 3.1.4.1. In principal, this algorithm is computationally expensive. Using Matlab, though, very efficient algorithms are available, making it, in a first approach, the fastest and most reliable of the methods under investigation and therefore the method of choice in the further development.

The second method, using a quaternion representation of rotations, is based on Davenport's *q-method* (e.g. [14]). The approach is based on the knowledge, that the rotation matrix can be determined from the quaternion using the relationship

$$A = (q_4^2 - |\underline{q}|^2) \cdot I + 2 \cdot \underline{q} \underline{q}^T - 2 q_4 \cdot [\underline{q} \times]. \quad (2.4)$$

Stepping back for a moment, and taking a look at (3.4), the equation can be transformed to yield

$$L(A) \equiv \sum_i a_i - tr(AB^T). \quad (3.7)$$

This formulation illustrates that the function $L(A)$ is minimized by maximizing the trace of AB^T . Stepping forward again, it is now possible to rewrite the trace using the quaternion representation

by writing

$$\text{tr}(AB^T) = q^T K q, \quad (3.8)$$

with

$$K = \begin{bmatrix} S - I \cdot \text{tr}(B) & \underline{z} \\ \underline{z}^T & \text{tr}(B) \end{bmatrix}. \quad (3.9)$$

It was convenient to define

$$S = B + B^T \quad (3.10)$$

and

$$z = \sum_i a_i \cdot \underline{b}_i \times \underline{r}_i. \quad (3.11)$$

Considering the normalization constraint, the equivalent formulation of the cost-function results in

$$g(q) = q^T K q - \lambda \cdot q^T q. \quad (3.12)$$

Differentiating this formulation with respect to q^T , and setting the derivative identical to „zero“, the following condition is obtained:

$$K q = \lambda q. \quad (3.13)$$

Substituting this expression in (3.8) results in

$$\text{tr}(AB^T) = q^T \lambda q = \lambda. \quad (3.14)$$

Since the trace was to be maximized, the solution to the system is the Eigenvector corresponding to the largest Eigenvalue. In the case of two identical Eigenvalues which represent the largest values, no solution is possible. This represents the case of only one, or collinear observations. The advantage of the *q-method* is that there are very robust algorithms available for solving the stated Eigenvalue problem. In a direct comparison of various algorithms under Matlab, it was shown that it is one of the fastest algorithms. In particular it should be noted that it is faster than the algorithm using the pseudo-inverse.

The main problem and thus the reason for the multitude of algorithms, is numerical robustness. Many of the algorithms are equivalent from a mathematical point of view, yet use different approaches leading to different numerical solutions with varying advantages regarding computational efficiency, accuracy and robustness. The algorithms compared under Matlab, with respect to robustness, accuracy, speed and ease of use were the *pseudo-inverse*, the *SVD*, *QUEST*, *FOAM*, *ESQ* and *ESQ2* and a nonlinear estimation. In this listing, the algorithms starting from *QUEST* are based on the *q-method*, the nonlinear estimation uses an approach which weights the different components of a single measurement differently, according to the knowledge gained from the investigations on the centroiding process, as presented in chpt. 3.1.2. The results of the comparison

regarding computation time and accuracy can be found in table 3.9. The particular characteristics of the various algorithms can be found in [39]. The comparison with respect to computation time and robustness can be found in table 3.9. The simulation is based on 80 systematic scans of the celestial sphere with 411 evenly spaced measurement points each. The different scans used the 3 to 10 brightest Stars in each direction and Gaussian error levels of $1/16^{th}$ to $10/16^{th}$ pixels (1σ). The Stars were taken from the Hipparcos Star-catalogue. The position of the Stars on the detector was determined and an individual error corresponding to the currently selected noise level was added to each Star position. Especially those algorithms based on *QUEST*, are highly sensitive to a denominator which might reach very small values, and thus might lead to near-singular results (see e.g. [39]). In order to avoid this, the reference system is rotated. This changes the value of the denominator term and the least critical value can be chosen. With the use of *a priori* knowledge, this rotation can be performed prior to the actual attitude determination by rotating the reference frame by 180° about the axis belonging to the largest value of the *a priori*-quaternion. If the largest value is the fourth component, no rotation is performed. Since an approximate attitude is available at most times, this is clearly preferable since it drastically reduces the number of necessary operations and thus computation time, as opposed to testing the various rotations for their least critical value.

An inherent shortcoming of all presented algorithms is their assumption of a homogeneous accuracy of the individual measurements. Thus, the results from chpt. 3.1.2, which showed the different accuracies in the x - and y -components of the measurements can not be put into use. This results in the idea to search for an alternative approach, to take these effects into account. In the frame of these studies, investigations on an alternate formulation of Wahba's problem were carried out. It was shown that, while posing the problem mathematically was easily accomplished, it does not seem to possess a trivial analytical solution. This is caused by changing the character of the cost-function from linear to quadratic in A . With this additional term, the standard solutions found so far can not be used. The derivation of the *Extended Wahba Problem* is given in the appendix A.1.2 (similar approach: Markley, [40]).

Since it was not possible to solve the system analytically, a numerical approach was used in order to investigate the use of various weighting functions, which were based on trigonometric relations between x and y . In order to show their impact on the attitude accuracy, the minimization was cast in a *nonlinear program*, which was being solved by the Matlab function „**fmincon**“. The corresponding cost-function was formulated as

$$L(q) = \sum_{i=1}^{\text{Number of Stars}} (\underline{b}_i - A(q) \cdot \underline{r}_i)^T \cdot W_i \cdot (\underline{b}_i - A(q) \cdot \underline{r}_i), \quad (3.15)$$

with A being defined by components of the quaternion, analogue to eq. (2.4). W_i is the matrix of

weights, being defined as

$$W_i = \text{diag}(w_{i,x}, w_{i,y}, w_{i,z}), \quad (3.16)$$

where the weights can be defined to be either constant, or a function of e.g. the Star's intensity and its position on the detector. The equality constraint was chosen to take into account the unity constraint of the quaternion:

$$g = q^T q - 1 = 0. \quad (3.17)$$

Simulations similar to those for the comparison between the different algorithms, but allowing for different noise levels in x - and y - axis, showed that the program was highly sensitive to the distribution of the Stars on the detector. Even when weighting functions similar to those generating the noise were used (e.g. noise in x is twice the noise in y), the results did not necessarily improve, when compared to the „standard“ algorithms. To eliminate the possibility of a local minimum, another program was used, which confirmed that **fmincon** truly found the global minimum. Simulations on this approach showed that, while there were cases where the accuracy was increased by a factor of approximately two, there were other instances, in which the error was worse than the solution of the standard algorithms. Therefore further investigations in that direction have not been pursued. Reasons for this choice were that the numerical simulations were not helpful in showing the immediate influence of weighting functions on the result, and that as a first estimate the increase in accuracy was expected of being no greater than the factor of two, which was occasionally observed. The only reason of making this approach beneficial, would be finding an analytical solution to guarantee weighting functions with a positive influence and to minimize the computational effort. It might be of interest to note that, through private communication with F.L. Markley, a conference paper by Brock ([41]) was found, which proved that in the case of an unconstrained pseudo-inverse solution, there is no benefit in using individual weights in the cartesian directions (see also [40]) as well as another reference by Shuster ([27]), which refers to the homogeneous distribution of accuracies for attitude determination as the QUEST measurement model. In particular it should be noted that in the case of two or three measurements even the weighting of the individual measurements has no influence on the overall result, when using an unconstrained matrix ([40]).

In order to enhance the attitude information and to determine the angular velocity of the satellite, a linearized kinematic Kalman-filter was set up, which thus uses the small angle approximation for quaternions. The states were chosen to be a subset of the quaternion, in order to remove the interdependency within the four quaternion entries due to the unity constraint. In this case, only the first three components were used. The sources of error to be taken into account are the uncertainty in the actual angular velocity and acceleration of the satellite, which are accounted for in the *process-noise covariance-matrix* \underline{Q} , and the uncertainty in the actual attitude, which is

accounted for in the *measurement-noise covariance-matrix* \underline{R} . The basis for the initialization of these covariance matrices, along with the additional *state covariance-matrix* \underline{P} , is performed by using the knowledge of the approximate accuracy in the attitude determination (see chpt. 3.1.6) for \underline{P} and \underline{R} , and the defined „agility“ of the satellite, meaning its angular rates in the nominal operation (approx. 0.1 °/s for a typical GEO-satellite), for \underline{Q} . Two filters were implemented, one using only attitude and angular velocity, the second providing the angular acceleration as third information. The angular rate is included as the information can be used in the image processing algorithms, e.g. for adaption of the threshold for star detection at higher rates. The desire to include the angular acceleration into the state came up in order to deal with jerks and accelerations, as they occur during maneuvers, more easily.

The differential equation for the first implementation is simplified as

$$\begin{bmatrix} \dot{q} \\ \dot{q} \end{bmatrix} = \begin{bmatrix} 0 & I_{3 \times 3} \\ 0 & 0 \end{bmatrix} \cdot \begin{bmatrix} q \\ \dot{q} \end{bmatrix}, \quad (3.18)$$

Table 3.9: Comparison of Attitude Determination Algorithms

Name	Time [s]	rel. Time	Calls	Standard Deviation, Pitch/Yaw [arcsec]	Standard Deviation, Roll [arcsec]
Test-Program	1296.578	100.0 %	1	-	-
NLO, using fmincon	1266.132	97.7 %	1000	3.3816	17.5822
ESOQ2	9.148	0.7 %	1000	3.2243	16.0000
QUEST	6.624	0.5 %	1000	3.2243	16.0000
ESOQ	2.011	0.2 %	1000	3.2243	16.0000
Unconstrained Least-Squares, accepting 2 measurements, different Pseudo-Inverse	1.881	0.1 %	1000	3.1845 ¹⁾	15.7602 ¹⁾
Unconstrained Least-Squares, accepting 2 measurements,	1.419	0.1 %	1000	11.8589 ¹⁾	91.8672 ¹⁾
Unconstrained Least-Squares,	1.351	0.1 %	1000	11.8589 ¹⁾	91.8672 ¹⁾
Davenport's q-Method	1.137	0.1 %	1000	3.2243	16.0000
FOAM	1.110	0.1 %	1000	3.2243	16.0000
Singular Value Decomposition	0.629	0.0 %	1000	3.2243	16.0000

1) : Three instances of a badly conditioned matrix were detected and excluded

the differential equation for the second case is derived accordingly. The resulting state-vectors were

$$\begin{bmatrix} \underline{q} \\ \underline{\dot{q}} \end{bmatrix} \quad (3.19)$$

and

$$\begin{bmatrix} \underline{q} \\ \underline{\dot{q}} \\ \underline{\ddot{q}} \end{bmatrix}, \quad (3.20)$$

respectively. The measurement used is the vector part of the quaternion \underline{q} . As expected, it turned out that the increase in the number of states does not improve the system's steady-state behavior. Thus, it is only of interest to include the higher order states in case applicable measurements, as for instance provided by gyros, are provided. A design covering all angular velocities of interest ($0 - 10^\circ/\text{s}$) proved to be difficult. An alternative approach, adapting the covariance matrix \underline{Q} to the estimated angular velocity, did not significantly improve the performance of the filter. Instead, it is proposed to use the raw measurements starting from a certain velocity (e.g. $0.5 - 1^\circ/\text{s}$) or to switch to a different filter. A wide range of investigations has been performed in the area of filtering attitude measurements, which range from increased modeling efforts, including the actual spacecraft's attitude dynamics (e.g. [42]), to enhanced filter methods, like the unscented Kalman-filter (e.g. [35]).

This chapter introduced a variety of algorithms available for attitude determination of satellites. It was shown that the additional knowledge of the accuracy in different axes is not easily introduced into the algorithms. Further investigations on increasing the attitude information by computational means therefore make sense only in the special case of high accuracy attitude determination, and were postponed in favor of readily available and numerically robust algorithms.

3.1.5 Star-Tracking

There are some cases where a unique or highly preferential identification of Stars is not possible. This, for example, can happen if not enough Stars are present in the field of view, or if the rotational rates of the Satellite during the initial Star-identification are too high. In these cases Star-tracking, as it will be presented in this chapter, provides the knowledge of the satellite's angular motion, without the need to perform a Star-identification. In the following, two versions will be presented which perform a pattern matching which is specifically tailored to be used with Star-images. In this sense it represents an adapted *optical flow* for the 2-D case: The algorithms are simplified by determining only the motion of those patterns belonging to previously extracted Stars, the extracted

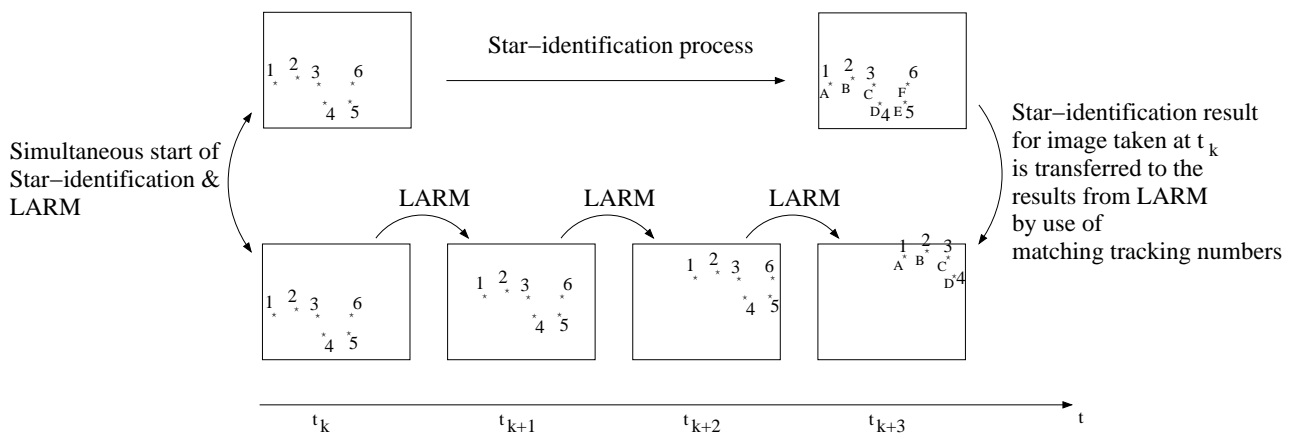


Figure 3.16: Schematic of parallel use of LARM and the Star-identification process.

motion can then be applied to the remaining image. For further information on *optical flow* be referred to [43].

In the data processing routines applied, two Star-tracking modes are treated: A *low-angular-rate mode* (LARM) and a *high-angular-rate mode* (HARM). The difference in these algorithms is the shape of the Star-images as obtained by the camera and the probability of observing more than two Stars. While in LARM, the image is not too different from the images as obtained in Earth-pointing orientation, in HARM the Stars are spread over more pixels due to the spacecraft's angular rate. This results in a lower signal for the individual pixels, reducing the magnitude-limit, to which Stars can be detected. In both modes, the Stars which are observed receive a tracking number, which remains unchanged as long as the Stars are continuously detected. This allows for a parallel Star-identification, which might take several image-cycles, to be applied to the tracked Stars. The schematic of this approach is shown for the example of LARM in fig. 3.16

3.1.5.1 Algorithms for Star-tracking

In the following a schematic step-by-step approach of Star-tracking is presented.

LARM

Step 1: Definition of a Temporary Star-Catalog

In order to relate two consecutive images without the need for an absolute attitude determination, a relative attitude determination is performed. This is done by definition of a temporary „Star-catalog“ which contains the measurement vectors of the current image in sensor coordinates. Accordingly, a temporary catalog containing the separation angles is built.

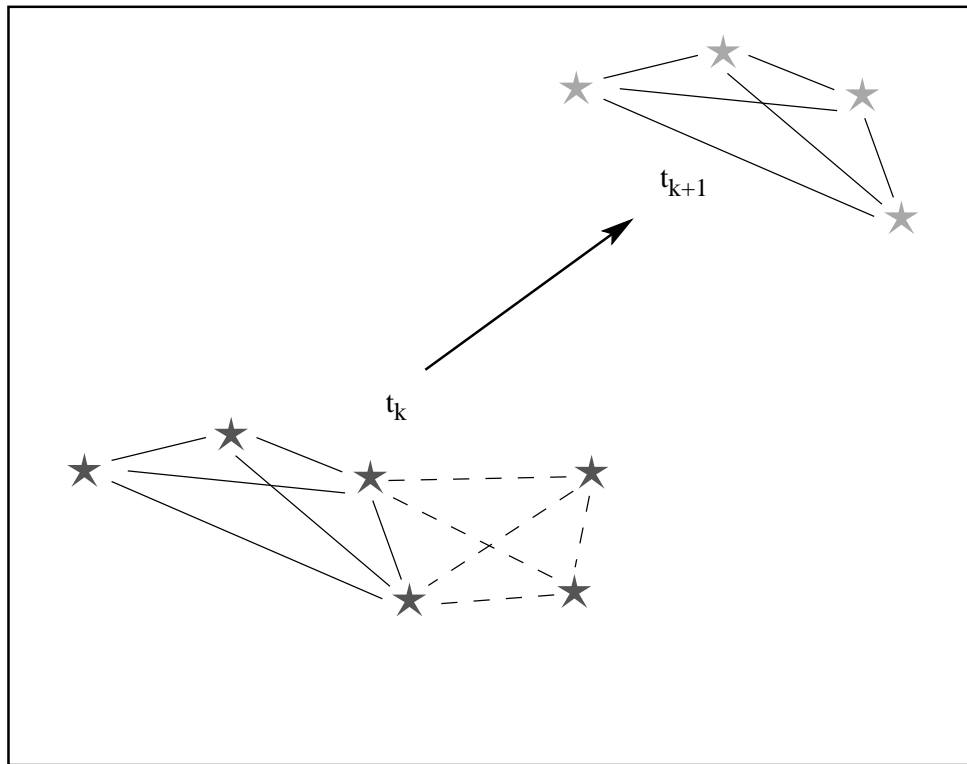


Figure 3.17: Schematics of LARM. The Star-tracking is performed using a reduced „Star-identification“ based on the Centroids of the previous image. In the image the matched Star-patterns are connected by solid lines, the unmatched Stars-patterns by dashed lines.

Step 2: Attitude Determination

After the definition of the temporary Star-catalog, the Star-identification process in the following image is performed as defined in chpt. 3.1.3 and followed by the attitude determination as described in chpt. 3.1.4. Both processes are carried out using the temporary Star-catalog for reference.

The schematics of this scheme are shown in fig. 3.17

HARM

Step 1: Threshold

In HARM the detection process needs to be modified in order to be able to detect Star-images which are deformed by a high rotational rate. Instead of searching circular Star-images, now the image is searched for line shapes. This is performed by moving a rectangular region R_i with its center pixel c_i at the detector position $(c_{i,x}, c_{i,y})$, a width of approx. 11 pixels and a length of approx. 11 pixels across the image and performing a summation of all inscribed pixels $(x_j, y_j) \in R_i$.

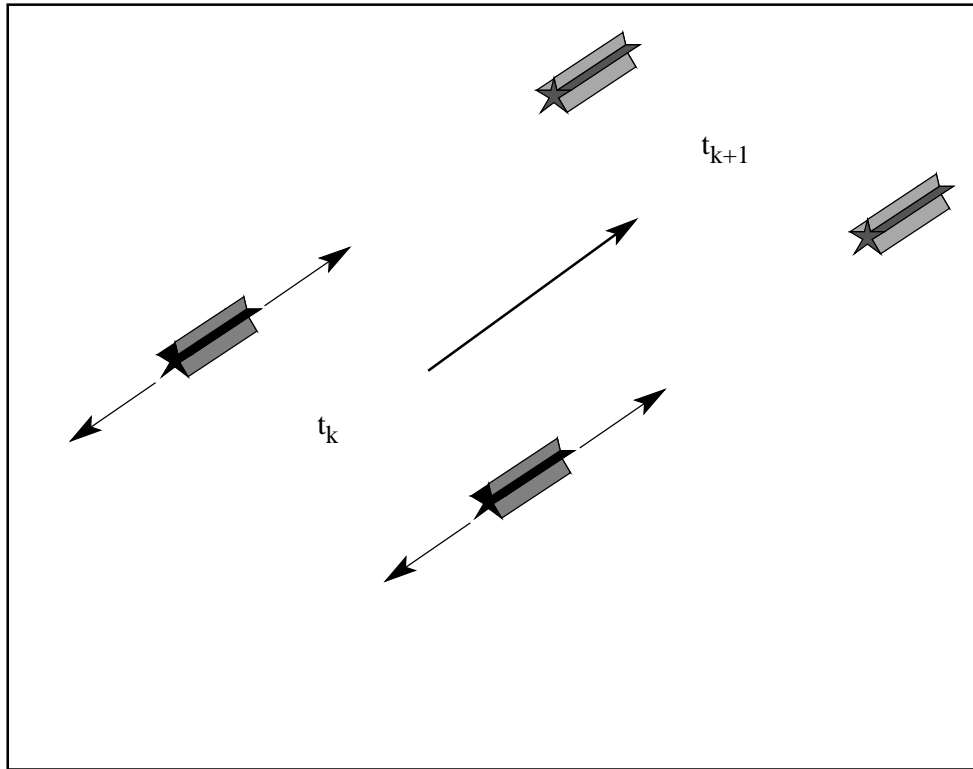


Figure 3.18: Schematics of HARM. The Star-tracking is based on two consecutive images, supplemented by the Star's trace, as it is observed due to the satellite's rotation during exposure.

The sum needs to exceed a threshold which is set to be approx. 104% of the full dynamic range of a single pixel with 65536 discretization steps given by the 16 bit data-format.

$$\sum_j \text{Signal}((x_j, y_j) \in R_i) > \text{Threshold} \quad | \quad \text{Threshold} = 68200$$

Additionally, the central pixel $(c_{i,x}, c_{i,y})$ needs to be brighter than its neighbours:

$$\text{Signal}(c_{i,x}, c_{i,y}) > \max R_i$$

A reduction in the computational load can be achieved by limiting the detection process to the fringes and a horizontal line through the center. This way all new Stars entering the image are detected. If the detector is rotated about the LOS, the Stars in the image are detected when they cross the central line.

Step 2: Requirements on the candidate region

Once a candidate region is found, the orientations of the line shapes are detected by changing the size of the rectangular region to a width of approx. 5 pixels and a length of approx. 11 pixels. This new region $R_{i,line}$ is rotated in steps of approx. 10° from 0° to 180° . Again a summation of all inscribed pixels is performed and the angle at which a maximum is reached is searched for.

The sum of this sub-region needs to exceed a threshold which is set to be approx. 97% of the full dynamic range.

$$\sum_j Signal((x_j, y_j) \in R_{i,line}) > Threshold \quad | \quad Threshold = 63360$$

This provides a first estimate on the orientation of the Star-trace.

Step 3: Determination of the Length of the Trace

The length of the Star-trace is determined by following the found angle in both directions until a stop criterion is met. Starting point $Start$ with the detector coordinates $(Start_x, Start_y)$ of this search is the central pixel $(c_{i,x}, c_{i,y})$ of the region R_i .

In the following a region $R_{i,sub}$, with a width of approx. 5 pixels and a length of approx. 5 pixels is defined which follows the approximate orientation of the found trace in steps of approx. 1 pixel. Its center being defined as $(c_{i,x,sub}, c_{i,y,sub})$. The sum of this sub-region needs to exceed a threshold which is set to be approx. 23% of the full dynamic range.

$$\sum_j Signal((x_j, y_j) \in R_{i,sub}) > Threshold \quad | \quad Threshold = 15000$$

If the sum is lower than the given threshold, the stop criterion and therefore the end of the trace is reached. If the sum is higher than the given threshold, the step is repeated.

The starting point of the next step is determined by setting the point at a distance of $\sqrt{2}/2$ relative to $(c_{i,x,sub}, c_{i,y,sub})$ in direction towards the brightest quadrant of the sub-region.

Step 4: Determination of the Sense of Rotation

The sense of rotation is determined using the successive image. By searching along the orientation of the detected Star, which is determined by finding the extremes of its extension, a continuation of its shape is looked for in both directions.

Step 5: Determination of the Rotational Rate and the Rotational Axis

The rotational rate can be determined by two possible approaches: the first approach is the determination of the rate by determination of the length of the observed Star-traces. The rotational axis is determined by the different individual lengths of the Star-traces, which lead to the center of the rotation. The second is the relative attitude determination as described for LARM with the vectors built from the center of the Star-traces as reference vectors. The second approach determines both, the rotational rate and the rotational axis in one step.

The schematics of this scheme are shown in fig. 3.18 (note: since in the the motion is nearly linear, the rotational axis is outside of the area shown).

In the following, further information on these algorithms is given.

3.1.5.2 Additional information on Star-tracking

In LARM, the Star-tracking is performed using a reduced Star-identification based on the time-varying temporary Star-catalogue defined in *Step 1*. The Star-identification (for detailed information be referred to chpt. 3.1.3) is therefore adapted to be used with this catalogue. It is obvious that this identification scheme, which is based on the order of 10 Stars, is by far faster, than using the complete catalogue, containing approx. 6000 Stars. In a following „attitude determination“, the relative attitude between the consecutive images, and thus the angular rate of the satellite can be deduced.

In HARM, the Star-tracking again is based on two consecutive images, supplemented by the Star's trace as it is observed due to the satellite's rotation during exposure. This mode is of particular interest during higher angular rates, which result in a reduced number of Stars, since the Stars are spread over several pixels. As an example: in case of an optical system, which is designed for detection of Stars with magnitude $m_V = 6$, the detection-limit reduces to Stars with $m_V \approx 1$ for angular rates which result in a trace of approx. 100 pixels in length. With a 0.1 sec. integration time, this is approximately equal to $\omega \approx 15^\circ/\text{s}$. Actually, the detection limit is higher, meaning more sensitive, than this estimate, as in the case of HARM a larger region is used for detection of the Stars. This allows for detection of a lower signal-to-noise ratio of the single pixels. Nevertheless, the overall decrease in the sensitivity reduces the number of observable Stars. As an example: If the limiting magnitude is $m_V = 2$ and the FOV is given with a total viewing angle of 25° , the probability of observing 2(3) Stars is already reduced to 70(27) %.

The reduction of available Stars for a valid Star identification is countered by using the Star's trace

for extraction of the approximate rotational axis and the corresponding angular velocity. As an alternative to *Step 3*, the orientation of the trace in the image can, for instance, be found by the trace's moments of inertia, which are defined as

$$I_x = \sum \text{Signal}(x, y) \cdot (y - y_0)^2, \quad (3.21)$$

and accordingly

$$I_y = \sum \text{Signal}(x, y) \cdot (x - x_0)^2. \quad (3.22)$$

The moment of deviation is defined as

$$I_{xy} = \sum \text{Signal}(x, y) \cdot (x - x_0)(y - y_0). \quad (3.23)$$

The principle axes can then be determined by solving the eigenvalue (λ) and eigenvector (v) problem of

$$Jv = \lambda v, \quad (3.24)$$

with

$$J = \begin{bmatrix} I_x & -I_{xy} \\ -I_{xy} & I_y \end{bmatrix}. \quad (3.25)$$

The solution is the corresponding eigenvector, which can then be translated to the angle relative to the horizontal, which results as

$$\beta = \frac{1}{2} \arctan \left(\frac{I_{xy}}{I_x - I_y} \right). \quad (3.26)$$

This approach additionally can replace *Step 1*, which determines the total intensity of the candidate region to apply a threshold criterion. It is computationally more demanding, yet it simplifies the detection process, in that the information provided by the moments of inertia already contains a certain knowledge on the distribution of the light's intensity.

The information of the approximate orientation of the trace is used in the case of fractionally found traces. They are joined by testing for parallelism and proximity, which as well rules out multiply found traces. False identifications in the trace determination are covered by consistency checks of two consecutive images. They put to use that the consecutive trace needs to start close to the end of that determined in the previous image. This check additionally provides the sense of rotation. Another check is the total length of the trace, which is a function of the rotational rate and the rotational axis.

An increase in computational efficiency was introduced by an alternative approach when searching for traces, which is shown in fig. 3.19. Instead of searching the whole image, only newly entering traces are detected by a search-region at the perimeter of the FOV. The newly found traces, entering

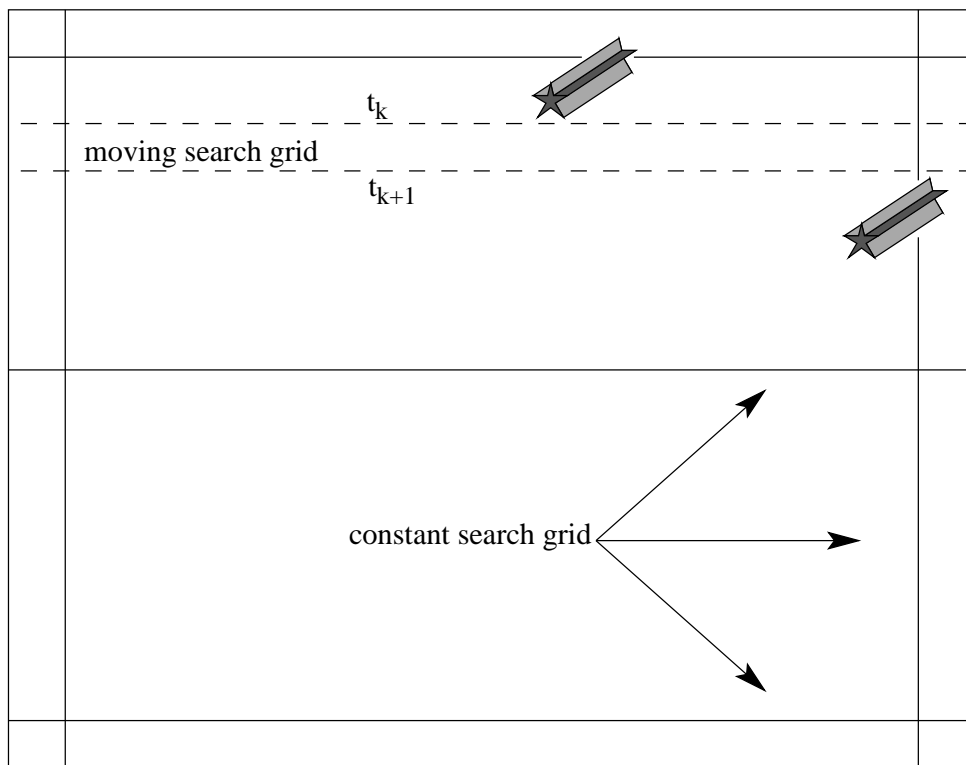


Figure 3.19: Schematics of HARM search grids

the FOV, are then tracked during their passage through the FOV. In order to include the case of a rotation about the LOS, an additional horizontal line is included in the center of the FOV. This is necessary, as in the case of a rotation about the LOS, it might be possible that no new Stars enter the FOV. A third case needs to be covered: in order to detect a stationary pointing, a horizontal line is moved about the image in discrete steps, proceeding on step each newly gathered image, searching for Stars. The step size is approximately equal to the height of the rectangular region used in the detection process. If the camera is motionless, in this way, the total FOV is consecutively searched for Stars. This last option is necessary if the HARM detection-mode is used during start-up of the sensor-system and should be performed using the same detection criteria as used in LARM. Alternatively, the regular LARM detection-mode can be used on the first image to eliminate the possibility of a motionless or slowly moving camera. The disadvantage is the longer time necessary for evaluation of the complete image.

The two Star-tracking modes were tested during a field experiment and proved to be satisfactory. The angular rate determination using consecutive images was sensitive enough to follow the Earth-rotation. In addition to their main purpose, in particular LARM can be used to perform consistency checks on the ID provided by the Star-identification process.

3.1.6 Initial estimate of the expected accuracy

In this section the expected accuracy of the attitude determination is estimated. As a first approximation, a simple stochastic assumption was made: If the accuracy of the position of a single Star is known, the accuracy of the attitude can be approximated to be proportional to the inverse of the square-root of the number of observed Stars.

$$\text{Noise} \propto \sqrt{\frac{1}{\text{„No. of Stars“}}} \cdot \text{„Centroiding-Accuracy“}$$

Additionally, most algorithms determining the satellite's attitude, provide the opportunity of an estimation of the attitude's covariance. As an example the first estimate of the covariance for QUEST is given in eq. (3.27).

$$P = \left[\sum_i a_i \cdot (\mathbf{I} - \underline{b}_i \underline{b}_i^T) \right]^{-1} \quad (3.27)$$

This estimation is in first order dependent on the centroiding-covariance ($1/a_i$) for the individual measurements (\underline{b}_i) and their distance from the center of the FOV. a_i itself is in general dependent upon the distance from the center of the FOV (see chpt. 3.1.2) as well as on the brightness of the corresponding Star (see chpt. 2). Setting $a_i = 1$ for all measurements results in a geometric interpretation of the covariance matrix and therefore resembles the *Geometric Dilution of Precision* (GDOP), as known from GPS measurements. In the case of GPS, GDOP denotes the accuracy to be expected due to the geometrical distribution of the GPS-satellites used. In the case of Star-sensors, the reason for the typically lower accuracy in roll is due to the geometric distribution of the Star-measurements, which are primarily taken from one direction. An identical accuracy about all three axes can be achieved, if the proposed system's second FOV is used for Star-observations, as in the case of multiple-FOV Star-sensors (e.g. StarNav III [44]). Alternatively, the boresight can be chosen to be aligned with the axis of least accuracy requirements. The covariance can then be determined to be

$$P^* = T P T^T, \quad (3.28)$$

with

$$A^* = T A, \quad (3.29)$$

and T as the alignment matrix from the Star-sensor system into the desired coordinate system denoted by the asterisk (see as well [27]). A list of typical mission requirements is given in Appendix A.

Another characteristic, not yet covered, becomes apparent at higher angular velocities: Due to the finite exposure time, the Star-image is no longer determined by its position on the detector only,

but by the motion during exposure and the corresponding rotational axis. This in turn renders the centroiding process using PSFs as determined for a pointing-mode, as given in chpt. 3.1.2, meaningless. Additionally, the noise is increased due to the lower illumination level of the individual pixels. Depending on the angular velocity, only a certain percentage of the exposure time is effectively used, resulting in a lower apparent magnitude and thus a higher noise level, as seen in fig. 3.5. Since the photon-noise induced centroiding error is proportional to the inverse of the square-root of the exposure time, which in turn is approximately inversely dependent on the angular velocity, it is expected that the photon-noise increases approximately proportional to the square root of the angular velocity. This results in the following approximation, using the assumption that $1 \text{ pixel} \simeq \alpha \times \alpha^{\circ 2}$, where $\alpha \approx 60''$. The effective exposure time amounts to

$$T_{\text{effective}} = T_{\text{exposure}} \cdot \frac{\alpha}{\alpha + \omega \cdot T_{\text{exposure}}} \quad (3.30)$$

Using the relationship

$$\text{Noise} \propto \sqrt{\frac{1}{T_{\text{effective}}}} \quad (3.31)$$

results in

$$\text{Noise} \propto \sqrt{\frac{1}{T_{\text{exposure}}} + \frac{\omega}{\alpha}} \quad (3.32)$$

For long exposure times, this formulation results in the reflections from above. It should be noted that this relation is only a crude approximation of reality, but should provide an understanding of the effects which are to be expected. Influences neglected are, for instance, the shape of the Star, the direction of motion and the change in the „angular dimensions“ of a pixel, when leaving the center of the FOV.

For a first assessment of the accuracy to be expected, though, these effects are legitimately neglected. This is due to the expected operation in a satellite with a slow change in attitude, which for common Earth-oriented satellites in normal mode is far below $1^\circ/\text{s}$.

Concluding, the accuracy of the attitude determination is dependent on a wide range of parameters. The most important parameter for the static accuracy, which is commonly referred to when using Star-sensors, is the centroiding accuracy. As in our case the centroiding is designed to be accurate to 0.1 pixel, the expected accuracy is in the range of $10''$ in the LOS, which will be confirmed by the simulations carried out in chpt. 4.1 and the field experiments presented in chpt. 7.2.1. The accuracy about the LOS is dependent on the distribution of the Stars on the detector. For a Star-sensor with a wide FOV, as the one presented, it is expected to be accurate to approx. $50''$. This shows that, even in the presence of low-cost components, a wide range of mission requirements can be met, when making better use of the knowledge on the system's characteristics in the evaluation of the gathered data.

3.2 Earth-Vector Determination

As shown in fig. 3.1, in addition to the attitude matrix, the Earth-vector is essential to the position determination of the spacecraft. In the sections to follow, the process from the horizon detection to the Earth-vector output, as shown in fig. 3.20, will be discussed. Main emphasis will be on the horizon detection in the visual regime and the best fit of the resulting horizon points when trying to determine the Earth-center.

3.2.1 Earth-Horizon Detection

In the special case of the sensor presented, the Earth sensor is realized as a sensor in the visible regime of the optical spectrum, thus resembling an *Albedo*-sensor. While an optical way of determining the Earth's center seems to be straightforward, there are several issues to be taken into account to provide an appropriate algorithm for the image analysis. Since in the case of imaging the Earth in the visible spectrum it is not seen as homogeneously as in the IR-spectrum commonly used in Earth sensors, the detection of the horizon represents a challenge, which has to be tackled in order to determine the Earth-center. The major sources, causing confusion are the terminator, i.e. the day/night division and, even more disturbing, cloud constellations showing similar local properties as the Earth's rim.

To overcome the issues of reliability and computation time, the conditions leading to the acceptance of a point as part of the horizon have to be specified.

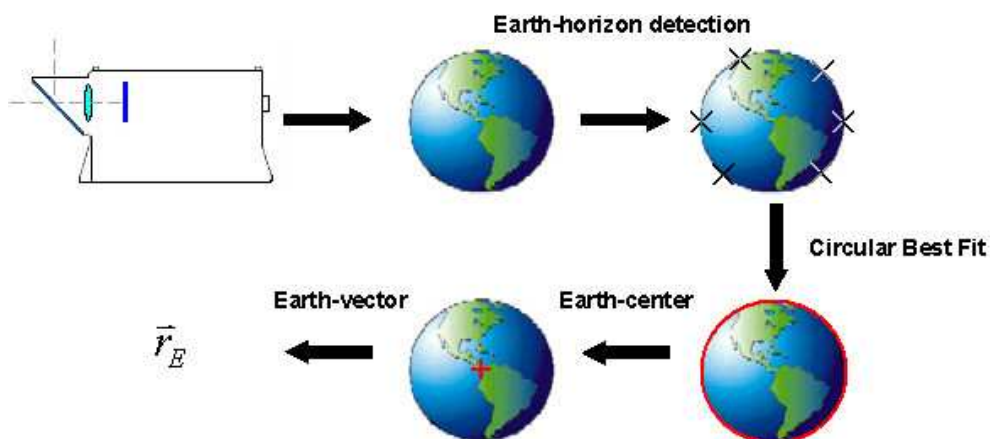


Figure 3.20: Flowchart Earth-Sensor

3.2.1.1 Algorithm for the Earth-Horizon Detection-Process

In the following a schematic step-by-step approach of the Earth-horizon detection-process is presented. The constants given are those used in the evaluation of images obtained by METEOSAT. Details on the sets of data obtained are given in chpt. 7 and in particular in chpt. 7.2.2.

Step 1: Construction of a Search Grid

A grid is introduced as shown in fig. 3.21, comprising each 10th line and column. The horizon is then searched for along these lines.

Step 2: Threshold

As a starting condition all pixels on the grid with their detector coordinates (x, y) exceeding a defined threshold are chosen as the center of a candidate region R_i . The size of each region is set to be 13 pixels \times 13 pixels. The threshold is set to be approx. 11 % of the full dynamic range of 256 discretization steps given by the 8 bit data-format.

$$\text{Signal}(x, y) > \text{Threshold} \quad | \quad \text{Threshold} = 30$$

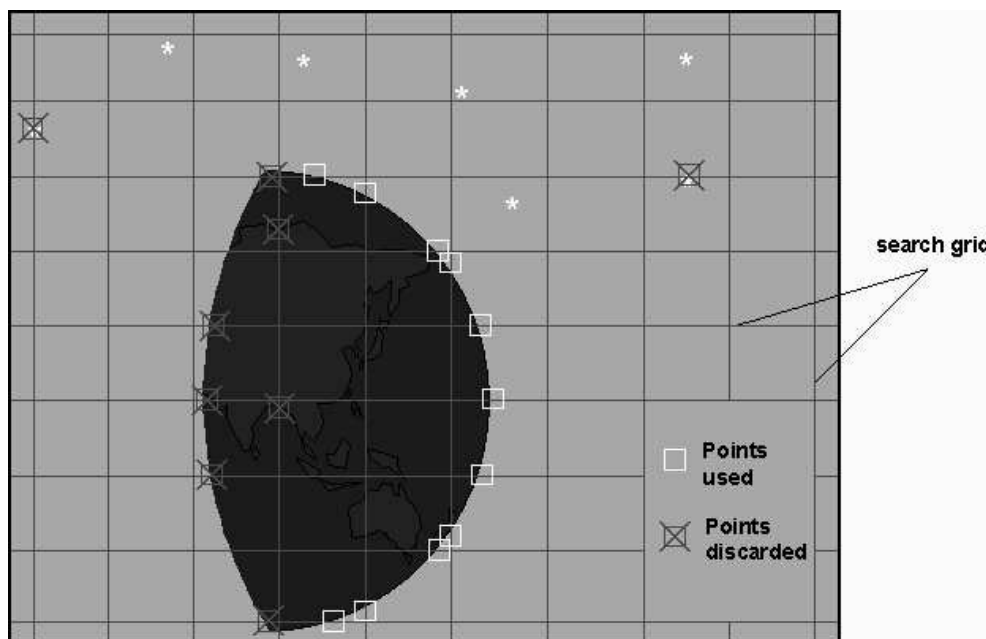


Figure 3.21: Search Grid using a GEO-observation as example

Step 3: Requirements on the candidate region

In order to assure that only points on the Earth-horizon are extracted, the candidate region R_i needs to fulfill the following requirements:

The number n_{dark} of points in the candidate region lower than the threshold needs to surpass a limit $n_{dark,min}$.

$$n_{dark} > n_{dark,min} \quad | \quad n_{dark,min} = 27$$

The number n_{bright} of points in the candidate region exceeding the threshold needs to surpass a limit $n_{bright,min}$.

$$n_{bright} > n_{bright,min} \quad | \quad n_{bright,min} = 27$$

The average pixel value of the subset $R_{i,dark}$, which contains the pixels darker than the threshold, needs to be lower than $Mean_{dark,min}$.

$$\text{mean}(R_{i,dark}) < Mean_{dark,min} \quad | \quad Mean_{dark,min} = 15$$

The average pixel value of the subset $R_{i,bright}$, which contains the pixels brighter than the threshold, needs to be greater than $Mean_{bright,min}$.

$$\text{mean}(R_{i,bright}) > Mean_{bright,min} \quad | \quad Mean_{bright,min} = 45$$

The distance between the centers of illumination intensity of $R_{i,dark}$ and $R_{i,bright}$ ($c_{i,dark}$ and $c_{i,bright}$) needs to be greater than $Distance_{dark-bright,min}$.

$$|c_{i,dark} - c_{i,bright}| > Distance_{dark-bright,min} \quad | \quad Distance_{dark-bright,min} = 10$$

Step 4: Determination of the Earth-horizon crossing

The crossing of the actual Earth-horizon m_i at the detector coordinates $(m_{i,x}, m_{i,y})$ is determined to be the first pixel on the line connecting $c_{i,dark}$ and $c_{i,bright}$ which exceeds the limit set by $(\min(R_i) + \max(R_i))/2$.

Step 5: Introduction of a Global Criterion

In order to remove points in the determination which have a distribution similar to the Earth horizon, in particular clouds, a global criterion is introduced.

This criterion makes use of the knowledge, that the Earth is a sphere and thus provides the image of, approximately, a circle on the detector. To use this knowledge, systematically a combination t_p of three measurements i , j and k is chosen, which is used to create a circle with the radius r_p and the center $c_{r,p}$ at the position $(c_{r,x,p}, c_{r,y,p})$. In the calculation the temporary variables \mathbf{G} , \underline{g}_1 and \underline{g}_2 are used.

$$\begin{aligned}\mathbf{G} &= \begin{bmatrix} m_{j,y} - m_{i,y} & m_{j,y} - m_{k,y} \\ m_{i,x} - m_{j,x} & m_{k,x} - m_{j,x} \end{bmatrix} \\ \underline{g}_1 &= \begin{bmatrix} m_{i,x} - m_{k,x} & m_{i,y} - m_{k,y} \end{bmatrix} \\ \underline{g}_2 &= -\frac{1}{2} \cdot \mathbf{G}^{-1} \cdot \underline{g}_1^T \\ c_{r,p} &= \frac{m_i + m_j}{2} + \underline{g}_2(1) \cdot \begin{bmatrix} m_{j,y} - m_{i,y} & m_{i,x} - m_{j,x} \end{bmatrix} \\ r_p &= |c_{r,p} - m_i|\end{aligned}$$

With this preliminary Earth-center and Earth-radius the distance of all measurements to the preliminary Earth-center is determined and compared to the preliminary Earth-radius. The number of measurements in the comparison corresponding to triplet i , $n_{\Delta,i}$, with a difference smaller than Δr_{max} is determined and compared to the total number of measurements n_{total} . These steps are carried out for all possible triplet combinations until the ratio is greater than $n_{ratio,min,upper}$. The corresponding preliminary Earth-center and Earth-radius and the agreeing measurements are then used in the further Earth-center determination process. If the ratio is never exceeded, the preliminary result for the best ratio obtained throughout the comparisons is used if the ratio is greater than $n_{ratio,min,lower}$. For all triplets of measurements t_n , with the total number of possible triplets $n_{triplets}$, the measurements m_k not used in the triplet are tested according to the following pseudo-code:

```

for  $p = 1$  to  $n_{triplets}$ 
  for  $k = 1$  to  $n_{total}$ 
    if  $|c_{r,p} - m_k| < \Delta r_{max}$ 
       $n_{\Delta,p} = n_{\Delta,p} + 1$ 
    end
  end
end

```

```

if  $n_{\Delta,p}/n_{total} > n_{ratio,min,upper}$  |  $n_{ratio,min,upper} = 95\%$ 
  → use result  $c_{r,p}$  and  $r_p$  in the following process
  break
end
end
if  $\max(n_{\Delta})/n_{total} < n_{ratio,min,upper}$ 
  if  $\max(n_{\Delta})/n_{total} > n_{ratio,min,lower}$  |  $n_{ratio,min,lower} = 50\%$ 
    → use result  $c_r(\max(n_{\Delta}))$  and  $r(\max(n_{\Delta}))$ 
    in the following process
    break
  end
end
end

```

In the further process no distinction is made between the two results. If the maximum ratio $\max(n_{\Delta})/n_{total}$ found is lower than the $n_{ratio,min,lower}$ the measurements are declared as invalid.

In the following, the individual steps are explained in greater detail.

3.2.1.2 Details of the Algorithm for the Earth-Horizon Detection-Process

Since it is not feasible to check all points of the detector for their affiliation to the Earth's horizon, in *Step 1* a search grid is introduced, as shown in fig. 3.21. The reason for using a grid, rather than horizontal or vertical lines only, lies in the necessity to detect steps, which is easier when the search direction is normal to the circle being searched for. This might lead to a low number of points in regions nearly tangential to those lines. Using two perpendicular directions results in a better coverage of these regions. In the special case of a LEO, where the horizon has a very small curvature, the use of two directions becomes essential.

In order to take into account the darker regions, e.g where the sunlight is nearly parallel to the Earth's rim, or where no clouds are present, the threshold needs to be adaptive meaning that the field needs to be moved along the line connecting the dark and light centers, for instance as performed in *Step 4*. The check is repeated as often as necessary, while it was shown that a single iteration generally is sufficient. It should be explicitly stated that a fixed threshold dramatically decreases the accuracy obtainable, because darker regions close to the poles or the terminator result in a „rim“ which is then closer to the Earth's center.

Global criteria as introduced in *Step 5* are used to check the consistency of the points selected by

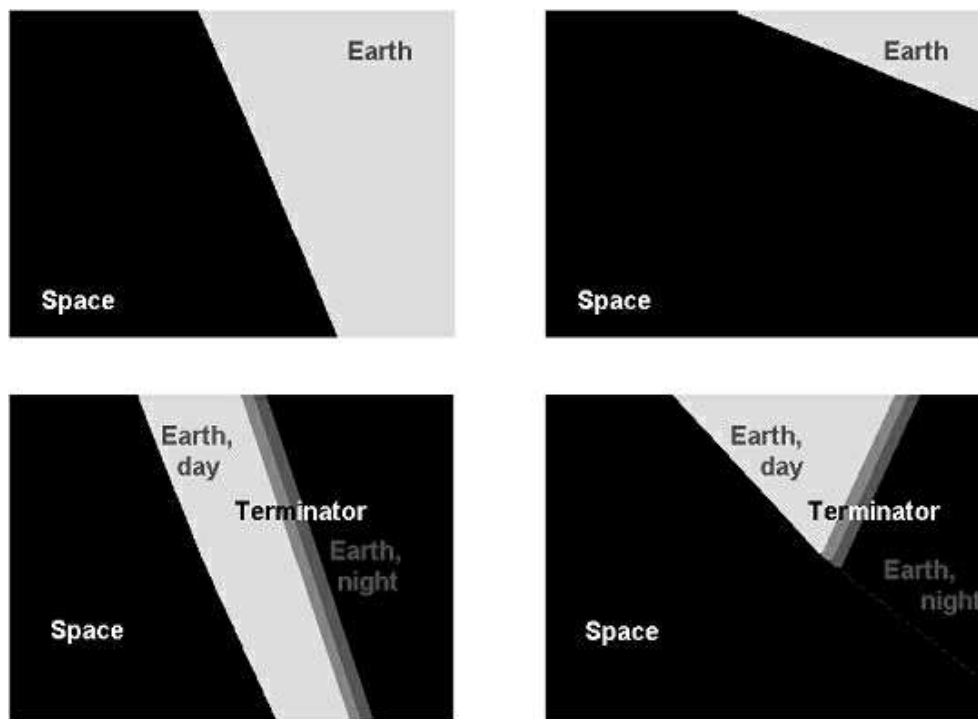


Figure 3.22: Possible Observations of the Horizon as seen from LEO (approx. 300 km orbit height)

the local criteria. Valid algorithms for instance would be a modified *Hough*-transformation, which in general searches for circular features within a picture. Alternatively, the intersections of the local intensity gradients can be used to determine an accumulation within a certain area.

As an additional feature, once a set of points is determined to be part of the Earth's rim, a second algorithm can search for additional points along the expected rim to enhance reliability and accuracy.

In the case of a LEO, an additional challenge arises: Since on top of the low curvature, the Earth has phases, as the Moon when seen from the Earth, the detectable horizon is reduced, which has an effect on the obtainable accuracy. Simulated schematics of possible observations are shown in fig. 3.22. An interesting feature of LEO-images is given through the fractional part of the Earth, which is observed: Since only a small portion of the Earth is seen, the Earth is „fully illuminated“ for a longer period of the orbit. The drawback is that, depending on the orbit, a long period of a partially lit or unlit Earth is equally possible.

Depending on the phase of the Earth, the number of correct horizon identifications varies, but provides sufficient information to determine the Earth-center correctly in most cases.

3.2.2 Earth-Center Determination

Since approximately 1996 algorithms exist for a direct solution of fitting ellipses and circles to measurements in a least square sense (see e.g. [45] and [46]). This leads to a suite of possible algorithms when trying to fit the measurements and solve for an optimal center.

3.2.2.1 Algorithm for the Earth-Center Determination-Process

In the following a schematic step-by-step approach of the Earth-center determination-process is presented. The example is based on the algorithms used in the evaluation of images obtained by METEOSAT. In these images the Earth is already approximately centered in the FOV and observed from within the equator plane, resulting in readily presentable 2D transformations. If this is not the case further transformations in the 3D space, which are dependent on the optics and the actual position of the camera relative to the Earth, become necessary. The following steps are visualized in fig. 3.23.

Step 1: Shifting the Measurements

Using the knowledge on the position of the preliminary Earth-center in detector coordinates c_r and the corresponding measurements m , as determined in the Earth-horizon detection-process, the measurements are shifted in order to form a circle with its center being located in the origin of the detector coordinate-axes.

$$m_{New} = m - c_r$$

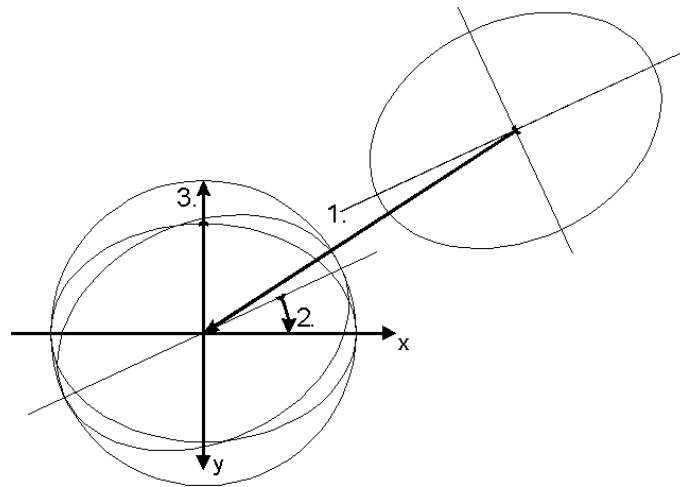


Figure 3.23: Visualization of the necessary transformations to enable circular fitting of measurements (exaggerated eccentricity)

Step 2: Rotating the Measurements

Using the knowledge on the orientation of the Earth-image relative to the detector axes as described by the matrix T_{Earth} , the transformed measurements m_{New} are rotated, such that the semi-major axis of the Earth is aligned with the x-axis.

$$m_{New} = [m_{New} T_{Earth}^T]^T$$

Step 3: Circularizing the Measurements

Due to the elliptical image of the Earth on the detector, as depicted in fig. 3.25, the measurements are distributed in the shape of an ellipse. As the direct fitting of points to an ellipse proved to be very sensitive to noise in the measurements, the knowledge of the Earth's eccentricity is used to transform the measurements to be distributed in the shape of a circle. This is performed by stretching the measurements in y-direction.

$$m_{New}(:,2) = m_{New}(:,2) \cdot \frac{1}{\sqrt{1-e_{Earth}^2}}$$

Step 4: Optimally Fitting a Circle to the Measurements

In this last step, a circle is optimally fitted to the measurements. The algorithm presented is taken from Gander ([47]).

$$\begin{aligned} B &= [m_{New}(:,1).^2 + m_{New}(:,2).^2, m_{New}(:,1), m_{New}(:,2), \text{ones}(\text{size}(m_{New}(:,1)))]] \\ [U, S, V] &= \text{svd}(B) \\ u &= V(:,4) \\ a &= u(1) \\ b &= [u(2); u(3)] \\ c &= u(4) \\ c_{r,New} &= -b/(2 \cdot a) \\ r_{new} &= \sqrt{(|c_{r,New}|^2 - c/a)} \end{aligned}$$

$c_{r,New}$ can be interpreted as a correction to the preliminary Earth-center, as in an ideal case the result would be 0, due to the shifting of the measurements in Step 1. To account for the transformations performed in steps 2 and 3, $c_{r,New}$ needs to be re-transformed. The preliminary Earth-center c_r is thus set to be

$$\begin{aligned} c_{r,New}(:,2) &= c_{r,New}(:,2) \cdot \sqrt{1-e_{Earth}^2} \\ c_{r,New} &= [c_{r,New} T_{Earth}]^T \\ c_r &= c_r + c_{r,New} \end{aligned}$$

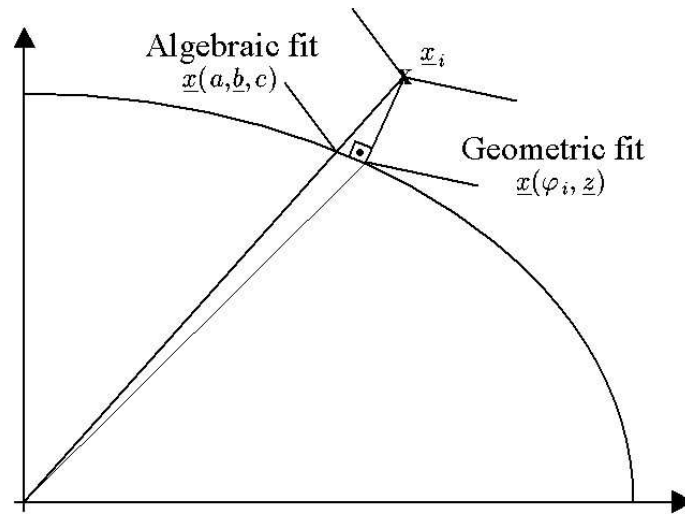


Figure 3.24: Explanation of the different cost-functions used in the optimal fitting of circles and ellipses

Steps 1 and 4 are repeated until the difference in two consecutive Earth-centers as determined by the algorithm is smaller than a chosen threshold, which in this case was set to be 0.1 pixel. The detector coordinates are then translated into a unit vector towards the Earth in the sensor coordinate-system using the same algorithms as for the Stars-centroids.

In the following, the individual steps are explained in greater detail.

3.2.2.2 Details of the Algorithm for the Earth-Center Determination-Process

The problem in using the theoretically more appropriate elliptical fit in the determination of the Earth-center is two-fold: First of all, using a direct method eliminates the possibility of using the well known *a priori* information on the Earth's eccentricity as well as on the orientation of the Earth within the FOV. Secondly, the direct solution solves for the minimization of the algebraic cost-function. This means it solves for the deviation of measurement points relative to the algebraic formulation of the ellipse, thus minimizing the error in the radius from the estimated center towards the measurements. The error therefore is the difference in radius of the measurement, relative to the radius of a point on the ellipse, which has the same angle to the semi-major-axis. It proved beneficial, though, to instead use a different formulation of the cost-function, resulting in minimizing the minimal distance of the measurements to the ellipse (see [47]). Though this sounds identical, fig. 3.24 shows the difference. The mathematical formulation for the algebraic fit is given as

$$F(\underline{x}) = \sum_{i=1}^m \left[(a \cdot \underline{x}_i^T \underline{x}_i + \underline{b}^T \underline{x}_i + c)^2 \right], \quad (3.33)$$

with \underline{x}_i being the m measurements and a, \underline{b} and c being parameters defining the center \underline{z} as

$$\underline{z} = \left(-\frac{b_1}{2a}, -\frac{b_2}{2a} \right) \quad (3.34)$$

and the radius r as

$$r = \sqrt{\frac{|\underline{b}|^2}{4a^2} - \frac{c}{a}}. \quad (3.35)$$

The formulation of the geometric fit in parametric form is given as

$$F(\underline{x}) = \sum_{i=1}^m [(x_{i,1} - x(\varphi_i))^2 + (x_{i,2} - y(\varphi_i))^2], \quad (3.36)$$

with

$$x_{i,1}(\varphi_i) = z_1 + r \cos \varphi_i \quad (3.37)$$

and

$$x_{i,2}(\varphi_i) = z_2 + r \sin \varphi_i. \quad (3.38)$$

The only case, in which the results are identical is an ideal circle with its center on the origin of the coordinate system. Using these more robust approaches results in a nonlinear program, which has to be solved for using numerical minimization.

Using a simple circular fit proved to be very robust, yet it results in different solutions, when the measurements are taken from part of the horizon only and opposite sides are compared. This is actually the case with the horizon measurements, which in general are only available for one side of the Earth, since the other side is in darkness. As a result, in the case of a GEO, the illuminated side changes, when the Sun passes noon. This in turn results in a different location of the Earth center in the afternoon than during morning, which, obviously, is not sensible. The reason for this effect lies in the eccentricity of the Earth: Using only measurements from one side of the ellipse and fitting them in an optimal fashion to a circle, results in an apparent Earth center which is systematically offset in direction towards the measurements. This can be explained, by observing that the optimal radius, determined in the process, is necessarily smaller than the semi-major-axis. Considering that the resulting circle is attracted by the measurements, the center is constantly mis-estimated in their direction. This effect is shown for two cases in fig. 3.25, while it should be noted that the Earth eccentricity has been exaggerated in order to make the effect visible. The first case has nearly homogeneously distributed measurements along one side. In the second case, the effect is even dramatized, by having more observations along the equator.

In order to reduce this effect several algorithms have been investigated. First of all, the algorithm for a direct elliptical fit was tested on the measurements. Tests using experimental data, which are further explained in chpt. 7.2.2, showed that even in the best cases only a minor advantage was drawn from the algorithm, while in many cases the noise was increased. Additionally a high

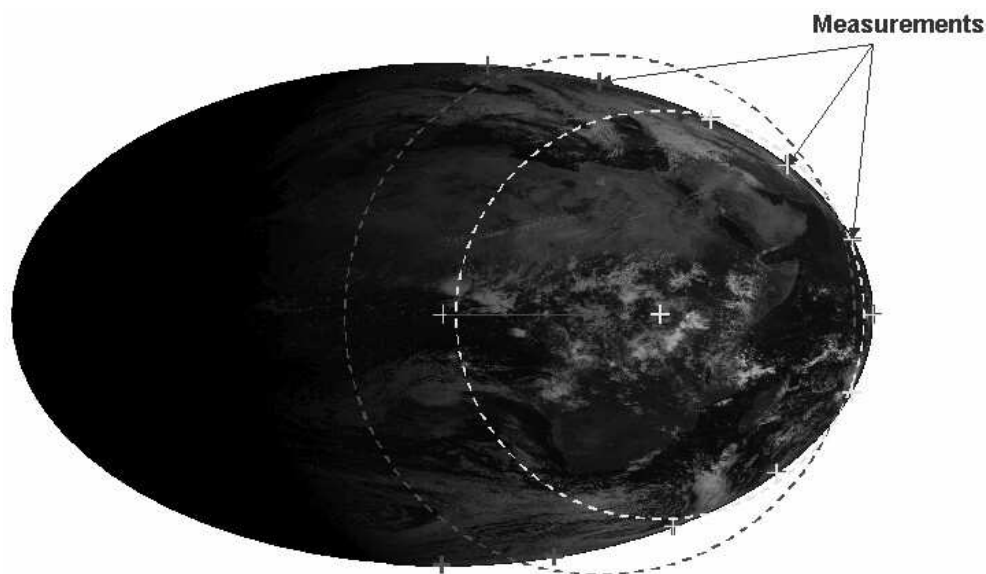


Figure 3.25: Visualization of the systematic mis-estimation due to fitting a circle to an ellipse (exaggerated eccentricity)

variation of the orientation of the semi-major axis showed the difficulties when using an elliptical fit. Further investigations were conducted on how to efficiently join the knowledge of the present ellipsoid and the robust methods of optimally fitting measurements to a circle. In a first attempt it was tried to use the preliminary result for the Earth center and the approximate orientation of the Earth-ellipsoid on the detector to start a nonlinear optimization, fitting the measurements to an ellipse. The reason for this was the idea that only very few iteration steps should be necessary for convergence. Unfortunately, this approach led to no robust solution, when only few measurements were available. It was finally concluded that the elliptical fit, as it was implemented, was not robust enough for the purpose of attitude and orbit determination.

This led back to the idea of using the robust circular fit and the approximately known step size when crossing noon for a deterministic correction of the measurements, based on the additional knowledge of the Sun incidence angle. This in principle would have solved the problem, but was not satisfactory from an analytical point of view.

To satisfy the aspiration of finding an analytical solution, a different approach was found: Instead of bluntly fitting the measurements to a circle and disregarding all knowledge of their nature, the measurements were transformed, as depicted in fig. 3.23 and explained in the description of the algorithm for the Earth-center determination. Experiments using Earth-images showed that about four iterations are necessary to reach a correction of less than 1×10^{-6} pixels in the center coordinates, which is already far below the expected accuracy. The experiments are addressed in chpt. 7.2.2.

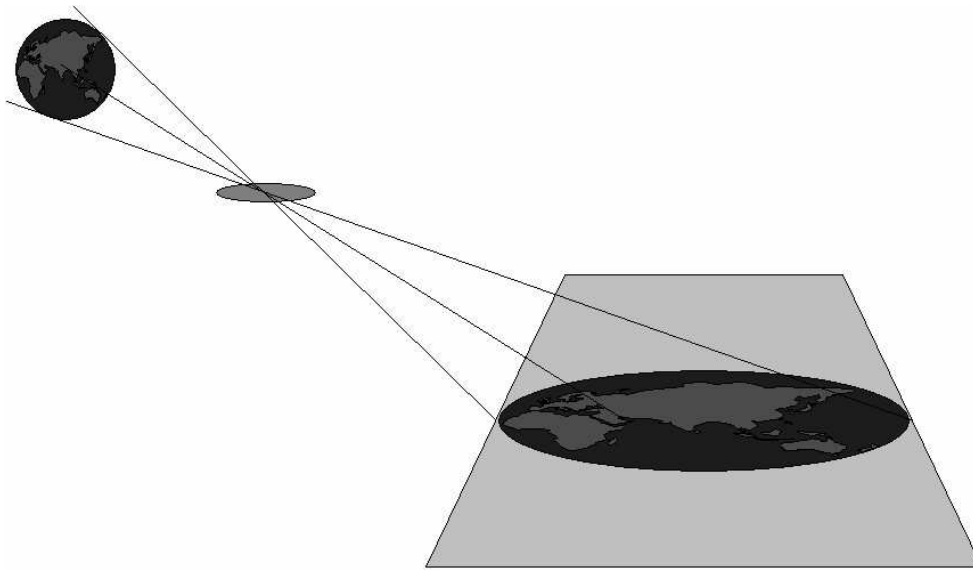


Figure 3.26: Schematics of the elliptical perception of the Earth as seen under large viewing angles

An additional correction might be necessary in case the Earth is not in the center of the FOV, since in that case the Earth is perceived as a conic section. This results from the characteristics of optical systems: Since all rays propagate through the effective center of the optics, the sphere of the Earth might end up as the image of an ellipse on the detector. This can be seen in fig. 3.26, while it should be noted that this drawing is a crude approximation of reality and only meant to explain the basic principle. A comparison of a circle and the simulated image of the horizon as seen from a LEO is shown in fig. 3.27. Apparently, in that case, no circle can be used as a global criterion, but an ellipse has to be used from the very beginning. It should be noted, though that this effect has only taken to be into account in LEO, where the Earth in general is observed tangentially, and therefore is not in the center of the field of view and opens a large cone, both of which changes the shape of the conic section to finally resemble a hyperbola. The nominal case in GEO uses a centered Earth, since the apparent diameter is smaller than the FOV, so the complete horizon can be observed, if it is adequately illuminated.

It turned out to be vital for the accuracy of the Earth-center determination to include the vignetting, meaning the light drop-off when leaving the center of the FOV, in the determination of the apparent Earth horizon. Since the horizon is determined using the Earth's intensity, the curvature changes, when the horizon is at different angles relative to the LOS. This effect is greatest in LEO, where the horizon nearly crosses the LOS as well as it leaves the FOV. Due to the different lighting conditions in the center as compared to the rim, resulting from the vignetting, the apparent diameter, and thus the apparent Earth-center, changes. This effect can only be neglected, if the Earth is perfectly

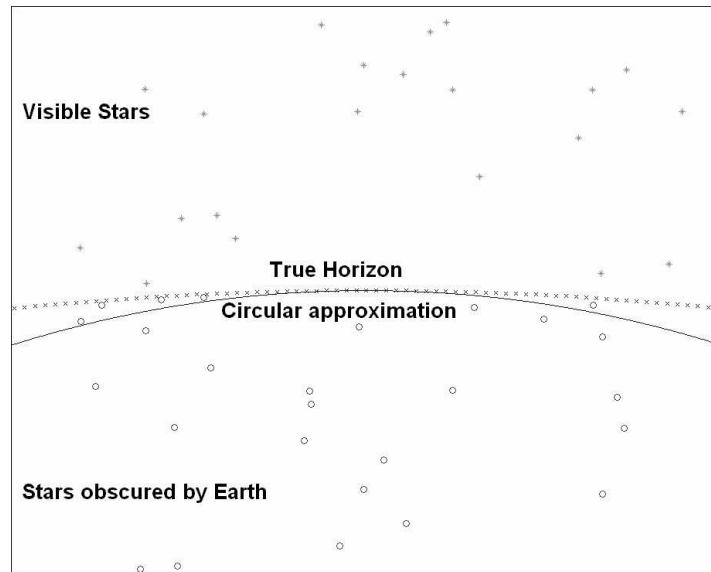


Figure 3.27: Comparison of a circle and the simulated image of the horizon as seen from a LEO

centered in the FOV and fully seen, as in the case for GEO, since in these cases, the vignetting effects the horizon symmetrically about the Earth-center. The apparent radius remains underestimated, though, and thus should not be used for distance determination. Another effect, leading to mis-estimation of the Earth-diameter is the systematic error induced by choice of the threshold defining the beginning of noticeable atmosphere and the change in the atmospheric height in the course of the year. As the effect is of systematic nature, it can, in general, not be filtered by an increased number of measurements. In general, this diffuseness is approximately symmetrical to the Earth's center and thus does not influence the center itself. The effect needs to be taken into account, though, when determining the satellite's distance from the Earth-center, which depends on the apparent diameter. As explained in chpt. 5.2, it is not necessary, to actually include an estimation of the distance into the measurements passed to the Kalman-filter used for an accurate position and orbit determination. This eliminates the need for the Earth's apparent diameter and the associated drawbacks. Nevertheless, the information is useful for initialization of the filter.

It should be noted that systematic mis-estimation in the Earth's diameter as well holds for IR-sensors. In particular, the stability of the CO_2 -emission, which is being observed, is about 0.2° .

A possibility to reduce the noise is to increase the number of measurements. Additional data might be obtained by using a preliminary fit and searching for additional horizon-points along the estimated horizon. This routine can be incorporated adaptively, to be used only in case of too few initial measurements, in order to verify the assumed horizon and increase the accuracy to a tolerable level.

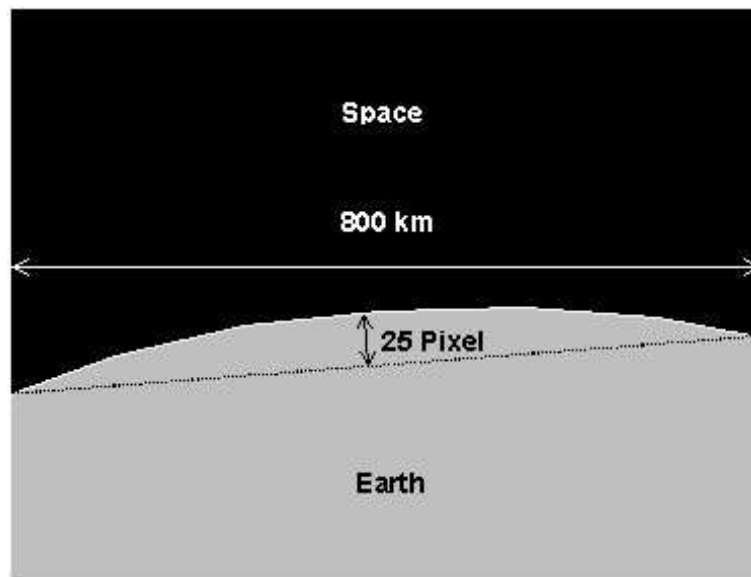


Figure 3.28: Curvature of horizon as seen from LEO

3.2.3 Initial estimate of the expected accuracy

In this section the expected accuracy of the Earth-center determination is estimated. A first approximation for LEO applications at about 300 km height is based on a detector with a 24° FOV and a detector area of 1280×1024 pixels². This results in a visible horizon height of approx. 25 pixels with respect to a secant connecting the two points where the horizon enters, respectively leaves, the FOV (see fig.3.28). Assuming an accuracy of 1 pixel in the determination of the horizon then results in an accuracy of approx. 0.3° in the determination of the Earth-vector.

This accuracy is assumed to be better in GEO due to better sighting conditions and a better defined horizon. Accuracy in GEO thus is expected to be about 0.1° , which is confirmed by applying the presented algorithms to Earth-images gathered by a geostationary weather-satellite (Meteosat) (see chpt. 7.2.2).

Summarizing, the performance of the algorithms presented for the proposed sensor-suite working in the visual regime is comparable to that of standard IR Earth-sensors, while yielding a wider range of applications. In our case, the same sensor can be used for a wide range of orbits. The combination of Earth- and Star-measurements and the prediction of the satellite's orbit further provides means for covering eclipse-phases and a three-axes Earth-reference, which can not be obtained using IR measurements. Using these pieces of additional information results in a sensor which is superior to standard IR Earth-sensors in possible applications and the information provided.

Chapter 4

Evaluation of the Image Processing Algorithms

4.1 Simulations on the Attitude Determination From Star-Measurements

4.1.1 Probability of success and computational burden

The following section will introduce the probability of success as a function of the Star-centroiding accuracy as well as the resulting computation time. These values are of relevance, when setting the tolerances of the Star-identification algorithm, and when setting the requirements on the computational power. In order to find the best relationship between the chosen tolerance and the expected noise-level, several simulations have been carried out in order to obtain information on identification reliability and computation time. The basic assumptions are a white noise in the measurement of the Star's position on the detector. The position on the detector at first is determined using a simulation of the observed Stars when scanning the celestial sphere. The observed Stars are „projected“ onto the detector, where the resulting nominal positions are disturbed by a normal-distributed noise with a standard deviation of σ , where typically $\sigma = 0.1$ pixel and $\sigma_x = \sigma_y$ (see fig. 4.1). The advantage of disturbing the positions on the detector, rather than disturbing the unit vectors to the Stars is a more realistic representation of the noise as well as the possibility of using individual noise levels in the two detector axis, as they are expected from the results as derived in chpt. 3.1.2.

The results of the simulations on the Star-identification confirmed the expectations: starting from a certain defined level of tolerance on the inter-Star-angle as defined in 4.2, the identification probability does not change significantly any more. Additionally, it was found that the computation

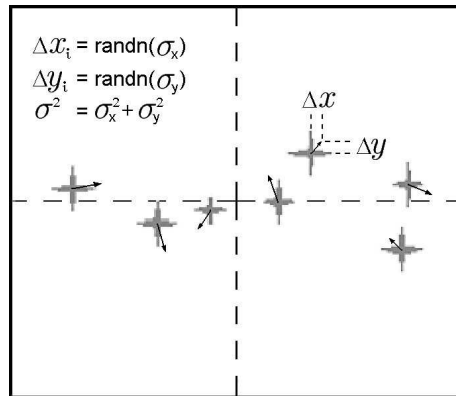


Figure 4.1: Introduction of noise (Δx , Δy) to the nominal Star-position

time is non-linearly dependent on the chosen tolerance.

These effects can be seen in fig. 4.3 and fig. 4.4. Different noise levels are represented by the parametric plot in fig. 4.3, which shows the probability of a correct Star-identification as a function of the chosen inter-Star-angle tolerance, which is given in multiples of the expected noise level. The parameters on the curves denote the simulated noise as multiples of $1/6^{\text{th}}$ pixel, which resembles approx. $10''$.

It seems to be essential to note that increasing the tolerance further than necessary might result in a degradation of the probability of a correct Star-identification. This is due to the fact that higher tolerances allow for more possible identifications. Since a low number of bad matches within a set, chosen as a possible identification, might be compensated by a large number of good matches, this might result in favoring a false identification over a correct solution. As mentioned above, singular misidentifications can be detected using a time history and/ or the use of a propagation of the Star-centroids in the form of *Star-tracking*. The probabilities shown, are those of a single identification, using no *a priori* knowledge.

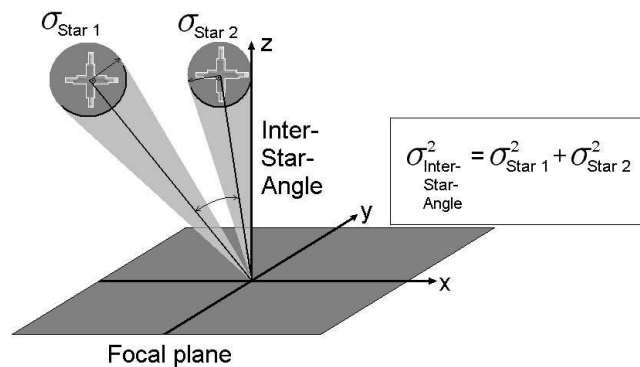


Figure 4.2: Definition of the inter-Star-angle and its nominal accuracy

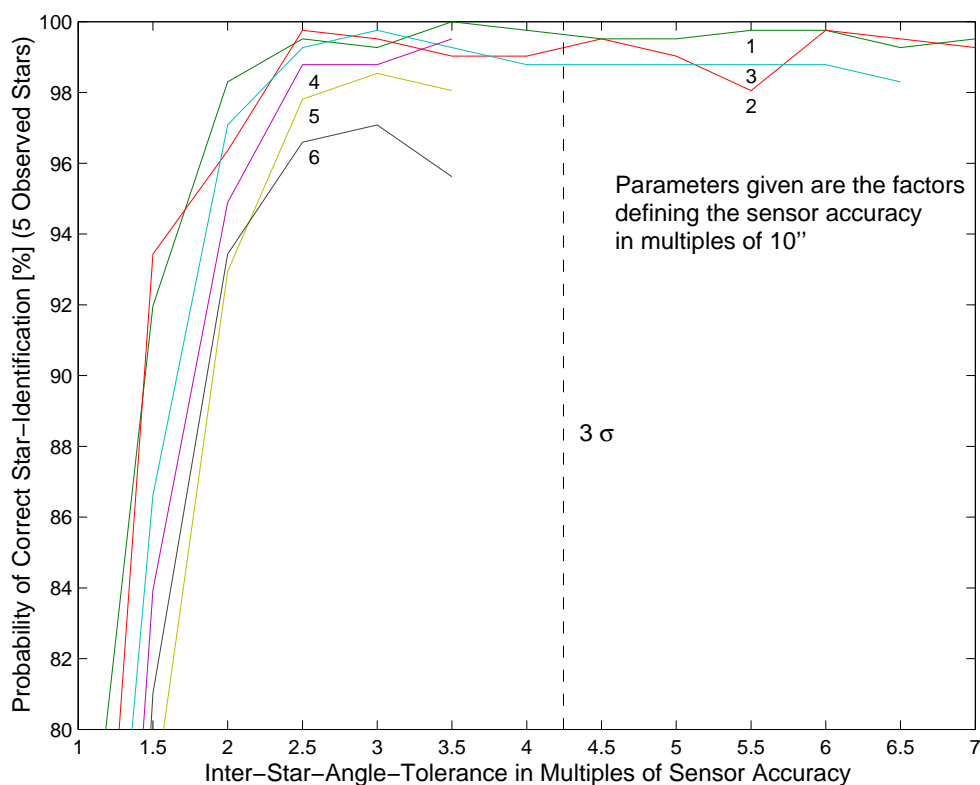


Figure 4.3: Probability of correct identification using 5 Stars for different sensor accuracies and different tolerances

As expected the computation time increases with increasing tolerance, because this increases the number of Stars that need to be checked. Since with each additional Star, the number of Star-pairs and their resulting triangles to be validated increases nonlinearly, the computation time increases nonlinearly as well. A fit of the measured times in fig. 4.4 shows an approximately quadratic dependency on the total tolerance.

It needs to be stressed that, while in fig. 4.3 the inter-Star-angle tolerance is given in multiples of the sensor accuracy, in fig. 4.4 the tolerance is given in arcseconds.

The result of this section is that the tolerance should be chosen as small as possible to reduce the computation time. A fair trade-off between a high identification probability and computational burden seems to be a tolerance of approximately three times the sensor accuracy.

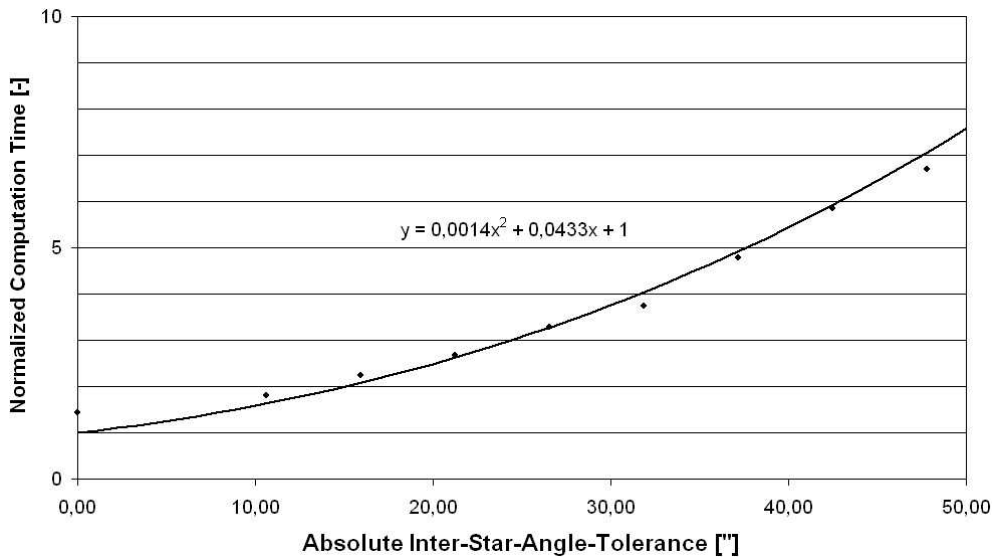


Figure 4.4: Computation Time as a function of tolerance, normalized to 0'' tolerance; Example: 30'' results in a 3.7 times higher computation time necessary for identification

4.1.2 Expected Attitude Accuracy from Star-Observations

A simulation which added a 10'' to 60'' noise-level to the Star-positions on the detector, resulted in fig. 4.5. The parametric plot shows the achieved accuracies in attitude when using a varying number of Stars and varying accuracies, which were then normalized for comparison. Sample size was 400, the position of the Stars on the detector varied throughout the simulation. As easily can be seen, the overall tendency is in agreement with the expected inverse square-root of the number of Stars, while the deviation from this idealized curve is due to the varying position of the Stars on the detector. This can be explained by the dependency of the attitude's variance on the distribution of measurement points, as determined by

$$P = \left[\sum_i a_i \cdot (I - \underline{b}_i \underline{b}_i^T) \right]^{-1}. \quad (3.27)$$

Concluding, the static accuracy is determined to be approx. 5'' in the LOS and approx. 25'' in the rotation about the LOS. This accuracy is based on a centroiding accuracy of 10'' (approx. 0.1 pixel, using the given camera system) in the centroiding process, and 5 Stars in the FOV. This matches closely with the performance achieved in field experiments (chpt. 7.2.1), which was determined to be approx. 10'' in the LOS in the presence of atmospheric disturbances. As apparent from the equations above, this accuracy is dependent on the distribution of the Stars on the detector and on the satellite's angular velocity. It was shown that, despite the use of simple commercial optics, the

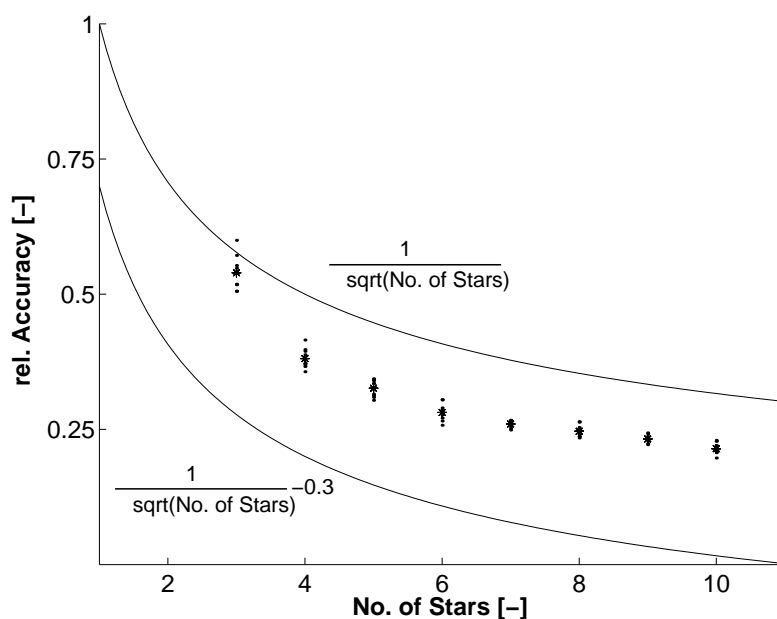


Figure 4.5: Attitude Accuracy as a function of number of observed Stars determined for different noise-levels as parameter (10''-60'' in steps of 10''). The star denotes the mean of the accuracy, the dots the results for the different noise-levels. The deviation from the expected inverse square-root of the number of Stars is mainly due to the varying position of the Stars on the detector.

accuracy can be tremendously increased, when including the knowledge of the applicable PSFs in the centroiding process, leading to a simple system which yields the required performances for a wide range of missions.

Thus, the approximation of the expected accuracy was confirmed by the simulations. Further experiments with actual hardware in space environment will be necessary, though, to provide real data, including additional effects like increased noise through radiation and aging effects as well as possible thermal deformations of the optical system.

4.2 Simulations on the Earth Center Determination

This section deals with the simulations performed on the Earth-horizon and -center determination. What will be shown is the intensity distribution on the detector when observing the horizon from LEO. While from GEO it is primarily seen as a step, in LEO an exponential increase in intensity is seen.

The reason for this is partially due to the long optical pathlength of the observation within atmosphere, as it is explained in fig. 4.6. Assuming an exponential function for air density and a uniform scattering of light proportional to the air density leads to an exponential decay of light scattered in direction of the observer, as a function of height. This decay is even enhanced due to the reduction of the optical pathlength, which can be thought of as a secant through the atmosphere, the length of which changes as a function of the height. Using these two parameters for an approximation, the expected relative intensity distribution can be seen in fig. 4.7. For the case of an orbit outside the atmosphere an approximation in a closed form solution was developed:

$$\text{Rel. Intensity}(\alpha) = -2 \cdot \frac{\rho_0 \cdot H_0}{I_0} \cdot \exp \left[-\frac{(R_{\text{Satellite}} \cdot \sin(\alpha) - R_{\text{Earth}})}{H_0} \right] \cdot \exp \left[-\frac{\sqrt{(H_{\text{Atm}} + R_{\text{Earth}})^2 - (R_{\text{Satellite}} \cdot \sin(\alpha))^2} - 1}{H_0} \right], \quad (4.1)$$

with ρ_0 being the air-density at sea-level and H_0 being a scaling height, which is set to match the air-density in a height of 100km. For orbit-propagation of spacecraft, starting from this height, the density is determined using the *Harris-Priest* air-density model, which is semi-empirical and

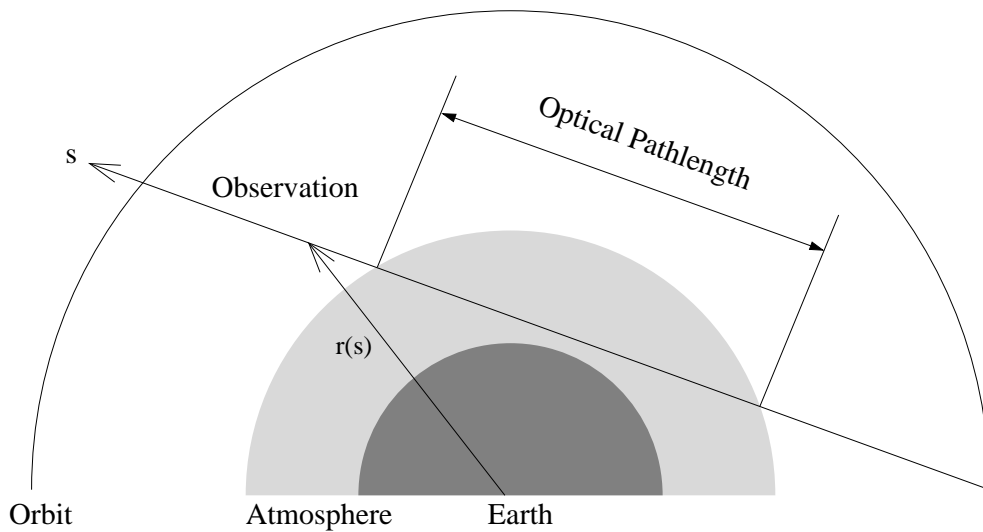


Figure 4.6: Visualization of optical pathlength when dealing with horizon measurements

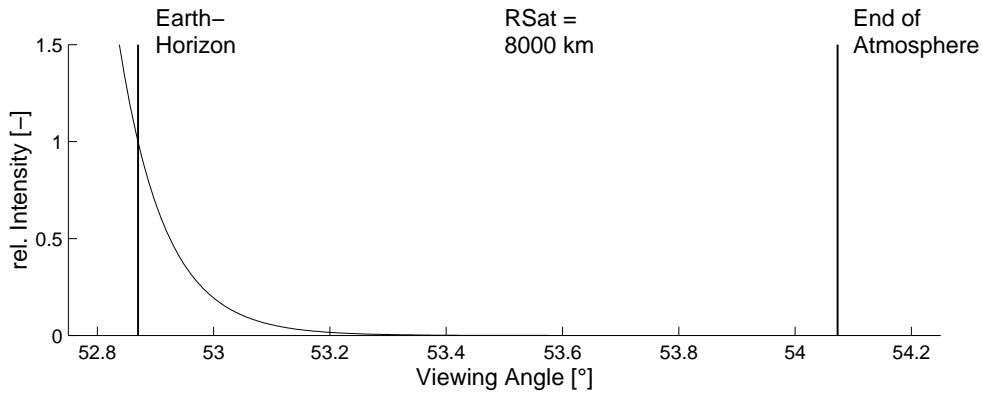


Figure 4.7: Intensity distribution normal to the horizon, analytical result using the preliminaries of an exponentially decreasing air-density and the optical pathlength as defined in fig. 4.6

dependent on the Sun's incidence angle (see e.g. [28]). I_0 is the nominal intensity at ground-level, which is determined by the formula, setting I_0 equal to one and α to the apparent angular diameter of the Earth, as seen from the spacecraft, while α in general denotes the angle between the satellite's position-vector and the line-of-sight. H_{Atm} is the height of the atmosphere, which for our purposes is set to 100km. If the satellite is within the atmosphere, the solution is not as compact. It should be noted, though that, when determining the atmosphere's brightness, it can be assumed not to extend further than to approx. 100km in height, which is below all satellite orbits of interest.

The feature of an exponential decrease in intensity has for instance been exploited in ref.[48], which uses a logarithmic detector (FUGA15d) and a simple threshold for horizon detection.

The exponential intensity decay lead to the idea, of using an exponential or polynomial filter to extract the horizon by means of shape, rather than by using thresholds, which are very sensitive to local intensity variations due to cloud coverage. A tool has been developed to determine the appropriate filter values from actual images of the Earth horizon. The results are given in the experimental section (7.2.2).

Chapter 5

Algorithms on Position and Orbit Determination

The following chapters deal with the position determination of a satellite using attitude and Earth-vector information. Since the algorithm will be shown to be independent of the satellite's attitude-dynamics and orbit, the sensor can be used without any knowledge of the host-satellite. The section introducing the point solution from a single image will be followed by a section on the orbit determination using appropriate filtering. Further results of the orbit determination are the increase in the accuracy of the position determination and another important information: the satellite's attitude in a *Local Vertical, Local Horizontal* reference frame.

5.1 Position Determination Using the Combined Earth-/Star-Sensor

As proposed in the patent on the „Combined Earth-/Star-Sensor“ ([1]), it is possible to determine the position of a satellite using the knowledge of the Earth-vector in combination with the observation of Stars. Commonly published algorithms are derived from a geodetical point of view. The „geodetical“ algorithms typically use the method of intersecting lines of sight, often referred to as „navigation fix“ (e.g. [49, p. 229 ff.], [50]). In essence, mostly a closer celestial body (e.g. Earth, Sun or Moon) and at least one other vector measurement (e.g. a Star-measurement) are combined to result in a position fix. In most approaches, the distance towards the closer celestial body is estimated using the apparent diameter (i.e. the angular diameter as perceived by the sensor) and relating it to the known actual diameter.

The set of algorithms which will be presented here is based on transformations of reference systems developed by Astrium GmbH, Germany (private communication: W. Fichter, K. Ebert). They were

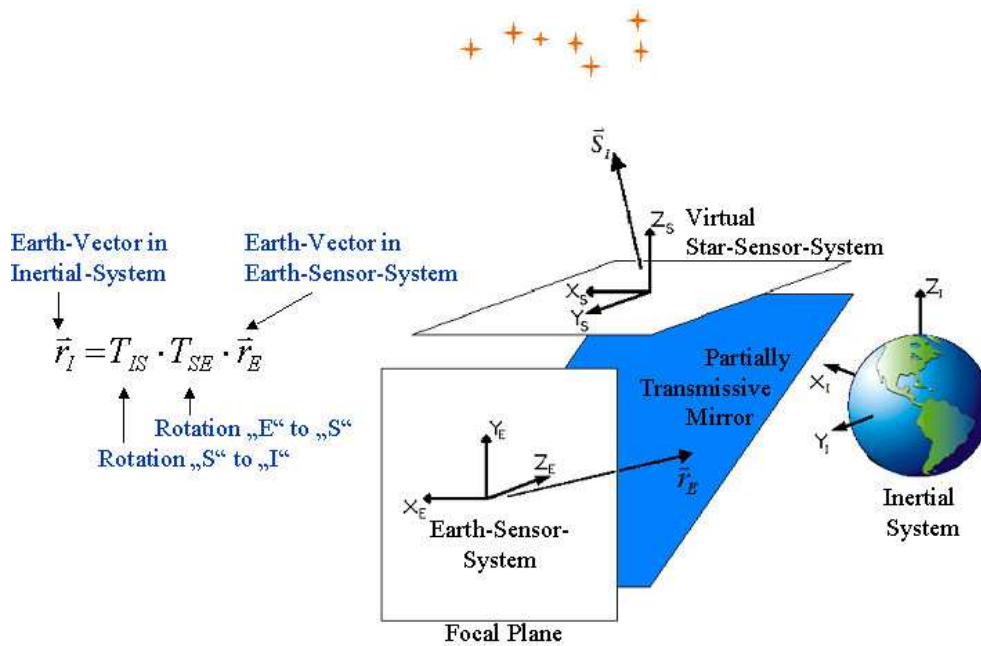


Figure 5.1: Coordinate Systems and final formulation of Position Determination Point Solution

further developed and adapted to be used with the proposed sensor.

In common with other approaches, the proposed algorithm, as depicted in fig 5.1, uses the reference of a closer celestial body, in this case the Earth, and those provided by Star-measurements. Instead of geometrically intersecting the lines of sight, however, a different approach is used: The knowledge of the inertial attitude matrix of the sensor, which is determined using Star-observations, is used to rotate the observed position of the second celestial body (e.g. the Earth), as sensed in the sensor's coordinate-system, into the inertial frame. This results in the „inertial position of the observed celestial body, relative to the sensor“. In order to determine the position of the sensor relative to the observed celestial body in inertial coordinates, it is sufficient to „flip“ the vector by multiplying it with (-1) . This shows that only two standard components for attitude determination are needed for the position determination of a satellite in the inertial reference system: The first feature is that of an *autonomous Star-tracker*, for attitude determination, the second is that of an Earth-sensor. It should be noted that in an initial position determination, the distance towards the closer celestial body is as well determined using its apparent diameter. In the process of the thesis it was found that such an algorithm has been developed independently by J.R. Wertz ([51]). Initially this was to be used with a combination of Earth-, Moon- and Sun-Sensors. It was further generalized to be used with an Earth-/Star-sensor combination (e.g. [52]). Investigations on the orbit determination will show that it is, in general, not necessary to use the information on the apparent Earth-diameter - and sometimes even beneficial to disregard it, since it serves as an

additional source of errors.

With this general introduction, the equation will now be rigorously deduced. This will be followed by an estimation of the expected accuracy.

5.1.1 Deduction of an algorithm for position determination of a satellite

Effectively, the formula for position determination using the combined Earth-/Star-sensor, has to rotate the Earth-vector, as determined from the Earth-images, into the inertial reference frame by use of the known relation between the Earth- and the Star-sensor and the known attitude matrix of the Star-sensor in the inertial space.

The reference systems entering into the evaluation are those of the Star-sensor- („ \underline{S} “), the Earth-sensor- („ \underline{E} “), the Mounting- („ \underline{M} “), the Body-fixed- („ \underline{B} “), the Reference- („ \underline{R} “), and the Inertial („ \underline{I} “)- system. The rotations necessary to transform a vector from a system x to the system y are denoted \underline{T}_{yx} . The transformations \underline{T}_{BR} , \underline{T}_{MB} , \underline{T}_{EM} , \underline{T}_{SE} as well as \underline{T}_{SI} can be assumed to be known, since the mechanical setup of the sensor is known as well as the inertial attitude (\underline{T}_{SI}), which is determined by evaluation of the Star-images. In this derivation it will be shown that most of these transformations need not to be performed, yet they lead to a simple formulation of the problem.

With the help of these transformations and the Earth-vector as supplied by the Earth-sensing part of the proposed system (in the following called „Earth-sensor“), the unit vector from the center of the Earth towards the satellite can be determined. The determination of the relative distance is addressed later.

At first, the Earth-vector, as it is perceived by the Earth-sensor will be determined using the satellites inertial position as well as the necessary rigid body rotations. This leads to

$$\underline{r}_E = \underline{T}_{EM} \cdot \underline{T}_{MB} \cdot \underline{T}_{BR} \cdot \underline{T}_{RI} \cdot (-\underline{r}_I). \quad (5.1)$$

Using the same transformations, the attitude matrix of the Star-sensor can be described as

$$\underline{T}_{SI} = \underline{T}_{SE} \cdot \underline{T}_{EM} \cdot \underline{T}_{MB} \cdot \underline{T}_{BR} \cdot \underline{T}_{RI}. \quad (5.2)$$

By comparison of equations 5.1 and 5.2 it can be shown that the common transformations can be combined to satisfy

$$\underline{T}_{EM} \cdot \underline{T}_{MB} \cdot \underline{T}_{BR} \cdot \underline{T}_{RI} = \underline{T}_{SE}^{-1} \cdot \underline{T}_{SI}. \quad (5.3)$$

This shows that the relation between the inertial vector from the satellite towards the Earth and the determined Earth-vector is solely dependent on the inertial attitude of the Star-sensor and the

transformation between the Star-sensor and the Earth-sensor reference frame. This leads to the reduced formulation

$$\begin{array}{ccccccc} \underline{r}_I & = & \underline{T}_{SI}^T & \cdot & \underline{T}_{SE} & \cdot & (-\underline{r}_E) \\ [3 \times 1] & & [3 \times 3] & & [3 \times 3] & & [3 \times 1] \end{array} \quad (5.4)$$

The property of rotation matrices has been put to use, which yields

$$\underline{T}_{yx}^{-1} = \underline{T}_{yx}^T. \quad (5.5)$$

As previously explained, the negative sign in the formulation is necessary to transform the result in a vector from the Earth's center towards the spacecraft as opposed to the originally resultant reverse vector. Furthermore, the distance to the Earth still has to be determined.

5.1.2 Initial estimate of the expected accuracy

In this section an estimate of the expected accuracy of the vector measurement will be given, which in itself already represents an interesting value. The importance of this value is even increased due to the fact that the determination of the spacecraft's distance to the Earth is dependent on this accuracy, when using a *Navigation Solution* for a complete determination of the satellite's position, as given in chpt. 5.2. In this connection *Navigation Solution* means the solution based on filtering for additional accuracy and state information.

To provide an estimate, several assumptions have to be made in order to facilitate an analytical solution. A typical approach is to assume a decoupled noise, in this case of the Star-sensor and the Earth-sensor. Further, as common practice for Star-sensor measurements (e.g. [23]), a white noise (Gaussian) process is assumed.

Starting with the Star-sensor, it is assumed that we have a decoupled noise in the three rotation axes, resulting in a rotation matrix \underline{T}_{SI}^* , due to mis-estimation of the satellite's attitude matrix, which can be defined as

$$\underline{T}_{SI}^* = \Delta \underline{T}_{SI} \cdot \underline{T}_{SI}, \quad (5.6a)$$

with the approximation for $\Delta \underline{T}_{SI}$ as

$$\Delta \underline{T}_{SI} = \begin{bmatrix} 1 & -\psi & \theta \\ \psi & 1 & -\phi \\ -\theta & \phi & 1 \end{bmatrix}. \quad (5.6b)$$

This can then be separated into the identity matrix and the remainder $\Delta^* \underline{T}_{SI}$ as follows:

$$\Delta \underline{T}_{SI} = I + \Delta^* \underline{T}_{SI}. \quad (5.6c)$$

This definition will be of value, when separating the ideal and the error components of the measurement \underline{r}_I^* .

The rotation matrix for errors in the Earth-vector determination is derived accordingly, with the difference that the accuracy is assumed to be identical in all three axes. It should be noted that, while this is not taken into account in the further derivation, this matrix could be augmented with the errors of the transformation matrix between the Star-sensor and the Earth-sensor in a first order assessment.

With the assumptions as stated above, the measurement, including the errors, can be written as:

$$\underline{r}_I^* = [(I + \Delta^* \underline{T}_{SI}) \cdot \underline{T}_{SI}]^T \cdot \underline{T}_{SE} \cdot (I + \Delta^* \underline{T}_{r_E}) \cdot \underline{r}_e. \quad (5.7)$$

Separating the ideal and the noise-induced terms results in

$$\underline{r}_I^* = \underline{r}_I + \Delta \underline{r}_I, \quad (5.8a)$$

with

$$\begin{aligned} \Delta \underline{r}_I = & [[\Delta^* \underline{T}_{SI} \cdot \underline{T}_{SI}]^T \cdot \underline{T}_{SE} \\ & + [\underline{T}_{SI}]^T \cdot \underline{T}_{SE} \cdot \Delta^* \underline{T}_{r_E} \\ & + [\Delta^* \underline{T}_{SI} \cdot \underline{T}_{SI}]^T \cdot \underline{T}_{SE} \cdot \Delta^* \underline{T}_{r_E}] \cdot \underline{r}_E. \end{aligned} \quad (5.8b)$$

The expectation for $\Delta \underline{r}_I$ is „0“, its variance can be derived from

$$\mathbf{v} = E[\Delta \underline{r}_I \cdot \Delta \underline{r}_I^T]. \quad (5.9)$$

As can be seen from closer observation of eq. (5.8b), the accuracy of the system is dependent on the satellites attitude as well as the position of the Earth on the detector. Additionally it should be noted that the Star-tracker's accuracy is dependent on the distribution of the Stars on the detector, and thus is time-varying.

As a first expectation, the total error would be the sum of the individual errors. For well defined cases, this can be verified: Assuming an Earth-vector in z -direction only, a Star-sensor orientation which coincides with the Earth-sensor and an attitude which in turn coincides with the inertial frame as well as neglecting second order terms, the error matrix contains the sum of the individual errors. Summarizing, the assumptions can be stated as

$$\begin{aligned} \underline{T}_{SE} &= I_{[3 \times 3]} \\ \underline{T}_{SI} &= I_{[3 \times 3]}. \end{aligned} \quad (5.10)$$

Thus, the linearized and maximal error matrix of the system can be written as

$$\Delta \underline{T}_{SI \& SE}^* = \begin{bmatrix} 0 & -(|\psi_{SI}| + |\psi_{SE}|) & (|\theta_{SI}| + |\theta_{SE}|) \\ (|\psi_{SI}| + |\psi_{SE}|) & 0 & -(|\phi_{SI}| + |\phi_{SE}|) \\ -(|\theta_{SI}| + |\theta_{SE}|) & (|\phi_{SI}| + |\phi_{SE}|) & 0 \end{bmatrix}. \quad (5.11)$$

For the general case of an arbitrary attitude matrix as well as Earth-vector, a covariance-analysis based on eq. (5.8b) results in a similar representation. Due to the coupling between the axes, the individual components of the system's covariance matrix turn out to be rather complex in structure. For demonstration purposes, the first element of the covariance matrix will be given and discussed in greater detail. The components are ordered according to their affiliation to the linear and nonlinear part of the equation. As demonstrated in the specialized case, a linear dependency becomes apparent when the nonlinear components are neglected.

$$\begin{aligned}
V_{linear} = & +r_E(1)^2 \cdot V(\psi_{SE}) \cdot \underline{T}_{SI}(3, 1)^2 \\
& +r_E(1)^2 \cdot V(\theta_{SI}) \cdot \underline{T}_{SI}(3, 1)^2 \\
& +r_E(1)^2 \cdot V(\theta_{SE}) \cdot \underline{T}_{SI}(2, 1)^2 \\
& +r_E(2)^2 \cdot V(\psi_{SI}) \cdot \underline{T}_{SI}(2, 1)^2 \\
& +r_E(2)^2 \cdot V(\psi_{SE}) \cdot \underline{T}_{SI}(1, 1)^2 \\
& +r_E(2)^2 \cdot V(\theta_{SI}) \cdot \underline{T}_{SI}(1, 1)^2 \\
& +r_E(2)^2 \cdot V(\phi_{SE}) \cdot \underline{T}_{SI}(2, 1)^2 \\
& +r_E(2)^2 \cdot V(\phi_{SI}) \cdot \underline{T}_{SI}(2, 1)^2 \\
& +r_E(3)^2 \cdot V(\theta_{SE}) \cdot \underline{T}_{SI}(1, 1)^2 \\
& +r_E(3)^2 \cdot V(\psi_{SI}) \cdot \underline{T}_{SI}(1, 1)^2 \\
& +r_E(3)^2 \cdot V(\phi_{SE}) \cdot \underline{T}_{SI}(3, 1)^2 \\
& +r_E(3)^2 \cdot V(\phi_{SI}) \cdot \underline{T}_{SI}(3, 1)^2 \\
& -2 \cdot r_E(1) \cdot r_E(2) \cdot V(\psi_{SE}) \cdot \underline{T}_{SI}(3, 1) \cdot \underline{T}_{SI}(1, 1) \\
& -2 \cdot r_E(1) \cdot r_E(2) \cdot V(\theta_{SI}) \cdot \underline{T}_{SI}(3, 1) \cdot \underline{T}_{SI}(1, 1) \\
& +2 \cdot r_E(1) \cdot r_E(3) \cdot V(\psi_{SI}) \cdot \underline{T}_{SI}(2, 1) \cdot \underline{T}_{SI}(1, 1) \\
& +2 \cdot r_E(1) \cdot r_E(3) \cdot V(\theta_{SE}) \cdot \underline{T}_{SI}(2, 1) \cdot \underline{T}_{SI}(1, 1) \\
& +2 \cdot r_E(2) \cdot r_E(3) \cdot V(\phi_{SE}) \cdot \underline{T}_{SI}(2, 1) \cdot \underline{T}_{SI}(3, 1) \\
& +2 \cdot r_E(2) \cdot r_E(3) \cdot V(\phi_{SI}) \cdot \underline{T}_{SI}(2, 1) \cdot \underline{T}_{SI}(3, 1)
\end{aligned} \tag{5.12}$$

In the equations (5.12) and (5.13) „ V “ denotes the variance of the corresponding values. The additive behavior of the system's variance can readily be seen in eq. (5.12), while the nonlinear terms are given in (5.13).

In addition to these stochastic errors this system, as most other systems, includes a certain level of errors due to misalignment and other deterministic errors. The advantage of this sensor as opposed to other systems is the compact setup which allows for a significant reduction of time varying misalignments (e.g. due to thermal deformations). This still leaves misalignments resulting from the manufacturing process, which can be measured and calibrated on equipment level, as well before launch as on orbit. Again a specific feature of the system and the formulation of the measurement-

$$\begin{aligned}
V_{nonlinear} = & -2 \cdot r_E(1) \cdot r_E(3) \cdot V(\theta_{SE}) \cdot V(\psi_{SI}) \cdot \underline{T}_{SI}(1,1) \cdot \underline{T}_{SI}(3,1) \\
& -2 \cdot r_E(2) \cdot r_E(3) \cdot V(\phi_{SE}) \cdot V(\phi_{SI}) \cdot \underline{T}_{SI}(3,1) \cdot \underline{T}_{SI}(2,1) \\
& +2 \cdot r_E(1) \cdot r_E(2) \cdot V(\psi_{SE}) \cdot V(\theta_{SI}) \cdot \underline{T}_{SI}(1,1) \cdot \underline{T}_{SI}(3,1) \\
& +r_E(1)^2 \cdot V(\psi_{SE}) \cdot V(\theta_{SI}) \cdot \underline{T}_{SI}(1,1)^2 \\
& +r_E(1)^2 \cdot V(\theta_{SE}) \cdot V(\psi_{SI}) \cdot \underline{T}_{SI}(1,1)^2 \\
& +r_E(2)^2 \cdot V(\phi_{SE}) \cdot V(\psi_{SI}) \cdot \underline{T}_{SI}(1,1)^2 \\
& +r_E(3)^2 \cdot V(\phi_{SE}) \cdot V(\theta_{SI}) \cdot \underline{T}_{SI}(1,1)^2 \\
& +r_E(1)^2 \cdot V(\psi_{SE}) \cdot V(\phi_{SI}) \cdot \underline{T}_{SI}(2,1)^2 \\
& +r_E(2)^2 \cdot V(\psi_{SE}) \cdot V(\psi_{SI}) \cdot \underline{T}_{SI}(2,1)^2 \\
& +r_E(3)^2 \cdot V(\phi_{SE}) \cdot V(\phi_{SI}) \cdot \underline{T}_{SI}(2,1)^2 \\
& +r_E(3)^2 \cdot V(\theta_{SE}) \cdot V(\psi_{SI}) \cdot \underline{T}_{SI}(2,1)^2 \\
& +r_E(1)^2 \cdot V(\theta_{SE}) \cdot V(\phi_{SI}) \cdot \underline{T}_{SI}(3,1)^2 \\
& +r_E(2)^2 \cdot V(\phi_{SE}) \cdot V(\phi_{SI}) \cdot \underline{T}_{SI}(3,1)^2 \\
& +r_E(2)^2 \cdot V(\psi_{SE}) \cdot V(\theta_{SI}) \cdot \underline{T}_{SI}(3,1)^2 \\
& +r_E(3)^2 \cdot V(\theta_{SE}) \cdot V(\theta_{SI}) \cdot \underline{T}_{SI}(3,1)^2
\end{aligned} \tag{5.13}$$

algorithms leads to a satisfying solution: since the algorithms do not depend on a perpendicular separation of the observation axis, the corresponding transformation can be adapted to virtually any layout. The only restriction results from the necessity to attenuate the Earth's brightness relative to that of the Stars. This results in a necessary minimal separation of the two lines-of-sight. For typical contemporary Star-trackers the so-called *Earth-exclusion-angle* (EEA) is approximately 20° . This translates to a minimal separation of about 45° , resulting from $20^\circ(\text{EEA}) + 2 \cdot 12.5^\circ$ ($2 \cdot$ half FOV).

As the angular separation between the two FOVs is introduced using the partially transmissive mirror, this mirror serves as a source for a constant misalignment. In the case of a $50 \times 50 \text{ mm}^2$ mirror an error of 0.01 mm while cutting a retaining groove on the top and the bottom of a 45° angle in the worst case results in an angular error of 0.03° , which is in the same order of magnitude as the stochastic error expected for the determination of the Earth-center. It should be mentioned, again that this error is deterministic and can be calibrated prior to launch and, in special cases, in orbit. These cases for instance include a calibration using the known position of the satellite.

In essence, the variance of the stochastic error to be expected is equal to the sum of the maximal variance in the Star-sensor and the variance of the Earth-sensor. In the case of the sensor as proposed, the error due to the Star-sensor can be neglected when compared to the inaccuracy introduced by the Earth-sensor. In the case for a GEO, the expected single-measurement accuracy is assumed to be in the order of 0.1° , corresponding to approx. 70km. This accuracy is

approximately equal to the position accuracy required for geostationary satellites ($0.05 - 0.1^\circ$). The accuracy for LEO is derived equivalently and amounts to the order of 0.3° , corresponding to approx. 36km. In chpt. 5.2 it will be shown that this accuracy can be improved. This is necessary, since the knowledge of the position should be better for considerations of safety and fuel saving.

5.2 Orbit Determination from Consecutive Position Measurements

The determination of the satellite's absolute position can be carried out in different fashions, two of which will be presented. The intuitive solution is using an estimate of the satellite's distance from the Earth based on its apparent diameter, as it has been proposed in chpt. 5.1. Yet, as briefly mentioned there as well, it is not generally necessary to explicitly obtain the distance through measurements. The following section will propose a Kalman-filter based approach for position determination and prove the observability of the proposed system. The advantage of the system is the additional information about the satellite's inertial velocity vector. This information can be used to generate a *Local Vertical, Local Horizontal*-reference system, as shown in fig. 2.3. This is composed using the „negative“ position vector as the z -axis, the vector perpendicular to the orbit plane as the y -axis (vector-product $\underline{Velocity} \times \underline{Position}$) and the x -axis being the cross-product of the y - and z -axis, which is oriented approximately parallel to the velocity vector. The reason for this additional reference system lies in its advantages in Earth-pointing satellites on circular orbits, which then have a reference system in which the nominal attitude does not vary.

5.2.1 Composition of a Kalman-Filter for Position and Orbit Determination

The determination of the satellite's orbit and position from measurements can be achieved using a variety of methods. For instance, the orbit could be derived from angular measurements and their timed separation using Kepler-elements, meaning

- a : semi major axis,
- e : eccentricity,
- i : inclination,
- Ω : right ascension of ascending node,
- ω : argument of perigee,
- v : true anomaly .

In the case of observations using ground stations, which are not within the satellite's orbit plane, three measurements are sufficient. It should be noted, though, that an explicit solution in our case needs four, instead of only three measurements, since, due to their nature, they are within the orbit plane of the „observed body“ (see [53, 28]). This solution seems not to be beneficial, due to the singularity in case of equatorial orbits, which is given by the undefined value for the right ascension of the ascending node. In the case of circular orbits, like a GEO, the argument of perigee as well is undefined. Additionally the measurements are in inertial coordinates, resulting in a nonlinear

and time-varying transformation, when casting the system in a Kalman-filter. Nevertheless, in the course of these studies, the use of Keplerian elements has been investigated. The idea to use this approach is based on the extremely slow variation of most of these parameters, with the *true anomaly* as the only exception. This results in the possibility of using a long filtering period and thus in a high accuracy of the LVLH-system. To eliminate the problems associated with the singularity of the *Right Ascension of the Ascending Node* (RAAN) when observing equatorial orbits, *Non Singular Keplerian Elements* (Equinoctial Elements) have been used. The appropriate elements then result as

$$\begin{array}{ll}
 a = a & : \text{ semi major axis,} \\
 h = e \cdot \sin(\omega + I \cdot \Omega) & \left. \vphantom{h} \right\} \text{ components of the eccentricity vector,} \\
 k = e \cdot \cos(\omega + I \cdot \Omega) & \left. \vphantom{k} \right\} \\
 p = \left[\tan\left(\frac{i}{2}\right) \right]^I \cdot \sin(\Omega) & \left. \vphantom{p} \right\} \text{ components of the ascending node vector,} \\
 q = \left[\tan\left(\frac{i}{2}\right) \right]^I \cdot \cos(\Omega) & \left. \vphantom{q} \right\} \\
 \lambda = M + \omega + I \cdot \Omega & : \text{ mean longitude.}
 \end{array}$$

In this notation I is the „retrograde“ factor, which is

$$I = \begin{cases} +1 : \text{ direct equinoctial elements,} \\ -1 : \text{ retrograde equinoctial elements.} \end{cases}$$

The use of the additional parameter I eliminates the singularity for $i = \pi$. The approach was made difficult by stability problems. One of the major problems is the bounded region of valid values for the eccentricity. This limited the choice of the state covariance-matrix, the process-noise covariance-matrix and the measurement-noise covariance-matrix. It might be of interest to pursue an approach using for instance „(over-)critical“ damping of the eccentricity to eliminate the necessity of a „bounding box“, which limits the region of valid values. Additionally, due to the use of a Keplerian orbit, the influence of the osculation in the Keplerian elements during an orbit is neglected. The resulting Kalman-filter was shown to settle slower than the alternative approach, which uses the satellites position and its velocity as states, yet approaching similar values in the overall accuracy. For further reference on the topic of high precision orbit propagation using Kepler elements be referred to [54].

Instead of using the Keplerian orbit representation, the approach presented is based on a Kalman-filter using the transition and propagation of the satellite’s position in the inertial reference frame. As mentioned before, the observation is already in inertial coordinates, facilitating this approach. The nature of the Kalman-filter allows the use of the knowledge about the system’s noise. Another advantage is inherent to this representation: the well known non-linear orbit models of higher precision, taking into account, among others, the influences of the triaxiality of the Earth and the

Table 5.1: Formulation of Kalman-Schmidt-filter

<u>System :</u>	
$\underline{x}_k = \underline{f}_{k-1}(\underline{x}_{k-1}) + \underline{w}_{k-1},$	$E(w_k) = \underline{Q}_k$
$\underline{z}_k = \underline{h}_k(\underline{x}_k) + \underline{v}_k,$	$E(v_k) = \underline{R}_k$
<u>Propagation of State and Measurement</u>	
$\hat{\underline{x}}_k^- = \underline{f}_{k-1}(\hat{\underline{x}}_{k-1}^+)$	
$\hat{\underline{z}}_k = \underline{h}_k(\hat{\underline{x}}_k^-)$	
<u>Linearization at operating point</u>	
$\underline{\Phi}_{k-1}^{[1]} \simeq \left. \frac{\partial \underline{f}_k}{\partial \underline{x}} \right _{\underline{x}=\hat{\underline{x}}_{k-1}^-}$	
$\underline{H}_k^{[1]} \simeq \left. \frac{\partial \underline{h}_k}{\partial \underline{x}} \right _{\underline{x}=\hat{\underline{x}}_k^-}$	
<u>Kalman-gain Update \underline{K}</u>	
$\underline{P}_k^- = \underline{\Phi}_{k-1}^{[1]} \cdot \underline{P}_{k-1} \cdot \underline{\Phi}_{k-1}^{[1]T} + \underline{Q}_{k-1}$	
$\underline{K}_k = \underline{P}_k^- \cdot \underline{H}_k^{[1]T} \cdot (\underline{H}_k^{[1]} \cdot \underline{P}_k^- \cdot \underline{H}_k^{[1]T} + \underline{R}_k)^{-1}$	
<u>Update of \underline{P} and $\hat{\underline{x}}$</u>	
$\underline{P}_k^+ = (\underline{I} - \underline{K}_k \cdot \underline{H}_k) \cdot \underline{P}_k^- \cdot (\underline{I} - \underline{K}_k \cdot \underline{H}_k)^T + \underline{K}_k \cdot \underline{R}_k \cdot \underline{K}_k^T$	
$\hat{\underline{x}}_k^+ = \hat{\underline{x}}_k^- + \underline{K}_k \cdot (\underline{z}_k - \hat{\underline{z}}_k).$	

gravity of the Sun and the Moon, can be included in the propagation step to further increase the system's accuracy.

The composition of the Kalman-filter for the current system requires two major steps: At first, the transition matrix $\underline{\Phi}$ needs to be found from the linearized function $\underline{f}(\underline{x})$, which relates the current state \underline{x}_k to the state to be expected at a later point in time (\underline{x}_{k+1}). In this context \underline{x} consists of the satellite's position and its velocity. The second step facilitates the possibility of not using any information about the satellite's distance from the Earth in the measurement \underline{z} . This results in the necessity to normalize the position of the satellite to a unit vector, which in turn leads to a nonlinear observation matrix \underline{H} , which is determined from the observation function $\underline{h}(\underline{x})$. In their union these changes lead to a so-called *Kalman-Schmidt-filter* with linearized dynamics and observations (see table 5.1 and [29]).

Step one

In the case of Kepler-motion the governing equation is merely dependent on the gravitational forces, leading to the differential equation

$$\ddot{\underline{r}} = -\mu \cdot \frac{\underline{r}}{(\underline{r}^T \underline{r})^{\frac{3}{2}}}. \quad (5.14)$$

Building the state vector \underline{x} from the position (\underline{r}) and the velocity (\underline{v}) results in a representation as

$$\dot{\underline{x}} = f(\underline{x}), \quad (5.15)$$

with

$$f(\underline{x}) = \begin{bmatrix} \underline{v} \\ \underline{\ddot{r}} \end{bmatrix}. \quad (5.16)$$

The linearization of $\underline{\ddot{r}}$

$$\underline{G} = \frac{\partial \underline{\ddot{r}}}{\partial \underline{r}}, \quad (5.17)$$

leads to

$$\underline{G} = \mu \cdot (\underline{r}^T \underline{r})^{-\frac{3}{2}} \cdot [I - 3(\underline{r} \underline{r}^T) \cdot (\underline{r}^T \underline{r})^{-1}]. \quad (5.18)$$

This matrix in turn can be used in

$$\Delta \dot{\underline{x}} = \begin{bmatrix} \underline{0} & \underline{I} \\ \underline{G} & \underline{0} \end{bmatrix} \cdot \Delta \underline{x}. \quad (5.19)$$

As in the Extended Kalman-Filter the system is linearized about the estimated state, the transition matrix needed is that for $\Delta \underline{x}$. For the system as presented, it is thus easier to develop $\Delta \underline{x}$ from the differential equation, than to actually determine $f(\underline{x})$ and the corresponding partial derivatives. In general the transition matrix ϕ , which transforms the state at time t (\underline{x}_{k-1}) to the state at time $t + \Delta t$ (\underline{x}_k), can be composed from the linear system with

$$\dot{\underline{x}} = A \underline{x} \quad (5.20)$$

as

$$\phi = \sum_{i=0}^{i=\infty} \left[\frac{1}{i!} A^i \cdot \Delta t^i \right] \quad (5.21)$$

where Δt is the time step. The linearized system is treated accordingly by appropriate substitution of A , leading to the linearized state transition matrix $\Phi_{k-1}^{[1]}$ as

$$\Phi_{k-1}^{[1]} = \sum_{i=0}^{i=3} \left[\frac{1}{i!} \begin{bmatrix} \underline{0} & \underline{I} \\ \underline{G} & \underline{0} \end{bmatrix}^i \cdot \Delta t^i \right], \quad (5.22)$$

resulting in

$$\Phi_{k-1}^{[1]} = \begin{bmatrix} \underline{I}_{3 \times 3} + \frac{\Delta t^2}{2} \cdot \underline{G} & \Delta t \cdot \underline{I}_{3 \times 3} + \frac{\Delta t^3}{6} \cdot \underline{G} \\ \Delta t \cdot \underline{G} + \frac{\Delta t^3}{6} \cdot \underline{G}^2 & \underline{I}_{3 \times 3} + \frac{\Delta t^2}{2} \cdot \underline{G} \end{bmatrix}. \quad (5.23)$$

In this case, the linearization was truncated to third order.

Step two

With x being defined as

$$x = \begin{bmatrix} \underline{r} \\ \underline{v} \end{bmatrix}, \quad (5.24)$$

the nonlinear observation is given as

$$\underline{z} = \frac{1}{|\underline{r}|} \cdot \underline{r}, \quad (5.25)$$

resulting in the linearized observation matrix as follows:

$$\begin{aligned} C &= [I_{3 \times 3}, \text{Zero}_{3 \times 3}] \\ r &= |C \cdot \hat{\underline{x}}_k^-| \\ H_{k, \text{nonlinear}} &= \frac{1}{r} \cdot C \\ H_{k, \text{linear}} &= \left. \frac{\delta \underline{z}}{\delta \underline{x}^T} \right|_{\underline{x}=\hat{\underline{x}}_k^-} \\ &= \left. \frac{\delta \frac{C \cdot \underline{x}}{[\underline{x}^T \cdot C^T C \cdot \underline{x}]^{\frac{1}{2}}}}{\delta \underline{x}^T} \right|_{\underline{x}=\hat{\underline{x}}_k^-} \\ &= \left. \frac{C \cdot r - C \cdot \underline{x} \cdot \frac{1}{2} r^{-1} \cdot 2 \underline{x}^T \cdot C^T C}{r^2} \right|_{\underline{x}=\hat{\underline{x}}_k^-} \\ &= \frac{1}{r} \cdot C \left(I_{6 \times 6} - \frac{\underline{x} \underline{x}^T \cdot C^T C}{r^2} \right) \Big|_{\underline{x}=\hat{\underline{x}}_k^-} \\ H_{k, \text{linear}} &= H_{k, \text{nonlinear}} \cdot \left(I_{6 \times 6} - \frac{1}{r^2} \hat{\underline{x}}_k^- \hat{\underline{x}}_k^{-T} \cdot C^T C \right). \end{aligned} \quad (5.27)$$

The filter will be initialized using either a position provided by the groundstation or a first approximation by the system itself in using the approximate distance derived from the apparent angular Earth-radius. To give an estimate of the initial accuracy: assuming an angular error of approx. 0.1° in the Earth-radius measurement results in an error of less than 2% in the estimated orbital radius. The state covariance-matrix (\underline{P}) is used to take this knowledge into account.

The process-noise covariance-matrix (\underline{Q}) as well as the measurement-noise covariance-matrix (\underline{R}) are fixed in this approach. It should be noted that the Star-sensor's covariance matrix is, in general, not constant, since it depends upon the distribution of Stars on the detector. Since the main driver for the decrease in accuracy, though, is the Earth-measurement, this dependency can be neglected in favor of a stable and well defined Kalman-filter. The process-noise can be explained as to take into account all effects which are not covered by the propagation, preferably those with an unbiased nature and a „white“ Gaussian noise.

The \underline{Q} -matrix is used to cover errors in the linearization, which are time dependent. In our case, with an Kalman-filter update rate of 1 Hz, the errors are taken to be better than the meter and millimeter/second range.

Since the \underline{R} -matrix covers the measurement noise, it is taken to be the geometric sum of Star- and Earth-sensor noise ($1/120^\circ$ and $1/10^\circ$, respectively). The resultant error is in the $1/10^\circ$ range and

assumed to be constant. The misalignment of the mirror is non-Gaussian in nature and therefore is calibrated prior to launch and not covered by the covariance matrix.

With these preliminaries, the Kalman-Schmidt-filter representation as shown in table 5.1 is chosen.

In the given system, the only nonlinear propagation is carried out to obtain the propagated state and the corresponding observation. All other propagations are carried out using the linear terms of the linearized transition matrix. In deriving the Kalman-gain (\underline{K}) by using finite differences, it can be shown that the constant parts of $\underline{H}_k^{[1]}$ are not used for its determination ([29]). This results in the sufficiency to express $\underline{H}_k^{[1]}$ using only the linear components. Using cartesian coordinates enables the explicit derivation of the linearized system, so no numerical differentiation is needed.

The Kalman-filter, as derived above, has been successfully used throughout the investigations and further improved to tolerate sensor outages, for instance during eclipse, when no Earth information is available, and during Sun intrusion, when no information can be extracted from the detector. In order to do so, the filter skips the update while still propagating the state and the state covariance. Additionally the information resulting from the system has been put to use in determining the spacecraft's attitude in the LVLH-system as defined in chpt. 2.

As additional feature, it is possible to include the estimated distance in the filter. This reduces the „nonlinearity“, in that part of the state becomes the observation, and thus eliminates the necessity of linearization. As mentioned previously, though, the determination of the Earth-cone angle is rather inaccurate: the cone angle accuracy is approximately equivalent to the accuracy of the Earth-vector determination, which is approx. 0.1° . This error results in an error in the distance determination by use of the Earth-radius. The inclusion of the distance information therefore might result in a noisier state, after the Kalman-filter has settled, but has the advantage of a much shorter settling time. Additionally it should be warned that the estimate might be biased due to cloud coverage and the dependency of the Earth-radius on the chosen initial threshold, when the image is searched for the Earth-horizon. If the use of the apparent Earth-radius is desired, it might be advantageous to include the measurement in form of a *Friedland*-filter (e.g. [55]). The best alternative, though, might be a combined method, using the distance information to reduce the settling time and then to switch to the raw vector-measurement to reduce the introduced noise and bias. A comparison of the different algorithms is shown in chpt. 6.2

Summarizing the results of this section, a successful algorithm for the position determination using the combined Earth- and Star-sensor has been established, using both, either pure vector measurements or measurements augmented by the information of the satellite's distance from the Earth. The orbit of the satellite can now be determined by use of straight-forward algorithms using the knowledge of position and velocity. Exemplary algorithms for Keplerian and Equinoctial Elements

are given in the Appendix A.1.3. The usefulness of these algorithms, however, is limited, as real orbits are time-varying, resulting in **osculating elements**, which either need to be expressed as a function of time, or by their mean value over a given orbit. Additionally it is possible to determine the satellite's LVLH-reference system, as shown in fig. 2.3, and its attitude within it by using the same results, namely position and velocity.

In general, it might be of interest to introduce an additional smoothing/low-pass filter prior to the determination of the satellite's position. This is due to the slow motion of the Earth-image in the FOV, resulting in the knowledge that high-frequency changes in the Earth-vector necessarily result from measurement errors.

5.2.2 Observability of the proposed system

With the formulation of the observation formula, which solves for the spacecraft's position, it is now necessary to determine its limitations. The investigations in this section will start with an observability analysis of the overall system in a Kalman-filter which does not use the information on the distance. This is essential, since the distance measurement introduces an error, which is not only large in comparison to the error of the vector measurements, but might be biased.

The system's observability has been demonstrated in the inertial system. The matrices in this case are more complicated and necessitate a linearization of the system along its operating point. The nonlinear observation matrix further complicates the analysis. It was shown, though, that, as expected due to the invariance of observability under reference-system rotations, the system is observable using a formulation in the so-called *Hill*-system (fig. 2.2).

In the Hill-systems only deviations of the spacecraft's position relative to a reference orbit are evaluated. This leads to a simpler formulation of the system's transition matrix. In combination with the appropriate observation matrix, this results in an analytical determination of the system's observability as well as the observability of misalignments.

Since the system determines the observability in a rotating reference system, the observation taken from the equation

$$\underline{r}_I = \underline{T}_{SI}^T \cdot \underline{T}_{SE} \cdot (-\underline{r}_E) \quad (5.4)$$

needs to be rotated accordingly. This is accomplished by introducing a further transformation matrix (\underline{T}_{HI}), rotating the spacecraft's inertial position into the Hill-system (\underline{r}_H).

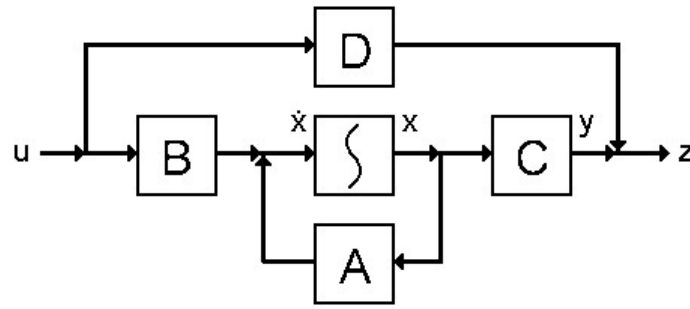


Figure 5.2: State Space Schematics of the Hill-System (defined by A and B) and the Corresponding Observation (defined by C and D)

The differential equations for the spacecraft's position in the Hill-system can be stated as follows:

$$\begin{bmatrix} \dot{\beta} \\ \dot{\beta} \\ \dot{\lambda} \\ \dot{\bar{z}} \\ \dot{\lambda} \\ \dot{\bar{z}} \end{bmatrix} = \begin{bmatrix} 0 & 1 & 0 & 0 & 0 & 0 \\ -\omega_0^2 & 0 & 0 & 0 & 0 & 0 \\ 0 & 0 & 0 & 0 & 1 & 0 \\ 0 & 0 & 0 & 0 & 0 & 1 \\ 0 & 0 & 0 & 0 & 0 & 2 \cdot \omega_0 \\ 0 & 0 & 0 & 3 \cdot \omega_0^2 & -2 \cdot \omega_0 & 0 \end{bmatrix} \cdot \begin{bmatrix} \beta \\ \dot{\beta} \\ \lambda \\ \bar{z} \\ \dot{\lambda} \\ \dot{\bar{z}} \end{bmatrix} + \begin{bmatrix} 0 & 0 & 0 \\ 1 & 0 & 0 \\ 0 & 0 & 0 \\ 0 & 0 & 0 \\ 0 & 1 & 0 \\ 0 & 0 & 1 \end{bmatrix} \cdot \begin{bmatrix} f_\beta \\ f_\lambda \\ f_{\bar{z}} \end{bmatrix}. \quad (5.28)$$

In this representation, the following definitions are put to use:

$$\begin{aligned} \beta &= -y_{Hill}/r \\ \lambda &= x_{Hill}/r \\ \bar{z} &= z_{Hill}/r, \end{aligned} \quad (5.29)$$

with r as the distance from the Earth-center to the satellite. f_β , f_λ and $f_{\bar{z}}$ are the errors introduced to the system by external forces which are not accounted for in the Hill-equation, such as the triaxiality of Earth, the atmosphere, the Solar pressure, the gravity of the Sun and the Moon, to name but a few. ω_0 is the orbital angular velocity of the satellite.

Rewriting these equations in the control system's state-space notation as visualized in fig. 5.2 results in:

$$\begin{aligned} \dot{x} &= A x + B u \\ y &= C x + D u \end{aligned} \quad (5.30)$$

and

$$\begin{aligned} x(t_0 + \Delta t) &= \underline{\Phi}(\Delta t) x(t_0) + \underline{\Psi}(\Delta t) u(t_0) \\ y(t) &= C x(t) + D u(t). \end{aligned} \quad (5.31)$$

In this notation, \underline{A} and \underline{B} are the matrices as defined in eq. (5.28), \underline{C} is the state-observation matrix and \underline{D} directly passes control inputs to the observation. In this case it is identical to „zero“, since the inputs do not have an immediate impact on the measurement.

The representation can be separated in the motion within (λ and \bar{z}) and transverse to (β) the orbit plane. This is implied by the decoupled formulation in those „subsystems“, when only taking first order terms into account. Using this formulation, a closed form solution can be obtained, which is then used for the determination of the linearized transition-matrix at each point of the orbit. In this formulation, $\underline{\Phi}$ from eq. (5.31) can be separated in $\underline{\Phi}_O$ and $\underline{\Phi}_I$, which denote the transition matrices of the „Out-Of-Plane-“ and the „In-Plane-“ motions, respectively. Accordingly, $\underline{\Psi}$ can be separated in $\underline{\Psi}_O$ and $\underline{\Psi}_I$, which are the transition matrices of the forces applied. The matrices are defined as the following:

$$\underline{\Phi}_O = \begin{bmatrix} \cos(\omega_0 t) & \frac{1}{\omega_0} \cdot \sin(\omega_0 t) \\ -\omega_0 \cdot \sin(\omega_0 t) & \cos(\omega_0 t) \end{bmatrix} \quad (5.32 a)$$

and

$$\underline{\Phi}_I = \begin{bmatrix} 1 & 6 \cdot [\omega_0 t - \sin(\omega_0 t)] & -\frac{1}{\omega_0^2} \cdot [3 \omega_0 t - 4 \cdot \sin(\omega_0 t)] & \frac{2}{\omega_0} [1 - \cos(\omega_0 t)] \\ 0 & 4 - 3 \cos(\omega_0 t) & -\frac{2}{\omega_0} \cdot [1 - \cos(\omega_0 t)] & \frac{1}{\omega_0} \cdot \sin(\omega_0 t) \\ 0 & 6 \omega_0 \cdot [1 - \cos(\omega_0 t)] & -3 + 4 \cdot \cos(\omega_0 t) & 2 \cdot \sin(\omega_0 t) \\ 0 & 3 \omega_0 \cdot \sin(\omega_0 t) & -2 \cdot \sin(\omega_0 t) & \cos(\omega_0 t) \end{bmatrix}. \quad (5.32 b)$$

Accordingly $\underline{\Psi}_O$ and $\underline{\Psi}_I$ result as

$$\underline{\Psi}_O = \begin{bmatrix} \frac{1}{\omega_0^2} \cdot [1 - \cos(\omega_0 t)] \\ \frac{1}{\omega_0} \cdot \sin(\omega_0 t) \end{bmatrix} \quad (5.33 a)$$

and

$$\underline{\Psi}_I = \begin{bmatrix} \frac{1}{\omega_0^2} \cdot [4 - 4 \cos(\omega_0 t) - \frac{3}{2} (\omega_0 t)^2] & \frac{2}{\omega_0^2} \cdot [\omega_0 t - \sin(\omega_0 t)] \\ -\frac{2}{\omega_0^2} \cdot [\omega_0 t - \sin(\omega_0 t)] & \frac{1}{\omega_0^2} \cdot [1 - \cos(\omega_0 t)] \\ \frac{1}{\omega_0} \cdot [4 \sin(\omega_0 t) - 3 \omega_0 t] & \frac{2}{\omega_0} \cdot [1 - \cos(\omega_0 t)] \\ -\frac{2}{\omega_0} \cdot [1 - \cos(\omega_0 t)] & \frac{1}{\omega_0} \cdot \sin(\omega_0 t) \end{bmatrix}. \quad (5.33 b)$$

The \underline{C} -matrix contains elements such that the resultant outputs correspond to λ and β . Those result from the transformation of the determined vector towards the satellite in polar coordinates. Having

the state vector \underline{x} as

$$x = \begin{bmatrix} \beta(t) \\ \dot{\beta}(t) \\ \lambda(t) \\ \bar{z}(t) \\ \dot{\lambda}(t) \\ \dot{\bar{z}}(t) \end{bmatrix}, \quad (5.34)$$

\underline{C} results from eq. (5.29) as

$$C = \begin{bmatrix} 0 & 0 & 1 & 0 & 0 & 0 \\ 1 & 0 & 0 & 0 & 0 & 0 \end{bmatrix}. \quad (5.35)$$

Using the derived formulation of the system, it is now possible to carry out an observability analysis. The observability condition results in

$$\text{rank} \left(\begin{bmatrix} C \\ C \cdot A \\ \vdots \\ C \cdot A^{(n-1)} \end{bmatrix} \right) \equiv n, \quad (5.36)$$

with n being the number of states. An analysis of the original system proved the algorithm's observability.

In the following, the system is augmented by constant misalignments along $\Delta\lambda$ and $\Delta\beta$, resulting in the following system:

$$\begin{aligned} \begin{bmatrix} \dot{x} \\ \Delta\dot{x} \end{bmatrix} &= \begin{bmatrix} A & \underline{\mathbf{0}} \\ \underline{\mathbf{0}} & \underline{\mathbf{0}} \end{bmatrix} \cdot \begin{bmatrix} x \\ \Delta x \end{bmatrix} + \begin{bmatrix} B & \underline{\mathbf{0}} \\ \underline{\mathbf{0}} & \underline{\mathbf{0}} \end{bmatrix} \cdot u \\ y &= C_{\Delta} \cdot \begin{bmatrix} x \\ \Delta x \end{bmatrix} + D \cdot u, \end{aligned} \quad (5.37)$$

with

$$\Delta x = \begin{bmatrix} \Delta\beta \\ \Delta\lambda \end{bmatrix}.$$

This leads to

$$C_{\Delta} = \begin{bmatrix} 0 & 0 & 1 & 0 & 0 & 0 & 0 & 1 \\ 1 & 0 & 0 & 0 & 0 & 0 & 1 & 0 \end{bmatrix}.$$

The analysis of these augmented systems showed that a constant misalignment in β can be observed. This does not hold for λ , though. A constant misalignment of the sensor resulting in a

mis-estimation of λ is treated as a shift along the satellite's orbit, which can not be detected with a first order system (see as well [8]).

The unobservability in λ necessitates a calibration of the system. This is preferably done during mission while having a known position. In the case of no such capabilities, a ground calibration can be carried out.

5.2.3 Initial estimate of the expected accuracy

An estimate on the accuracy to be expected from the filtering process is difficult to assess prior to simulations and highly depends upon the choice of the parameters set in the \underline{P} , \underline{Q} and \underline{R} matrix. Regardless of the exact value, though, the accuracy can be assumed to increase by at least a factor of 10, resulting in an angular error which is in the order of 0.01° and a resulting 3D-error, which in the case of a GEO is in the order of 7 km. A better estimate will be the result of simulations, as presented in chpt. 6.2.

Chapter 6

Evaluation of the Algorithms on Determination of Position and Orbit

6.1 Simulations on the Position Determination Using the Combined Earth-/Star-Sensor

Using the results obtained in chpt. 5.1.2, numerical simulations confirmed that the maximal error which occurs in the position determination, is the sum of the maximal variance in the attitude, as determined from the Star-image, and the variance of the Earth-vector. For the simulations as presented, the input of the Earth-vector and the attitude matrix was artificially disturbed by noise, which was added to the two systems according to their expected accuracy. Assuming a constant Earth-vector and a varying attitude matrix, the result of a simulation for the accuracy of the satellite's position in the x -axis (ECI) is shown in fig. 6.2. The sphere can be thought of as the celestial sphere, which in turn sets the basis for the simulation of the attitude. The Star-sensor's

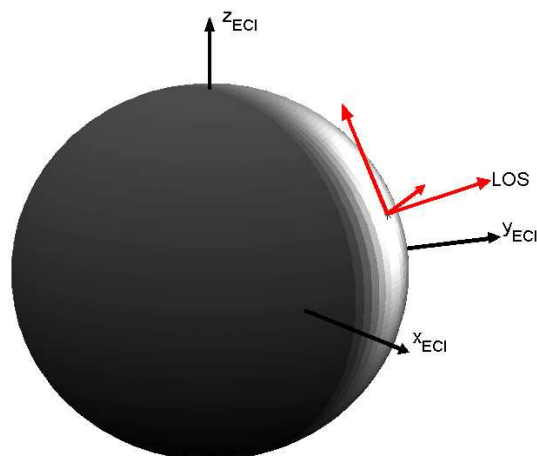


Figure 6.1: Construction of the Star-sensor coordinate system for simulations

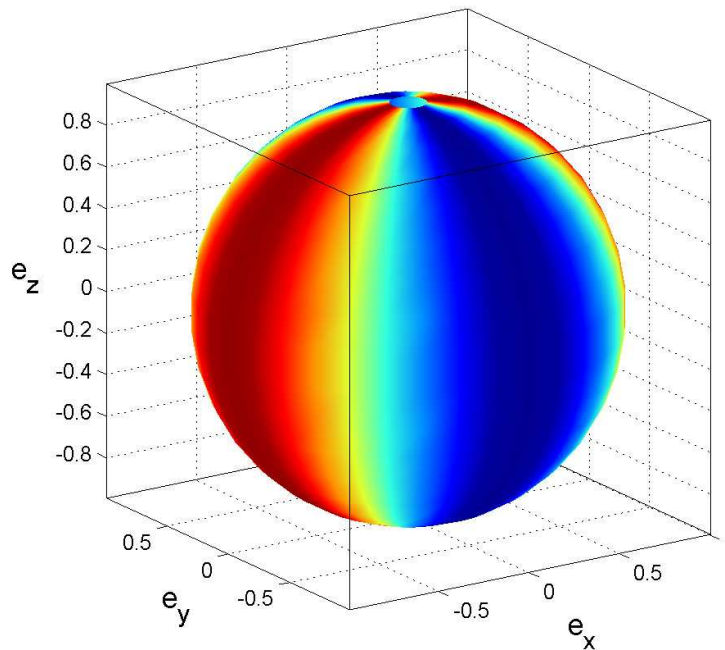


Figure 6.2: x -Position Accuracy of the satellite in the ECI reference system, for varying attitudes. The red-colored areas are areas of low accuracy, the blue areas those of high accuracy. e_x , e_y and e_z are the components of the Star-sensor's LOS-vector.

coordinate system is defined as shown in fig. 6.1.

For the simulation, it is assumed that the Star-sensor's line-of-sight points away from the Earth, which is assumed to be in the center of the sphere. The second axis is tangential to the sphere and in the plane defined by the position-vector and the z -axis of the ECI-reference system. The last axis completes the right-hand coordinate system. The Star-sensor's line-of-sight was then moved, spiraling over the sphere in 411 steps. In the graphic shown in fig. 6.2, the Earth was assumed to be in the center of the FOV. The accuracies were chosen according to the results given in the previous chapters. The effect of interest, though, is independent of the chosen accuracies and will be explained in more detail. The red-colored areas are areas of low accuracy, the blue areas those of high accuracy. It can be seen that the accuracy is dependent on the area in which the line-of-sight is located. In general, the accuracy is dependent on the attitude matrix and the Earth-vector, as obvious from equations (5.12) and (5.13).

The variability of the accuracy is due to the fact that only the accuracy of the position's x -component is shown. When adding up the variances of all three components, the difference is negligible (1×10^{-6} rad). This behavior is expected and confirmed by the linear part of equations

(5.12) and (5.13). It should be noted, though, that the error in one axis varies only by the difference in the Star-sensor's variances. Since this variation is by orders of magnitude smaller, than the error introduced by the Earth-sensor, it is a valid assumption to take the maximal experienced error as the total error. This result shows that the mounting of the sensor is not limited by the demands on the overall accuracy and thus can be chosen to satisfy other mission requirements.

6.2 Simulations on Orbit Determination from Sequential Position Measurements

This section will introduce the methods used in the nonlinear simulation of the orbit and the Earth- and Star-vectors, as they are later used for tests of the orbit determination algorithm using the combined Earth- and Star-sensor.

For the simulation of the satellite's orbit the following forces are accounted for:

1. Triaxiality of Earth up to 2^{nd} order zonal , 3^{rd} order tesseral
2. Atmosphere
3. Solar pressure
4. Sun
5. Moon

For an overview on possible sources of perturbations and their dependance on the orbit height be referred to the Appendix A.4.2. The propagation is incorporated in the developed Extended Kalman-Filter, using a fourth order Runge-Kutta algorithm. The orbit propagator was implemented under Matlab in a project on „high precision orbit propagation“ at EADS Astrium GmbH, Germany ([56], based on [28]).

The orientation of the coordinate systems involved, in particular the Earth-sensor system and the Star-sensor system and the mounting were chosen to be compliant to the MITA-experiment ([9]). Since the Stars are mirrored onto the detector by means of a beam-splitter, their position on the detector is not obtained by a pure rotation, but in addition needs to account for the reflection on the partially transmissive mirror, leading to a determinant of -1 in the transformation matrix. For a LEO, as used by MITA, and having the camera's effective FOV of about 17° , in a true Earth-pointing orientation the complete FOV would be covered by the Earth, leaving no available space for Star observation. Therefore, the sensor was mounted in an angle of 71° rotated off Earth orientation towards flight direction. This resulted in a tangential view of the Earth horizon in

approximately the center of the FOV, as seen for instance in fig. 3.28. To enhance the simulation capabilities, it is furthermore possible to include attitude motion of the simulated satellite.

The calculation of the simulated measurement data is performed by transforming the inertially known direction towards Earth and the applicable Star-vectors into the sensor's coordinate system. The directions, as perceived by the sensor, are then transformed into their images on the detector. These sets of data are disturbed by superimposing Gaussian noise and then fed to the algorithms for attitude and position determination. This sets the basis for the evaluation of the algorithms developed in the frame of this thesis. Algorithms tested are the Star-identification, the attitude determination and the consecutive position determination. This position is then fed into several Kalman-filters displaying different features. The first distinction to be made is that of the „normalized“ Kalman-filter, which works with unit-vectors of the satellite's position, to that of the „real“ Kalman-filter, working with the true position. The second distinction is the feature to outlast sensor outages. In order to simulate failures, it is simply necessary to set the input to „zero“. This is in particular done for the cases, when the Earth-sensor can not detect the Earth, due to adverse lighting conditions, where either the Sun is in the FOV, which as well averts Star-measurements and thus attitude determination, or when the Sun is behind the Earth, such that no horizon can be seen.

A comparison of the different algorithms, based on a geostationary orbit, is shown below. The systems compared are:

1. **with** / **without** distance information (fig. 6.3)
2. **with** / **without** sensor outage (fig. 6.4)
3. **with** / **without** high precision orbit propagation (without: Keplerian orbit) (fig. 6.5).

In the plots given, **green** and solid will refer to „with“, **red** and dotted to „without“. The outage times, if applicable, are given in **blue** and can easily be distinguished due to their step shape. The criterion under investigation is the accuracy of the orbit radius, which in case of no employment of the apparent Earth-diameter is the most critical parameter. It was shown during the simulations that the $3D$ -error is approximately equal to the error in the orbit radius, making the criterion even more valuable.

It can be readily seen in fig. 6.3 that the inclusion of the distance reduces the settling time. The total accuracy, though, is comparable. In the period between 200 000sec to 300 000sec the mean and standard deviation as compared to the simulation compare as 144 m : 548 m and 222 m : 1539 m, respectively, with the values being the results in the form *with radius information* : *without radius information*. In the period between 300 000sec to 350 000sec the mean and standard deviation

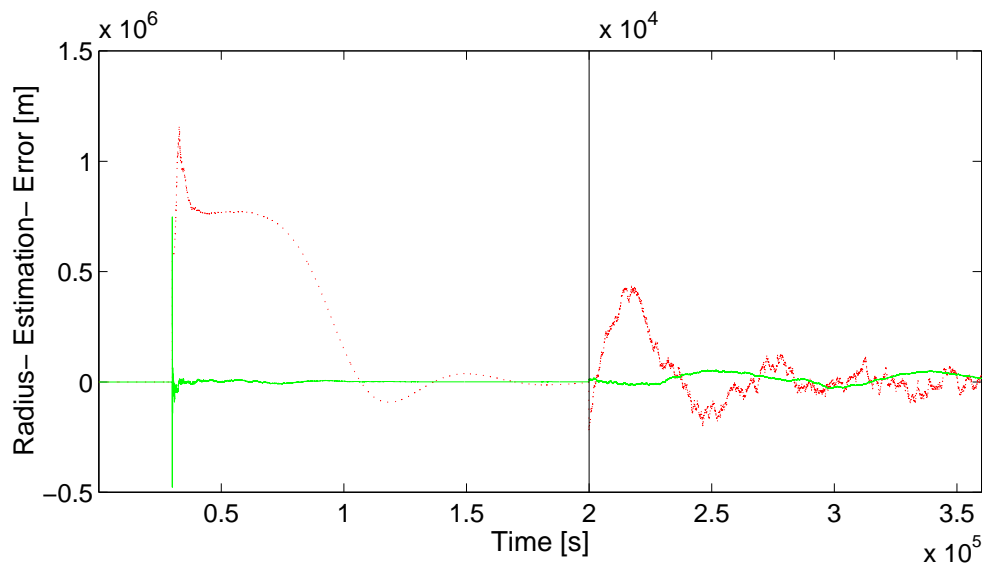


Figure 6.3: Comparison of error in the orbit radius determination with (green,solid) to without (red,dotted) distance information (GEO, orbit duration 86164 sec)

as compared to the simulation compare as 184 m : -18 m and 253 m : 400 m, respectively. The conclusion to be drawn is that, while the inclusion of the Earth-diameter is of interest with regard to settling time, it is not necessarily needed for successful position and orbit determination. This represents a simplification in the algorithms: As mentioned previously, the determination of the Earth-diameter might be biased. Excluding it from the orbit determination relieves the algorithm from accounting for this uncertainty.

The simulation of sensor outages resulted in nearly no degradation of the system's performance, which primarily proves that the propagation during sensor outages is highly accurate (see fig. 6.4). In the period between 200 000 sec to 300 000 sec the mean and standard deviation as compared to the simulation compare as 156 m : 144 m and 268 m : 222 m, respectively, with the values being the results in the form *with outage* : *without outage*. This encourages the use of this system for position and orbit determination, in proving its reliability during outage times. The reason for the outage time of approx. 75 min is given by Sun-presence in the sensor's FOV.

The comparison of the high precision orbit propagation to the Keplerian orbit, as given in fig. 6.5, shows nearly no degradation in accuracy, leading to the conclusion that the low precision algorithms, which yield a lower load on the on-board computer, are sufficient. In this nomenclature „high precision“ includes disturbing forces of the Sun, the Moon, the Earth's triaxiality, solar pressure and atmospheric drag (which, of course, is not present in GEO). The different parts in the Earth's triaxiality are different levels of accuracy, including different orders of higher (spherical)

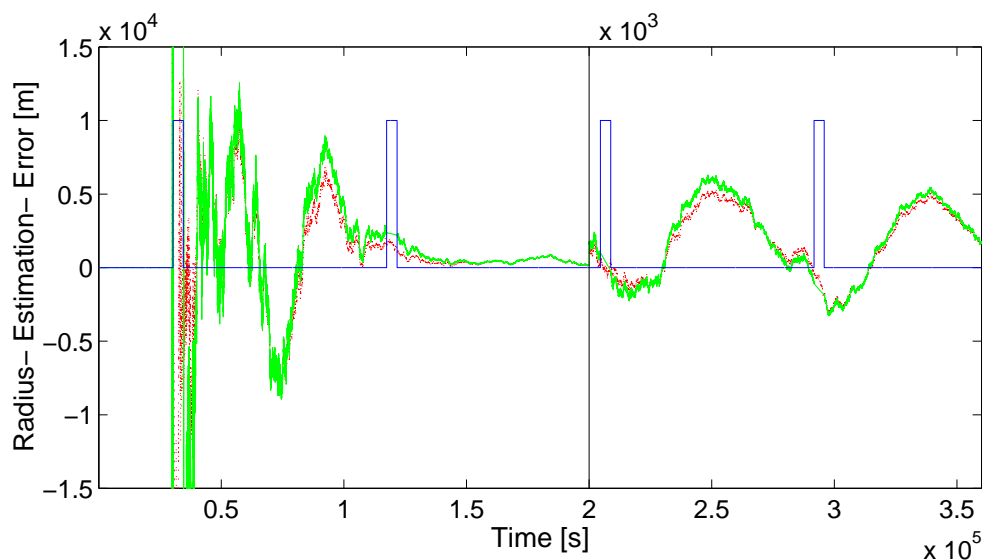


Figure 6.4: Comparison of error in the orbit radius determination with (green,solid) to without (red,dotted) sensor outage (blue, step function, duration approx. 75 min) (GEO, orbit duration 86164 sec)

harmonics to model the true gravitational field. For a point mass, so a spherical, homogenous Earth, the only non-zero component would be called „J1“, a simple rotational ellipsoid would as well include „J2“. In the period between 200000sec to 300000sec the mean and standard deviation as compared to the simulation compare as 156m : -170m and 268m : 410m, respectively, with the values being the results in the form *high precision orbit propagation* : *Keplerian orbit propagation*. It should be noted that, while the difference in the propagated position to the true position is in the order of 100m after one completed geostationary orbit, the main difference in the propagation is not to be expected after a complete orbit, but during this orbit, due to oscillatory effects. Therefore, in order to cover longer outages, the high precision orbit propagation should still be considered.

The image processing algorithms have been tested on experimental data obtained from in-orbit flight experiments, laboratory and field experiments. This is in particular the Star-detection and centroiding, the Earth-horizon detection, and the Earth-vector determination. The results will be shown in detail in chpt. 7.

The same Kalman-filter, with no changes in structure and covariances, proved to be stable from LEO to GEO, including inclined orbits. When dealing with highly eccentric orbits, the problem is not in the algorithms, but in the optical system, which might require the satellite to change its pointing direction. In the case of not using any distance information, a sensitivity analysis has been carried out, which confirmed that the filter is stable for a wide range of false initializations. In the

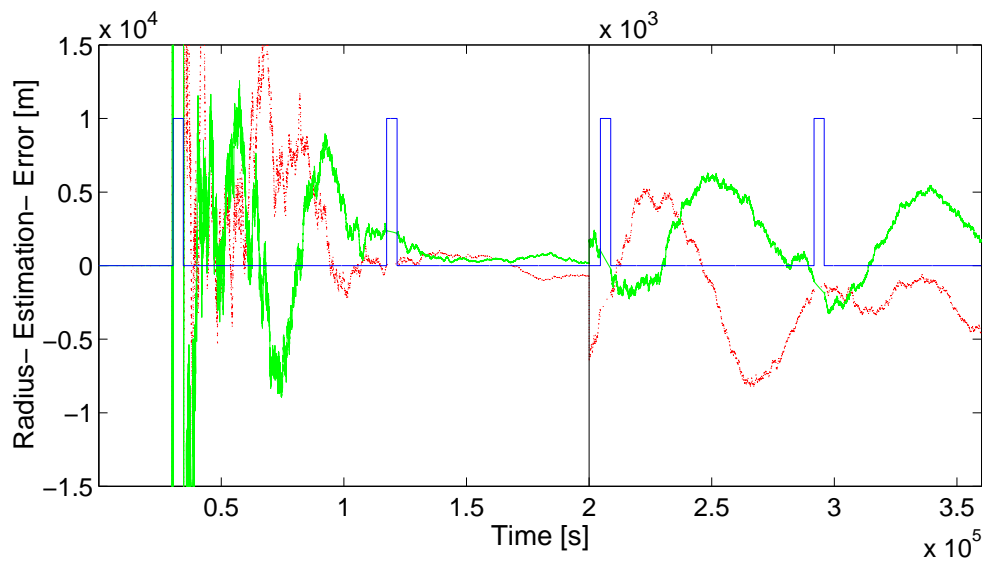


Figure 6.5: Comparison of error in the orbit radius determination with (green, solid) to without (red, dotted) high precision orbit propagation, both with sensor outage (blue, step function, duration approx. 75 min) (GEO, orbit duration 86164 sec)

example of a GEO, this holds for all initial orbit radii from 1 Earth radius to 100 Earth radii. This might indicate that a further optimization of the Kalman-filter in terms of steady-state accuracy can be performed, at the loss of universality and tolerance to initialization errors.

Chapter 7

Experimental Validation of the Developed Algorithms

The purpose of the experimental part is to test the performance of the proposed sensor suite in combination with the developed algorithms concerning the image processing, the Star-identification and the determination of the Earth-center. Data from the MTS-AOMS experiment provide an authentic experimental basis for the evaluation, representing the only flight data of such a system available to date. However, due to the fact that the sensor development was not the main purpose of this experimental satellite, a number of additional experimental data had to be obtained for a thorough analysis of the system performance. For this purpose, essential sensor components were assembled to allow for laboratory and field experiments under well controlled conditions. In addition, data-sets from another satellite equipped with an optical sensor were used. The following chapter summarizes the experimental sources exploited in the course of the project, explaining their setup and purpose, and ends with a presentation of the results obtained. In general, the structure is organized in starting with the in-orbit experiment flown on MITA, which are followed by the laboratory experiments, and concluded by field experiments. The set of data is complimented by images obtained from the regular METEOSAT operation.

7.1 Experiments - Sources

7.1.1 MITA Satellite Experiments

7.1.1.1 Experiment Environment

A key experiment to the verification of the sensor's feasibility was carried out as part of ESA's *Technology Flight Opportunity* (TFO)-program: the flight experiment on the Italian micro-satellite

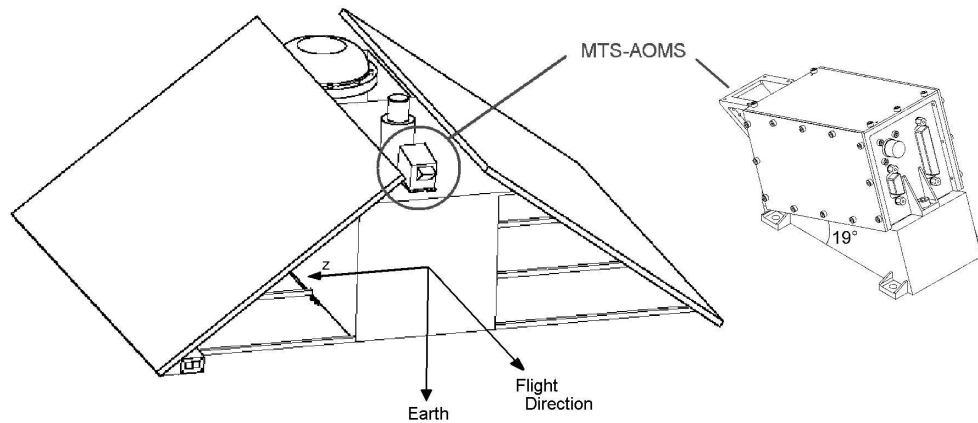


Figure 7.1: Schematics of Italian micro-satellite MITA (*Minisatellite Italiano a Tecnologia Avanzata*) with Flight Experiment MTS-AOMS; Orbit: 450km, 87.3° (nearly Sun-synchronous [SSO])

MITA (fig. 7.1). The satellite was placed on a nearly Sun-synchronous orbit with an inclination of 87.3° at an altitude of approx. 450km. Essential data of the MITA satellite are shown in table 7.1.

The flight experiment uses a common optics for Earth- and Star-observation. The desired different LOS were achieved by use of a partially transmissive mirror. The mirror, which consisted of a coated gray-filter, attenuated the brightness of the Earth by a factor of 4000, while maintaining 91% of the Star-intensity. The overall intensity difference between the fully illuminated Earth and

Table 7.1: Technical Data of Flight-Experiment Platform

Satellite	MITA, Fuchs-Group
Dimensions (w/o Solar-Panel)	$1800 \times 1400 \times 700 \text{ mm}^3$
Mass	170 kg
Power	70 W, avg.
Attitude Control	3-axes-stabilized, $\pm 1^\circ$ accuracy
Orbit	LEO: 450 km nearly circular ($421 \times 476 \text{ km}$) 87.3° Inclination
In-Orbit Time	Begin of Mission: 15.07.2000 End of Mission: 15.08.2001

Stars is about 50000, leaving the Earth as the brighter object. In case the Earth is observed at night, the constant attenuation results in too low an Earth signal, leading to the idea of an adaptive attenuation.

Since the MITA platform was placed in LEO, an Earth-pointing orientation of the camera system would lead to a FOV completely covered by the Earth. As this would result in the inability of determining the horizon as well as observing Stars, the sensor is mounted such that it tangentially observes the horizon in flight direction, having the Earth covering approx. $1/3^{rd}$ of the $12.7^\circ \times 17.2^\circ$ FOV. Using a mounting as depicted in fig. 7.1, a simultaneous view on the Earth and Stars was achieved. For redundancy, accuracy and functional test, the sensor was augmented with a fluxgate sensor for determination of the local magnetic field by the *Fraunhofer Institute of Microelectronic Circuits and Systems* (FHG-IMS), Dresden, and an angular rate sensor (ARS) by the Robert Bosch GmbH, Stuttgart, based on *Micro Electro Mechanical System* (MEMS) technology. The ARS used in the MTS-AOMS is a commercial device developed for the dynamic control system in cars.

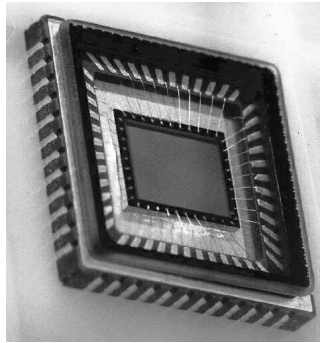
7.1.1.1.1 Active Pixel Sensor In the sensor as flown, the optically sensing device was an APS-detector. The APS-technology differs from CCD-technology, in that they are processed in a CMOS-process and include the charge-to-voltage converter as well as the analog-to-digital converter on each pixel, which can be addressed and read-out directly. The main advantage in the proposed setup, though, is their high resistance against cross-talk between neighboring pixels. This allowed for the sensor's functionality of observing dim objects in the proximity of very bright ones. The feature as well inhibits the saturation of the whole detector, when observing bright objects. It should be noted, though, that this does not effect the influences of the optics being used, such as reflections on optical surfaces, which might lead to ghost-images and blur.

The specific detector used is the IBIS1 by IMEC, Leuven (Belgium), the technical data of which is given in table 7.2. At the time of the experiment, it represented the „State of the Art“ Active Pixel Sensor.

The detector's photosensitive area is $6.5 \times 5.3 \text{ mm}^2$, consisting of 386×290 quadratic pixels with $14 \mu\text{m}$ sides. The fillfactor resulted as 72 %. The electronics allowed for exposure times of 30 ms, 100 ms, 400 ms and 1600 ms.

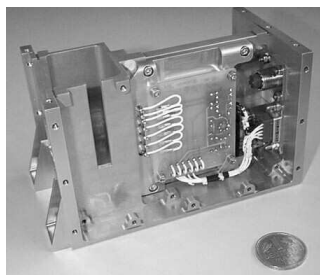
7.1.1.1.2 System The overall parameters of the sensor suite, as it was flown on the Italian MITA platform are given in table 7.3.

Table 7.2: Technical Data of Active Pixel Sensor



Sensor	IBIS1, IMEC
Size	$6.5 \times 5.3 \text{ mm}^2$
No. of Pixels	386×290
Pixel size	$14 \times 14 \mu\text{m}^2$
Power	2.1 W, max
A/D	10 bit
Exposure Times [RMS]	30 ms, 100 ms, 400 ms, 1600 ms
Sensitivity	5 mV (min. visual magnitude)
Accuracy (Centroid)	approx. 0.005° (16 ")

Table 7.3: Technical Data of the MTS-AOMS System



Sensor	MTS-AOMS, Astrium
Size	$172 \times 78 \times 90 \text{ mm}^3$
Mass	1200 g
Power	980 mW
S/C Interface	12 bit parallel (Image Data) 0...5 V (DRS, FGS)
Temperature Range	$-40^\circ\text{C} \dots +60^\circ\text{C}$
Vibration Environment [RMS]	16.2 g
Radiation Tolerance	2.2 krad (Si) over 3 Years

7.1.1.2 Data provided by the MITA mission

Data from the MTS-AOMS experiment, as shown in figures 7.6 and 7.13 was obtained from July 2000 to March 2001. In July 2001 the satellite re-entered into the atmosphere, due to the low orbit and an unfavorable orientation of the solar panels, which increased the atmospheric drag. This orientation was necessary for the main mission of the unit (Nina-2), which was developed for the observation of solar and galactic cosmic rays. This orientation caused a limitation in the data obtained from the MTS-AOMS, as it used a different data-bus, which was not designed to transmit the experiment's data. 174 images delivered by the sensor were transmitted during the mission. Due to memory restrictions, only four consecutive images were stored between ground station contacts, thus preventing the verification of the orbit determination algorithms. Data from the secondary sensors (Magnetic Field Sensor and ARS) were not acquired simultaneously with this data. Data of the secondary sensors was gathered at four times, two of which comprised complete orbits (approx. 5900 sec.), with a data rate of 0.5 Hz for the first 200 seconds and each 30 seconds thereafter. The position of the satellite in the orbit can be recalculated with high accuracy from the flight data and the time information. This, however, is not true for the recapture of the orientation of the satellite at a given time, due to the scarce information flow from the secondary sensors. A full characterization of the reliability of position and attitude determination was therefore not possible from these data alone.

7.1.2 Laboratory Experiments with a Complete Sensor Suite

7.1.2.1 Experiment Setup

In the laboratory experiment a test environment for a sensor as proposed in the patent on the „Combined Earth-/Star-Sensor“ ([1]) was set-up and operated. The main purpose of the laboratory experiment is the functional test of the system and the suite of algorithms developed in the scope of this thesis. The overall arrangement can be seen in fig. 7.2. In order to provide a simulated Earth- and Star-environment, the Opto-Electrical-Star-Simulator (OESS) is complemented with a sphere for Earth simulation. The sensor suite for the laboratory setup, in functionality identical to the flight experiment on MITA, comprises of a partially transmissive mirror combining the two lines of sight, and the APS detector. The beamsplitter provides a ratio of 70/30 between transmitted to reflected intensities. This ratio differs significantly from the beam splitter in place for the real system (approx. 9/91). In this sense the setup shown is slightly different from the MTS-AOMS, in which the Stars were mirrored and the Earth was seen with a highly reduced intensity.



Figure 7.2: Laboratory setup as assembled and used for functional tests

The detector was an APS-camera by PixeLink, using the PCS-2112 APS detector, with an improved performance compared to the camera used in the MTS-AOMS setup. Detailed technical data are given in the appendix in table A.11.

Special care was taken to create a somewhat realistic view of the „Earth“. For this purpose, a sphere with a diameter of 30 cm is illuminated by a light source which has an exit-diameter slightly larger than the sphere itself. This geometry is close to the realistic lighting conditions by the Sun. Different levels of brightness can be chosen by using combinations of different light-bulbs. Since the light source can be moved relative to the sphere, several lighting conditions can be simulated.

The OESS was previously used for functional tests of Star-sensors. It provides a 4° FOV. Within the FOV, up to 10 Stars with individual visual magnitudes as well as an artificial background-noise can be commanded. The 4° FOV limits its possibilities in the simulations carried out, as it does not take full advantage of the large FOV provided by the camera. They are sufficient for functional tests, though, which were intended for this setup. Specific details can be found in references [57, 58].

A new simulation software was developed rather than using the provided OESS user-interface, while using the same control-software. The user-interface of the simulation software can be seen in fig. 7.3. A feature, which has been included in the simulation software, is the rotation of the Star-field with a specified rotation rate, simulating a rotation of the satellite. In addition to this,

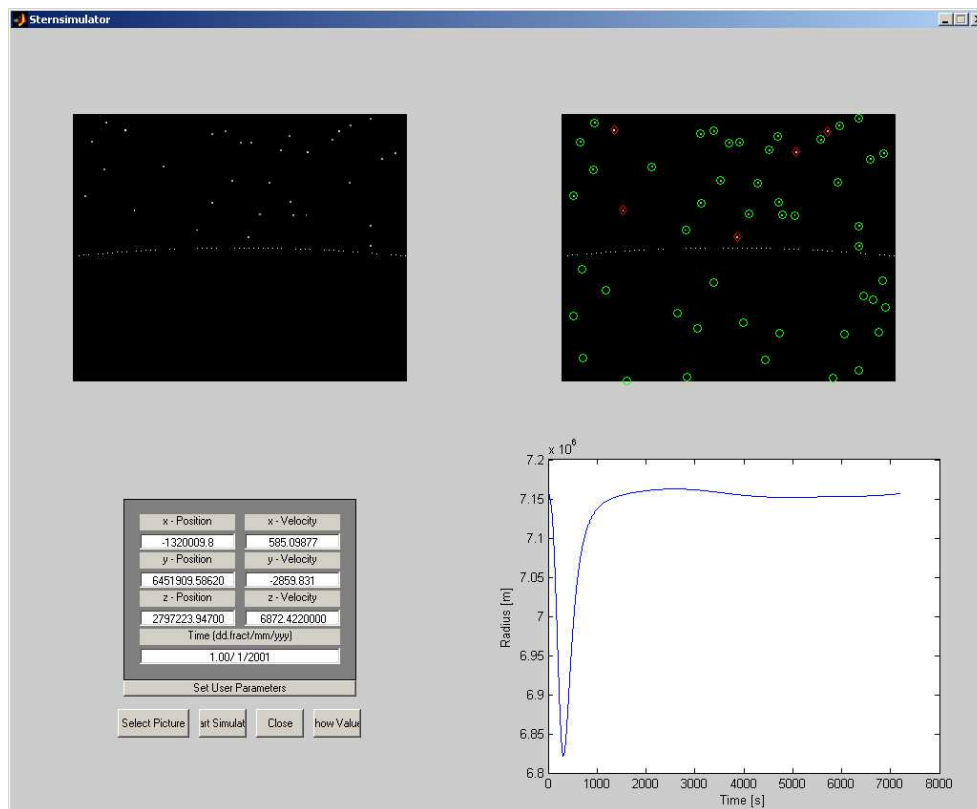


Figure 7.3: Graphical User Interface of Simulation-Software

the user can freely choose the orbit, the satellite's orientation and various other parameters by using the panels in the lower left. The software package also includes an on-line image acquisition and analysis of the frames acquired by the sensor package. The image corresponding to this input is shown in the upper left. The extracted Stars as well as the Earth-horizon calculated from the camera data are shown in the upper right. Parameters obtained from the image analysis, e.g. the distance from the Earth-center, as determined by the Kalman-filter, are displayed in the lower right. The only limitation is that the Earth-image is given by the hardware position of the sphere. This Earth-vector has to be determined prior to - and used as an input for - the simulation. The same software can as well be used to work with images gathered by in-orbit experiments. A closer explanation on the capabilities of the simulation environment is given in the appendix, A.2.1.

7.1.2.2 Data provided by the laboratory experiment

The laboratory experiment primarily was intended to provide sensor image data together with the input data of the Star-field simulation. In this way the position and orientation of the satellite is given in an absolute way, allowing for an analysis of the accuracy of the position data obtained by the image processing and the position and orbit determination algorithms. The system was used to

produce sets of data throughout the simulated orbit of the satellite. A drawback of the laboratory setup is the not really realistic view of the Earth, which is over-idealistically simulated by the sphere. Effects of shape deviation from a perfect sphere and, even more difficult to simulate, of clouds and other deteriorations from a perfect horizon are neglected. Besides this, the simulation process might omit complications due to non-listed Stars and other irregularities, which show up only in real images. Also, the effect of smear of the Star-images at higher rotation speeds of the satellite is not adequately reproduced. Another limitation consisted in the small FOV given by the OESS. These issues, however, were treated using real images taking in field experiments and from METEOSAT data (see chapters 7.2.1 and 7.2.2).

7.1.3 Field Experiments

7.1.3.1 Experiment Setup

The **field experiments** can be divided into two sets of experiments: The first consisted of an APS-detector based camera by FillFactory (IBIS4b, which is a successor of the IBIS1 as flown on the in-orbit experiment), the technical data of which can be found in the Appendix in table A.10. A standard 4-lense objective, as given in fig 3.6, was used. The experimental setup is shown in the left hand part of 7.4. In addition experiments with a second detector using the Pixelink-camera were performed. The experiments were carried out on the Maxlrainer Alm in the Bavarian Alps (right



Figure 7.4: Setup in the Bavarian Alps for verification of the Star-identification algorithm

hand part of the Figure). In this environment the amount of stray light is very low. Nevertheless, a light baffle had to be used around the camera to reduce the noise level. This was particularly necessary to allow for higher exposure times that show the effect of the rotation of the Earth in form of Star-traces on the image. In fact, different images taken in a well-determined time interval had to be used to simulate this effect.

7.1.3.2 Data provided by the field experiment

The field experiments were used to provide real-sky data of known regions for tests of the Star-detection-, the Centroiding- and the Star-identification-algorithms. Image series and combined images to artificially produce Star-traces further allowed for tests concerning the LARM and HARM tracking modes. A Star-image taken by the IBIS4b-camera is given in fig. 7.8. A combined image to simulate the trace of Stars, taken by the PixeLink camera, can be seen in fig. 7.11.

A further source has been put to use: pictures taken by a ground-based telescope using a 35 mm camera (Provided by amateur astronomer Martin Closs). The system's focal-length summed up to 75 mm, the original image size was $41.4 \times 54.8 \text{ mm}^2$, resulting in $2608 \times 3456 \text{ pixels}^2$ using a 1600dpi-scan.

7.1.4 METEOSAT Data

7.1.4.1 Experiment Environment

In addition to these data a set of images provided by Eumetsat, captured by the GEO weather-satellite METEOSAT (see fig. 7.5) were used. Unlike the MITA satellite, the orientation of the METEOSAT is not 3-axes-stabilized. The satellite is spin-stabilized, rotating about its axis of largest moment of inertia. Scanning from east to west thus is achieved through the spin of the satellite. Scanning from south to north is achieved by small incremental steps in the pointing of the telescope. At each satellite rotation during the imaging process, the spin clock delivers a signal to the scanning motor electronics, which has the effect of rotating the telescope through an angle of $1.25 \cdot 10^{-4}$ radians (nearly $26''$).

7.1.4.2 Data provided by METEOSAT

The *Meteosat Visible and InfraRed Imager* (MVIRI) is a high resolution radiometer with three spectral bands. With a mass of nearly 63 kg and a total height of 1.35 m, it constitutes the main

payload of Meteosat. It provides the basic data of the Meteosat system, in the form of radiances from the visible and infrared parts of the electromagnetic spectrum. The radiation is gathered by a reflecting telescope with a primary mirror diameter of 400 mm. The instrument allows continuous imaging of the Earth, with radiance data from the full Earth disc being acquired during a 25 minute period. This is followed by a five minute retrace and stabilization interval, so that one complete set of full Earth disc images is available every half hour. The data needed to be adapted in order to make the uncorrected pixel values usable. Since the images are sampled by two pixels, which are not exactly lined up, every second line was shifted with respect to the immediately adjacent line ([59, 60]). In order to eliminate this effect without the need for a sub-pixel shift of one of these lines, and since the image had a by far higher resolution than those of the camera used in the flight and laboratory experiments, every second line, and correspondingly every second column, to maintain a square image, was eliminated. An image with the corresponding Earth-center, as determined by the developed algorithms will be presented in fig. 7.15.

7.2 Experiments - Results

7.2.1 Experiments on Star-Measurements

This chapter will introduce the experiments carried out and evaluated on behalf of the Star-related algorithms and discuss the results obtained. The main features of the system under investigation is its large FOV, combined with a low quality lense-system. The chapter will start with the in-orbit experiments on MITA ([9]) which proved the system's feasibility and showed the wide range in centroiding accuracy accepted by the Star-identification algorithm, followed by experiments car-

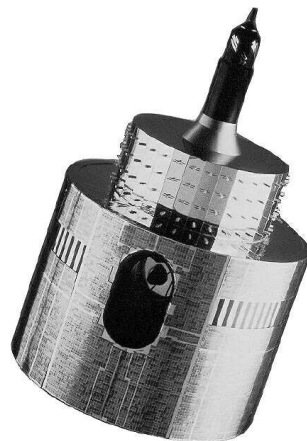


Figure 7.5: Eumetsat's geostationary weather-satellite METEOSAT

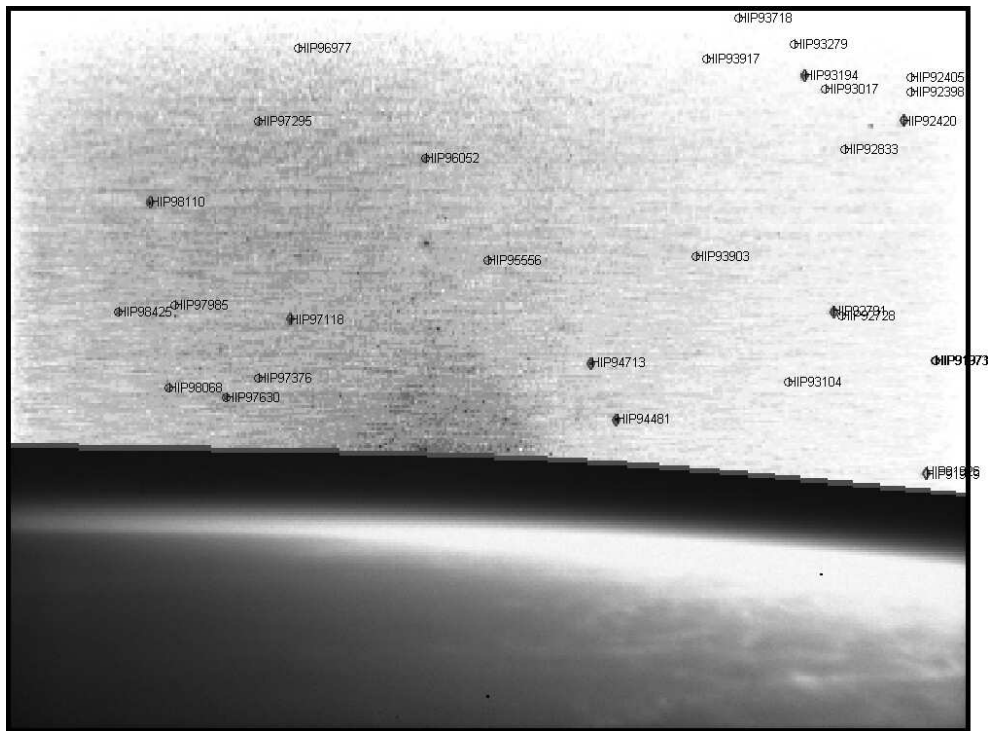


Figure 7.6: Image obtained using the FillFactory IBIS1 APS-detector Camera

ried out in the laboratory, performed to prove the concept and will close with the field experiments, verifying the Star-identification and the expected Star-intensity limits.

7.2.1.1 Tests using Experimental Data from MITA

The image shown in fig. 7.6 was taken during the flight experiment on MITA. For reasons of visibility, it has been split in two parts: the upper part has been inverted and enhanced in brightness and contrast to have a better view of the Star-background. The lower part is the image as it would be seen without any changes. In order to be able to correctly identify the Stars using an uncorrected optics, the tolerance had to be set to $240''$, proving, the enhanced capabilities of the Star-identification algorithm. The determined Star-identifications are superimposed on the image seen in fig. 7.6. The diamonds denote the Stars which were used for the identification process. The circles denote the Star-locations as expected for the attitude determined using the identification and using an ideal optical system for imaging. The presence of errors in the real optical system thus explains the difference in the observed and expected positions. The attitude as determined by the image compares well with the nominal satellite attitude to within 1° . A precise determination of the attitude accuracy was not possible due to the low requirements ($\pm 1^\circ$) set for the MITA satellite and the absence of a precise reference attitude.

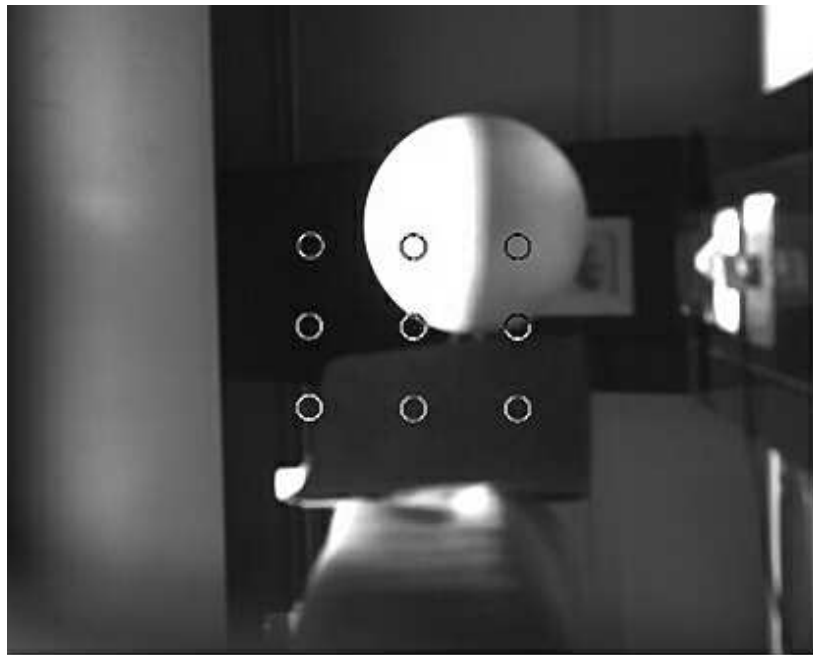


Figure 7.7: Image obtained using the laboratory setup. The circles denote the position of calibration-„Stars“ given by the OESS. The „Stars“ are seen directly the Earth through the partially transmissive mirror.

7.2.1.2 Tests using Experimental Data from Laboratory Experiments

The laboratory experiment was used to test the basic functionality of the algorithms. An image as taken by the PixeLink camera is shown in fig. 7.7. Here the raw image is presented in order to visualize the principle. The circles denote the position of calibration-„Stars“ given by the OESS. In the simulation, they are replaced by the simulation of the Stars visible by the Star-sensor part of the optics.

One of the advantages of using the OESS is that also the noise level can be increased artificially by increasing the noise level in the simulation parameters. It was shown though, that the noise present was in the range of $1/10^{th}$ pixel even in absence of a commanded noise. This noise is introduced by three major sources: the detector, the OESS and the timing mismatch between the OESS and the camera, which results in a time-varying brightness of the Stars observed and thus a higher variation of the Star's center when Star-brightnesses below the requested values were observed. Since the commanded Stars were, obviously, known, it was easy to test the results for agreement. It was thus possible, depending on whether or not the Stars were identified as those simulated, to chose the resulting spacecraft position as update or false measurement. Another problem arouse from the design of the OESS, which was planned for a Star-sensor with a much smaller FOV. This necessarily resulted in a reduction of the used detector area. Again, it was advantageous to have

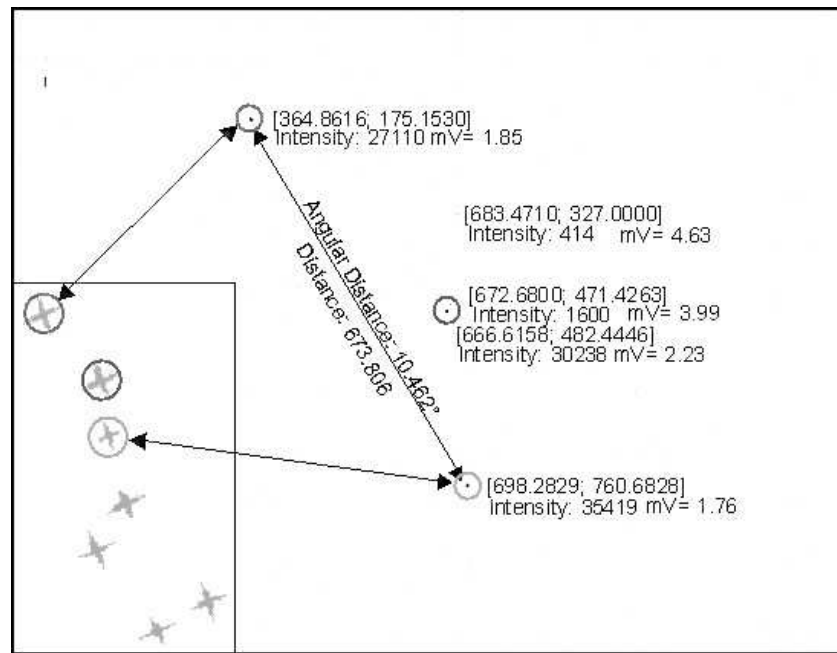


Figure 7.8: Image obtained during a field experiment, including identification of the Stars. The insert shows the location of the identified Stars within the „Big Dipper“

the results of field experiments to validate the camera's focal length. This was used in order to determine the simulator's effective focal length such that the error made in the determination of the simulated Stars was minimized.

7.2.1.3 Tests using Experimental Data from Field Experiments

In figures 7.8 - 7.12 the Star-identification algorithm is applied to various data-sets obtained by field experiments.

Figure 7.8 shows the identification of Stars grabbed with the IBIS4b. It was taken during a field experiment carried out in the Bavarian alps. The confirmation of this image's Star-identification was simplified by the knowledge of the camera's approximate orientation throughout the experiment. The „Big Dipper“ was aimed at and later-on successfully identified. The tolerance necessary for the determination was approx. 240". This value again was due to an uncalibrated optics and thus even larger than one pixel ($7 \times 7 \mu\text{m}^2$).

For comparison to the simulated Star-shapes as presented in chpt. 3.1.2, figure 7.9 shows the image of a Star captured using the PixeLink camera. The image is centered about the brightest pixel, the Star was observed 6.6° off of the LOS and under an angle of 30° about the LOS relative to the

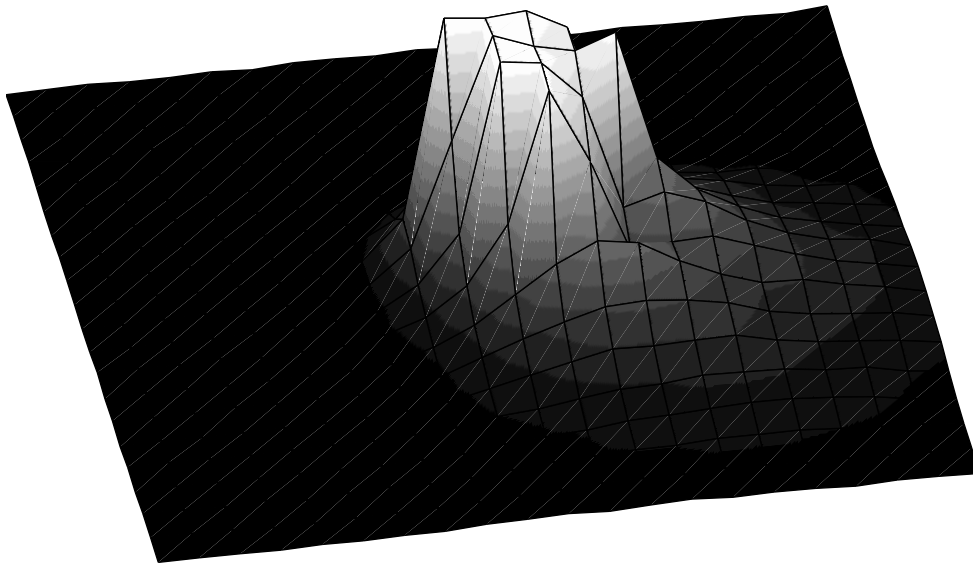


Figure 7.9: Shape of a Star observed 6.6° off of the LOS, image centered about the brightest pixel

x -axis. By closer observation, the similarity to the simulated case of a detector plane 0.1 mm in front of the focal plane and a Star 8° off of the LOS is evident.

Figure 7.10 shows the Earth spin-rate, which is obtained using the LARM tracking mode as described in chpt. 3.1.5. The data, which is sampled at a frequency of 0.193 Hz, is unfiltered and yields a mean of $4.32 \cdot 10^{-3} \text{ }^\circ/\text{s}$, as compared to the constant line, representing the nominal Earth spin-rate of $4.16 \cdot 10^{-3} \text{ }^\circ/\text{s}$. The standard deviation is $1.01 \cdot 10^{-3} \text{ }^\circ/\text{s}$, translating to a standard deviation of approx. 13.3'' in the single-frame attitude. A closer examination on the rates determined for the individual axes showed that the accuracy in pitch and yaw is by a factor 4.2 better, than in roll. In particular, this leads to accuracies of approx. 4.4'' (pitch,yaw) and 18.3'' (roll) at a mean of 5 observed Stars.

In fig. 7.11 an image comprising 46 exposures to simulate a trace of Stars with a length of approx. 1° , taken by the PixeLink camera, can be seen. It was put to use in the testing of the HARM tracking mode (chpt. 3.1.5). It can easily be seen that, due to the desire of capturing as many Stars as possible, a certain number of false measurements enters the algorithm. In the particular image this effect was engraved by the two horizontal lines of increased noise, which were a result of an error in the camera read-out, which later-on was fixed. As explained in the chapter dealing with HARM, the false measurements can be eliminated by comparison with a second image. On this image, the HARM tracking mode extracted traces of Stars down to magnitude $m_V = 5$. This is not representative of an actual image: If the image is actually obtained by a longer integration time at the same rate, the noise in that image is lower, but the bias imposed by dark current is higher. This

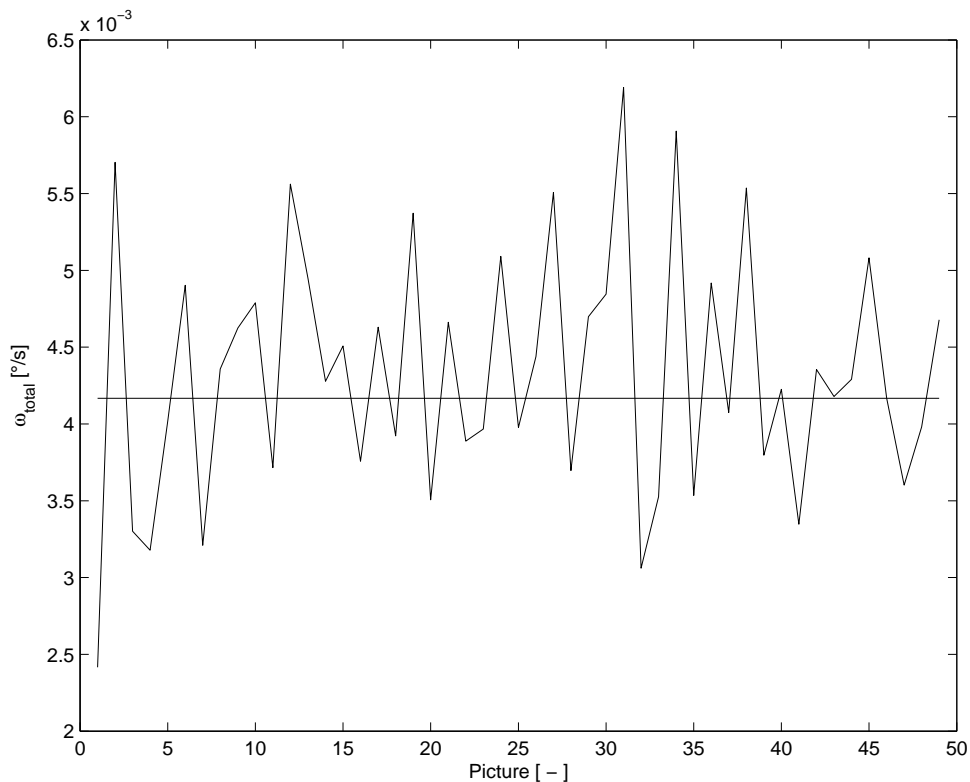


Figure 7.10: Spin rate of Earth as determined by LARM during field experiment from consecutive images

results from the read-out time of the detector between the consecutive images in the experiment, which actually reduces the exposure time. If the total exposure time is the same, the dark current is representative, but the noise in the actual image is higher, as the rotation rate needs to be higher in order to result in the same length of the trace. This results in less photons reaching the individual pixels. If the image is the result of a higher rotational rate, the dark current in the actual image is representative if the total exposure time of the experiment is chosen for normalization, but the noise will be higher, as the composed image effectively reduces the noise and, again, less photons reach the individual pixels. Nevertheless, the experiment was highly helpful in validating the functionality of the HARM tracking mode. A very interesting effect was observed by closer examination of the images: the individual traces of Stars sometimes were influenced by a „shadow“, which first was interpreted as a halo, but then turned out to be the second Star in a double-Star system. If the two Stars are separated by very small angles and are similar in brightness, they can not be discriminated from each other. Therefore these measurements need to be detected as not applicable by either their extension or the different orientation of the axis connecting the two ends of the trace, if the orientation varies considerably from that detected in the remaining image.

In fig. 7.12 the Star-identification on a picture taken by the ground-based telescope can be seen.

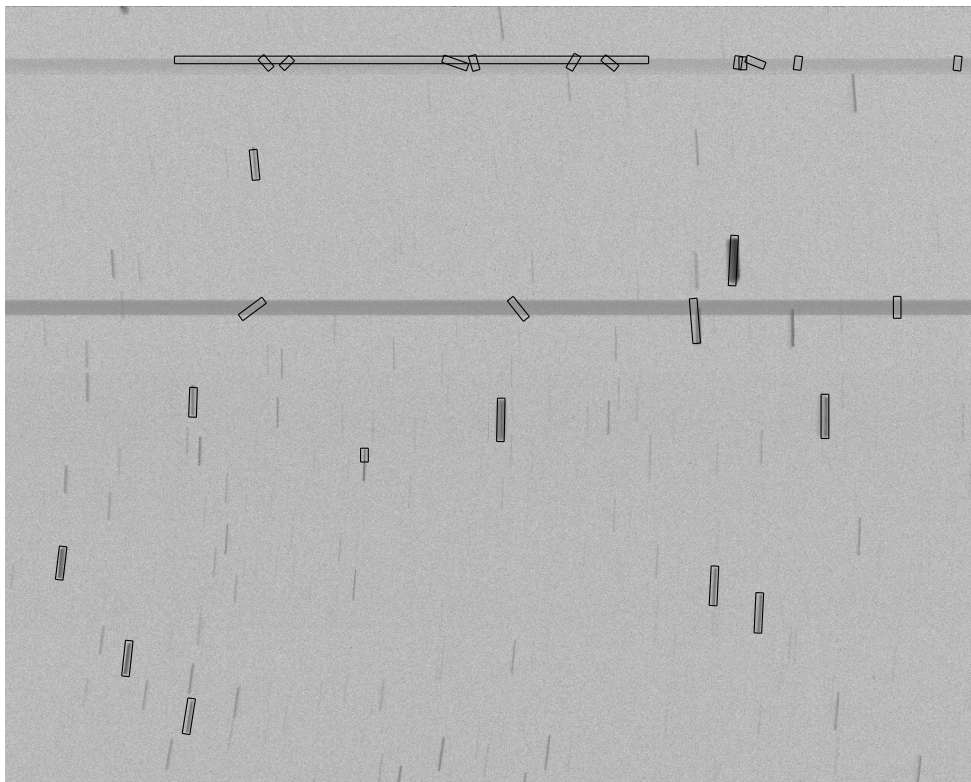


Figure 7.11: Artificial 1° Star-smear by superposition of 46 consecutive images taken during field experiment

The advantage of this image is the unambiguity due to the high number of Stars, which can be used as reference. In this special case, the identification has been carried out using five Stars only, and been manually verified by observing the match of the remaining Stars. The Stars used for the identification process are marked with diamonds, the Stars expected with circles. Additionally a „Star“ used for identification is marked with a square, which was not matched, since it is not present in the Star-catalog, which only covered Stars down to a visual magnitude of $6m_V$.

7.2.1.4 Accuracy of the Star-Measurements

In summary, it was shown that the Star-identification algorithm designed is appropriate for use with large-FOV Star-sensors, and has a high probability of success, even in first acquisition mode and under use of uncalibrated optics. The algorithm as presented has been used throughout all phases of the project and has proved its value in the evaluation of the experiments carried out. The attitude determination algorithm proved its conceptual correctness in the comparison to MITA-data and the field experiments. A first estimate on the achieved attitude accuracy using the field-experiment data shows a standard deviation in the single-frame attitude of approx. $13.3''$. As this accuracy is

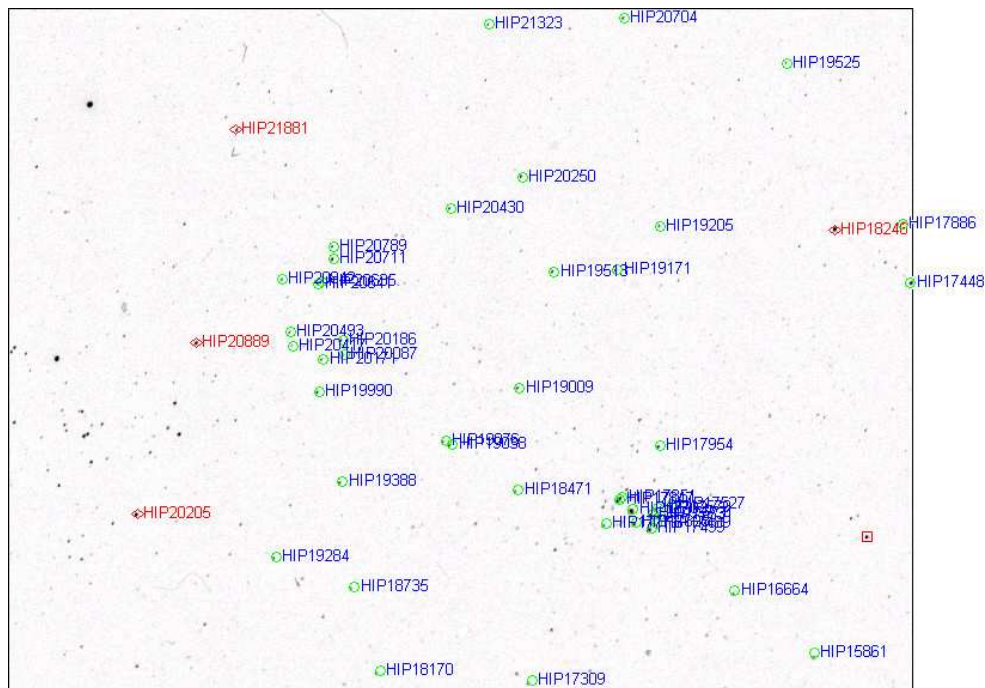


Figure 7.12: Image obtained using a 75 mm ground-based telescope, including identification of the Stars.

obtained with no further calibration of the camera and in presence of atmospheric turbulences, the nominal attitude accuracy can be expected to surpass this value, thereby proving the expectation of the attitude accuracy as given in chpt. 3.1 to be correct.

7.2.2 Experiments on Earth-Measurements

This chapter will deal with the experiments carried out in the field of Earth center determination in the LEO and GEO case, and demonstrate the results obtained.

Two series of experiments have been evaluated with two different objectives. The first was to check various ideas of possible filters for the applicability on Earth horizon detection. The second series was performed to then validate the selected and developed algorithm on a series of consecutive images to get a better estimate on the standard deviation of the Earth-center determination when using real measurements.

7.2.2.1 Tests using Experimental Data from MITA

The first application of algorithms to extract the Earth horizon from images was carried out using the data obtained by the flight experiment. This was primarily done to take advantage of the flight

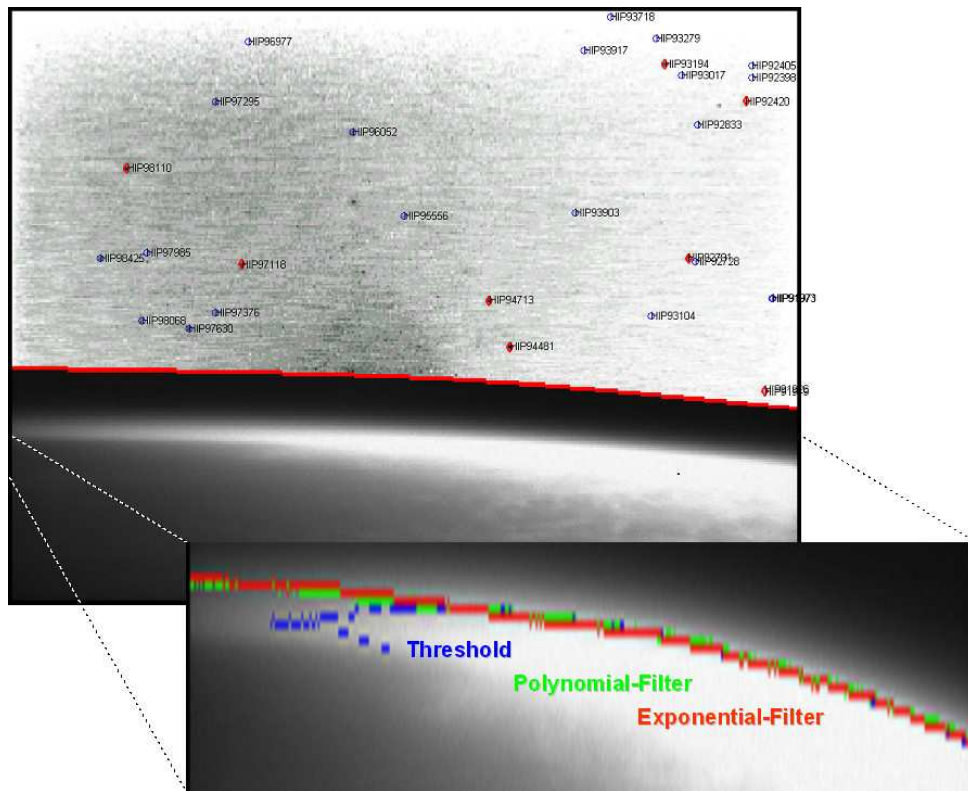


Figure 7.13: Comparison of various filters for Earth horizon detection

data, providing an image of the horizon in LEO. The advantage of LEO data lies in the intensity distribution normal to the horizon. While from GEO it is primarily seen as a step, in LEO the exponential increase can easily be seen.

The results as obtained by three different filters, one using an exponential filter, the other a fifth order polynomial fit and, for comparison, a third using a simple threshold, can be seen in fig. 7.13. Since this is the same image, as fig. 7.6, which has been used for the Star-identification, the results can be used for the determination of the satellite's position. It should be noted that these results did not undergo a further refinement or validation using any *a priori*-knowledge about the circular shape of the Earth or further verification of possible horizon points using surrounding pixels. Though it is apparent that a simple threshold is by no means the ideal solution, since it follows variations in the horizon's intensity too easily, it was decided upon due to its low computational demands. The variations were reduced by choosing an adaptive threshold and excluding false identifications by means of additional local and global criteria.

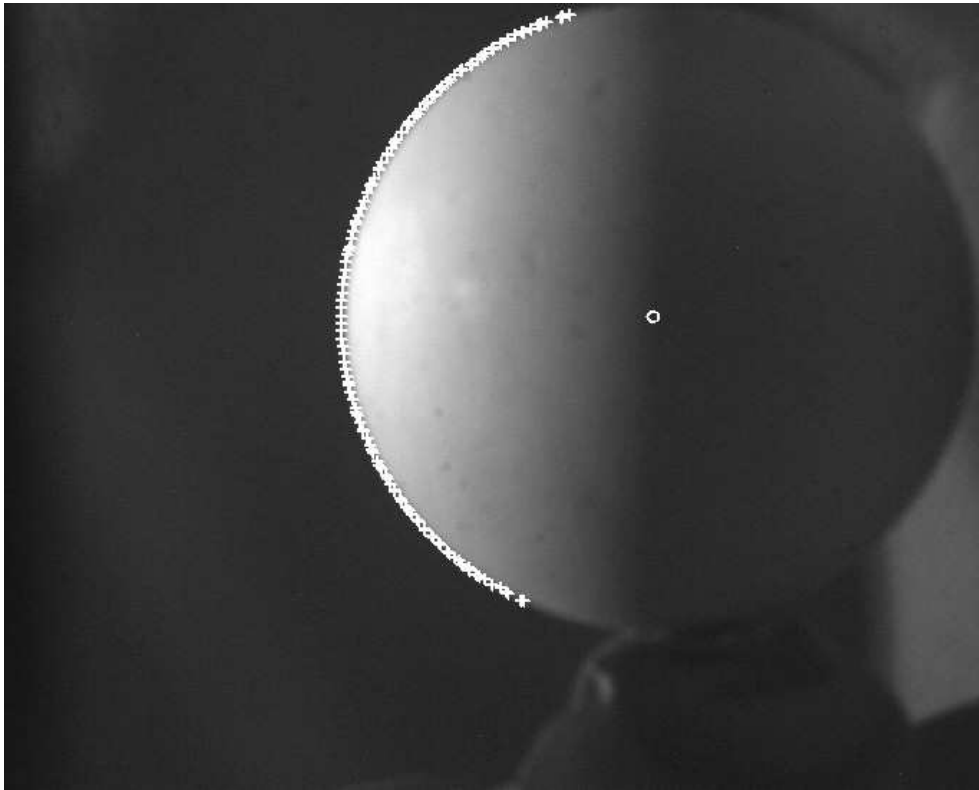


Figure 7.14: „Earth“ -horizon and -center determination as tested in the laboratory

7.2.2.2 Tests using Experimental Data from Laboratory Experiments

The laboratory setup, though limited in its capability of providing realistic data for Earth-images, was used to determine the stability of the Earth-center determination algorithm. This is of particular value, as the lighting conditions as well as the surface of the „Earth“ do not change throughout the experiments. An image showing the Earth as it is perceived by the PixeLink camera is shown in fig. 7.14. The image is not representative for complete simulation in that the laboratory background can be seen. The horizon as detected is marked, as is the center of the sphere, as determined by the Earth-center determination algorithms. The temporal noise was determined to be approx. 0.06pixels in the „south-to-north“ direction and approx. 0.17pixels in the „east-to-west“ direction. For the given system this translates to approximately 0.001° and 0.003° , respectively. The Earth-radius is estimated with an accuracy of approx. 0.15pixels, yielding approximately the accuracy of the worse axis. These results are better than the expected accuracy as given in chpt. 3.2, yet not necessarily representative of a true Earth image with its time-varying cloud- and surface-structure.

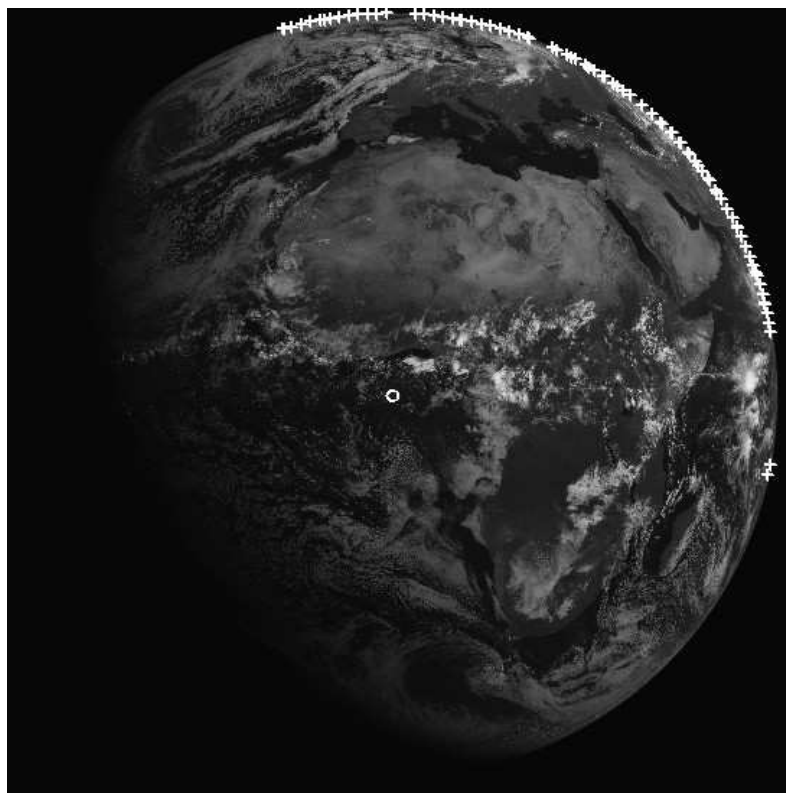


Figure 7.15: Image acquired by the METEOSAT-satellite with the result of the Earth-center determination as presented

7.2.2.3 Tests using Images from METEOSAT

The Earth-center determination algorithm, as explained in chpt. 3.2 was tested using image series taken from GEO by METEOSAT. Throughout the evaluation, various series were investigated. To take into account the variation of the Sun incidence angle throughout the year, four full day cycles have been chosen at the extreme points: the equinoctial points (*vernal equinox* (March 21st) and *autumnal equinox* (September 23rd)) and the solstices (*summer solstice* (June 21st) and *winter solstice* (December 21st)). An example of an image by METEOSAT with the Earth-center being determined by the algorithms for the GEO case, as presented in chpt. 3.2, can be seen in fig. 7.15. The image was taken June 22nd at 9 am, Greenwich Mean Time (GMT). Due to the effects of fitting a circle to an ellipse, as explained in chpt. 3.2.2, the resulting steps at noon can be seen in fig. 7.16.

As can easily be seen in fig. 7.16, the apparent step is greatest in Spring and Autumn. The reason for this, though, is only a combination of the ecliptic's influence, which results in a tilted illumination relative to the equator, and that only the x -position is shown. It was verified that the total step size is approximately equal in all cases (approx. 0.2°). A comparison between the direct methods for elliptical and circular fits showed that, while the ellipse slightly reduces the step size, the noise

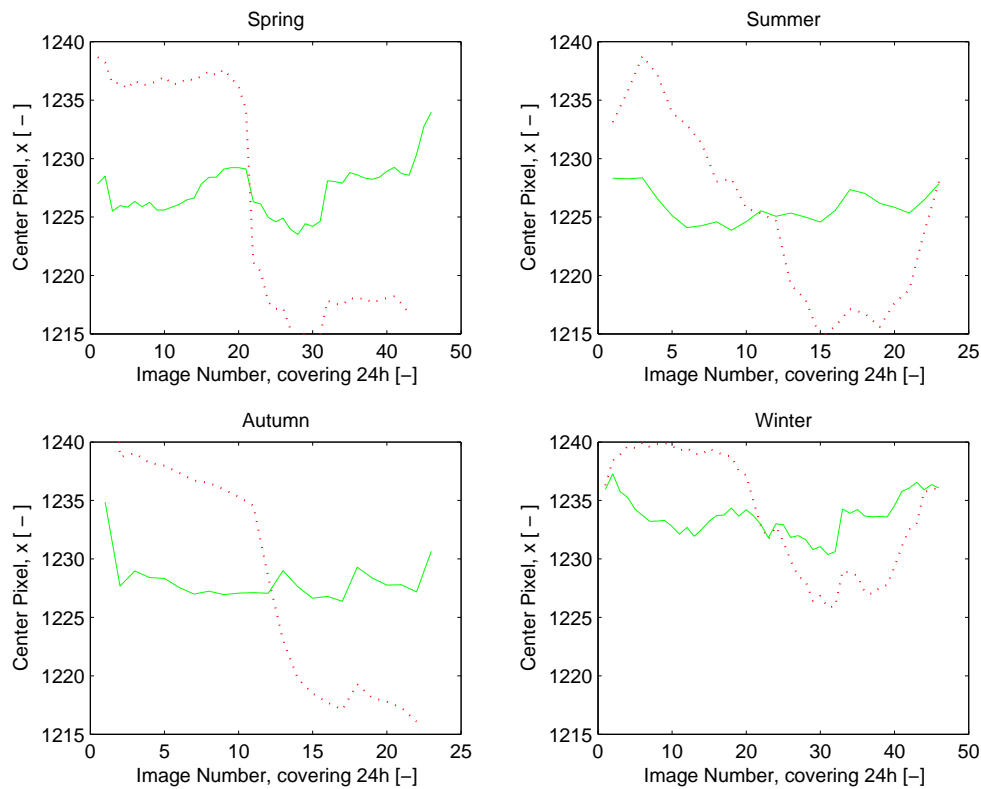


Figure 7.16: x -Position of Earth center throughout a day's cycle, circular fit (dotted) and adapted circular fit (solid)

throughout the two plateaus is increased.

In a next step, an adapted circular fit, using the known eccentricity and orientation of the Earth, as presented in chpt. 3.2.2 and visualized in fig. 3.23, was implemented. This in itself already reduced the mis-estimation of the Earth-center by a factor of about two. An additional reduction was made possible by introducing an *apparent eccentricity*, which was originally meant for compensation of the lower illumination levels at the poles. Interestingly enough, the Sun incidence angle does not have a major effect: when implementing the apparent eccentricity, it was designed to include the Sun incidence angle, so as to correct the apparent ellipse accordingly. It was shown, though, that this did not improve the determination of the Earth-center. The explanation for this is supported by the assumption made for instance in [14], stating that the highest fraction of incident sunlight is reflected diffusely. In an ideally diffuse reflecting body, this would result in an apparently homogeneous illumination. Another source might be the higher average cloud density at the equator throughout the year. A study on cloud coverage of the Earth ([61]) published the average density distribution as seen in fig. 7.17, supporting this hypothesis. A third explanation might result from the line-scanning device, which gathered the information: since the pictures were not calibrated, they might still include errors due to the line-scanning mechanics. This results in a

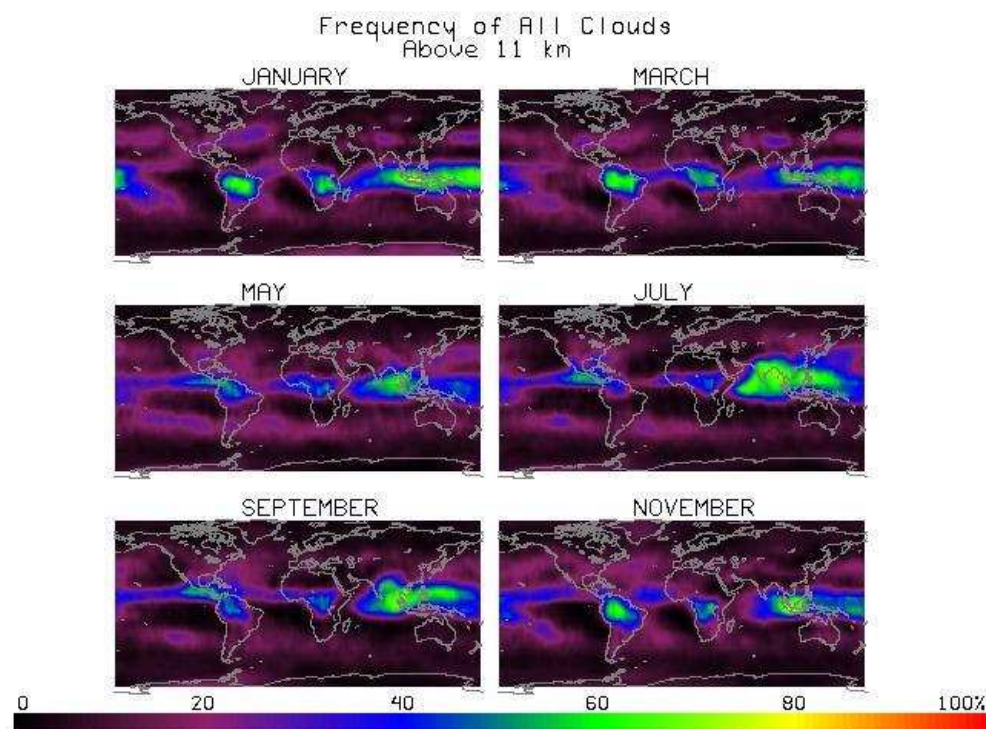


Figure 7.17: Cloud coverage throughout the year

deformation of the image, resembling an additional eccentricity. The optimal apparent eccentricity as extracted from data covering several days by Meteosat amounts to be approx. $e_{apparent} = 0.075$. The orientation is aligned with the Earth-equator, therefore resulting in a total eccentricity of approx. $e_{total} = 0.16$. As a comparison: the eccentricity of the Earth amounts to $e_{Earth} = 0.081$. It seems like it might be beneficial to introduce a time varying apparent eccentricity to cover variations occurring throughout the year. The reason for this is the change in the apparent Sun-diameter due to the Earth's slightly eccentric orbit about the Sun, resulting in a different angle for the sunlight from the Sun's horizon when finally reaching Earth. Even without the introduction of these additional parameters, the standard deviation of the Earth-center was reduced to below 0.1° .

7.2.2.4 Accuracy of the Earth-Measurements

Applying the improved Earth-center determination algorithm for LEO to the images gathered by MITA resulted in an overall performance of better than $\pm 2^\circ$ in the determination of the Earth-center (see as well chpt. 7.2.3). It should be noted that this value is affected by the relatively low resolution of the camera system flown on MITA. Additionally, the comparison to the flight data assumes a slowly changing orbit and a constant attitude. Since the orbit is a LEO, which is highly affected by the atmosphere, and since the satellite's attitude control was designed to perform in

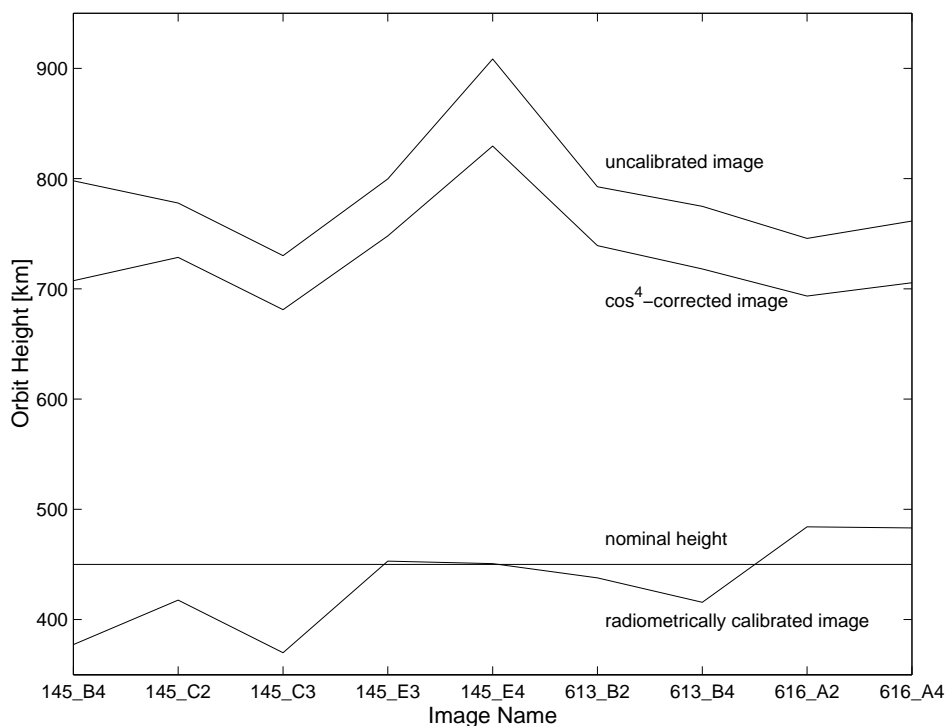


Figure 7.18: Orbit height as determined from MITA images (reference orbit height approx. 450 km)

the range of $\pm 1^\circ$, the performance of the Earth-center determination still seems to be adequate. The mean accuracy is furthermore reduced due to images, which included the terminator, which in general yield a lower accuracy. Finally, not all horizon-points were being used, which allows for further improvement.

As apparent from fig. 7.18, the estimated Earth diameter is highly dependent upon a radiometrically calibrated image. If a standard correction using a \cos^4 -attenuation towards the edges of the FOV is used, the horizon as determined by the horizon detection results in a smaller apparent Earth-diameter and thus in too high an orbit. This can be explained by the attenuation, which reduces the brightness at the rim of the FOV, implying a retracting horizon. This in turn would represent a smaller diameter, and thus a higher orbit, from which the Earth is being seen. The experiments showed an accuracy of ± 45 km in orbit height, which is equivalent to the above-mentioned $\pm 2^\circ$ in the apparent Earth-radius, and thus the Earth-vector, which is directly dependent upon the estimated Earth's angular diameter.

Considering the drawbacks imposed by the low resolution of the detector as used in the MTS-AOMS experiment and emphasizing the results of the evaluation of the METEOSAT-data, which showed an accuracy of better than 0.1° , the performance of the system can be concluded to surpass our expectations.

7.2.3 Experiments on the Position-Determination

As the position-determination can only be carried out by the combined Earth-/Star- sensor and can only be validated by experimental data, the experiments on position determination concentrated on the data provided by the flight experiment on MITA.

7.2.3.1 Tests using Experimental Data from MITA

The final test of the algorithms was performed on flight data from the MITA mission. Using the latest version of the image-processing tools, the algorithms for position determination and the satellite's ephemeris data as provided by *Analytical Graphics* for the *Satellite Tool Kit*[®] (STK), the results were compared to the nominal data. As discussed before, the satellite's orbit was well within the atmosphere, which leads to a rapid change in the orbit-elements, requiring the use of updated ephemeris data, which needs to be valid as close to the measurement as possible. This necessity arose from the unknown actual position of the spacecraft at the time interval of interest. Additionally, the satellite's attitude accuracy was specified only to within $\pm 1^\circ$, which allowed only for an „order of magnitude“-verification of the attitude determination.

Processing the image given in figures 7.6 and 7.13, without any further changes in the software, results in a deviation of approx. 1.5° as well in the attitude determined by the Star-measurements, as in the determined Earth-vector, when compared to the respective nominal values. The nominal attitude additionally does not include any information on the deformation of the satellite's structure or misalignments of the sensor with respect to the body-fixed system, which further reduces the comparability of these attitudes.

7.2.3.2 Accuracy of the Position-Measurements

The position finally was determined using the relation given in eq. (5.4). Comparison to the nominal position was accomplished by using a set of ephemeris data, which was available for the day prior to the actual experiment. The comparison was then performed by finding the minimal angular error between the nominal position-vector and the one determined experimentally. The result was a match to within 2.5° at a time which differed only by 5 seconds from the time-tag provided with the image. The radius is accurate to approx. 0.5 km, resulting in a single-measurement 3D-error of approx. 300 km. This is less accurate than predicted, which is due to the absence of reference images for LEO to further improve the LEO-algorithms and a lower resolution of the detector.

Considering this variation of the satellite's data as found by the experiment from its nominal atti-

tude results in the following explanation on the overall accuracy: As the position deviates from the nominal position by 2.5° , this is the geometric sum of the errors induced by the Earth-center and attitude determination and mirror misalignments. As it can be assumed that, even with the uncorrected optics used, the attitude is accurate in the order of 0.03° , which is equal to the mean angular pixel size, and neglecting misalignments, one can conclude that the Earth-center determination is accurate approximately equal to the position accuracy, which is about 2° . This in turn indicates a deviation of the sensor's attitude from its nominal attitude by approx. 1° , which might either be due to deformation of the satellite's structure, misalignments or due to a deviation of the satellite from its nominal attitude. In particular, it was shown that the axis of the satellite which should be aligned with the velocity-vector, deviates from its nominal orientation by 1.5° . The major amount in this error is due to a rotation about the nominal position-vector, meaning the satellite has an angle of sideslip equal to approx. 1.2° .

Taking these effects into account, the accuracy is very well within the prediction, proving the effectiveness of the approach.

7.3 Experiments - Conclusions

This chapter will summarize the results of the experiments carried out and compare them to the expectations drawn from the analysis and the simulations in the previous chapters. In table 7.4, the quantitative comparison shows a good agreement between the values under investigation.

The Earth-reference accuracy is as predicted, with the additional comment, that the imaging system had a higher resolution than the proposed sensor and thus should lead to better results. Nevertheless, as the Earth covers a large number of pixels at a high horizon curvature, the accuracy is representative.

The Star-related accuracies show a close to perfect match with respect to the target values. This performance is expected to be increased by calibration of the camera system and the use of Star-images not disturbed by the atmosphere. The actual centroiding accuracy can not be specified, as the measurements do not provide the means of determining them directly, yet they can be deduced from the overall „Inertial Attitude“ accuracy.

The position accuracy as determined by the MTS-AOMS experiment is worse than predicted. This is a result of the low-accuracy consumer optics used, the low-resolution APS detector and the use of LEO data as opposed to images taken from GEO. Considering a higher grade optics, a high resolution detector and a larger number of images in order to further improve the algorithms necessary for Earth-center determination in low Earth-orbits, this accuracy will increase.

Table 7.4: System Accuracies

Value	Analysis/ Simulation	Experiment
Single Frame Earth-Reference	0.1°	<0.1°
Single Star Centroiding	10''	approx. 30'' (deduced from Inertial Attitude)
Inertial Attitude	6'' [pitch, yaw] (25'' [roll])	4.4'' [pitch, yaw] (18.3'' [roll])
Position		
Point Solution	60km (GEO)	300km (LEO)
Navigation Solution (after 2 – 3 orbits)	5 km	n/a

Accuracies given are 1 σ values

The 5 km in the accuracy are a conservative estimate. The simulation results after 2 – 3 orbits were in the order of 500 m in radial direction, 1500 m down-track and 500 m cross-track. In total, the accuracies are in the same order of magnitude as predicted and can be expected to meet the prognosticated values after further improvements on the components of the proposed system.

Chapter 8

Operational Aspects

This chapter will introduce some of the operational aspects when dealing with purely optical means of attitude and orbit determination. Emphasis is put on the GEO case, which is then extended to different missions and mission phases, including results from the flight experiment where applicable.

8.1 Acquisition

The initial procedure, which occurs in all applications using optical sensors, is the acquisition of the desired target. In the following, an Earth-sensor is assumed to be present, in order to comply with the desire to use the Earth as reference system.

In the case of a „classical configuration“, as seen in fig. 1.2, consisting of Sun- and Earth-sensors, the acquisition is typically simplified by the fact that a suite of Sun-sensors provides full coverage of the celestial sphere. Earth acquisition is then performed by using the *a priori* information of the Sun-vector: If the satellite’s position is approximately known by using a rough orbit model, the satellite is oriented such that the Sun-vector and the Earth-sensor’s LOS comprise the predicted angle. The satellite is then rotated about the Sun-vector in order to capture the Earth when it enters the Earth-sensor’s FOV. If no such knowledge is available, the Earth-sensor’s LOS needs to start spiraling about the Sun-vector.

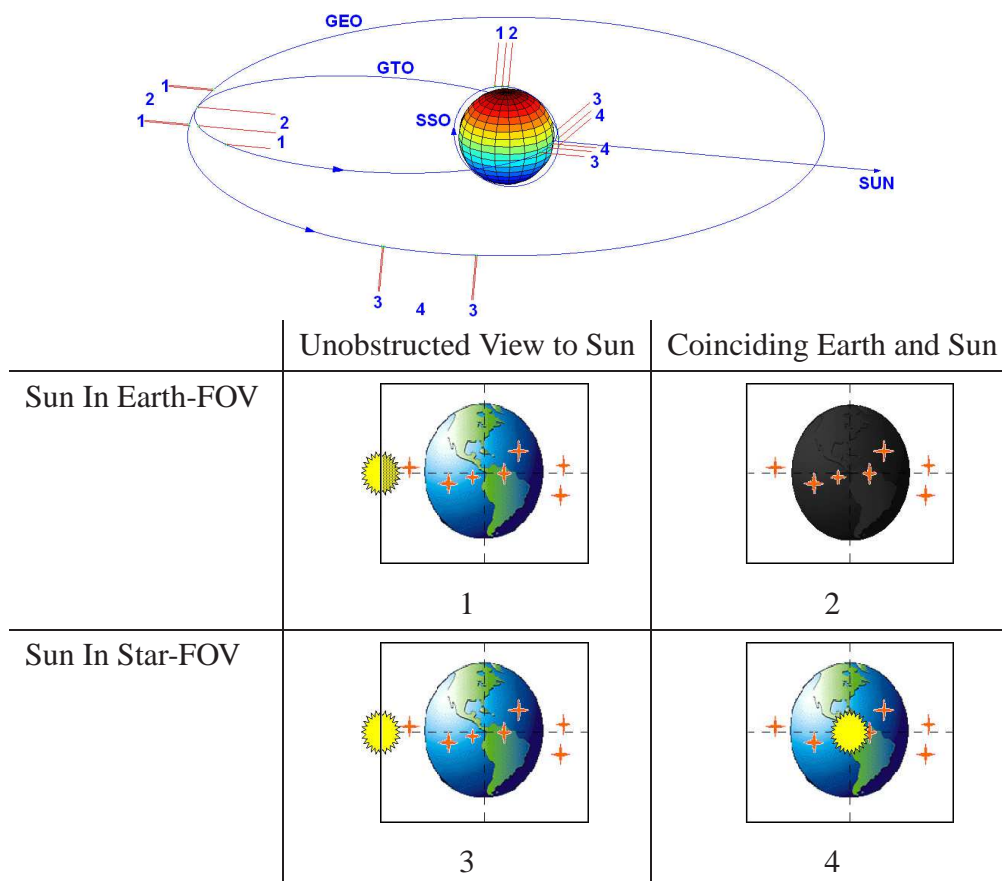
Using Star-sensors instead of Sun-sensors results in a readily known attitude as long as Stars can be detected and identified. Using the *a priori* knowledge on the satellite’s position, the Earth-vector is known in body coordinates, and the satellite can be pointed accordingly. If no such knowledge is available, the satellite’s known attitude allows for a deterministic search, for instance orienting the satellite such that its Earth-sensor’s LOS is within the expected orbit plane and rotating about the orbit-normal, or spiraling the Earth-sensor’s line-of-sight across the celestial sphere.

8.2 Critical Mission Phases

In most missions, critical phases can occur, which either preclude determination of the satellite's attitude or might even damage the sensors due to Sun incidence. These situations need to be analyzed prior to the mission, in order to prevent loss of the satellite or sensors.

Using conventional CCD-based Star-sensors, in acquisition mode for example, it is of importance to guarantee that neither Earth nor Sun are in the Star-sensor's FOV, since they would destroy the CCD. This limitation can be relaxed, when dealing with APS-detector based Star-sensors. It was shown during the MITA flight-experiment that the APS-detector withstands direct Sun-exposure (see table 8.1, states 1), 3) and 4) as well as fig. 8.2). The advantage in this case is that the information of Sun-presence in the FOV can serve as a preliminary information on the satellite's attitude. The same holds for Earth-presence, which can easily be distinguished from the Sun by their different apparent diameter. The Moon does not represent a major problem, since it is only about as bright as the Earth, at a size of about $1/2^\circ$, as seen from an Earth orbit. The main source of irritation - which is „Moon-rise“, respectively „Moon-set“ - was shown not to be an issue in

Table 8.1: Definition of sensor-states



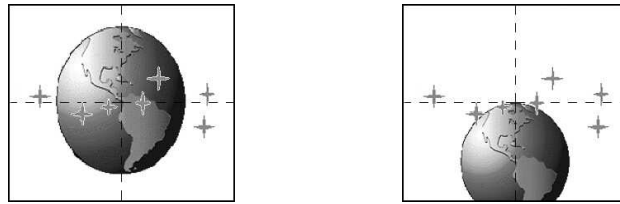


Figure 8.1: Centered vs. oblique view of Earth, Example: GEO

Earth-center determination, since the few measurements disturbed by the Moon are treated as false measurements.

Once the satellite has reached its nominal (Earth-pointing) attitude, autonomous attitude and orbit determination can be performed. Some limitations have to be considered, though, which mostly depend on the satellite's orbit and need to be accounted for.

The first issue when dealing with optical sensors for determination of the Earth-vector is the eclipse, i.e. when the Sun is behind the Earth (see table 8.1, states 2)). As in the case of „New Moon“, in the case of an eclipse, no Earth is visible and thus no center can be determined, when using sensors in VIS. The eclipse has (nearly) no effect when using IR-sensors, since the Earth is always warmer than its surrounding. As shown in the simulations on the orbit determination in chpt. 6.2, in particular in fig. 6.4, the unknown Earth-vector can be propagated with high ac-

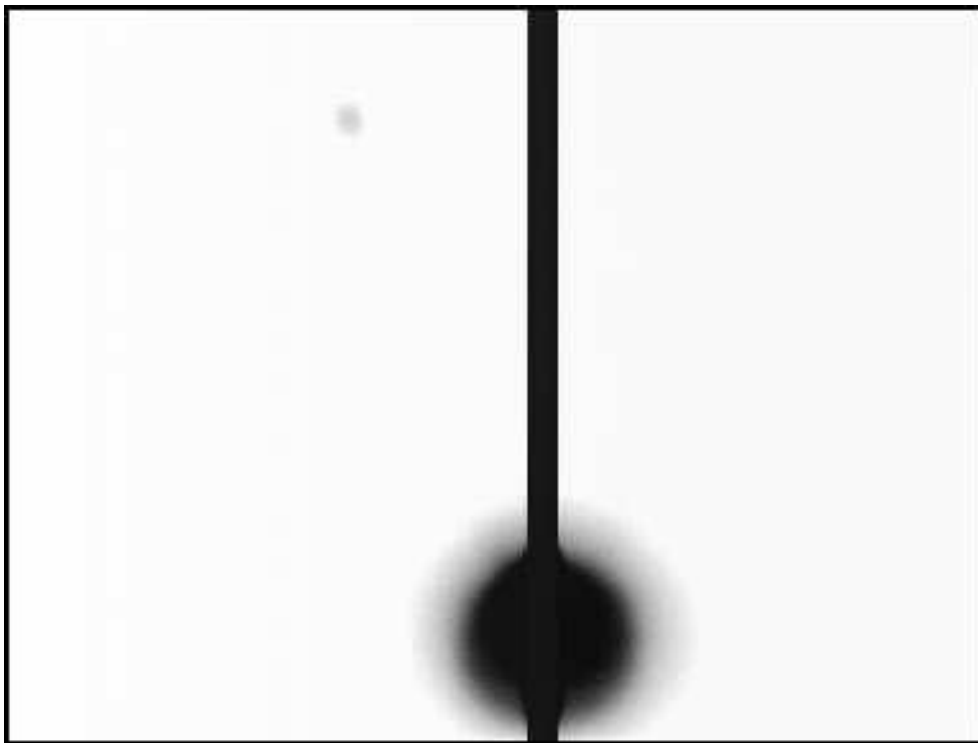


Figure 8.2: Image of Sun in unattenuated Star-FOV

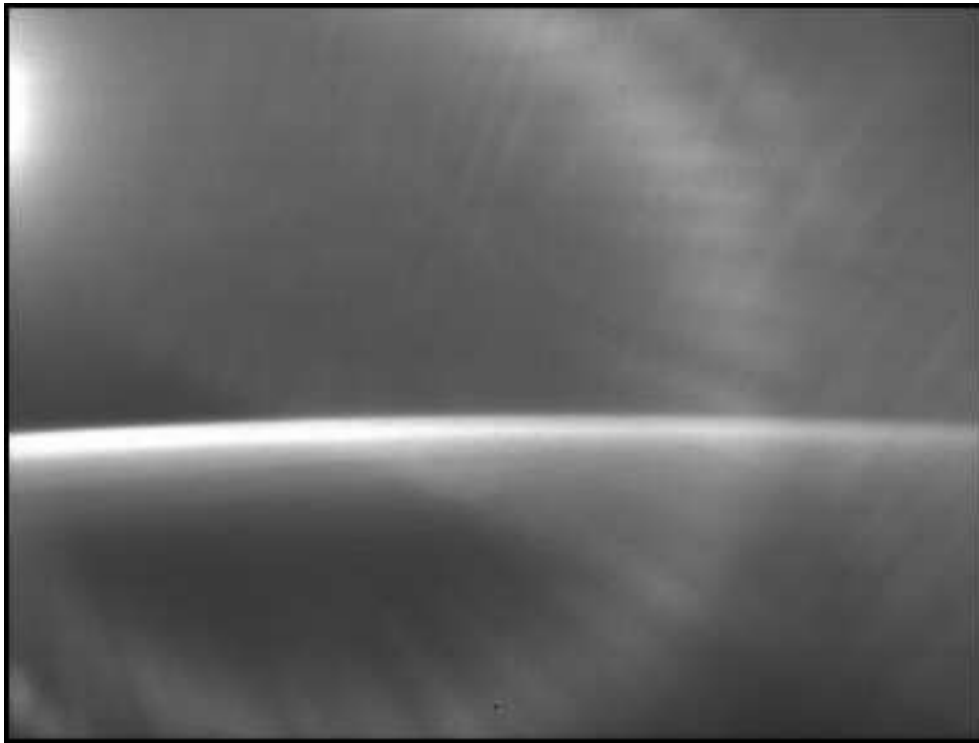


Figure 8.3: Image of Sun at Rim of Earth-FOV

curacy during eclipse and therefore does not represent a problem. In this context, the accuracy of a purely Keplerian Orbit in GEO is approximately 1 m/orbit as a secular deviation, with an approx. 2.5 km periodical component. In LEO the errors amount to 20 m/orbit, with a 6 km swing. The high precision orbit propagator (HPOP) can be assumed to be accurate. Juckenhöfel ([8, p. 40 ff.]) determined a difference of approx. 270 m/orbit for GEO satellites. This already includes errors in the position determination from ground and initialization errors, which are not part of the actual propagation error. The larger deviations in LEO can be explained by the higher influence of non-Keplerian effects, in particular air-drag. Combining the propagated position with the full knowledge of the attitude using the Star-image, information on the Earth-vector can be deduced. Obviously, eclipse-phases have a different duration in different orbits, depending on height and inclination. Due to the high accuracy in the propagation of satellite orbits and the availability of attitude information, though, it can be concluded that the eclipse does not represent a major limitation.

The second issue, which is not as easily overcome, is Sun-incidence. Sun-incidence can be obviated for the Star-FOV, during nominal operation, since its pointing direction is not constrained by the need for specific target Stars. There are satellite-dependent limitations for the mounting angle of Star-sensors, as for instance the presence of solar-panels, thrusters and payload components as well as environment-dependent limitations like Earth and Sun. In GEO applications, these

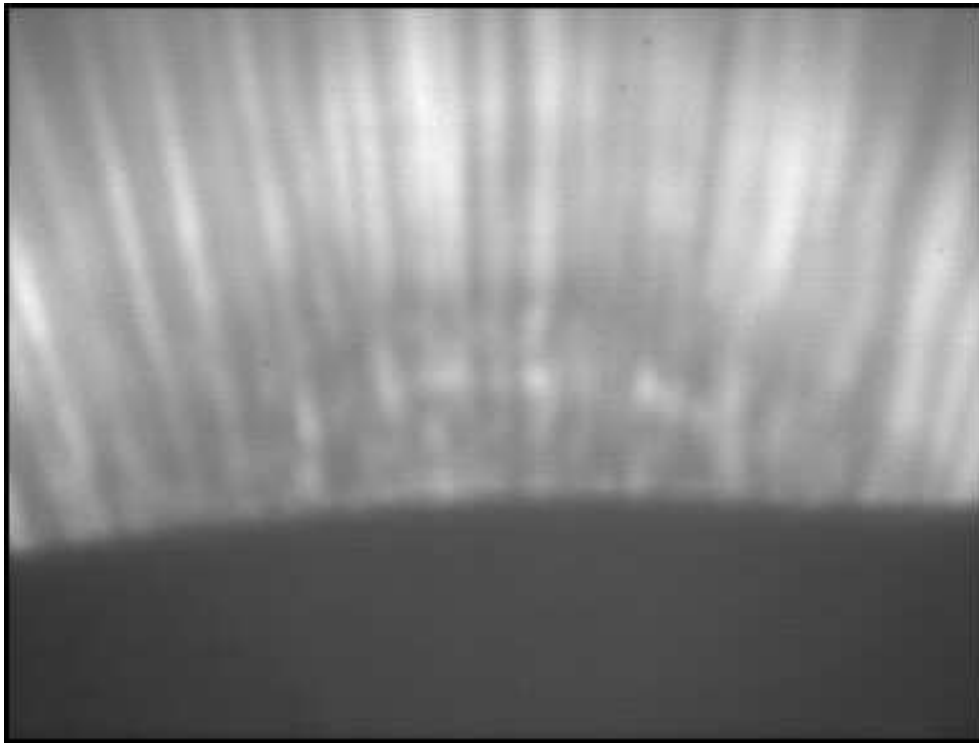


Figure 8.4: Image of Sunrise in Earth-FOV

limitations lead to a typical mounting angle of 46° to 70° with respect to the equator-plane (see [62]). The pointing direction of the Earth-FOV, though, is set by the necessity of Earth-observation. Except for very few occasions, this leads to an at least „once-per-orbit“ Sun-incidence in the Earth-FOV. In the GEO case as shown, using a centered Earth (fig. 8.1), Sun-incidence in the Earth-FOV occurs twice per orbit, if the Sun passes behind the Earth. As the equator is not parallel to the Earth's orbit-plane, there are periods, during which the Sun passes behind the Earth (spring, autumn), some at which it passes just above or below the Earth, but within the FOV and then others, where it passes outside the FOV (summer, winter). As became obvious during the flight experiment, due to the Sun's brightness and optical imperfections, even Sun-presence in the attenuated Earth-FOV resulted in an unobservability of Stars in the combined image (see table 8.1, state 1 as well as figs. 8.3 and 8.4). This, in addition to the loss of the Earth-vector, causes the loss of attitude information. While the satellite's position still can be propagated, the attitude information is lost, when solely relying on the combined Earth-/Star-sensor. To cover the loss of attitude information, several options need to be evaluated. They include attitude propagation, shutters to prevent the Sun from entering the optics, a redundant Star-sensor or other means providing an attitude reference. Other means, for instance in the case of LEO and low MEO, are magnetometers, resulting in an accuracy of approx. 0.1° . Alternatively, gyros can be used in any orbit, with the limitation of losing accuracy with time (depending on gyro, typically: $0.1^\circ/h$). Depending on the satellite's

requirements on attitude accuracy, the emerging MEMS gyros, as investigated as part of the flight experiment ([2]), might be used, which currently have a reduced accuracy when compared to other means of rate determination (e.g. Ring Laser Gyro). It should be noted that, contrary to common believe, they do not, in general, reduce system cost: even though the cost of the sensing element is drastically reduced, this does not change the system costs considerably, since the sensing element only amounts to about 2% of the overall prize. The major fraction of the sensor's cost results from Space-qualified electronics and the extensive testing, which is necessary to guarantee lifetime and performance. Nevertheless dimensions, mass and complexity are reduced, resulting in a technologically interesting alternative to e.g. Ring Laser Gyros. Furthermore, it is predicted that they will provide a higher reliability and longer life, allowing for a continuous use over a time period of more than ten years. This is advantageous to current designs, which, in general, use gyros to cover periods with no attitude information and switch them off for the remaining mission. Concluding, due to the possibility of Sun-presence in either the Earth- or the Star-image in most orbits, the need for alternative attitude references arises. An effect, similar to these incidences, is caused by the *South Atlantic Anomaly* (SAA), which causes *Single Event Upsets* (SEUs), which in turn might prevent detection or identification of Stars, and thus lead to a loss of knowledge on the satellite's attitude. The SAA, which is a radiation belt formed by the Earth's magnetic field, is restricted to special orbits, including some LEOs and GTOs. The difference to situations with Sun-incidence is that the effects of the SAA can not be solved by shutters, since they directly affect the detector and its electronics. Solutions are the augmentation of the system by gyros and/ or magnetometers.

Since the Earth-horizon always needs to be observed, an off-set pointing, as shown on the example of a GEO in fig. 8.1, is required in the case of LEO and non-circular orbits: This is in particular true for a SSO, with a constant height of approx. 800km and the *GEO-Transfer-Orbit* (GTO) which extends from a height of approx. 200km to 36000km. Examination of the experienced outage times will be given for these cases.

8.2.1 Mission Scenarios

In figures 8.5- 8.10 the expected worst-case outage-periods for GEO, GTO and SSO are shown, showing different types of deterministic outages. In the figures, and as shown in table 8.1, where 0) denotes full sensor performance. 1) denotes a Sun-incidence in the Earth-FOV and 2) denotes eclipse, which is a Sun in the Earth-FOV, while the Sun is located on the other side of the Earth, leading to loss of Earth-center information. Similarly, 3) denotes Sun-incidence in the Star-FOV, 4) Sun-incidence in the Star-FOV when coinciding with the Earth-image. In general, situations 1), 3) and 4) need to be avoided, where it should be mentioned that, under nominal conditions,

situations 3) and 4) will not occur.

8.2.1.1 GEO Outages

Figure 8.5 shows the predicted sensor outage times during a GEO. In this case, the Earth-LOS is pointing towards the Earth-center, and the sensor is mounted, such that the Earth-LOS and the Star-LOS are located in the orbit plane, leading to Sun-incidence in the Star-FOV. In this orientation, the Sun passes the Earth-FOV from top to bottom. In fig. 8.6, the Star-LOS is perpendicular to the orbit plane, resulting in a longer Sun-presence in the Earth-FOV, due to the rectangular shape of the detector, and no Sun-presence in the Star-FOV, since the Sun is always approximately perpendicular to its LOS. The Sun passes the FOV from right to left. Since in the „unique“ case of a GEO, the Earth-LOS is pointed towards the center of the Earth and the orbit is circular, the outage times are „symmetrical“: When looking at either the Earth- or the Star-FOV outages, the periods 1) and 3) before and after states 2) and 4), respectively, are the same. It might be advantageous to orient the satellite, such that the horizon is located in the center of the FOV. The reason for this is a larger area available for Star-identification. As an example for the difference in a centered and oblique view of the Earth, as perceived from a GEO, be referred to fig. 8.1. Since the oblique view results in a generally non-symmetrical placement of the Earth on the gathered image, this consequentially results in non-symmetrical outage-times.

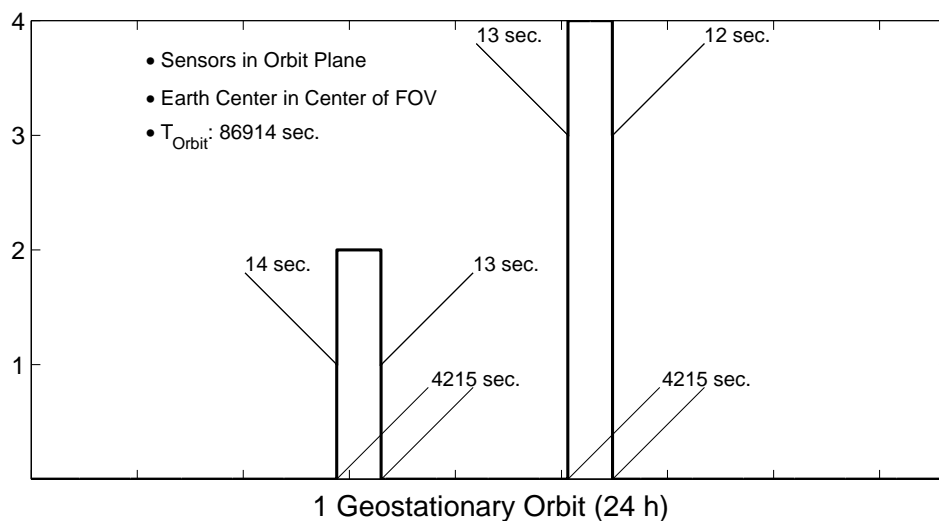


Figure 8.5: Sensor Outages in GEO, centered Earth, Star-LOS in orbit plane

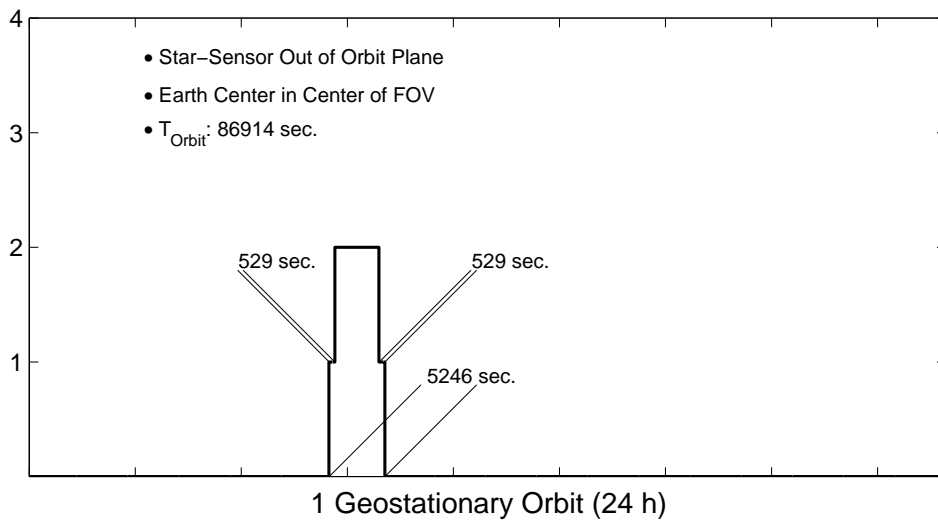


Figure 8.6: Sensor Outages in GEO, centered Earth, Star-LOS out of orbit plane

8.2.1.2 SSO Outages

As an example for an important LEO, the SSO was chosen. The SSO is special, in that their orbit-plane revolves by $360^\circ/\text{year}$ about the normal to the ecliptic. This leads to illumination conditions on the Earth, which repeat every orbit. This again can be exploited when the inclination and height of the orbit are chosen adequately: In the case of *Radarsat*, the inclination was chosen to be 98.6° , the height to be 798 km. This results in a SSO, whose orbit-normal was set to be the Earth-Sun vector. The constellation leads to a seemingly constant illumination of the Earth, allowing for instance for the generation of maps by combining consecutively gathered images. Other orbits,

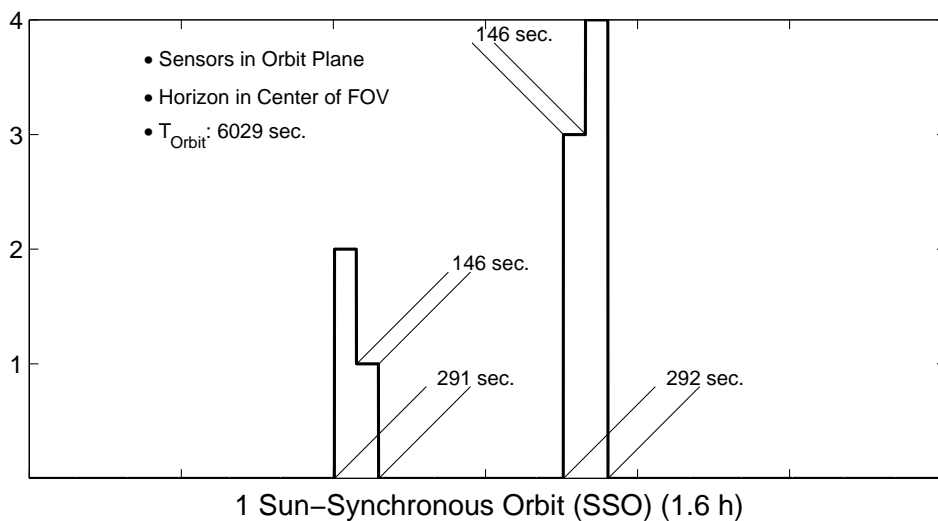


Figure 8.7: Sensor Outages in SSO, oblique Earth, Star-LOS in orbit plane

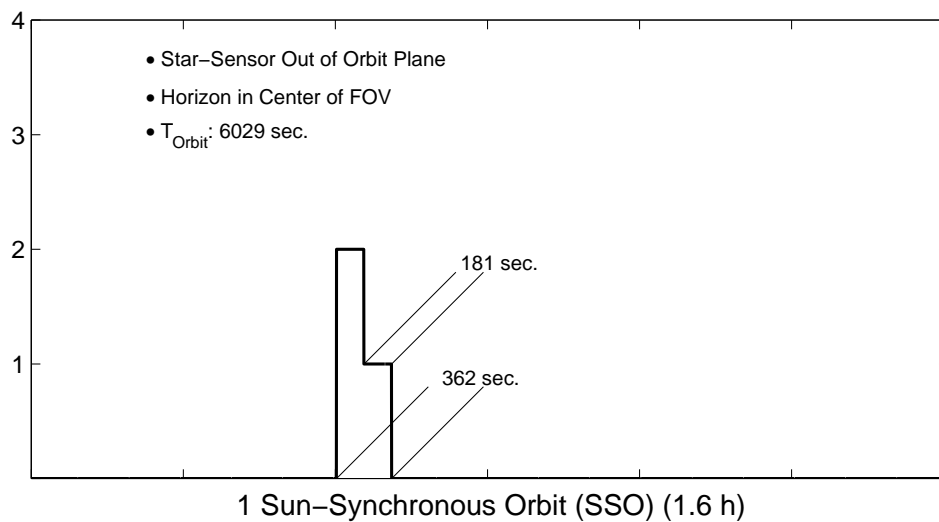


Figure 8.8: Sensor Outages in SSO, oblique Earth, Star-LOS out of orbit plane

for instance in surveillance satellites, are chosen such that a certain area is always passed at the same time, allowing for observation of changes in the landscape without the necessity to account for changes in shadowing.

For our sensor, which needs information on the Earth-horizon, due to the low orbit, an oblique observation of the Earth is necessary. As in the case for an oblique observation from GEO, this results in a non-symmetrical outage of the sensor. Yet, since the orbit examined is circular, the outage-times for the Earth- and the Star-FOV are equivalent. The simulation results can be seen in figs. 8.7 and 8.8, again showing the difference for a Star-sensor in- and out-of the orbit plane. The orbit as used for the simulations was a noon-midnight SSO. This means, the satellite observes the Earth below at either local noon or local midnight. This results in a dawn during each orbit, which is represented by case 1) and can be seen in fig. 8.4. Another special SSO, the dawn-dusk SSO, always stays on local dawn or dusk, never experiencing sunrise or sunset in the sensor's FOV, thus no outages will occur throughout nominal mission. In general, SSOs will lie somewhere in between these two extremes, exhibiting outages in every orbit for some mission periods, not experiencing any outage in others.

8.2.1.3 GTO Outages

The final orbit to be examined is the GTO. It combines many features already known from GEO and SSO, in that it starts as a LEO and reaches GEO. Yet, it has something more to offer: For a GTO, the satellite needs to track the Earth horizon, since the orbit is no longer circular. This means the off-set angle is no longer constant, as in the case of a circular LEO, like the SSO

presented above. The eccentricity furthermore changes the apparent diameter of the Earth and the angle between the Earth-vector and the horizon throughout an orbit, potentially resulting in different horizon-determination algorithms for different fractions of the orbit. This follows from the change in the atmosphere's apparent height. In particular, the elliptic orbit results in variable outage times, which depend on the satellite's position on the orbit and the relative Sun-position. In the simulation shown in figs. 8.9 and 8.10), the orbit was specifically chosen to show the longest and (approximately) shortest outage times. This was realized by aligning the orbit's semi-major axis with the Sun-vector. Thus, since the satellite is slowest in the apogee, the Earth-FOV's outage time is longest for this geometry. The Star-FOV's outage occurs close to the perigee, thus being close to the shortest possible outage time. Any outages in a GTO, for either the Earth- or the Star-sensor will be between these two extremes.

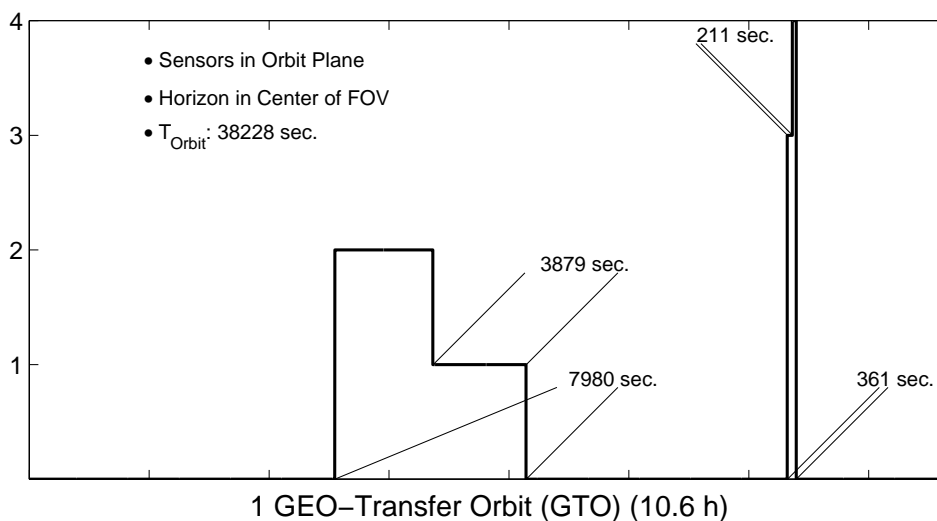


Figure 8.9: Sensor Outages in GTO, oblique Earth, Star-LOS in orbit plane

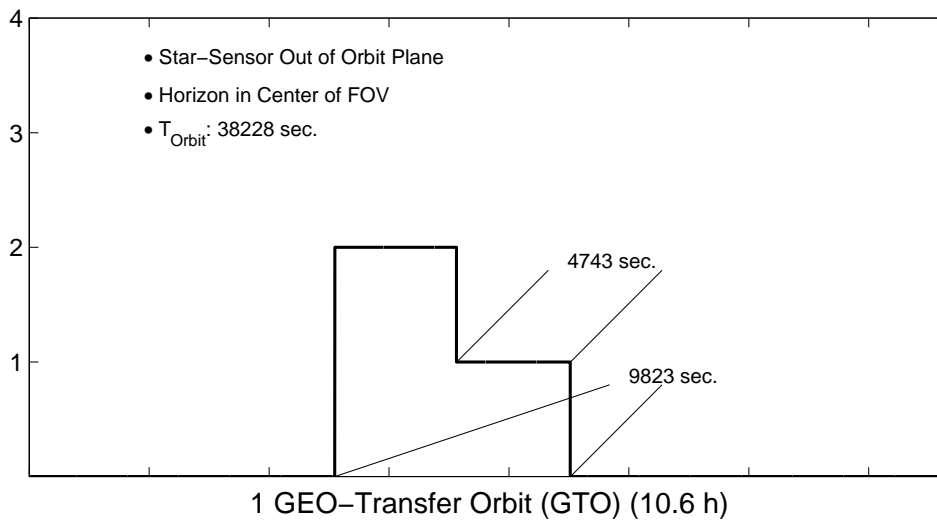


Figure 8.10: Sensor Outages in GTO, oblique Earth, Star-LOS out of orbit plane

8.2.2 Interpretation of the results

For interpretation of the figures, it has to be minded that the Sun might pass through any part of the image, thus the ratio between the times for states 1) and 2) as well as 3) and 4), might change, while maintaining the overall outage time of „1) + 2)“ and „3) + 4)“. The total time changes only if the Sun's path is not parallel to the detector's axes. This situation in general decreases outage times, except for when the path is close to any of the detector's diagonals, in which case they amount to the geometrical sum of the outages as presented. Furthermore, in the case for LEO, as soon as the orbit is inclined, the figures represent the worst case. In some orbit-passes the sensor might never see the Sun. In the special case of a dawn-dusk SSO, no outages will occur throughout nominal mission, while in a noon-midnight SSO, as in GEO, it occurs in every revolution.

In practical operations, the geometrical conditions leading to situation 1) can not be eliminated. In order to further obtain information on the spacecraft's attitude, some kind of shutter mechanism should be considered. Alternatively, the spacecraft's attitude could be propagated, as long, as the predicted outage times and the attitude accuracy requirements are not too severe. Be aware that using the Sun-and Earth-vector for attitude determination in this case results in a poor knowledge of the three-axis attitude, due to the near-co-alignment of Sun and Earth.

Situation 2) does not represent major difficulties, since, as demonstrated in chpt. 6.2, the spacecraft's position can be propagated with sufficient accuracy over a longer period of time, while the attitude can still be observed by the Star-FOV. The corresponding Earth-center can then be determined using this information.

Situations 3) and 4) represent the major challenges. For all practical purposes, Star-sensors are located and oriented such that they do not point at the Sun in any period of the satellite's nominal mission. Such, these cases represent an abnormal situation. If situations like these need to be covered without shutters, the demands on the propagation of the satellite's attitude are severe. If the Star-FOV can be attenuated, the Earth-center information can further be used for two-axes attitude determination, the third axis would still need to be propagated in case of complete shut-off of the Star-FOV. This is equivalent to a sensor-suite consisting of Earth- and Sun-sensors during eclipse, which only leaves the Earth-reference for two-axes attitude determination. Depending on the spacecraft's setup, the motion of this axis might be coupled with the other two, simplifying this effort. In case the FOV can be attenuated enough as not to saturate the detector, at least in situation 3) the sensor-suite could act as a combined Earth-/Sun-sensor, allowing for resolving the three-axes attitude. This leaves situation 4) as the one most difficult to cover, since at times differentiation between Earth and the coinciding Sun might not be possible. Further enhancement of the image-processing techniques and improvement of the mechanical layout could cover this, but lead to a more complex system. For instance, at these times, the attenuated Star-FOV could be completely shut-off each second exposure, allowing for discrimination of the Sun's signal in the combined images.

One further possibility to cover situations 3) and 4) might be realized in case the Star-FOV can be shut-off: Since the Sun is seen in the Star-FOV, this implies that the Earth is partly lit - in our case to about 50%. This results in two prospects: The use of the terminator, so the day-/night-division, and landmarks, e.g. coastal lines, for three-axes attitude-determination. Feasibility tests on METEOSAT-images on using the terminator for determination of the Sun-direction lead to accuracies of approx. 7° about the LOS and 20° in the Earth-Sun-satellite plane, where the parameter of interest in general is only the angle about the LOS. This changes only, if the observation is to be used as a Sun-sensor replacement. The low performance can be explained by the „fuzzy“ nature of the terminator, which highly depends on the local landscape and cloud coverage. This leads to the conclusion that, even though the use of landmarks is computational burdensome and more difficult to tackle, it might lead to better results, if the landmarks are not obstructed by clouds. The idea of using the terminator for attitude determination is as well pursued by Mortari ([63]) and Svensson ([18]).

As a conclusion, it can be stated that, regardless of the different FOVs and methods when dealing with Sun incidence, Sun incidence remains a nuisance in the attitude determination. Nevertheless, Sun-incidence can be avoided, as far as the Star-FOV is concerned, and does not represent a problem during eclipse, where the position can be propagated and the attitude can be determined by the Star sensor. This leaves only state 1), which has to be dealt with, where additionally in

some cases the outage time for state 1) is that of „1)+2)“ of the case presented. Depending on the required attitude accuracy, this time can be covered by pure propagation, the use of gyros, or the use of shutters, which close the Earth-FOV and thereby allow for attitude determination using the Star-FOV. If no shutters are used, the two FOVs can not be treated independently, since their images are combined onto a single detector.

8.3 General Considerations

To minimize the cost and complexity of autonomous attitude and orbit determination, gyroless operation is of great interest. To date, it has successfully been implemented in a wide range of satellites and missions (e.g. Intelsat V (MBB), ERS-2 (ESA), Beppo-Sax (Alenia Spazio), SOHO (ESTEC, Matra Marconi Space). Various algorithms have been developed, taking into account different levels of modeling and thus different states of the filters used. These range from purely kinematic relations to the inclusion of the craft's angular momentum and modeled as well as stochastic external torques (e.g. [24, 27]). The difference in the sensor as proposed in this thesis is that in general, due to their smaller FOV, the outage times of systems using IR-sensors are far below those expected for our system, as long as no precautions against Sun-blinding are taken. It needs to be stressed, though, that the attitude of the satellite about the IR-sensor's boresight as well needs to be propagated during eclipse, since in general, an IR Earth-sensor is augmented by a Sun-sensor for three-axis reference (see fig. 1.2). In case of eclipse and (near-)collinearity, which means, when the Earth, the satellite and the Sun form a straight line, information on the attitude about this axis can not be obtained. The main advantage of gyros, apart from their insusceptibility to optical influences, is their higher bandwidth, the main drawback their drift and drift rate, which require frequent calibration. With conventional Star-cameras (definition see chpt. 1), using Star-tracking for rate determination, as introduced in chpt. 3.1.5, reduces the computational load, but does not cover a higher bandwidth than the Star-sensor, as long as the same hardware is used. The bandwidth in this case is limited by physics, rather than computational power: Since the SNR for Star-detection and centroiding has to be high enough to be discernible from photon-noise and other noise-sources, the exposure time needs to be high enough to guarantee observability of Stars with a certain magnitude. Alternatively, the optics could be changed, which would change the system's specifics. A higher sensitivity would require a larger lense diameter, which, for physically realizable systems, reduces the FOV. The negative effects are twofold: First, the FOV was specifically designed to be large enough to cover the Earth and Stars simultaneously. Second, the increased sensitivity results in the necessity to account for galaxies in the Star-observation, since they can be detected starting from approx. $m_V = 7$ (e.g. [64]). For an optical system designed for highest

sensitivity with a given FOV, this leaves the exposure time, and thus the frame rate, as the only variable. Considering that the system needs an exposure time of approx. 1 sec. for detection of Stars with magnitude $m_V = 6$, the detection-limit reduces with increased angular velocity, since the Star is spread over several pixels. In the case given, this results in the necessity of Stars with $m_V < 2$ for angular rates with $\omega > 3^\circ/\text{s}$. The probability of observing 3(2) Stars with $m_V < 2$ in a FOV with a total viewing angle of 25° is already reduced to 70(27)%. Due to the detector's rectangular shape, the effective FOV is reduced to about 20° . This reduction has been taken into account in the probability-calculation. The constraint of a close to 100% observation probability can be relaxed, since a larger fraction of the celestial sphere is covered due to satellite motion. Three observed Stars are preferred, especially when their magnitude is close to the detection limit, since they allow for a higher identification probability to guarantee the tracking process captured the same Stars in two consecutive images.

In the position determination, as discernible from the simulation results in chpt. 6.2, in general it is desirable to perform at least one complete orbit about the Earth (see [53]). This as well holds for other reference-bodies, e.g. Mars. In the case of interplanetary missions, with the Sun as reference, this is not feasible, demanding for a higher accuracy in the initialization (AutoNav on DeepSpace1: Settling time ≈ 1 month [65]). Another interesting application would be a mission in one of the Lagrangian points of the Earth-Sun and the Earth-Moon system. As estimations show that the Earth can be observed up to a distance in the order of 30 a.u., the Earth can still be used as reference body.

Chapter 9

Lessons Learned and Conclusions Drawn

9.1 Lessons Learned

In addition to the overall positive results presented, there are further possible improvements. This chapter introduces some proposals for future investigations. Though not all improvements can be covered, they illustrate the target of this project and the results obtained.

9.1.1 Lessons Learned From MITA

Since the space industry does not request great quantities of MST components, it is not a driver for new developments in this technological area. To profit from developments in this fast expanding field it is advantageous to look for off-the-shelf components or components in an advanced status of development. To close the gap to space, „rapid prototyping“ to specific space needs and early „in-orbit demonstration“ is helpful. The objectives of the MTS-AOMS flight experiment were:

- to select MST components which have the potential to substitute components in traditional Attitude and Orbit Measurements Systems (AOMS),
- to build a functional model and to bring it into space quickly,
- to determine the performance and reliability under space conditions.

The benefit of this experiment was to get early experience of the behavior of MST in space and to promote its further application in satellite systems. Furthermore, the augmentation of the optical system by other means of attitude and attitude rate measurements made the experiment inherently more significant.

The experiment was successfully completed after 229 days in orbit. This makes the experiment the so far longest in-orbit test of MST components.

The evaluation of flight results from the MTS-AOMS experiment indicated the following additions for future missions: In all, the evaluation of the flight data was made difficult because not all information on the state of the satellite were available. This in particular prevented the comparison of the spacecraft's position as determined by the algorithms developed to the actual position. The use of ephemeris data as means of *a posteriori* determining this value proved to be insignificant due to the low orbit of the satellite, which introduced a high deviation from the theoretical data due to atmospheric drag.

9.1.1.1 Optical System

Depending on the detector, another effect has to be taken into account: the difference in the read-out time when comparing the upper-left to the lower-right pixel. Since in many cases, especially conventional CCD-cameras and current „standard“ APS-detectors, the pixels are addressed consecutively, the exact point of time, at which the pixel's exposure starts, is different for each pixel. This leads to an additional apparent motion of the Stars in case the attitude changes throughout the read-out time of the array. Knowledge of the camera's motion can be used to take this effect into account. Additionally, this effect changes the angular separation between the Stars, thus the need for higher inter-Star-angle tolerances arises, in case the sensor is not in tracking mode. In case of „high speed“ maneuvers, the centroiding itself is effected, not only due to smear, but due to the fact that the „upper“ part of the Star-image is gathered earlier than the „lower“ part, thus shearing the Star, depending on the change in attitude. To eliminate this effect, it is desirable to use information on the spacecraft's angular velocity, e.g. determined by rate sensors, to increase the accuracy and bandwidth especially at higher angular velocities, which might be covered using MEMS gyros. As solution to this problem, there are on-going developments using APS-detectors to enable a synchronous exposure time of the whole detector area (as it is the case with some film cameras) to eliminate this effect.

While the APS-detectors are not destroyed by direct Sun incidence, it was shown that the incident Sun otherwise inhibits Star-identification by flooding the detector with straylight. Thereby the experiment demonstrated the vital necessity to adaptively attenuate at least the Earth-FOV.

A natural addition to any optical sensor is an adequate baffle design, which only due to restrictions in the system's dimensions was not included in the experiment.

9.1.1.2 MEMS Components

In the post-processing of the flight data it was advantageous that the acquisition of the magnetometer data was performed simultaneously to that of the on-board magnetometer, which allowed for a direct comparison.

Had the sensors been operated simultaneously, the information gained from the optical system, could have been used for validation of the magnetic-field sensor as well as the integrated gyro-signal.

The reverse process as well is valid: Using this information, in addition to the Earth-vector and the Star-identification, the consequent attitude determination could have been validated more easily.

Since the satellite did not use any rate sensors, the comparison of the MEMS to a known system was difficult, yet a comparison of the processed data obtained from the gyros and the magnetometer showed a consistent behavior ([2]). The comparison could have been further improved, had the magnetometer data been corrected using the satellite's position and the known magnetic field of the Earth. Further investigations on possible ways of obtaining rate information led to the conclusion that, while it is possible to use delayed quaternion measurements, this reduces the bandwidth while increasing noise, due to the derivation of the signal and the relatively low frequency, with which the attitude is determined.

Therefore in future missions the data of complementary systems should be synchronized simultaneously available.

9.2 Recommendations

From the observed behavior, recommendations for future development arise. These include algorithmic, software, hardware and experimental modifications.

In **future experiments**, more data should be gathered in order to validate the system's predicted accuracies. These data-sets need to include the complete state of the satellite at each sample point. In particular this would be the position, an attitude and a rate reference, as it could for instance be provided by the satellite's AOCS. Additionally, the information from the experimental sensors involved should be gathered simultaneously, in order to allow for their combination.

The inherent advantage of a combined system, using **Star-sensors** and **gyros** is the mutual benefit: The gyros can be calibrated for bias and certain fractions of the drift during slow maneuvers, while the Star-sensor can be supported during fast maneuvers (see e.g. [2]). The additional advantage

of angular velocity information is the use in predictive centroiding of Stars, thus reducing the time necessary for Star-detection and identification, while increasing the system's accuracy.

While the **Star-identification algorithm** as presented is an „acquisition“-algorithm, not using any *a priori* information, its speed can be dramatically increased by prediction of the sensor's attitude for the next step. This information can be used by implementing a Star-catalog which is divided in sub-catalogs to be searched for the detected Stars. Alternatively, the position of individual Stars' in the next frame can be propagated, using for instance a Kalman-filter, and performing *Star-tracking* rather than *Star-identification*.

The use of a **Kalman-filter** additionally might increase the system's accuracy, either actually filtering the attitude itself (e.g. [25]), or the individual Star-positions (e.g. [23]). The advantages in the tracking of Stars are the lower identification time and the possibility of eliminating false Stars from the identification process.

Using the expected **asymmetric accuracy** for each measurement direction (x, y) , rather than using the same accuracy for both measurements, as mentioned previously (chpt. 3.1.4), results in the interest to find an alternative algorithm for attitude determination using Star-measurements. Especially in the case of simple commercial optics combined with a large FOV, this might lead to higher accuracies, without any changes in the hardware used.

In order to remove the inaccuracies due to the different read-out time, the arising technology in APS-detector, allowing for simultaneous start and end of exposure for all pixels, should be further investigated.

The most important change, which should be implemented, is an **adaptive filter** for at least the Earth-FOV, if possible for both FOVs. The development of Liquid Crystal Displays (LCD) fortu-

Table 9.1: Extensions to a „multi-mode sensor“ by choice of (adaptive) filters

Filter for → combined with ↓	Star-observation	Earth-observation	Sun-observation
Star-observation	Increased accuracy about LOS	Earth-bound on-board autonomous navigation	Interplanetary on-board autonomous navigation
Central-body observation	Central-body bound on-board autonomous navigation	-	-

nately was accompanied by emerging filters, based on the same technology: Filters and shutters based on liquid crystal technology were developed, which by now have a rather high attenuation (approx. 1000 for shutters, 100 for variable filters [e.g. CRL-Opto]) and a variation speed which is far above our needs. Using, for instance, a shutter and a filter in union, would result in a high dynamic range, with variable filter settings, thus allowing an increased range of applications (e.g. Sun-sensing, increased reliability). Even a single shutter in front of the Earth-FOV would prevent the saturation of the detector in case of incident sunlight close to the eclipse condition, and therefore allow uninterrupted attitude measurements using the Star-FOV. An additional solar array which provides the shutter with the necessary power for switching to the „off“ position would as well result in a safe design, in case the solar array only provides enough power when the sensor is pointing towards the Sun. Using an adaptive filter would allow the detection of a larger fraction of the limb during low lighting conditions. A combination of both might lead to a variable „multi-mode sensor“, which for instance could be switched to a „Star-Star Sensor“-mode, so a Star-sensor with two lines of sight, which in top of increasing the accuracy about the boresight would introduce a simple means for autonomous on-board calibration of the sensor. This, for instance, would as well facilitate investigations on the actual behavior of the partially transmissive mirror under thermal stress. Examples of further extensions are given in tab. 9.1. This idea has been manifested in a pending patent ([6]) by the author and affiliates. The available technology needs to be tested and maybe altered for use in Space. To our knowledge no Space-applications have been developed so far, using these systems, even though they might be advantageous in that they avoid moving elements.

A different way of increasing the system's accuracy is to allow for Star-observation in the center of the FOV. The reason for this is the deviation of the Star-images from the expected circular shape, as shown in chpt. 3.1.1, resulting in a lower accuracy in at least one of the two directions. One way of achieving this new observation strategy, is to move the image of the Earth in the four corners, leaving empty space for Stars in the center, while only insignificantly reducing the accuracy of the Earth-horizon detection. The schematics can be seen in fig. 9.1. The idea has been submitted as a patent ([7]). Due to the rather high complexity of the proposed system, though, it might be a better trade-off to invest in higher accuracy optics.

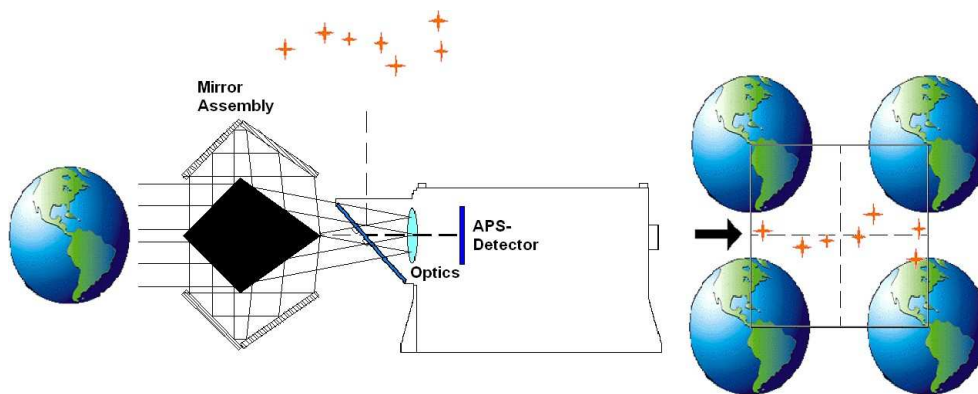


Figure 9.1: Freeing the center of the FOV for Star-observations

9.3 Conclusion

Based on the Ph.D-thesis „Einsatz richtungsmessender Sensoren in der autonomen Bahnregelung geosynchroner Satelliten“ by Juckenhöfel ([8]), the patent on a „Combined Earth-/Star-Sensor System and Method for Determining the Orbit and Position of Spacecraft“ developed at Daimler-Chrysler ([1]) and the encouraging results obtained by the MTS-AOMS flight experiment on MITA ([9]), this work successfully demonstrated the feasibility of the combined Earth- and Star-sensor for means of attitude and orbit determination. Technologically, this work is based on the emerging APS-detector technology in combination with low-cost consumer optics. In the process of the thesis, the limitation to GEO was dropped, since it was shown that the algorithms hold for virtually all orbits.

This work was engaged in determining the algorithms necessary and the performance of the system, the evaluation of experiments and the investigation of further improvements. The flight experiments have been amended by field and laboratory experiments, in order to validate the algorithms. The investigations on the algorithms showed that even the most-critical parameter, the distance from the Earth towards the satellite, can be determined either directly by using the apparent Earth-diameter, or by adequate filtering (e.g. Kalman-filtering). It should be noted, though, that a tremendous increase in accuracy is achieved once the satellite completed one orbit. Afterwards, accuracy increases only gradually.

The expected system accuracies at the current point, which compare well with the results obtained in the experiments carried out in the frame of this thesis, are summarized in table 9.2.

Table 9.2: Expected System Accuracies

Single Frame Earth-Reference	0.1° (1 σ)
Single Star Centroiding	10" (1 σ)
Inertial Attitude	6" [pitch, yaw] (25" [roll]) (1 σ)
Position	
Point Solution	60 km (1 σ)
Navigation Solution (after 2 – 3 orbits)	5 km (1 σ)

Even though the autonomous attitude and orbit determination using optical sensors might not reach the position accuracy of other systems, e.g. GPS, the accuracies achieved are satisfactory for many missions - and its advantage is obvious: The system is completely independent of any infrastructure and orbit and can be used with any target planet by a mere change of software.

In total, using the emerging APS- and MEMS-technology, an innovative system was successfully tested. This work facilitates the use of simple means to obtain full attitude and orbit information of a satellite, which can further be improved by the possibility of self-calibration. Encouraged by these positive results, the implementation of the gathered knowledge in a follow-up mission has been proposed to ESA.

Thus, the sensor presented is another step towards the „Final Frontier“.

Bibliography

- [1] H. Diehl; W. Platz; H. Zinner; E. Gottzein. Kombiniertes Erd-Sternsensor für gleichzeitige Bahn- und Lagebestimmung. *Patent: DE 19846690 A1*, 1998.
 - [2] D. Behrenwaldt. Drehratensensoren zur Stützung optischer Systeme. Master thesis, Universität Stuttgart, Germany, 2002.
 - [3] C.T.F. Kuehl; M. Melf; H. Diehl; E. Gottzein. Micro-Tech.-Sensor for Attitude and Orbit Determination, AAS 03 – 001. *Advances in the Astronautical Sciences*, 2003.
 - [4] C.T.F. Kuehl; M. Melf; H. Diehl; E. Gottzein. Flight Test Results of the Micro-Tech.-Sensor for Attitude and Orbit Determination. In *Fourth Round Table on Micro/ Nano Technologies for Space*. ESTEC, May 2003.
 - [5] C.T.F. Kuehl; M. Melf; H. Diehl; E. Gottzein. Experimental Evaluation of the Micro-Tech.-Sensor for Attitude and Orbit Determination. In *16th IFAC Symposium on Automatic Control in Aerospace*. IFAC, June 2004.
 - [6] C.T.F. Kuehl; M. Melf. Verfahren und Anordnung zur Steuerung des Strahlungseinfalls in einen optischen Empfänger eines Raumfahrzeuges. *Pending Patent: P610949*, 2003.
 - [7] C.T.F. Kuehl; M. Melf. Verfahren und Empfänger zur gleichzeitigen Erfassung und Auswertung von mindestens zwei elektromagnetischen Signalen. *Pending Patent: P610946*, 2003.
 - [8] O. Juckenhöfel. Einsatz richtungsmessender Sensoren in der autonomen Bahnregelung geosynchroner Satelliten. PhD thesis, Universität Stuttgart, Germany, 2001.
 - [9] M. Melf; S. Manhart; C. Kuehl; D. Behrenwaldt. MTS-AOMS - MicroTechSensor for Attitude and Orbit Measurement Systems. Final Report MTS-TR-007, Astrium GmbH, Germany, 1994.
 - [10] W. Fichter; A. Konrad; P.A. Krauss; M. Mitnacht; P. Ruhland; T. Vogel. The MosaicAODS Technology for Autonomous Spacecraft GNC Systems. In *ESA Workshop on On-Board Autonomy*. ESTEC, October 2001.
 - [11] G. Falbel. Three axis earth/star sensor. *U.S.Pat.No. 5,189,295*, 1991.
-

-
- [12] R.J. Magee. An Automatic Space Sextant for Space Navigation. In *Space Flight Report to the Nation*. American Rocket Society, October 1961.
- [13] A.D. Mikelson. Integrated Orbit/ Attitude Determination. In *AGARD Spacecraft Pointing and Position Control*. AGARD, November 1981.
- [14] J.R. Wertz [Ed.]. *Spacecraft Attitude Determination and Control*. Kluwer Academic Publishers Group, 1994.
- [15] U. Schmidt; D. Wunder; E. Graf. Intelligent Modular Star and Target Tracker- A New Generation of Attitude Sensors. In *Proceedings Third ESA Conference on Spacecraft Guidance, Navigation and Control Systems, ESA SP-381*, pages 53– 57. ESTEC, November 1996.
- [16] J.L. Joergensen; C.C. Liebe; A.R. Eisenmann; G.B. Jensen. The Advanced Stellar Compass Onboard the Oersted Satellite. In *Proceedings Third Conference on Spacecraft Guidance, Navigation and Control Systems, ESA SP-381*, pages 303– 308. ESTEC, February 1997.
- [17] C. Beard; G. Hayhurst. The MOSAIC Earth Sensor - A Novel Sensor Development For Geostationary Spacecraft. In *Proceedings Second Conference on Spacecraft Guidance, Navigation and Control Systems, ESA WPP-071*, pages 209– 215. ESTEC, April 1994.
- [18] L.B.M. Svensson; S. Lindau; P.B. Bjur us; S. Hansson; A. Agoston. Yaw Earth Sensor Engineering Model. In *International Workshop on Spacecraft Attitude and Orbit Control, ESA WPP-129*, pages 223– 234. ESTEC, IFAC, September 1997.
- [19] J.A. Billing-Ross; D.B. Pledger; T.A. Fritz. Apparatus for determining 3-axis space craft attitude. *U.S.Pat.Nos. 5,319,969 and 5,319,968*, 1992 and 1994.
- [20] J.A. Billing-Ross; T.A. Fritz; D.B. Pledger; R. Castain; W. Saylor. A Low Cost Ultraviolet Solid State Sensor System for the Three Axis Attitude Determination, AAS 93 – 013. *Advances in the Astronautical Sciences*, 81(1):25– 32, 1993.
- [21] N. Blanc. CCD versus CMOS - has CCD imaging come to an end? *Photogrammetric Week '01*, pages 131– 137, 2001.
- [22] ESOC/ESA. <http://www.esoc.esa.de/external/mso/hipparco.html>, November 1997.
- [23] M.A. Samaan; T.C. Pollock; J.L. Junkins. Predictive Centroiding for Star Trackers with the Effect of Image Smear. *Journal of the Astronautical Sciences*, 50(1):113–123, 2002.
- [24] Y. Oshman; F.L. Markley. Sequential Gyroless Attitude/ Attitude-Rate Estimation Using Integrated-Rate Parameters, AIAA 98 – 4508. *Journal of Guidance, Control and Dynamics*, 22(3):385–394, 1999.
-

-
- [25] B. Quine; H.F. Durrant-Whyte. An Improved Navigation Algorithm for On-Board Attitude Determination, AAS 95 – 011. *Proceedings of the Rocky Mountain Guidance and Control Conference*, 1995.
- [26] G.N. Rao; T.K. Alex; M.S. Bhat. Incremental-Angle and Angular Velocity Using a Star Sensor. *Journal of Guidance, Control and Dynamics*, 25(3):433–441, 2002.
- [27] M.D. Shuster. Kalman Filtering of Spacecraft Attitude and the QUEST Model. *Journal of the Astronautical Sciences*, 38(3):377– 393, 1990.
- [28] O. Montenbruck; E. Gill. *Satellite Orbits: Models, Methods, Applications* . Springer-Verlag, Berlin, 2000.
- [29] M.S. Grewal; A.P. Andrews. *Kalman Filtering: Theory and Practice Using MATLAB* . Wiley-Interscience, John Wiley & Sons, New York, 2001.
- [30] S.P. Airey; G. Berrighi; D. Procopio. Seeing Through Dust - Tracking Stars from within a Cometary Dust Cloud, AAS 03 – 022. *Advances in the Astronautical Sciences*, 2003.
- [31] D. Kavaldjiev; Z. Ninkov. Subpixel sensitivity map for a charge-coupled device sensor. *Optical Engineering, SPIE*, 37(3):948– 954, 1998.
- [32] M.A. Samaan; T.C. Pollock; J.L. Junkins. Recursive Mode Star Identification Algorithms. *AAS/AIAA Flight Mechanics Meeting, Santa Barbara*, AAS 01 – 149, 50(1):113–123, 2002.
- [33] D. Mortari; B. Neta. k- Vector Range Searching Techniques, AAS 00 – 128. *Advances in the Astronautical Sciences*, 105(1):449– 463, 2000.
- [34] D. Mortari; J.L. Junkins; M.A. Samaan. Lost-In-Space Pyramid Algorithm For Robust Star Pattern Recognition, AAS 01 – 004. *Advances in the Astronautical Sciences*, 107:49–68, 2001.
- [35] B. Quine. *Spacecraft Guidance Systems-Attitude Determination using Star Camera Data*. PhD thesis, Robotics Research Group, Department of Engineering Science, University of Oxford, 1996.
- [36] H.L. Fisher; T.E. Strikwerda; C.C. Kilgus; L.J. Frank; M.D. Shuster. Autonomous, All-Stellar Attitude Determination Experiment: Ground Test Results. *Advances in the Astronautical Sciences, Guidance and Control*, 74:69– 83, 1991.
- [37] G. Wahba. A Least Squares Estimate of Spacecraft Attitude. *SIAM Review*, 7(3):409, July 1965.
-

-
- [38] F.L. Markley; D. Mortari. Quaternion Attitude Estimation Using Vector Observations. *Journal of the Astronautical Sciences*, 46(2 and 3):359–380, April-September 2000.
- [39] F.L. Markley. How to Estimate Attitude from Vector Observations, AAS 99 – 427. *Advances in the Astronautical Sciences*, 103(3):1979– 1996, 1999.
- [40] F.L. Markley; I.Y. Bar-Itzhack. Unconstrained Optimal Transformation Matrix. *IEEE Transactions on Aerospace and Electronic Systems*, 34(1):338– 340, 1998.
- [41] J.E. Brock. Optimal Matrices Describing Linear Systems. *AIAA Journal*, 6(7):1292– 1296, 1968.
- [42] J.L. Crassidis; F.L. Markley. Predictive Filtering for Attitude Estimation Without Rate Sensors. *Journal of Guidance, Control and Dynamics*, 20(3):522– 527, 1997.
- [43] B.K.P. Horn; B.G. Schunck. Determining Optical Flow. In *Artificial Intelligence*, volume 17, pages 185– 207, 1981.
- [44] D. Mortari. StarNavIII: A Three Fields of View Star Tracker. *IEEEAC Paper No.50*, 2001.
- [45] A. W. Fitzgibbon; M. Pilu; R. B. Fisher. Direct Least Square Fitting of Ellipses. *IEEE Transactions on Pattern Analysis and Machine Intelligence*, 21(5):476– 480, 1999.
- [46] R. Halíř and J. Flusser. Numerically stable direct least squares fitting of ellipses. In *Proc. 6th International Conference in Central Europe on Computer Graphics and Visualization. WSCG '98*, pages 125– 132. CZ, Plzeň, Czech Republic, February 1998.
- [47] W. Gander; G.H. Golub; R. Strebler. Fitting of Circles and Ellipses Least Square Solution. Technical Report TR-217, ETH Zürich, Schweiz, 1994.
- [48] D. Meller; P. Sipruetkiat; K. Makovec. Digital CMOS Cameras For Attitude Determination. *Proceedings of the 14th AIAA/USU Conference on Small Satellites*, August 2000.
- [49] R. H. Battin. *Astronautical Guidance*, page 229 ff. McGraw-Hill, 1964.
- [50] M. Vasile; M. Romano; F. Trainiti. An Optical Based Strategy for Deep Space Autonomous Navigation. In *Proceedings Fourth ESA Conference on Spacecraft Guidance, Navigation and Control Systems, ESA SP-425*, pages 549– 554. ESTEC, November 2000.
- [51] J.R. Wertz. Autonomous Spacecraft Navigation System. *U.S.Pat.No. 5,109,346*, 1990.
- [52] S.D. Dawson; L.W. Early; C.W. Potterveld; H.J. Königsmann. Low-Cost Autonomous Orbit Control About Mars: Initial Simulation Results. *3rd IAA International Conference on Low-Cost Planetary Missions*, 1998.
-

-
- [53] A.J. Claus. Orbit Determination For Communication Satellites from Angular Data Only (ARS-2624 - 62). In *17th Annual Meeting And Space Flight Exposition*. American Rocket Society, November 1962.
- [54] G.H. Born; D.B. Goldstein; B. Thompson. An Analytical Theory for Orbit Determination. *Journal of the Astronautical Sciences*, 49(2):345- 362, 2001.
- [55] B. Friedland. Treatment of Bias in Recursive Filtering. *IEEE Transactions on Automatic Control*, 14(4), 1969.
- [56] A. Konrad. MosaicGNSS Receiver - Orbit Perturbation Models. Technical Description MosaicGNSS-48-100, Astrium GmbH, Germany, 2001.
- [57] W. Seitz; H. Steiner. OESS Technical Description. Technical Description OESS-TD-2100-01-02 Rev.C, DaimlerChrysler Aerospace, Germany, 2000.
- [58] W. Seitz; H. Steiner. OESS for Melco. Maintenance and User's Manual OESS-mm-0100-01-00 Rev.B, Daimler-Benz Aerospace, Germany, 2000.
- [59] EUMETSAT. The Meteosat Archive - User Handbook, 2003.
- [60] EUMETSAT. www.eumetsat.de/en/mtp/space/radiometer.html, 2.6 edition, November 2001.
- [61] D.P. Wylie; W.P. Menzel; H.M. Woolf; K.I. Strabala. Four Years of Global Cirrus Cloud Statistics Using HIRS. *Journal of Climate*, 7(12):1972- 1986, 1994.
- [62] R.W.H. van Bezooijen. Autonomous Star Tracker for Geostationary Satellites. *Proceedings of SPIE*, 2812:847- 858, 1996.
- [63] D. Mortari; S. Gigli. Earth-Sun Attitude Sensor: Hardware Design and Ground Tests, AAS 99 - 438. *Advances in the Astronautical Sciences*, 103(3):2145- 2159, 1999.
- [64] T. Riis; J.L. Joergensen. Tracking Non- Stellar Objects on Ground and in Space. In *ESA 4th Symposium on Spacecraft Guidance Navigation and Control*. ESTEC, 1999.
- [65] J.E. Riedel. Using Autonomous Navigation for Interplanetary Missions: Mission Operations with DeepSpace1 AutoNav. In *ESA Workshop on On-Board Autonomy*. ESTEC, October 2001.
-

Appendix A

Appendix

A.1 Algorithms

A.1.1 Star-Identification, Example

In the following, an example for the Star-identification process is given. It is to be taken as an illustration for the steps covered in chpt. 3.1.3.1.

The Star-image to be identified is shown in fig. A.1. It includes the information on the optical coordinates of the Star-centers in units of pixels. The Star-catalog shall consist of two constellations as shown in fig. A.2.

For **Step 1**, the unit vectors to the measurements need to be determined using the centroiding process and the angles between them need to be calculated and stored in a way that maintains the information on the relation between the measurements and the angles. In this result, measurement 4 is placed in the center of the FOV and the focal length f is chosen as 3432 pixels. The result is a table as the one given in tab. A.1. The resulting table containing the angular separations between the measurements is given in tab. A.2. The Star-catalogue chosen for this example is given in tab. A.3. The corresponding angular separations are given in tables A.4 and A.5. The reason for having two distinct parts of the catalogue is, that the angles between Stars taken from the two different parts are larger, than the size of the FOV. This means, that Stars from the two parts can not be detected simultaneously. According to the angular separation, the matches are given in tab. A.6.

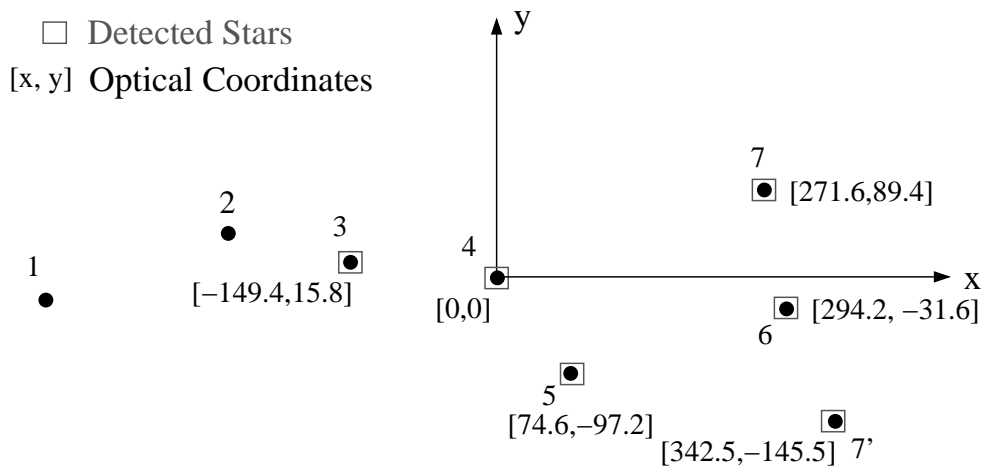
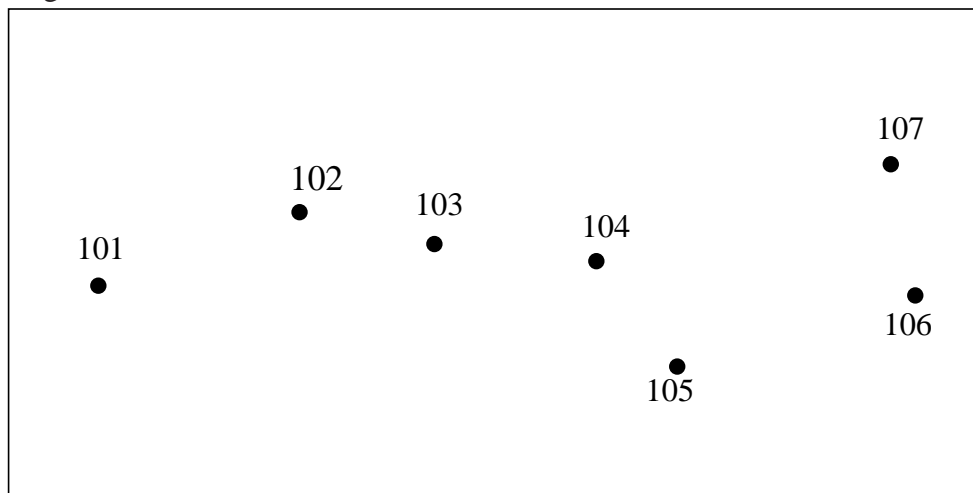


Figure A.1: Image to be identified

a) Star-catalogue - Part 1



b) Star-catalogue - Part 2

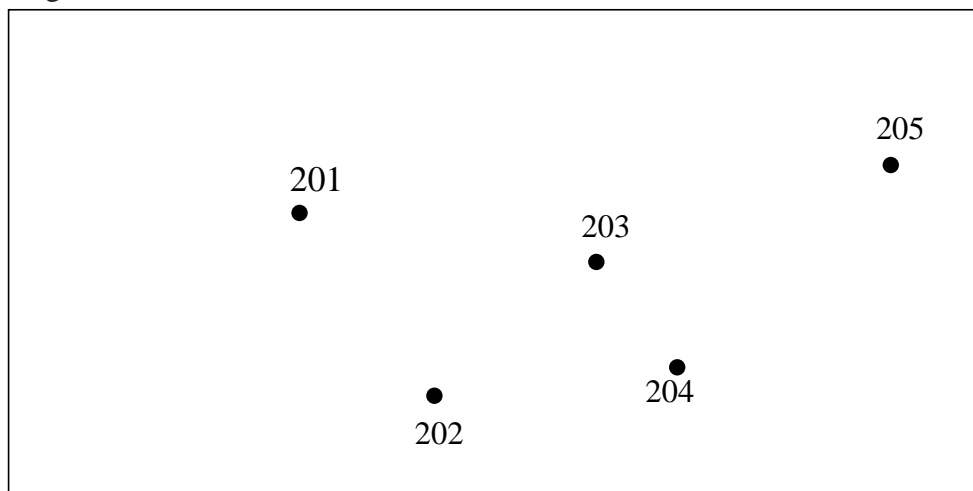


Figure A.2: Star-patterns contained in the Star-catalogue

Table A.1: Unit vectors to the measurements [-]

„3“	[-0.0430	0.0046	0.9991]
„4“	[0.0000	0.0000	1.0000]
„5“	[0.0217	-0.0283	0.9994]
„6“	[0.0854	-0.0092	0.9963]
„7“	[0.0789	0.0260	0.9965]
„7*“	[0.0992	-0.0422	0.9942]

Table A.2: Angles between measurements [°]

Measurement number	„3“	„4“	„5“	„6“	„7“	„7*“
„3“	-	2.4787	4.1598	7.4062	7.0975	8.5905
„4“		-	2.0436	4.9275	4.7655	6.1888
„5“			-	3.8151	4.5231	4.5231
„6“				-	2.0511	2.0511
„7“					-	4.0778
„7*“						-

In **Step 2**, where finally Star-pairs are combined to triangles, each measurement is chosen as a „Pivot Star“. This means, that the measurement is chosen as a starting point of two angles. In addition to using two angles which are connected to this measurement, they both need to comprise the same Star. According to tab. A.6 this means that, if measurement „7“ is chosen, valid combinations would be either two of $103 \leftrightarrow 107$, $104 \leftrightarrow 107$, $105 \leftrightarrow 107$ and $106 \leftrightarrow 107$, or the combination of $203 \leftrightarrow 205$ with $204 \leftrightarrow 205$. The end-points of the two chosen combinations then compose an additional Star-pair, e.g. $203 \leftrightarrow 204$, which is searched for in the already identified matching angles, i.e. in table A.6. If the pair is present in the table and combines the correct measurements, the triangle is declared to be a candidate for the further process. All triangles fulfilling these requirements are given in tab. A.7. As obvious from the column containing the Star-IDs, the lines marked with an asterisk contain invalid triangles, which are excluded by the criterion, that the three IDs and the three measurements need to be distinct. Therefore these lines do not enter the identification process and are only given for completeness.

In **Step 3** the sense of rotation of the triangle on the detector is compared to that of the corresponding Star-candidates. The results are given in tab. A.7 along with the found triangles. Those triangles, for which the senses of rotation match are kept, those, where the sign differs are discarded.

Table A.3: Unit vectors contained in the Star-catalogue [-]

„101“	[-0.9911	0.0065	0.1327]
„102“	[-0.9941	0.0131	0.0795]
„103“	[-0.9990	0.0046	-0.0430]
„104“	[-1.0000	0.0000	0.0000]
„105“	[-0.9994	-0.0283	0.0217]
„106“	[-0.9963	-0.0092	0.0854]
„107“	[-0.9965	0.0260	0.0789]
„201“	[0.9967	0.0131	-0.0797]
„202“	[0.9984	0.0359	-0.0435]
„203“	[1.0000	0.0000	0.0000]
„204“	[0.9994	-0.0283	-0.0217]
„205“	[0.9965	0.0260	-0.0789]

Table A.4: Angles between Stars in catalogue - Part 1 [°]

Measurement number	„101“	„102“	„103“	„104“	„105“	„106“	„107“
„101“	-	3.0772	10.0912	7.6351	6.6858	2.8713	3.2939
„102“		-	7.0537	4.6337	4.0882	1.3208	0.7387
„103“			-	2.4787	4.1598	7.4062	7.0975
„104“				-	2.0436	4.9275	4.7655
„105“		symm.			-	3.8151	4.5231
„106“						-	2.0511
„107“							-

Table A.5: Angles between Stars in catalogue - Part 2 [°]

Measurement number	„201“	„202“	„203“	„204“	„205“
„201“	-	2.4527	4.6337	4.0882	0.7387
„202“		-	3.2333	3.8858	2.1091
„203“			-	2.0436	4.7655
„204“		symm.		-	4.5231
„205“					-

In **Step 4** the remaining triangles are combined along common sides, where again care is taken, that the measurement, as well as the Star-candidates match. In the given example, this results in polygons with the corners as given in tab. A.8.

Table A.6: Matching Angles

Measurement number	„3“	„4“	„5“	„6“	„7“	„7*“
„3“	-	103 ↔ 104	103 ↔ 105	103 ↔ 106	103 ↔ 107	-
„4“		-	104 ↔ 105	104 ↔ 106	104 ↔ 107	-
		-	203 ↔ 204	-	203 ↔ 205	-
„5“			-	105 ↔ 106	105 ↔ 107	105 ↔ 107
			-	-	204 ↔ 205	204 ↔ 205
„6“				-	106 ↔ 107	106 ↔ 107
„7“		symm.			-	-
„7*“						-

Table A.7: Matching Triangles

Measurements	Sense of Rotation	Star-IDs	Sense of Rotation
„3“ „4“ „5“	-1	103 104 105	-1
„3“ „4“ „6“	-1	103 104 106	-1
„3“ „4“ „7“	1	103 104 107	1
„3“ „5“ „6“	1	103 105 106	1
„3“ „5“ „7“	1	103 105 107	1
„3“ „6“ „7“	1	103 106 107	1
„4“ „5“ „6“	1	104 105 106	1
„4“ „5“ „7“	1	104 105 107	1
		203 204 205	1
„4“ „6“ „7“	1	104 106 107	1
* „4“ „7“ „7“	-	104 107 107	-
„5“ „6“ „7“	1	105 106 107	1
„5“ „6“ „7*“	1	105 106 107	-1
* „5“ „7“ „7*“	-	105 107 107	-
* „6“ „7“ „7*“	-	204 205 205	-
* „6“ „7“ „7*“	-	106 107 107	-

Table A.8: Matching Polygons

Solution 1	„3“	„4“	„5“	„6“	„7“	103	104	105	106	107
Solution 2		„4“	„5“		„7“	203	204	205		

In **Step 5** the most likely solution is chosen by a user-defined criterion. In the present case, the most appropriate selection is that of the largest polygon. In the Star-identification algorithm as implemented, the additional information on the error made in the construction of the triangles is taken into account. This error is introduced by the measurement noise and inaccuracies of the optics. As a result the selection is based on the ratio „*mean error per triangle*“/„*number of triangles*“. In the given example, the measurements are exact. A typical value for real-sky measurements with the set-up as described in chpt. 7 is approx. 30” in the individual measurement, so the error per side is approx. $30'' \cdot \sqrt{2}$ (= 42.4”). If noise is introduced, both selection methods identify the correct „Solution 1“. During the identification process the false measurement was detected and removed.

A.1.2 Extended Wahba Problem

As mentioned in chpt. 3.1.4, an investigation on an alternative solution to the *Wahba-Problem* might be of interest when dealing with simple optics, providing different accuracies in the two sensing directions. This section will show the approach necessary and briefly discuss the achieved solutions.

The starting point to this approach is the original *Wahba-Problem*, which is stated as follows:

$$L(A) = \sum_i a_i \cdot (b_i - \underline{A} r_i)^2 \quad (\text{A.1})$$

The idea is, to find a way of differently weighting the individual components, according to their accuracy. This can be done by „scaling“ the vectors by use of a transformation matrix. Thus, the function might be rewritten as

$$L(A) = \sum_i (\underline{D}_i \cdot (b_i - \underline{A} r_i))^2 \quad (\text{A.2})$$

or alternatively

$$L(A) = \sum_i (b_i - \underline{A} r_i)^T \cdot \underline{D}_i^T \underline{D}_i \cdot (b_i - \underline{A} r_i) \quad (\text{A.3})$$

where a_i is substituted by $\underline{D}_i^T \underline{D}_i$, which corresponds to $\text{diag}([a_i(x), a_i(y), a_i(z)])$, with $a_i(j)$ as weight for the individual component j . This equation can further be expanded to lead to

$$L(A) = \sum_i \begin{bmatrix} b_i^T \cdot \underline{D}_i^T \underline{D}_i \cdot b_i \\ - 2 r_i^T \underline{A}^T \cdot \underline{D}_i^T \underline{D}_i \cdot b_i \\ + r_i^T \underline{A}^T \cdot \underline{D}_i^T \underline{D}_i \cdot \underline{A} r_i \end{bmatrix}. \quad (\text{A.4})$$

In A.4 it can easily be seen that the first line does not contribute to the optimization process, since it is independent on \underline{A} . Furthermore, the second component can be rewritten in the form

$$\sum_i -2 r_i^T \underline{A}^T \cdot \underline{D}_i^T \underline{D}_i \cdot b_i = -2 \text{tr}(\underline{A}^T \cdot \underline{D}_i^T \underline{D}_i \cdot b_i r_i^T), \quad (\text{A.5})$$

which again can be subsumed as

$$-2 \text{tr}(\underline{A}^T \cdot \underline{D}_i^T \underline{D}_i \cdot b_i r_i^T) = -2 \text{tr}(\underline{A}^T \cdot \underline{B}_S), \quad (\text{A.6})$$

which is the well known nomenclature for the standard *Wahba-Problem*. The problem associated with the expansion to a more universal formulation arises from the third line. In combination with the second, this leads to a nonlinear cost-function, which can, in general, not be solved as easily as the case for homogeneous weights. Note that, in case of $\underline{D} \equiv a_i \cdot \underline{I}$, the third line becomes independent of \underline{A} and thus the formula reduces to the original formulation.

An attempt was made, explicitly solving the system's cost-function, but did not lead to a system that is easily solved. The investigations were performed for the formulation in \underline{A} as well as in quaternion-notation.

While in this process, no analytical solution was found, numerical solutions showed that the formulation of an adequate functions defining the weights seems to bear its own set of challenges. Even in the case that the functions used for disturbing the simulations were used in the weights, the results did not necessarily improve. The nonlinear program was successfully tested for global convergence, leaving the definition of the weights as the critical parameter. As long, as no analytical solution to the problem is found, it will be difficult to define the right functions leading to an optimal solution. At the current point, after analysis of a wide range of simulations, which showed that, while there are cases, where the accuracy in attitude is increased, there are cases, where it is dramatically decreased, the author proposes to use the present solutions. Should the analytical solution be possible, though, it might be an alternative to increase the accuracy of simple systems.

A.1.3 Orbit Determination

This section shows two possible representations of orbital elements. The first set of equations derives the „classical (Keplerian)“ orbital elements from position and velocity, the second derives the „non singular (equinoctial)“ elements. The difference between the two representations is how the orbits with $i = 0$ and $e = 0$ are handled. In the classical orbital elements, this situation leads to an indeterminate state which needs to be detected and handled accordingly.

Classical (Keplerian) Orbital Elements

Taken from [28]:

$$\mu = 398600.44 \cdot 10^9 [km^3s^{-2}]$$

$$\underline{h} = \underline{r} \times \underline{v}$$

$$\underline{W} = \underline{h} / \|\underline{h}\|$$

$$p = \|\underline{h}\|^2 / \mu$$

$$a = \left(\frac{2}{r} - \frac{\|\underline{v}\|^2}{\mu} \right)^{-1}$$

$$e = \sqrt{1 - \frac{\|\underline{h}\|^2 / \mu}{a}}$$

$$i = \arctan \frac{\sqrt{W(1)^2 + W(2)^2}}{W(3)}$$

$$\Omega = \arctan -\frac{W(1)}{W(2)}$$

$$E = \arctan \left(\frac{\underline{r}^T \cdot \underline{v} / \sqrt{a \cdot \mu}}{1 - \|\underline{r}\| / a} \right)$$

$$M = E - e \cdot \sin(E)$$

$$u = \arctan \left(\frac{r(3)}{-r(1)W(2) + r(2)W(1)} \right)$$

$$v = \arctan \left(\frac{\sqrt{1-e^2} \cdot \sin(E)}{\cos(E) - e} \right)$$

$$\omega = u - v$$

Non Singular (Equinoctial) Elements

a , μ and \underline{W} are defined as above. The other components equal to (taken from [28]):

$$\begin{aligned}
 p &= \frac{W(1)}{1+W(3)} \\
 q &= \frac{-W(2)}{1+W(3)} \\
 \underline{A} &= \underline{v} \times (\underline{r} \times \underline{v}) - \mu \frac{\underline{r}}{\|\underline{r}\|} \\
 \underline{f} &= \frac{1}{1+p^3+q^2} \begin{bmatrix} 1-p^2+q^2 \\ 2pq \\ -2p \\ 2pq \\ 1+p^2-q^2 \\ 2q \end{bmatrix} \\
 \underline{g} &= \frac{1}{1+p^3+q^2} \begin{bmatrix} 1-p^2+q^2 \\ 2pq \\ -2p \\ 2pq \\ 1+p^2-q^2 \\ 2q \end{bmatrix} \\
 h &= \frac{A\underline{g}}{\mu} \\
 k &= \frac{\underline{A}f}{\mu} \\
 \beta &= \left(1 + \sqrt{1-h^2-k^2}\right)^{-1} \\
 X_1 &= \underline{r}^T \cdot \underline{f} \\
 Y_1 &= \underline{r}^T \cdot \underline{g} \\
 F &= E + \omega + \Omega \\
 \cos(F) &= k + \frac{(1-k^2\beta)X_1 - hk\beta Y_1}{a\sqrt{1-h^2-k^2}} \\
 \sin(F) &= h + \frac{(1-h^2\beta)Y_1 - hk\beta X_1}{a\sqrt{1-h^2-k^2}}
 \end{aligned}$$

Using these results, the eccentric longitude and the mean longitude can be determined.

A.2 Simulations

A.2.1 Simulation Environment

In the scope of this thesis, a simulation environment has been developed to facilitate various ranges of simulations and experiments. The tool was designed modular, such that it is possible to investigate different aspects. The first intention was a simulation of the satellite's orbit and the resulting images, as perceived by the sensor. This resulted in an orbit and attitude simulation, which checks for Earth- and Sun- presence in either of the FOVs and visualizes the appropriate output. The simulation was then augmented by the algorithms for position determination, testing different stages of its development, which finally resulted in a filter capable of coping with sensor outages. Step by step the simulation was extended by attitude determination, Star-identification, Star-detection, centroiding algorithms, horizon extraction and Earth-center determination. The low-level image-processing algorithms were not tested on simulated images, but verified in experiments prior to their implementation. The result is a simulation tool, which comprises all elements of the actual sensor. As mentioned, the simulation does not make use of the image-processing algorithms. These can be tested with real images, as provided by either the flight experiment, the field experiments or, in the case of Earth-images, by METEOSAT-data. Another opportunity arose with the inclusion of the optical testbed: since the Star-images were provided by an optoelectronic Star-simulator, this resulted in the possibility of including the camera-control and read-out algorithms as well as the image-processing in the simulation, which thereby constitutes part of the experimental setup. In these experiments, where only the Stars can be simulated, the Earth-vector was assumed to be known and subjected to white noise. The attitude dynamics have so far been restricted to ideal Earth/horizon pointing, but can easily be extended to cover real satellite dynamics. In a further extension of the optical experiment setup, an image of the Earth was provided by means of an illuminated sphere and a beamsplitter to resemble the actual sensor's arrangement. The drawback of the Earth simulation is that the Earth-vector is fixed, thus not allowing for any arbitrary dynamical motion.

The accuracy of the orbit-propagation for simulation and orbit determination can be chosen from *Keplerian* to *HPOP* in a setup file and by means of a graphical user interface (GUI), as seen in fig. A.3. The type of simulation as well is chosen by either a setup file or a GUI, as shown in fig. A.4. For a SSO, and the simulation parameters as set in the figures, the main window of the simulation tool will result in an image as given in fig. 7.3. In order to further improve the image processing algorithms, the tool was extended by the possibility of viewing the pixel values in an area close to the cursor. The resulting main window can be seen in fig. A.5.

In total, the simulation tool provides means for

- Attitude and Orbit simulation,
 - Attitude and Orbit determination algorithm verification,
 - Evaluation of real images,
 - Low-Level Image-Processing algorithm verification,
 - Control of Experimental equipment.
-

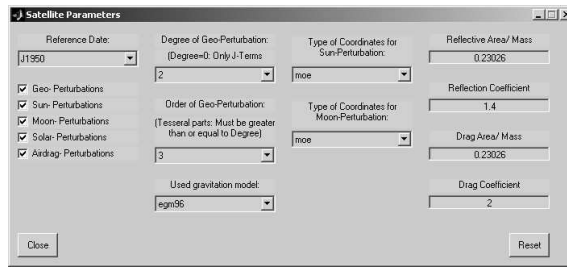


Figure A.3: Parameter Settings Concerning the Orbit Propagation

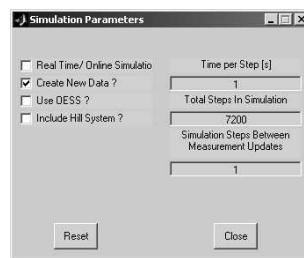


Figure A.4: Parameter Settings Concerning the Simulation

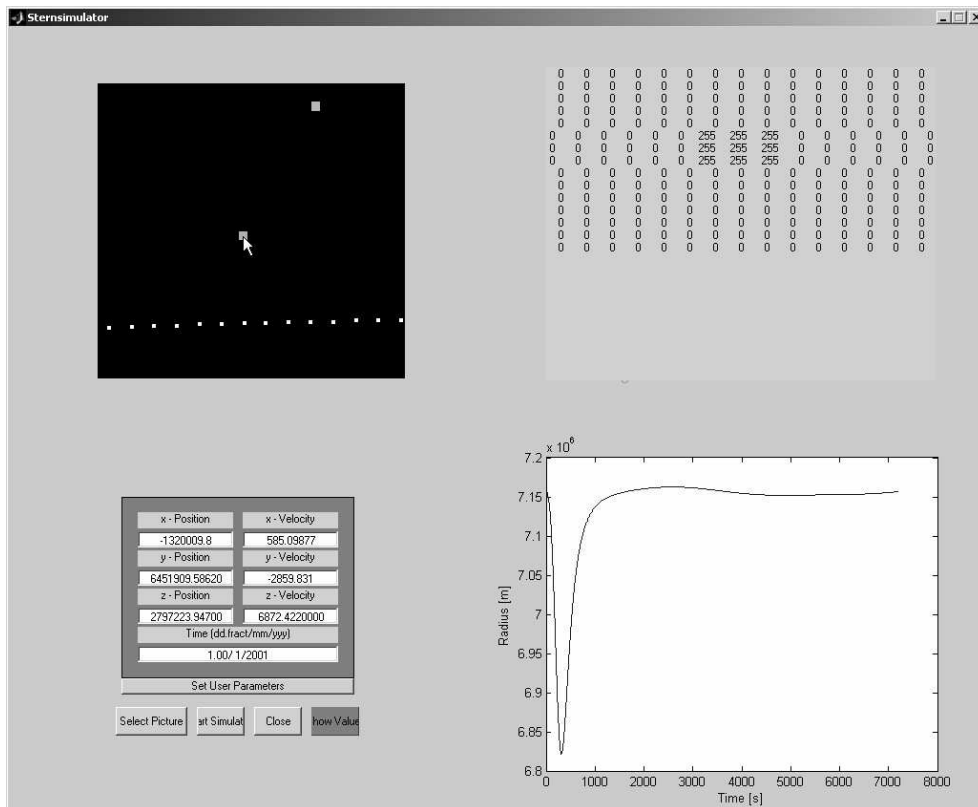


Figure A.5: Graphical User Interface, diagnostic mode

A.3 Experiments

A.3.1 Camera Parameters for cameras used in the experiments

Table A.9: Technical Data IBIS1-APS-Detector (Flight-Experiment)

Size [mm ²]	6.5 × 5.3
Pixel Size [μ m ²]	14 × 14
No. of Pixels [-]	290 × 386
Quantization [bit]	10
Fillfactor [%]	72
Dark Current Noise [mV (Photon Equivalent)]	
00°C	23
20°C	24 (100)
40°C	28

Table A.10: Technical Data IBIS4b-APS-Detector (Laboratory-Experiment, Field-Experiment)

Size [mm ²]	8.96 × 7.17
Pixel Size [μ m ²]	7 × 7
No. of Pixels [-]	1280 × 1024
Quantization [bit]	10
Fillfactor [%]	58
Dark Current Noise [electrons/s]	
20°C	800

Table A.11: Technical Data PCS-2112-LM-x-APS-Detector (Laboratory-Experiment, Field-Experiment)

Size [mm ²]	6.5 × 5.3
Pixel Size [μ m ²]	7.5 × 7.5
No. of Pixels [-]	1280 × 1024
Quantization [bit]	10
Fillfactor [%]	51
Dark Current Noise [bit]	
20°C	5

A.3.2 Flight Experiment

Prior to this project, an In-Orbit Experiment, as mentioned in chpt.7, has been carried out. This section contains detailed information on the secondary sensors used.

A.3.2.1 Magnetic Field Sensor

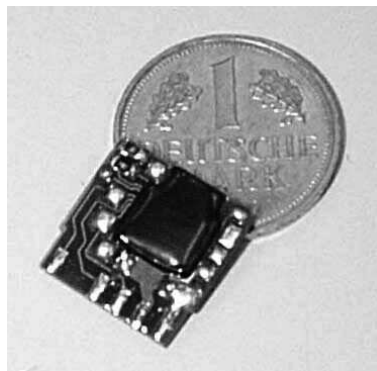
As magnetic field sensor (MFS), the FGS1/COB05 by the *Fraunhofer Institute of Microelectronic Circuits and Systems*(IMS), Dresden, was chosen (for technical data see table A.12).

It consists of two planar fluxgate sensors with precisely oriented perpendicular sensitive axes (X,Y) and an ASIC for sensor supply, readout and signal processing, built on an printed circuit board.

The two-axes fluxgate sensor is fabricated in a CMOS compatible planar technology. The sensor consists of an arrangement of flat three-dimensional coils, surrounding a ferromagnetic core. Driven by a excitation current, the core is periodically saturated. Due to the changes of magnetic flux inside the core a voltage is induced in the pick-up coils. The second harmonic of this voltage depends on the external field. The signal processing is done by a special designed ASIC using second harmonic detection combined with a zero field compensation method realized by a feedback loop.

The sensor is powered with +5 Volts and gives an analogue output voltage in the range of 0.5...4.5 Volts corresponding to the external magnetic field in the maximum detectable range of $\pm 80 \mu\text{Tesla}$ for each axis. Due to the existence of disturbing magnetic field inside and outside the MTS-AOMS experiment the mounting position has to be chosen carefully, which is why in many experiments, the MFS is mounted on a boom. The MFS output voltages are fed into the MITA telemetry channel where they are 12 bit A/D converted. The sampling rate is 1 Hz.

Table A.12: Technical Data of Magnetic Field Sensor



Sensor	FGS1/COB05, FHG-IMS
Size	$46 \times 12 \times 0 \text{ mm}^3$
Mass	5 g
Power	130 mW
No.of Axes	4
Measurement Range	$\pm 80 \mu\text{Tesla}$
Sensitivity	$28.6 \text{ mV}/\mu\text{Tesla}$
Noise [RMS]	$< 0.2 \mu\text{Tesla}$
Drift	$< 0.2 \mu\text{T}/110 \text{ min}$
Temperature Range	$-40 \text{ }^\circ\text{C} \dots +80 \text{ }^\circ\text{C}$
Shock Insusceptibility	200 g (10 ms)

A.3.2.2 Angular Rate Sensor

An important component of the experiment was the angular rate sensor (ARS). It was to be shown that a commercially available sensor, based on MEMS technology is capable of improving the attitude and angular rate information of a satellite, and thus providing a second reference in the case no optical observations are available. In the frame of these studies, a master-thesis ([2]) showed that it is indeed possible to maintain an accuracy of $1.5 (10)^\circ$ in pitch/yaw (roll), for about 40 minutes, when taking into account an additional thermal calibration of the sensor. These values can even be increased to approx. $0.1 (0.7)^\circ$ in pitch/yaw (roll) by use of a better Star-sensor for calibration.

The angular rate sensor (ARS) is a commercial device by Robert Bosch GmbH, Stuttgart (D), as seen in fig.A.6, developed for the dynamic control system in cars (for technical data see table A.13). The sensor part is encapsulated in a hermetic sealed metallic housing. The module is produced in serial production and is tested and calibrated with standard methods. The module contains an angular rate sensor, a linear inertial sensor and the evaluation electronics, all components realized on one hybrid. The functional principle of the angular rate sensor is based on two vibratory masses equipped with conductor paths carrying an alternating current. The masses are located in a homogeneous magnetic field, thus the Lorentz force acts on the moving masses. If the masses are subjected to a rotation an additionally Coriolis force is affecting the masses. This additional acceleration due to the Coriolis forces is detected and transformed to a signal which is proportional to the angular rate. The sensor is placed in the MTS-AOMS experiment in such a way that it records the satellite's rotation around its orbital axis.

The angular rate sensor's nominal output signal is in the range 0.5...4.5 Volts, equivalent to an angular rate of $-100...+100^\circ/\text{s}$. In the MTS-AOMS experiment the output signal is 12-bit digital converted and transmitted in the same way as the magnetic field sensor signals to the satellites telemetry channel. A second output is bandwidth limited to 1 Hz and amplified to provide a better angular resolution of $0.08^\circ/\text{s}$ (1σ) in a reduced measurement range of $-10...+10^\circ/\text{s}$. In this „high resolution“ mode the sensor is sensitive enough to resolve the satellite's rotation around the orbital axis in its nominal nadir pointing mode (360° in 83 min = $0.07^\circ/\text{s}$). In each test campaign the ARS was operated together with the MFS over one complete orbit (83 min). Data acquisition is every second for the nominal and the high resolution output. In the process of evaluating the flight data, it was shown that the filtered output failed and was thus disregarded in the further process.

In the frame of this project, the performance of the sensors was compared by integrating the gyro signal and differentiating the magnetometer signal. The comparisons showed that the overall behavior agreed well with the expectations, as the processed data of one sensor agreed with the

unprocessed of the other. The only divergence was given during the times of polar passages, since in these cases, the Earth magnetic field tends to change its direction and thus imply a motion of the satellite, in case the magnetic field is not modeled and taken into account in the attitude measurements.

The evaluation of the flight data confirmed that it is indeed possible to observe the Earth and Stars on the same detector. Contemporaneously, it was shown that additional components, such as gyros and possibly magnetic-field sensors, should be used in order to guarantee reliable information at all times.

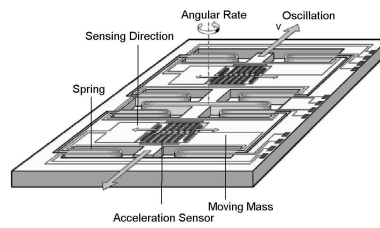
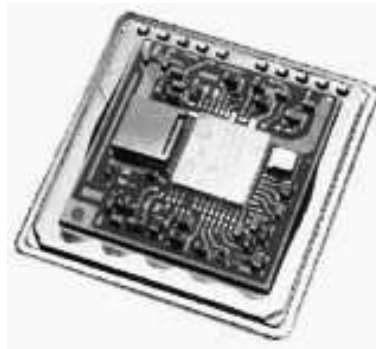


Figure A.6: Measurement Principle of Angular Rate Sensor (DRS-MM1.0, Bosch)

Table A.13: Technical Data of Angular Rate Sensor



Sensor	DRS-MM2.0, Bosch
Size	$16 \times 12 \times 3 \text{ mm}^3$
Mass	20 g
Power	980 mW
No. of Axes	1
Measurement Range	$\pm 100^\circ/\text{sec}$
Sensitivity	$17.5 \text{ mV}/(^\circ/\text{sec})$
Noise [RMS]	$0.22^\circ/\text{sec}$
Drift	$< 0.15^\circ/\text{sec}/\sqrt{h}$
Temperature Range	$-40^\circ\text{C} \dots +80^\circ\text{C}$
Shock Insusceptibility	200 g (10 ms)

A.4 Miscellaneous

A.4.1 Accuracy Requirements

Table A.14: Accuracy Requirements (3σ) of Typical Missions

Mission	Example	Orbit Height	Orbit Inclination	Position Accuracy	Attitude Accuracy
LEO	Globalstar	$\simeq 1000$ km	$0^\circ < \alpha < 180^\circ$	1 km	0.01° - 1°
MEO	Galileo	$\simeq 20000$ km	$0^\circ < \alpha < 180^\circ$	1 m	0.01° - 0.1°
HEO	Molnya, GTO	400×36000 km (GTO)	0°	< 1 km	0.5° - 1°
GEO	Telecommuni- cation and TV-Broadcast	36000 km	0°	35(70) km	0.01° - 0.1°
Science	-	all heights	$0^\circ < \alpha < 180^\circ$	highly mission dependent, down to or- der of several meters	0.001° - 0.01°

A.4.2 Sources of Perturbations

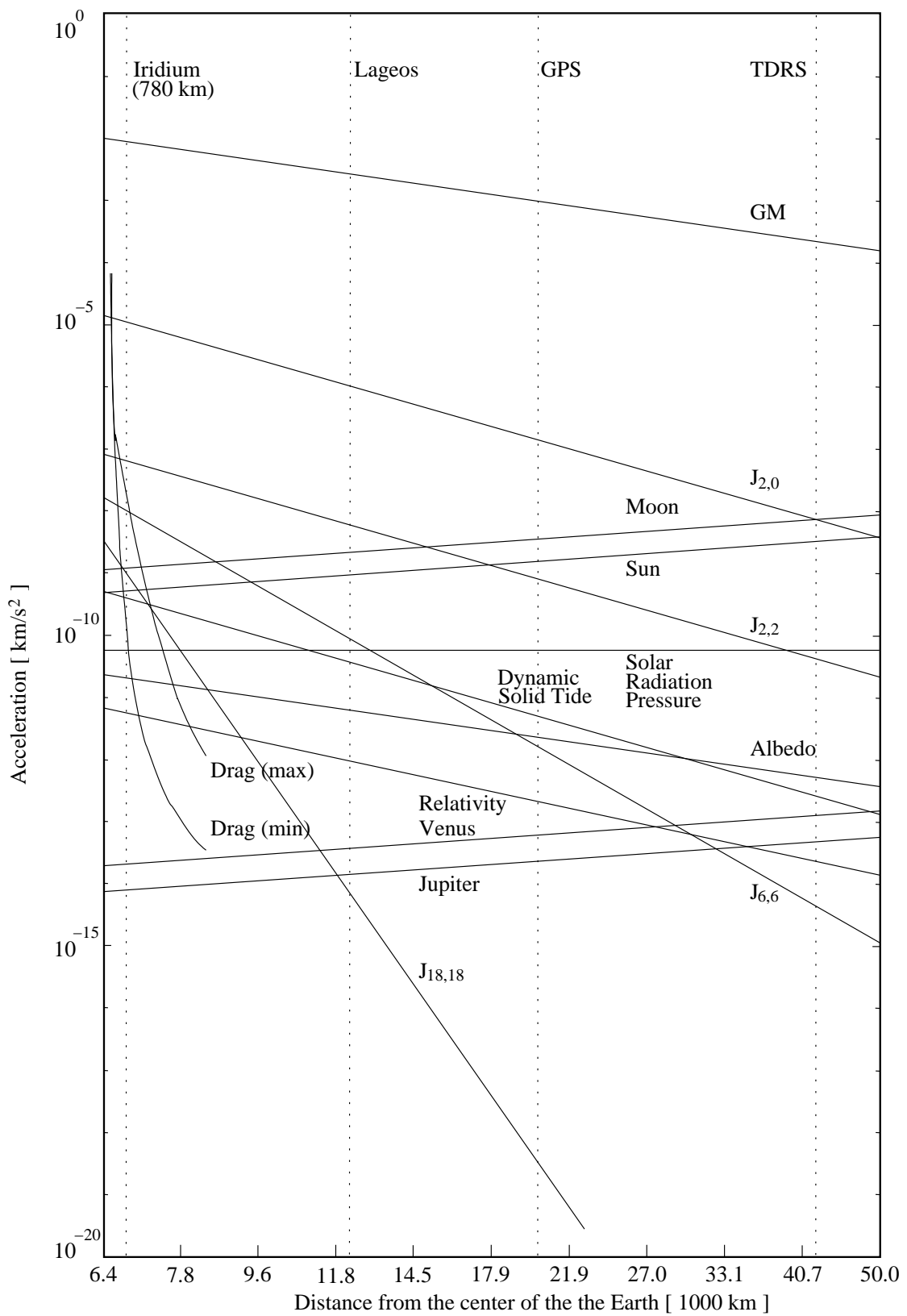


Figure A.7: Perturbations as a function of orbit radius (see [28])

A.4.3 Abbreviations & Nomenclature

Abbreviations

a.u.	Astronomical Units (approx. 150×10^9 m)
APS	Active Pixel Sensor
ARS	Angular Rate Sensor
DCM	Direction Cosine Matrix
DJO	Jena-Optronik GmbH
ECI	Earth-Centered-Inertial (reference system)
EEA	Earth Exclusion Angle
EMF	Earth Magnetic Field
FOV	Field Of View
GEO	Geostationary Earth Orbit
GMT	Greenwich Mean Time
GTO	GEO-Transfer Orbit
GUI	Graphical User Interface
HARM	High Angular Rate Mode
HEO	Highly Eccentric Earth Orbit
HPOP	High Precision Orbit Propagator
IR	InfraRed (light spectrum)
IRES	InfraRed Earth Sensor
JPL	Jet Propulsion Laboratory
LARM	Low Angular Rate Mode
LEO	Low Earth Orbit
LOS	Line Of Sight
LVLH	Local Vertical, Local Horizontal (reference system)
MBB	Messerschmitt- Bölkow- Blohm GmbH
MEMS	Micro-Electro-Mechanical-Systems
MEO	Medium Earth Orbit
MFS	Magnetic Field Sensor
MITA	Minisatellite Italiano a Tecnologia Avanzata
MST	Micro-System-Technology
MVIRI	Meteosat Visible and InfraRed Imager
NEA	Noise Equivalent Angle
NLO	Non-Linear Optimization
OBCU	On Board Computer Unit

OFTB	Optical Functional Testbed
SAA	South Atlantic Anomaly
SAR	Synthetic Aperture Radar
SCI	Sun-Centered-Inertial (reference system)
SEA	Sun Exclusion Angle
SEU	Single Event Upset
SLR	Satellite Laser Ranging
S/N	Signal-to-Noise (ratio)
SSO	Sun Synchronous Orbit
STK	Satellite Tool Kit [®] by <i>Analytical Graphics</i>
TFO	Technology Flight Opportunity
UV	UltraViolet (light spectrum)
VIS	Visible (light spectrum)

Nomenclature

A	Attitude (direction cosine) matrix
\underline{b}	Star-vector in Sensor-system
f	Focal length of the optical system
\underline{q}	Quaternion, ([q1,q2,q3],q4)
\underline{r}_x	Unit Vector in x -System, in special cases: Star-vector to x^{th} Star in ECI
\underline{P}	state covariance-matrix
\underline{Q}	process-noise covariance-matrix
\underline{R}	measurement-noise covariance-matrix
$Signal(x, y)$	Pixel value of pixel at position (x, y) on the detector
T_{uv}	Transformation from u to v

Indices

B	Body-fixed
E	Earth-sensor
I	Inertial
M	Mounting
R	Reference
S	Star-sensor

Auxiliary Variables

c_r	Coordinates of Center of a circle
$c_{r,x}$	x -Coordinates of Center of a circle
$c_{r,y}$	y -Coordinates of Center of a circle
c_x	x -Coordinates of Center of Illumination
c_y	y -Coordinates of Center of Illumination
Δr_{max}	Maximum difference between Earth-radius as determined from the individual measurement to the reference radius as determined from a measurement triplet
e_{Earth}	Earth Eccentricity (approx. $e_{Earth} = 0.081$)
$Inner_i$	Inner subset of candidate region (see fig. 3.3)
G	Temporary variable in the Earth-detection process
\underline{g}_1	Temporary variable in the Earth-detection process
\underline{g}_2	Temporary variable in the Earth-detection process
m	List of Measurement-Coordinates
m_i	Coordinates of Measurement i
$m_{i,x}$	x -Coordinate of Measurement i
$m_{i,y}$	y -Coordinate of Measurement i
m_{New}	List of Transformed Measurement-Coordinates
$Mean_{bright,min}$	Minimum Mean of the pixels brighter than a given threshold
$Mean_{dark,min}$	Minimum Mean of the pixels darker than a given threshold
$n_{[\dots]}$	Star-polygons consisting of measurements/ Stars with indices $[\dots]$
n_{bright}	Number of Points brighter than a given threshold
$n_{bright,min}$	Minimum Number of Points brighter than a given threshold
n_{dark}	Number of Points darker than a given threshold
$n_{dark,min}$	Minimum Number of Points darker than a given threshold
$n_{\Delta,i}$	Number of Measurements within the tolerance Δr_{max} for the comparison corresponding to triplet i
$n_{ratio,min,lower}$	Second (Lower) Minimum Ratio for $n_{\Delta,i}/n_{total}$
$n_{ratio,min,upper}$	First (Upper) Minimum Ratio for $n_{\Delta,i}/n_{total}$
n_{total}	Total Number of Measurements
$n_{triplets}$	Total Number of possible Triplets
$Outer_i$	Outer subset of candidate region (see fig. 3.3)
p_{ij}	Star-pair consisting of measurements/ Stars with indices i and j , respectively
R_i	Candidate region i
$R_{i,bright}$	Subset of R_i which contains the pixels brighter than a given threshold

$R_{i,dark}$	Subset of R_i which contains the pixels darker than a given threshold
$R_{i,line}$	Line-shaped sub-set of Candidate region R_i
$R_{i,sub}$	Sub-set of Candidate region R_i
T_{Earth}	Orientation of the Earth relative to the detector-axes
t_{ijk}	Triangles consisting of measurements/ Stars with indices i,j and k , respectively
t_p	p^{th} Triangle under investigation

A.5 Curriculum Vitae

Personal Information

Christopher T.F. Kühl
 Born: 24.12.1975 in Mainz, Germany
 Marital Status: Single, no children
 e-mail: c.t.f.kuehl@gmx.net



Current Position

System Engineer at Jena-Optronik GmbH, Germany

Education

1982– 1986	Georg- August- Zinn- Elementary School in Darmstadt- Wixhausen, Germany
1986– 1995	Edith- Stein- Schule, private Catholic High School in Darmstadt, Germany
21.08.1995– 15.10.1995	Internship (machining, welding, soldering) at Lufthansa, Airport Frankfurt
10/1995– 10/2000	Aerospace Engineering at the University of Stuttgart Diploma-Grade „Sehr Gut“ [scale: „Sehr Gut“(1): best, „Gut“(2), „Befriedigend“(3), „Ausreichend“(4), „Mangelhaft“(5): failed]
01.10.1997– 31.03.1998	Internship at the University of California, Los Angeles (Flight Systems Research Center)
01.07.1999	Accepted as Daimler-Chrysler Scholarship Holder
27.07.1999– 30.10.1999	First Master Thesis at the University of California, Los Angeles (Flight Systems Research Center) Title: „Gust Load Alleviation Using Finite Element Modeling“ Letter Grade: A+ (translated to 1.3)
01.05.2000– 31.10.2000	Second Master Thesis at the University of Stuttgart, Germany (Institute of Space Systems) Title: „Determining the Concentration of Atomic Nitrogen for Character- ization of Re-Entry-Simulations for Space-Transport-Systems Using Laser Induced Fluorescence“ Numerical grade 1.0
08.01.2001– 30.09.2004	Astrium GmbH, Ottobrunn (Munich), Ph.D.-Student at the Department of Flight Dynamics and Control at the Uni- versity of Stuttgart Title: „Combined Earth-Star-Sensor for Autonomous Attitude And Orbit De- termination In Geostationary Orbits“
since 01.10.2004	System Engineer at Jena-Optronik GmbH, Germany Project Manager: Robust Algorithms for Star Trackers

Interests

psychology, biology, art, literature, saxophone